Strongly Variable Viscosity Flows in Mantle Convection

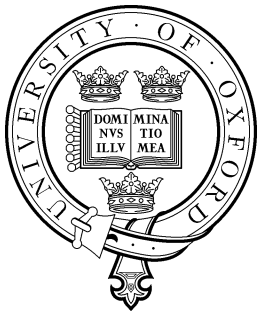

Tania S. Khaleque

Oriel College

University of Oxford

A thesis submitted for the degree of

Doctor of Philosophy

Trinity Term 2015

To my parents and two sisters
for their unending blessing and encouragement

Acknowledgements

I would like to thank my supervisors, Professor Andrew Fowler and Professor Peter Howell, for their invaluable direction, insightful comments, encouragement and support throughout the last four years. I have been very fortunate to have such excellent supervisors who tirelessly explained me various things, but above all believed in me.

I would also like to thank Dr. Michael Vynnycky of University of Limerick, now in KTH, for his useful suggestions regarding the numerical model. I had a fine time with my fellow students and other faculty members in OCIAM and OCCAM but my special thanks goes to Gemma, Emma, Patrick, Chang, Nick and Julia.

On a personal note, I thank my younger sister Tahirah, whose support and humour through the highs and lows of the past four years has been truly invaluable. I am thankful to my elder sister Sonia for all her practical advice, which I follow in my subconscious mind. I am indebted to my mother simply because she has made me brave enough to face the challenges in life. Lastly, I am eternally grateful to my father for all his silent prayers for me.

I also express my warmest gratitude to the Banglaedeshi families living in Oxford to offer me a home away home. I will never forget the memories and the friends I made through Oxford University Bangladesh Society.

I gratefully acknowledge the financial support of the Felix Scholarship.

Statement of Originality

I confirm that this thesis is wholly my own original work, and that no part of my thesis has been accepted or is currently being submitted for any degree, diploma, certificate or other qualification at the University of Oxford or elsewhere. All methods and techniques used in this thesis that have been developed by other authors have been acknowledged by citation of the relevant publication.

Strongly Variable Viscosity Flows in Mantle Convection

Tania S. Khaleque

Oriel College
University of Oxford

A thesis submitted for the degree of Doctor of Philosophy

Trinity Term 2015

Convection in the Earth's mantle is a complicated phenomenon that causes various tectonic activities and affects mantle evolution on geologic time scales (billions of years). It is a subject as yet not fully understood. The early success of the high Rayleigh number constant viscosity theory was later tempered by the absence of plate motion when the viscosity is more realistically strongly temperature dependent. A similar problem arises if the equally strong pressure dependence of viscosity is considered, since the classical isothermal core convection theory would then imply a strongly variable mantle viscosity, which is inconsistent with results from post-glacial rebound studies. We consider a mathematical model for Rayleigh-Bénard convection in a basally heated layer of a fluid whose viscosity depends strongly on both temperature and pressure, defined in an Arrhenius form. The model is solved numerically for extremely large viscosity variations across a unit aspect ratio cell, and steady solutions are obtained. To improve the efficiency of numerical computation, we introduce a modified viscosity law with a low temperature cut-off. We demonstrate that this simplification results in markedly improved numerical convergence without compromising accuracy. Continued numerical experiments suggest that narrow cells are preferred at extreme viscosity contrasts. We are then able to determine the asymptotic structure of the solution, and it agrees well with the numerical results. Beneath a stagnant lid, there is a vigorous convection in the upper part of the cell, and a more sluggish, higher viscosity flow in the lower part of the cell. We then offer some comments on the meaning and interpretation of these results for planetary mantle convection.

Contents

List of Figures

List of Tables

Chapter 1

Introduction

Convection in the mantle is an important method of heat transport within the Earth. It is also the driving mechanism for plate tectonics, which is the process ultimately responsible for producing earthquakes, mountain ranges and volcanoes. In this introduction we will begin by giving a general overview, discussing the interior of the Earth and the gradual emergence of the concept of mantle convection.

1.1 Structure of the Earth

Around 4.6 billion years ago the solar system was formed by gravitational collapse of a localized, dense region of a large interstellar molecular cloud. Contraction of this cloud led to the accretion of a central star surrounded by a rotating disk of gas and dust, termed the *solar nebula*. The planets of the solar system grew by collisions, starting with the aggregation of tiny dust particles within the solar nebula and culminating in giant collisions between large planetary bodies. The Earth accreted most of its mass by collisions which were highly energetic and raised the temperature of Earth's interior by thousands of degrees, causing widespread melting and the formation of magma oceans. In these oceans, the denser metallic iron and its alloys easily separated from the molten silicate and segregated towards the centre, and eventually formed the most stable arrangement of a rotating, self-gravitating mass of material - an oblate spheroid. Thus, accretion and core formation were intimately linked and, as metal segregation is thought to happen much faster than accretion, the rate of Earth's accretion can be determined by dating the formation of the Earth's core. The core-formation events (one event per giant impact or collision) are particularly important because core formation is the biggest differentiation process of the Earth: it involves one-third of the Earth's mass and a large energy release, because the iron is about twice as dense as the silicates. To a substantial extent, it also defines the composition

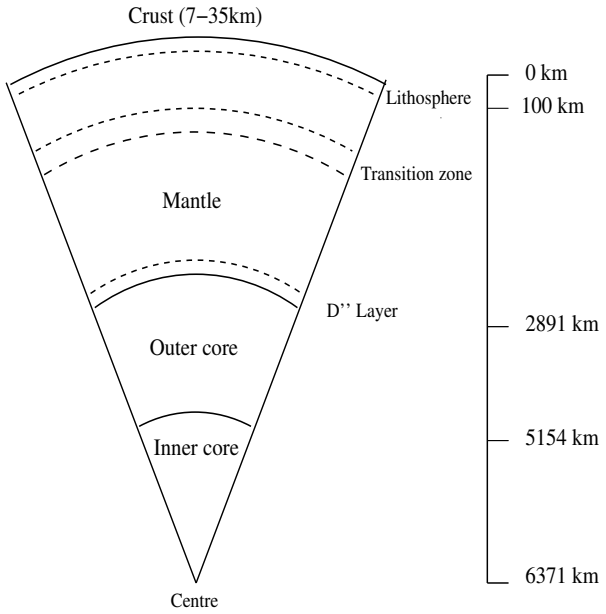

Figure 1.1: Schematic diagram of the major components of the Earth's interior.

of the Earth's mantle. Our understanding of planet formation is based on information from various sources, including meteorites and samples from the Earth and Moon. By combining results from isotopic dating of these materials with dynamic modelling of the solar nebula and planet formation, researchers can reconstruct the accretion and early evolution of planetary bodies during the first 100 million years (approx.) of solar system history (Dalrymple, 2001, Kleine and Rudge, 2011, Stevenson, 2008, Tackley, 2012).

The study of the seismic waves generated by earthquakes also provides information regarding the internal constitution of the Earth. The waves which follow various paths through the interior of the Earth are known as body waves, and by measuring their travel times to different locations around the globe it is possible to determine its large scale layering. It is also possible to make inferences about the physical properties of these layers from a consideration of the velocities with which they transmit the seismic waves. P waves correspond to elastic deformation by compression and S waves correspond to elastic deformation of the transmitting medium by shearing and cause the particles of the rock to oscillate at right angles to the direction of propagation. P and S waves are the two types of body waves. Since the rigidity of a fluid is zero, S waves cannot be transmitted by such a medium.

The major divisions of the Earth's interior are shown in Figure 1.1. The crust, mantle and core were recognized in the early part of the 20th century following Mohorovičić's 1909 discovery of the crust-mantle boundary (Moho) and Gutenberg's

determination of the core-mantle boundary at a depth of 2891 km, the outer core radius (Gutenberg, 1913). Lehmann (1936) inferred the existence of the inner core and Jeffreys (1939) produced compressional and shear wave velocity profiles featuring a transition zone between about 400 km and 1000 km depth in the mantle.

The rocks exposed at the surface of the Earth are part of the *crust*. This crustal layer, which is rich in silica, is on average 35 km thick beneath the continents and 7-8 km thick under the oceans. Continental crust appears to be extensively folded and faulted and preserves evidence of being subjected to multiple tectonic events, whereas oceanic crust is much more stable and has suffered relatively little deformation except at plate margins. Wave-speeds increase abruptly at the Moho in both continental and oceanic environments.

The *mantle*, which constitutes 82% of the Earth's volume, extends from the Moho, at a mean depth of about 21 km, to the core-mantle boundary at a depth of roughly 2891 km. Between 410 and 660 km wave-speed increases rapidly in a stepwise fashion which is known as the mantle *transition zone* and it separates the upper mantle from the lower mantle. Both P and S velocities increase progressively in the lower mantle. In the uppermost mantle, the dominant rock type is peridotite with 5-10% eclogite, whereas the dominant mineral in the deep mantle is a magnesium silicate (Davies, 1999). High pressure mineral physics experiments indicate that mantle discontinuities are most likely associated with solid-solid phase transitions not compositional changes (Bercovici, 2009). The lowest 200-300 km of the mantle, Layer D'' is often characterized by a decrease in seismic velocity, which is probably related to an increased temperature gradient above the mantle-core boundary (Kearey et al., 2009). The lower layer shows large lateral changes in seismic velocity, indicating that it is very heterogeneous. Laboratory experiments suggest that the liquid iron of the core reacts with mantle silicates in the D'' layer, with the production of metallic alloys and nonmetallic silicates from perovskite. Layer D'' thus is important because it governs core-mantle interactions and also may be the source of deep mantle plumes (Kearey et al., 2009).

The Gutenberg discontinuity marks the boundary between the core and the mantle at a depth of 2891 km, at which the velocity of P waves decreases abruptly. S waves are not transmitted through the *outer core*, which is consequently believed to be in a fluid state. At a depth of 5150 km the P velocity increases abruptly and S waves are once again transmitted. As a result, the *inner core* is believed to be solid. The core is inferred to be composed mainly of iron, but a significant proportion of the outer

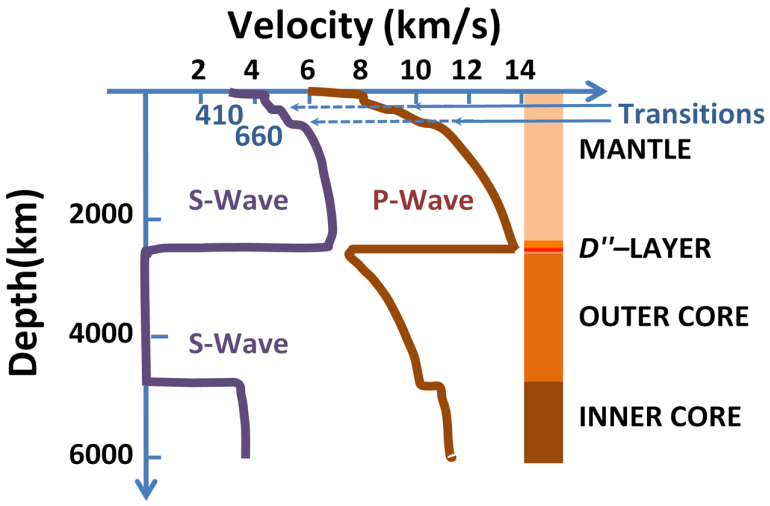

Figure 1.2: Seismic wave velocities as functions of depth in the Earth (reproduced from Helffrich and Wood (2001)).

core material (perhaps 10-20%) comprises elements of lower atomic weight, such as oxygen, sulphur or silicon (Davies, 1999, Jeanloz, 1990).

The variation of seismic velocities with depth results from a number of factors. The increase of pressure with depth causes a rapid increase in bulk modulus, elastic modulus, and density over the topmost 5 km as pores and fractures are closed (Kearey et al., 2009). Thereafter the increase of these parameters with pressure is balanced by the decrease resulting from thermal expansion with increasing temperature so that there is little further change in velocity with depth. Abrupt velocity discontinuities are usually caused by changes in chemical composition, while more gradational velocity boundaries are normally associated with phase changes that occur over a discrete vertical interval (Kearey et al., 2009). A velocity-depth curve for both P and S waves is shown in Figure 1.2.

1.2 Continental drift

The development of the concept of mantle convection started with the theory of continental drift. Since the 16th century, cartographers have noticed the jigsaw-puzzle fit of the continental edges. From the 19th century, geologists have known that some fossil plants and animals are extraordinarily similar across the globe, and some sequences of rock formations in distant continents are also strikingly alike. On the basis of these facts the German meteorologist Alfred Wegener (1915) proposed the theory of continental drift. Although the hypothesis of continental drift is quite

rightly associated with the name of Alfred Wegener, Taylor (1910) might be the earliest writer who suggested this idea. According to this theory, the paleontological patterns and jigsaw-puzzle fit could be explained if the continents had migrated across the Earth's surface, sometimes joining together, sometimes breaking apart. Wegener (1915) argued that for several hundred million years during the late Paleozoic and Mesozoic eras (200 million to 300 million years ago), the continents were united into a supercontinent that he labelled Pangaea - all Earth. Another idea supporting movement of the continents was the glacial till deposits in the southern hemisphere. With the continents in their present positions, the till deposits indicate erratic glacier motion. When the continents are fitted together, they show a much more streamlined motion of the glacier from southern Africa and Northern Australia outward. Wegener collected ancient climate information to confirm his glacial data. For the glaciers to have been present with the continents in their current positions, much of the world should have been under ice. But this wasn't the case. Sedimentary rock examination showed a change in climates, and the only possible explanations were continental drift or movement of the poles.

Despite all the evidence, Wegener's ideas were not widely accepted at that time as critics thought that the evidence was not strong enough, that the underlying cause of the drift was not explained and that the drift was impossible. In fact, his ideas challenged scientists in geology, geophysics, geography and paleontology, and it demonstrates the reactions of different communities of scientists. Part of the problem was that Wegener had no convincing mechanism for how the continents might move. At the beginning Wegener proposed a mechanism that focused on his assertion that the rotation of the Earth created a centrifugal force towards the equator. He believed that Pangaea originated near the south pole and that the centrifugal force of the planet caused the protocontinent to break apart and the resultant continents to drift towards the equator. This idea was quickly rejected by the scientific community primarily because the actual forces generated by the rotation of the Earth were calculated to be insufficient to move continents. Wegener also came to realize that his own proposed mechanism was inadequate for continental drift. Thus his immediate goal was to have the concept openly discussed. These modest goals did not spare him. The authorities in the various disciplines attacked him because even the possibility of continental drift was a huge threat to the authorities in each of the disciplines (Oreskes, 2003). These reactions eventually shut down serious discussion of the concept. However, Wegener eventually considered the possibility of mantle convection, and made passing reference to it as a plausible driving force in the final edition of his book (Wegener, 1929).

But Wegener chose not to promote it as the cause of continental drift, and the idea languished once again (Schubert et al., 2001).

Holmes (1931, 1933) proposed that the mechanisms of *thermal convection* in the mantle were the driving forces of continental drift. This idea is based on the fact that as a fluid is heated, its density decreases and it rises to the surface until it is cooled and sinks again. This repeated heating and cooling results in a current which may be enough to cause continents to move. Arthur Holmes suggested that this thermal convection was like a conveyor belt and that the upwelling pressure could break apart a continent and then force the broken continent in opposite directions carried by the convection currents. Since the scientific community was not ready to consider 'mantle' as a fluid even on a long time scale, this idea received very little attention at that time. In fact, not until the 1960s did Holmes' idea receive any attention.

In the early 1960s, Dietz (1961) and Hess (1962) proposed that continental drift might be accomplished by a process named *seafloor spreading*. Hess proposed that not only were the continents moving, but the sea floor was also moving. Motion of the sea floor in a conveyor belt fashion explains the phenomenon of the youngest rocks being found only at the mid-ocean ridges, and the rocks getting progressively older as you move away from the ridge. By that time, geophysicists discovered that the Earth's magnetic field periodically reverses; i.e. the north magnetic pole becomes the south pole and vice versa. Hence, the Earth has experienced periods of reversed polarity alternating with times of normal polarity. If this idea is correct, alternating stripes of normal and reversed polarity should be arranged symmetrically about mid-ocean spreading centres. Measurements of magnetic variations discovered such magnetic stripes and provided powerful evidence that sea-floor spreading occurs. If the sea floor is spreading, then clearly the continents could diverge from one another. Hess's explanation of the motion of the sea floor was *mantle convection*. It has been understood that the Earth's mantle behaves plastically. Thus through the discovery of palaeomagnetic pole paths and seafloor spreading, it was finally possible to support Wegener's theories and convert the critics.

1.3 Plate tectonics

Plate tectonics is a model in which the outer shell of the Earth, termed the *lithosphere*, is broken into a number of thin rigid plates. Because of their low temperature, rocks in the lithosphere resist deformation on time scales of up to 10^9 yr. In contrast, due to high temperatures, rocks beneath the lithosphere can flow by subsolidus viscous

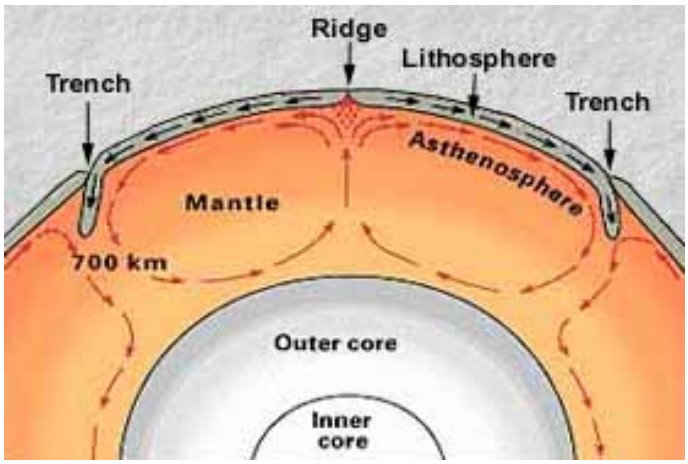

Figure 1.3: Schematic of the whole mantle convection in the Earth.
Source: http://www.geology.sdsu.edu

creep and this region is called the *asthenosphere*. The average thickness of the tectonic plates is about 100 km and they move with respect to one another. The relative velocities of the plates are of the order of a few centimetres per year. The concept of rigid plates with deformations primarily concentrated near plate boundaries provided a comprehensive understanding of the global distribution of earthquakes (Isacks et al., 1968). The three types of structures used to define plate boundaries are ridges, trenches, and transform faults. At ocean ridges, adjacent plates move apart in the process of seafloor spreading. As the adjacent plates diverge, hot mantle rock ascends to fill the gap. The hot, solid mantle rocks behave like a fluid because of solid-state creep processes. As the hot mantle rock cools, it becomes rigid and accretes to the plates, creating new plate area. For this reason, ocean ridges are also known as accretionary plate boundaries. Since the surface area of the Earth is constant, there is a complementary process of plate consumption. This occurs at ocean trenches. When the plates move away from ocean ridges, they cool and thicken and their density increases due to thermal contraction. As a result, the lithosphere becomes gravitationally unstable with respect to the warmer asthenosphere beneath and because of its negative buoyancy the lithosphere bends and sinks into the interior of the Earth creating an ocean trench (Schubert et al., 2001). The process in which the surface plates bend and descend into the interior of the Earth is known as *subduction*.

Plate tectonic theory predicts that the majority of the Earth's tectonic activity takes place at the margins of plates. It follows, then, that the location of earthquake epicentres can be used to define plate boundaries. Volcanoes, like earthquakes, are strongly clustered at plate boundaries, mainly subduction zones. As a plate subducts

it expels water into the overlying mantle, causing that area of mantle above the descending plate to melt a little and the resulting volcanism at the surface builds volcanic chains like the Andes of South America and the Aleutian Islands of Alaska. Some of the world's most destructive volcanoes and the world's largest earthquakes occur at these places. The very deepest parts of the world's oceans are associated with plate convergence at subduction zones.

It is really these plates that are in motion as the thermal boundary layer of mantle convection and they carry the continents with them. What we recognize as continental drift is a direct consequence of plate tectonics. However, the exact picture of how plate motions are caused by convection is far from complete. With the recognition of the importance of slab pull, and that subducting slabs are essentially cold downwellings, it is becoming more widely accepted that the plates are an integral part of mantle convection (Davies and Richards, 1992).

1.4 Plate mode and plume mode

The evidence of convective flow in the mantle, from seismic tomography and studies of the regional elevation and subsidence of the Earth's surface, strongly suggests that there are two main driving forces for this convection. The negative buoyancy of cold subducting lithosphere would appear to determine the main sites of downwelling, and the positive buoyancy of hot, low viscosity material originating in the lowermost, D'' layer of the mantle determines the upwellings. These two complementary modes of convection in the mantle have been termed the *plate* and *plume modes*, respectively (Davies, 1999). The plate mode arises from the strong cooling at the surface, and the weak internal heating of the mantle. It is responsible for the majority of the heat transfer out of the Earth. The plume mode is associated with narrow, thermal upwellings in the mantle that may be rooted at the core-mantle boundary. It arises because the mantle is heated from below by the core. The plume mode accounts for only a small fraction of the heat transfer out of the Earth. The plate mode is crucial in cooling the mantle, by the creation of oceanic lithosphere, and the plume mode releases heat from the core. The heat released by the plate mode is thought to be much greater than that released from the core. One might expect therefore that the plate mode is dominant. However, these two very different modes of convection need not necessarily be strongly coupled (Kearey et al., 2009).

1.5 Mantle property: viscosity

One of the most distinguishable characteristics of the mantle is its viscosity and it plays a vital role in mantle convection. The mantle is primarily assumed to be solid as the seismic shear waves pass through it efficiently. However, when the mantle is subjected to longer-term stresses, it flows like a fluid: the rate of deformation is proportional to the size of the stress. This is known from glacial isostatic rebound. The ice sheets that covered Canada, Scandinavia and Finland during the last ice age melted at about 11,000 years before present. Since then, relative sea-level in those regions has been falling, indicating a rebound of the land surface. This drop in sea-level is approximately exponential, with a time-constant of 4.6 kyr. This information is used to approximate the viscosity of the mantle. The analysis of Davies (1999) equates the isostatic force causing rebound with the viscous resistance force of mantle flow back into the area. Isostasy requires that pressure is constant at a depth D in the mantle. A column of rock with density ρ_m that was unaffected by the ice sheet has pressure $\rho_m g D$ at its base. In the affected area, there is a depression of depth h left by the ice after it melts. If this depression is filled with water of density ρ_w, then it has pressure $g(\rho_w h + \rho_m(D-h))$ at its base. The pressure difference between these two columns of rock is thus

$$\Delta P = g(\rho_m - \rho_w)h = g\Delta\rho h. \tag{1.1}$$

The force arising from this pressure difference can be roughly approximated by the area of a circle with radius R over which it is applied as

$$F_h = \pi R^2 g \Delta\rho h. \tag{1.2}$$

This driving force is resisted by a viscous force in the mantle, as mantle rock flows into the area that is rebounding. If the flow speed is v, then a representative velocity gradient is v/R. The viscous resisting stress can be approximated as

$$\tau_r = 2\eta\left(\frac{v}{2R}\right), \tag{1.3}$$

where η is the viscosity. Again by multiplying the area over which the stress is applied, we obtain the total force,

$$F_r = \frac{\pi R^2 \eta v}{R}. \tag{1.4}$$

Since the mantle has no appreciable momentum, the forces must balance: $F_h + F_r = 0$. This gives

$$\pi R^2 g \Delta\rho h - \frac{\pi R^2 \eta v}{R} = 0, \tag{1.5}$$

where the negative sign comes from the fact that the forces are in opposite directions. We can rearrange to find

$$v = \frac{g\Delta\rho R h}{\eta}. \tag{1.6}$$

The rate of flow v must be about equal to the rate of change of h, so we can write this as

$$\frac{1}{h}\frac{dh}{dt} = -\frac{g\Delta\rho R}{\eta} \tag{1.7}$$

and this differential equation has the solution

$$h(t) = h_0 e^{-t/t_0}, \tag{1.8}$$

where $t_0 = \eta/(g\Delta\rho R)$. In other words,

$$\eta = g\Delta\rho R t_0. \tag{1.9}$$

By using the approximate values $g = 10\ \mathrm{m\,s^{-2}}$, $R = 1000$ km, $\Delta\rho = 2300\ \mathrm{kg\,m^{-3}}$ and $t_0 = 4.6$ kyr, we obtain $\eta \approx 3 \times 10^{21}$ Pa s. A more rigorous analysis by Haskell (1937) yielded $\eta \approx 10^{21}$ Pa s. This is a very high value, which is why strain-rates in the mantle are very small. So, glacial isostatic rebound shows that the mantle flows over geological time and gives an approximate value for its viscosity.

Now comes the most obvious question: why should the plates that constitute the lithosphere be rigid, if the mantle is a convecting viscous fluid? The explanation lies in the rheology of crystalline rocks.

At temperatures that are a substantial fraction of their melting temperatures, crystalline solids deform slowly like a fluid. This creep deformation occurs under an applied stress due to thermally activated motion of atoms and ions associated with crystalline defects such as dislocations and atomic vacancies (Schubert et al., 2001). The principal deformation mechanisms associated with mantle convection are atom/ion migration (known as diffusion creep) and dislocation migration (or dislocation creep). The applicability of these processes to the deformation of the mantle was first proposed by Gordon (1965).

Experiments and theory indicate a general form of relationship between strain rate $\dot{e}$ and deviatoric stress τ valid for both diffusion and dislocation creep which is given by

$$\dot{e} = A\left(\frac{\tau}{\mu}\right)^n \left(\frac{b}{d}\right)^m \exp\left[-\frac{E^* + pV^*}{RT}\right], \tag{1.10}$$

where A is the pre-exponential factor, μ is the shear modulus, d is the grain size, b is the magnitude of the Burgers vector, E^* is the activation energy per mole, R is the

universal gas constant, T is the absolute temperature, V^* is the activation volume per mole and p is the pressure. The multiplicative factor A varies with water content, melt content and mineralogy. Typical values of n and m are $n = 1$ and $m = 2.5$ for diffusion creep and $n = 3.5$ and $m = 0$ for dislocation creep (Schubert et al., 2001). For diffusion creep, the relation between strain rate $\dot{e}$ and deviatoric stress τ is linear, resulting in a Newtonian viscosity. For dislocation creep, the relation between strain rate $\dot{e}$ and deviatoric stress τ is strongly nonlinear, resulting in a nonlinear viscous rheology. The generalized strain rate-deviatoric stress relation is

$$\dot{e}_{ij} = \frac{1}{B}\left(\frac{||\tau||}{\mu}\right)^{n-1} \exp\left[-\frac{E^* + pV^*}{RT}\right]\tau_{ij}, \tag{1.11}$$

$$B = \left(\frac{A}{\mu}\right)^{-1}\left(\frac{b}{d}\right)^{-m}, \tag{1.12}$$

where $||\tau||$ is the square root of the second invariant of the deviatoric stress tensor, and the coefficient B includes dependence on both rigidity and grain size. From (1.11) and the relation

$$\dot{e}_{ij} = \frac{1}{2\eta}\tau_{ij}, \tag{1.13}$$

we can identify the viscosity function as

$$\eta = \frac{1}{2A^*||\tau||^{n-1}} \exp\left[\frac{E^* + pV^*}{RT}\right], \tag{1.14}$$

where $A^* = \mu^{1-n}/B$. This is known as the Arrhenius form of viscosity.

According to Schubert et al. (2001), it is generally concluded that laboratory studies favour dislocation creep as the dominant deformation mechanism for the shallow upper mantle. If dislocation creep also characterized the entire mantle, it would imply a strongly nonlinear rheology for the mantle with $\eta \sim \tau^{-2.5}$ as shown in (1.14). However, studies of mantle rheology based on postglacial rebound show that the adjustment of the mantle to shifts in surface loads is adequately described by a linear Newtonian behaviour. A rationalization of these conclusions is possible if the flow associated with postglacial rebound is superimposed on a convecting mantle. If the deviatoric stresses associated with rebound are less than the deviatoric stresses associated with mantle convection, a linear behaviour would be expected for rebound even in a non-Newtonian mantle (Weertman and Weertman, 1975, Wu, 1995). Another interpretation is that diffusion creep characterizes all of the mantle except its shallowest depths and much of the deformation causing postglacial rebound indeed occurs in the linear Newtonian regime.

In the upper mantle, temperature variations control the behaviour of the viscosity function, while in the lower mantle it is likely that pressure variations are equally important. Since temperature increases rapidly with increasing depth through the lithosphere, the effective viscosity drops rapidly from very high values through the lithosphere, reaching the observationally constrained range of 10^{19-21} Pa s in the asthenosphere. In the lower mantle, the influence of increasing temperature and increasing pressure act in opposite directions, so the inference of either a uniform viscosity throughout most of the lower mantle or a viscosity increasing with depth in the lower mantle is reasonable from a mineral physics perspective, although neither behaviour is required (Schubert et al., 2001).

However the characteristic of mantle is quite different near the surface where at cold temperature and at high stress, viscous behaviour breaks down. In fact, at low temperatures and for short time behaviour, the mantle is elastic. A common description of both elastic and creeping behaviours can be represented by assuming a Maxwell viscoelastic fluid, whose constitutive law can be represented schematically by the superposition of the fluid strain rate and the elastic strain rate as

$$\dot{e} = \frac{\tau}{2\eta} + \frac{\dot{\tau}}{E_M}, \tag{1.15}$$

where η is the viscosity given by (1.14), τ is the stress, and E_M is the Young's modulus. The ratio

$$t_M = \frac{2\eta}{E_M}, \tag{1.16}$$

defines a Maxwell time scale, such that for changes on a time scale $t \ll t_M$, the material behaves elastically, and on longer time scales $t \gg t_M$, the material behaves like a viscous fluid. This provides the explanation for why seismic waves (time scales of $1-100$ s) propagate elastically and why mantle convection (time scale of $1-100$ Myr) occurs in a fluid-like manner (Fowler, 2011, Schubert et al., 2001).

1.6 Mathematical model of mantle convection

Various studies over the years have established the fact that mantle heat transfer efficiency governs the thermal history, volcanic and tectonic evolution, magnetic field history; degree of chemical differentiation (Bercovici, 2009, McKenzie and Weiss, 1975, Reese et al., 1999, Schubert et al., 1979, Stevenson and Turner, 1979). The theory of mantle convection was originally developed to understand the thermal history of the Earth and to provide a driving mechanism for continental drift. The success of

mantle convection theory in explaining plate velocities, sea-floor subsidence, volcanism, gravity anomalies, etc., led to its further application to other terrestrial planets such as Venus and Mars, which also sustained unique forms of mantle convection, evident from volcanic activity. However, the mantle rheology is so complex that modelling mantle convection mathematically in an appropriate manner is one of the most difficult challenges of the present day.

Convection in a fluid involves heat transport by motion of the fluid caused by positive or negative buoyancy of some of the fluid, that is, density contrasts or gradients within it. Indeed one tends to think of a convecting fluid layer as being heated from below and cooled from above, in which case there is a hot thermal boundary layer at its base and a cold thermal boundary layer at the top. When the temperature difference across the layer is large enough, the stabilizing effects of viscosity and thermal conductivity are overcome by the destabilizing buoyancy, and an overturning instability ensues as thermal convection.

The Earth's mantle is primarily driven by the surface cooling of a mantle that is more or less uniformly heated by radioactivity, and is also losing primordial or fossil heat; such a configuration of distributed heat production and surface heat loss typically leads to convection dominated by cold downwelling currents, which are synonymous with subducting slabs (Bercovici, 2009). However, the precise distribution of the heat source due to radioactive material is not known and the release of heat from the core is also sufficient in itself to drive vigorous convection in the mantle (Fowler, 2011).

1.6.1 Convection with constant viscosity

The first attempt to model mantle convection was made by Turcotte and Oxburgh (1967). They performed a boundary-layer analysis of two-dimensional steady state convection of a constant viscosity fluid at high Rayleigh number. They showed that the flow consists of an isothermal interior surrounded by thermal boundary layers, and their estimated mean surface velocity compared well with observed lithosphere plate velocities in the range 1-10 cm/year. They also predicted values for heat flux to the Earth's surface which were in good agreement with measurements carried out on the ocean floors. Thus their convection model presented an analogy for mantle convection beneath (active) oceanic lithosphere, which identifies midoceanic ridges with upwelling regions, and oceanic trenches (subduction zones) with downwellings. Later Roberts (1979), Olson and Corcos (1980) and Jimenez and Zufiria (1987) presented improved boundary layer analyses for mantle convection. Various numerical results

of Moore and Weiss (1973), McKenzie et al. (1974), Jarvis and McKenzie (1980) and Jarvis and Peltier (1982) confirmed the predictions of these analyses.

However, it became clear that these results were not so simply applicable as might be wished, for a number of reasons. While the active plate tectonic style of convection on Earth resembles these earlier studies, such convection is not seen on the nearest analogues, Venus and Mars, although there is evidence of active tectonics on Venus some 500 Ma ago (Schaber et al., 1992). It turns out that convection on Venus and Mars is more what one would expect, and the Earth's active style is anomalous. The reason for this lies with the complicated rheology of mantle rocks.

1.6.2 Convection with variable viscosity

As discussed in section 1.5, the effective viscosity of the mantle is a strong function of temperature, pressure and stress. The temperature and stress dependence are well documented experimentally; the pressure dependence is less constrained, but reasonable estimates for all these dependences are available (Kirby 1983, Karato and Wu 1993). It is a consequence of the temperature dependence of the viscosity that the cold upper thermal boundary layer, which is in fact the lithosphere, is extremely viscous, and this causes it to be effectively rigid and immobile. The resulting form of convection is called stagnant lid convection. Formation of an immobile lithosphere at large viscosity contrast was investigated theoretically by Morris and Canright (1984) and Fowler (1985a), and a feature of both sets of analyses is that the rapid convection in the interior of the cell causes the temperature to be isothermal (and thus isoviscous). In seeking to extend the asymptotic theory to the more realistic temperature and pressure dependent viscosity case (what we term the *thermobaroviscous* case), the theory encounters a significant problem, however. While rapid convection promotes an isothermal interior, this leads, in a thermobaroviscous fluid, to an interior viscosity which increases dramatically with depth, a result which is inconsistent with the observed, relatively constant, sub-lithospheric viscosity. This was pointed out by Fowler (1983), and it was suggested by Fowler (1993a) that a resolution might consist of rapid thermobaroviscous convection taking the form of a rapidly convecting interior which was isoviscous rather than isothermal. However, sporadic efforts to elucidate such a structure have since then failed.

The temperature-dependent case was studied numerically by Christensen (1984a,b), Moresi and Solomatov (1995), Solomatov and Moresi (1997) and Kameyama and Ogawa (2000), and they concluded that the formation of an immobile lithosphere on

terrestrial planets like Mars and Venus seems to be a natural result of temperature-dependent creep. Regardless of the pattern of convection, the immobilization of the top thermal boundary layer leads to convection that is unlike the Earth, with unit aspect-ratio cells and an immobile lithosphere (Bercovici et al., 2000). The active style of tectonics on Earth is generally thought to be a consequence of weakening at high stresses, either due to stress-dependent viscosity or plastic yielding (Bercovici 1993, 2003, Tackley 1998, 2000*a*,*b*, Fowler 1993b, Fowler and O'Brien 2003).

Studies have been done by Gurnis and Davies (1986), Cserepes (1993), Bunge et al. (1996) with depth-dependent (i.e. pressure-dependent) viscosity, whereas Parmentier et al. (1976), Larsen et al. (1993) investigated the effects of stress dependence of viscosity. These studies indirectly indicate that mantle rheology must be considered very carefully. In fact, the simultaneous effect of temperature and pressure dependent viscosity has become a problem of high relevance to the study of convection in the Earth's mantle, but one which does not appear to have attracted the attention it deserves, either analytically or computationally. This is undoubtedly due to the fact that from both points of view, it is a very difficult problem. The influence of temperature and depth-dependent viscosity on convection has been explored in two-dimensional numerical experiments by Houston and De Bremaecker (1975), Christensen (1984b), Fleitout and Yuen (1984), Doin et al. (1997), Dumoulin et al. (1999), Stemmer et al. (2006). Christensen (1984b) showed that additional pressure dependence of viscosity strongly influences the flow regimes, even if the magnitude of viscosity variation by pressure is relatively small compared to the temperature dependence. Dumoulin et al. (1999) used numerical models to study the relationship between surface heat flow and the viscosity at the base of the lithosphere. In a 2D axi-symmetrical model, Shahraki and Schmeling (2012) examined the simultaneous effect of pressure and temperature-dependent rheology on convection and geoid above the plumes. More recently, Rozel et al. (2015) and Bello et al. (2015) have studied convection with temperature, pressure and stress dependent viscosity in 2D and 3D spherical geometry.

In this thesis, we aim to study high Rayleigh number mantle convection with variable viscosity which is strongly influenced by temperature and pressure.

1.6.3 Numerical modelling

Numerical modelling of mantle convection was initiated in the late 1960s by Torrance and Turcotte (1971), McKenzie et al. (1974), and various methods like finite element, finite difference, spectral method or finite volume method have been used to solve

the problem of mantle convection. Confronted with the goal of computing convective solutions in which the potential viscosity variations are by factors in the region of 10^{50}, the challenge is to approach such extreme contrasts sufficiently that the correct asymptotic structure is reached. Very early attempts foundered on the computational difficulty which extreme viscosity contrasts caused. In the 1980s, Christensen and his co-workers (Christensen and Harder, 1991, Christensen, 1984a,b, Christensen and Yuen, 1985) were able to compute models with viscosity contrasts up to about 10^6. Great progress in computer architecture along with improved numerical techniques have helped advance the field of mantle convection. Subsequent studies were able to extend these results up to viscosity contrasts around 10^{15} (Moresi and Solomatov, 1998, 1995, Reese et al., 1999, Reese and Solomatov, 2002). One would naturally expect that such extreme values attain the structure of the asymptotic limit, and while this is true for temperature-dependent viscosity, it is not obviously true for temperature and pressure dependent viscosity. The state of the art in computational models now is that there is no effort to compute results for more extreme viscosity contrasts, rather the research effort is devoted to the inclusion of more realistic physical constraints, for example phase changes, spherical geometry, etc. or to applications of previously developed models; see for example Orth and Solomatov (2011), Stein and Hansen (2013), Deschamps et al. (2015).

It is relevant to add here that in particular, finite element methods are effective in solving differential equations with complicated geometry and material properties (Bercovici, 2009). Finite element methods have been widely used in studies of mantle dynamics by Christensen (1984b), Baumgardner (1985) and later codes like ConMan (King et al., 1990) and Citcom/CitcomS (Moresi and Gurnis, 1996, Zhong et al., 2000) were used.

1.6.4 Arrhenius versus Frank-Kamenetskii

The complete viscosity function (1.14) is cumbersome to use in numerical modelling and accordingly it is often simplified. One common simplification is the Frank-Kamenetskii form which is an exponential dependence of viscosity on temperature like

$$\eta = \eta_0 \exp\left[-\alpha(T - T_b)\right], \tag{1.17}$$

where α is a constant, T_b is the temperature at the bottom boundary, and η_0 is the viscosity at $T = T_b$. This form is an adequate approximation over restricted temperature intervals. It reduces the viscosity contrast in the lithosphere to save com-

putational resources. The absence of active plates in the models with temperature-dependent viscosity is a natural consequence of the simple Newtonian rheology assumed in (1.17). Comparing results obtained by the commonly used forms of the Arrhenius and the Frank-Kamenetskii approach, same change in flow behaviour from mobile-lid to stagnant-lid convection is observed. The differences are only of quantitative nature: In the stagnant-lid regime, some Arrhenius formulations lead to a thinner top boundary layer which results in values of lithospheric thicknesses being more realistic. Various studies have been done on this open issue (Noack and Breuer, 2013, Stein and Hansen, 2013) and it has to be kept in mind, that in numerical models the realistic viscosity contrast appearing over the mantle can neither be coped with by the Arrhenius nor the Frank-Kamenetskii approach.

1.7 Overview

In chapter 2, the full governing equations for mantle convection and the appropriate boundary conditions for classical Rayleigh-Bénard convection in a two-dimensional rectangular cell are described. The governing equations are non-dimensionalized and the dimensionless parameters are identified. Our emphasis is on the effect of viscosity on the mantle convection, so firstly, we treat viscosity as a constant in this chapter. This is in line with many previous models and it is a vast simplification of the real mantle, as we neglect the internal heating, viscous dissipation and thermochemical reactions. We also ignore the effects of compressibility, solid phase change and partial melting; but we believe the insights that can be gained are useful. We present solutions for high Rayleigh numbers and benchmark our code. The boundary layer theory is briefly described and the Shanks transformation is applied to find the proportionality constant in the asymptotic relation between Rayleigh number and Nusselt number, the dimensionless heat transfer rate at the surface.

In chapter 3, the mathematical model with variable viscosity is introduced and simulations are performed with purely temperature dependent viscosity. As before, the model neglects compressibility, melting, phase change and internal heating. Numerical results for extreme viscosity variations are presented after they are compared with benchmark values. The solutions display a cold and stiff thermal boundary layer at the top surface as expected but fail to explain the concept of subduction. In the later sections, a boundary layer analysis shows the asymptotic relation between Rayleigh number, Nusselt number, viscous temperature parameter ε and aspect ratio and numerical results are used to verify the asymptotic relation.

The mathematical model in chapter 4 incorporates both temperature- and pressure-dependent viscosity defined in an Arrhenius form. This is the model we are mainly concerned with. Firstly, the model is solved numerically in a unit-aspect-ratio cell for extremely large viscosity variations and steady solutions for temperature, isotherms and streamlines are obtained. To improve the efficiency of numerical computation, we introduce a modified form of viscosity with a low temperature cut-off. We demonstrate that this simplification results in markedly improved numerical convergence without compromising accuracy. Continued numerical investigation suggests that narrow cells are preferred at extreme viscosity contrasts and motivates us to study the effect of aspect ratio on mantle convection. So, we vary the aspect ratio of the convection cell and find that the model can be solved in increasingly narrow cells as the viscosity contrast is increased. We also observe that the cell aspect ratio $a \approx 3\varepsilon$ is the most stable choice. As the viscosity contrast increases, we notice that the convection may switch off completely. Linear stability analysis is done to determine the critical Rayleigh number for the onset of convection and the dominant post-onset behaviour.

From the numerical results, it is evident that there is a stagnant lid in the cell and the convecting part of the flow is neither isothermal nor isoviscous. This leads us to consider the solutions at different parts of the cell separately. As a result, the whole cell is roughly divided into stagnant lid, asthenosphere, upper mantle, lower mantle, transition zone between upper mantle and lower mantle and basal thermal boundary layer. The asymptotic analysis is done for each region and matched between them. In doing so, we have followed two different approaches based on two different assumptions concerning the slope of the high-viscosity lid. Our analyses for both approaches are described in detail in chapters 5 and 6. In chapter 5, our main focus is on the upper mantle and we investigate the lid base profile, whereas in chapter 6, we study the convection in the lower mantle and estimate the lower mantle temperature from analysis. We also examine how the upper mantle and lower mantle are related to each other.

Chapter 2

Convection with Constant Viscosity

2.1 Introduction

The characteristic time constant of the geological processes related to mantle convection, typically 10 My (3×10^{14} s), is so long that the mantle, although stronger than steel and able to transmit seismic shear waves, can be treated as a fluid. It is not the equations themselves, but their parameters that characterize their applicability to mantle dynamics.

Convection in a layer of fluid heated along its base is known as Rayleigh-Bénard convection. Rayleigh's stability analysis predicted the conditions necessary for the onset of convection, as well as the expected size of convection cells (relative to the layer thickness). It is found that the onset of convection is controlled by a dimensionless number called the *Rayleigh number*. The Rayleigh number Ra measures the vigour of convection in terms of the gravitationally induced thermal buoyancy that acts to drive convective flow, and the dissipative or resistive effects of both fluid viscosity, which retards convective motion, and thermal diffusion which acts to diminish thermal anomalies (Bercovici, 2009). The Rayleigh number is generally written as

$$Ra = \frac{\rho g \alpha \Delta T d^3}{\eta \kappa}, \tag{2.1}$$

where ρ is the density, g is the gravitational acceleration, α is the thermal expansion coefficient, ΔT is the typical temperature difference between the hottest and the coldest parts of the fluid layer, d is the depth of the layer, η is the dynamic viscosity and κ is the thermal diffusivity coefficient.

Over the years, Rayleigh-Bénard convection has become a benchmark problem in computational geophysics as a paradigm for convection in the Earth's mantle that is the driving mechanism of plate tectonics. Plate tectonics provides a remarkably

accurate kinematic description of the motion of the Earth's crust but a fully dynamical theory requires the properties of plates and of the mantle to be related to a systematic study of convection. Though the forces which maintain the plate motions appear to be governed by the equations of fluid dynamics, the form of these equations differs from those which determine the motions of the oceans and atmosphere.

2.2 Governing equations

We consider a classical Rayleigh-Bénard convection in a two-dimensional rectangular cell with a fixed temperature difference ΔT between the horizontal boundaries. The convective cell is assumed to be a part of a periodic structure in an infinite horizontal layer. We take $\hat{\boldsymbol{i}}$, $\hat{\boldsymbol{j}}$ and $\hat{\boldsymbol{k}}$ to be the unit vectors in the positive directions of x, y and z respectively. The governing equations ensure the conservation of mass, momentum, and energy and are completed by a suitable thermodynamic equation of state. The Navier–Stokes equations which describe the motion are

$$\frac{\partial \rho}{\partial t} + \nabla \cdot (\rho \boldsymbol{u}) = 0, \tag{2.2}$$

$$\rho \left[\frac{\partial \boldsymbol{u}}{\partial t} + (\boldsymbol{u} \cdot \nabla) \boldsymbol{u} \right] = -\nabla p + \nabla \cdot \boldsymbol{\tau} - \rho g \, \hat{\boldsymbol{k}}. \tag{2.3}$$

The energy equation for heat transfer is

$$\rho C_p \left[\frac{\partial T}{\partial t} + \boldsymbol{u} \cdot \nabla T \right] = \nabla \cdot (k \nabla T) + H + \Phi, \tag{2.4}$$

and the equation of state is

$$\rho = \rho_0 \left[1 - \alpha \left(T - T_0 \right) \right]. \tag{2.5}$$

Here ρ is the density, $\boldsymbol{u} = (u, 0, w)$ is the fluid velocity, t is time, p is the pressure, g is the assumed constant gravitational acceleration acting downwards (the variation of g across the mantle is so small that it is taken as constant), $\boldsymbol{\tau}$ is the deviatoric stress tensor, T is the absolute temperature, C_p is the specific heat at constant pressure, k is the thermal conductivity, H is the rate of internal heating per volume and Φ is the viscous dissipation function. In the equation of state (2.5), α is the thermal expansion coefficient, ρ_0 is the reference density and the isothermal compressibility is neglected. The components of the deviatoric stress tensor, $\boldsymbol{\tau}$ are given by

$$\tau_{ij} = \eta \left[\frac{\partial u_i}{\partial x_j} + \frac{\partial u_j}{\partial x_i} - \frac{2}{3} \delta_{ij} \nabla \cdot \boldsymbol{u} \right] = 2\eta \left[\dot{e}_{ij} - \frac{1}{3} \delta_{ij} \nabla \cdot \boldsymbol{u} \right], \tag{2.6}$$

where η is the viscosity, $\dot{e}_{ij}$ is the strain rate tensor and δ_{ij} is the Kronecker delta. The viscous dissipation function, Φ is defined as

$$\Phi \equiv \tau_{ij} \frac{\partial u_i}{\partial x_j}. \tag{2.7}$$

Most models of mantle convection treat the mantle as a *Boussinesq fluid*; this means that while density is a function of temperature, the density fluctuations are so small that the fluid is still essentially incompressible except when the density fluctuations are acted on by gravity. Thus the fluid is virtually incompressible, but can still be driven by buoyancy (Bercovici et al., 2000). We therefore assume that the Boussinesq approximation is valid so that

$$\nabla \cdot \boldsymbol{u} = 0, \tag{2.8}$$

$$\rho \left[\frac{\partial \boldsymbol{u}}{\partial t} + (\boldsymbol{u} \cdot \nabla)\boldsymbol{u} \right] = -\nabla p + \nabla \cdot \boldsymbol{\tau} - \rho g \hat{\boldsymbol{k}}, \tag{2.9}$$

$$\boldsymbol{\tau} = \eta \left[\nabla \boldsymbol{u} + (\nabla \boldsymbol{u})^T \right]. \tag{2.10}$$

In general, as we have discussed in chapter 1, η is a function of temperature, pressure and stress but in this chapter, we will consider viscosity as a constant.

For the energy equation, we will neglect the internal heating. The radiogenic heating may be significant but we will consider basal heating as the dominant driving source of the convection. In this thesis we also assume that the coefficient of expansion α and the thermal conductivity k are constant. As a result, the energy equation takes the form

$$\rho C_p \left[\frac{\partial T}{\partial t} + \boldsymbol{u} \cdot \nabla T \right] = k \nabla^2 T + \frac{\tau^2}{2\eta}. \tag{2.11}$$

We will consider a unit aspect-ratio cell with free-slip boundary conditions (i.e. normal velocities and tangential stresses vanish) on all boundaries. The temperatures at the bottom and the top boundaries are constant and thermal insulation is assumed on the vertical sides. These conditions imply

$$w = 0, \quad \frac{\partial u}{\partial z} = 0, \quad T = T_b \quad \text{on} \quad z = 0, \tag{2.12}$$

$$w = 0, \quad \frac{\partial u}{\partial z} = 0, \quad T = T_s \quad \text{on} \quad z = d, \tag{2.13}$$

$$u = 0, \quad \frac{\partial w}{\partial x} = 0, \quad \frac{\partial T}{\partial x} = 0 \quad \text{on} \quad x = 0, d. \tag{2.14}$$

It should be noted here that the assumption of a 2D Cartesian geometry is not appropriate for the mantle, but the basic thrust of our results will not be affected.

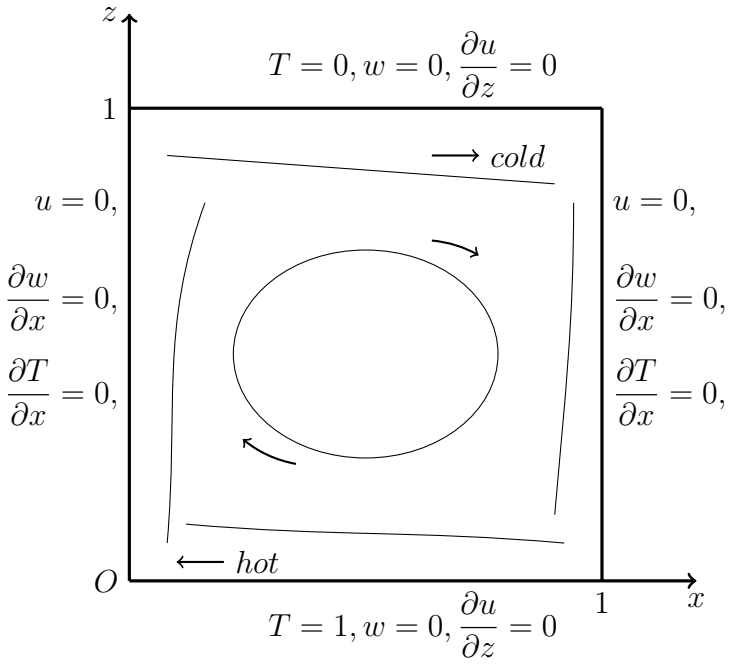

Figure 2.1: Schematic diagram of a basally heated non-dimensional unit aspect-ratio cell in mantle.

2.3 Non-dimensionalisation and simplification

Following Fowler (2011) and Jarvis and Peltier (1982), we non-dimensionalize as follows

$$\begin{aligned} (x,z) = d(x^*,z^*), \quad T = \Delta T\, T^* + T_s, \quad \boldsymbol{u} = \frac{\kappa_0}{d}\boldsymbol{u}^*, \quad t = \frac{d^2}{\kappa_0}t^*, \\ \eta = \eta_0\eta^*, \quad \rho = \rho_0\rho^*, \quad \boldsymbol{\tau} = \frac{\eta_0\kappa_0}{d^2}\boldsymbol{\tau}^*, \quad p = \rho_0 g d(1-z^*) + \frac{\eta_0\kappa_0}{d^2}p^*, \end{aligned} \tag{2.15}$$

where d is the typical depth of the mantle, $\Delta T = T_b - T_s$ is the temperature difference across the layer, κ_0 is the thermal diffusivity scale given by $\kappa_0 = \frac{k}{\rho_0 C_p}$. Substituting these variables in equations (2.8)-(2.11), we obtain the following dimensionless equations by dropping the asterisks:

$$\nabla \cdot \boldsymbol{u} = 0, \tag{2.16}$$

$$\frac{1}{Pr}\rho\left\{\frac{\partial \boldsymbol{u}}{\partial t} + (\boldsymbol{u}\cdot\nabla)\boldsymbol{u}\right\} = -\nabla p + \nabla^2\boldsymbol{u} + Ra\, T\, \hat{\boldsymbol{k}}, \tag{2.17}$$

$$\frac{\partial T}{\partial t} + \boldsymbol{u}\cdot\nabla T = \nabla^2 T + \frac{D}{Ra}\frac{\tau^2}{2\eta}, \tag{2.18}$$

where the dimensionless parameters are

$$\text{Prandtl number,} \qquad Pr = \frac{\eta_0}{\rho_0 \kappa_0}, \tag{2.19}$$

$$\text{Rayleigh number,} \qquad Ra = \frac{\rho_0 \alpha g \Delta T d^3}{\eta_0 \kappa_0}, \tag{2.20}$$

$$\text{and dissipation number,} \qquad D = \frac{\alpha g d}{C_p}. \tag{2.21}$$

Using the typical parameter values for the mantle as shown in Table 2.1, we find that $Pr \approx 10^{23}$ and $D \approx 0.6$. Thus, Pr can be taken as infinite and the ratio of D and $Ra \gg 1$ can be safely ignored in the equations. Hence the reduced dimensionless equations become

$$\nabla \cdot \boldsymbol{u} = 0, \tag{2.22}$$

$$\nabla p = \nabla^2 \boldsymbol{u} + Ra\, T \hat{\boldsymbol{k}}, \tag{2.23}$$

$$\frac{\partial T}{\partial t} + \boldsymbol{u} \cdot \nabla T = \nabla^2 T, \tag{2.24}$$

where the inertia and the viscous dissipation terms are neglected and the only dimensionless parameter that remains is the Rayleigh number Ra.

The associated free-slip boundary conditions are

$$\begin{aligned} w = 0, \quad \frac{\partial u}{\partial z} = 0, \qquad T = 1 \quad \text{on} \quad z = 0, \\ w = 0, \quad \frac{\partial u}{\partial z} = 0, \qquad T = 0 \quad \text{on} \quad z = 1, \\ u = 0, \quad \frac{\partial w}{\partial x} = 0, \quad \frac{\partial T}{\partial x} = 0 \quad \text{on} \quad x = 0, 1. \end{aligned} \tag{2.25}$$

2.4 Analysis of the model

2.4.1 Onset of convection

Stability analysis predicts that the onset of convection, triggered by the least stable mode, will occur when Ra is of the order of 1000; this varies between $Ra = 657.511$, for free-slip top and bottom boundaries to $Ra = 1707.762$ with the more resistive rigid or no-slip top and bottom boundaries (Chandrasekhar, 1961). This value of Ra for the onset of convection is usually referred to as the *critical Rayleigh number* and denoted by Ra_{cr}.

Table 2.1: Typical parameter values for numerical models of mantle convection.

Parameter	Symbol	Value
Depth	d	3×10^6 m
Thermal expansion coefficient	α	2×10^{-5} K^{-1}
Reference density	ρ_0	4×10^3 kg m^{-3}
Gravitational acceleration	g	10 m s^{-2}
Temperature at the base of the lithosphere	T_s	300 K
Temperature at the core-mantle boundary	T_b	3000 K
Temperature difference	ΔT	2700 K
Thermal conductivity	k_0	4 W m^{-1}K^{-1}
Specific heat at constant pressure	C_p	10^3 J kg^{-1} K^{-1}
Thermal diffusivity coefficient	$\kappa_0 = \dfrac{k_0}{\rho_0 C_p}$	1×10^{-6} m^2 s^{-1}
Dynamic viscosity	η_0	10^{21} Pa s
Rayleigh number	Ra	$10^7 - 10^9$

2.4.2 Linear stability

We wish to find the critical Rayleigh number for our problem where free-slip conditions are applied on all boundaries of a square cell. From equations (2.22)-(2.25), it is evident that the basic conductive steady state is one of no motion (Fowler, 2011), i.e.

$$\begin{aligned} \boldsymbol{u} &= \mathbf{0}, \\ T &= 1 - z, \\ p &= -\frac{1}{2} Ra\,(1-z)^2\,. \end{aligned} \tag{2.26}$$

To study the linear stability of the steady state solution (2.26), we will perturb the equilibrium solution. To facilitate the analysis, we define a stream function ψ by

$$u = -\psi_z, \qquad w = \psi_x, \tag{2.27}$$

and the temperature is expressed as

$$T = 1 - z + \theta. \tag{2.28}$$

Eliminating p by cross-differentiation and neglecting the nonlinear advective terms in the heat equation, we obtain the following linearised system from (2.23)-(2.24):

$$\begin{aligned} \nabla^4 \psi + Ra\,\theta_x &= 0, \\ \theta_t - \psi_x &= \nabla^2 \theta. \end{aligned} \tag{2.29}$$

The boundary conditions corresponding to (2.25) are

$$\begin{aligned} \psi_{zz} = \psi = \theta = 0 \quad \text{on} \quad z = 0, 1 \\ \text{and} \quad \psi_{xx} = \psi = \theta_x = 0 \quad \text{on} \quad x = 0, 1. \end{aligned} \tag{2.30}$$

We apply the method of separation of variables and consider a solution like

$$\begin{aligned} \psi &= Ae^{\lambda t} \sin m\pi x \sin n\pi z, \\ \theta &= Be^{\lambda t} \cos m\pi x \sin n\pi z, \end{aligned} \tag{2.31}$$

where λ is the growth rate, A, B are unknown constants and $m, n \in \mathbb{N}$. The basic state (2.26) is stable if $Re(\lambda) < 0$ and unstable otherwise. Substituting (2.31) in (2.29), we obtain

$$\begin{aligned} \left(m^2 + n^2\right)^2 \pi^4 A - m\pi RaB = 0, \\ m\pi A - \left\{\left(m^2 + n^2\right)\pi^2 + \lambda\right\} B = 0. \end{aligned} \tag{2.32}$$

For a non-trivial solution, the determinant of the coefficient matrix of (2.32) must be equal to zero, i.e.

$$\lambda = \frac{m^2 Ra}{\pi^2 \left(m^2 + n^2\right)^2} - \pi^2 \left(m^2 + n^2\right). \tag{2.33}$$

Now λ is positive if

$$Ra > \frac{\pi^4 \left(m^2 + n^2\right)^3}{m^2}, \tag{2.34}$$

and Ra_{cr}, the minimum value of Ra, is the value when m, n are minimum, i.e. $m, n = 1$. Hence, the critical Rayleigh number for this case is

$$Ra_{cr} = 8\pi^4 \approx 779.273. \tag{2.35}$$

It should be noted here that this Ra_{cr} is for a unit aspect ratio convection cell. If the aspect ratio was not fixed, then for the stress-free boundaries Ra_{cr} would be $\frac{27}{4}\pi^4 \approx 657.51$ and the preferred aspect ratio (ratio of cell width to height) would be $\sqrt{2}$.

Next we consider the nonlinear problem to establish the stability of the convective state for $Ra > Ra_{cr}$.

2.4.3 Nonlinear stability analysis

According to Drazin and Reid (1981), the linear stability theory of a steady basic flow generally gives a spectrum of independent modes, each with velocity perturbation of the form

$$\boldsymbol{u}'(\boldsymbol{x}, t) = \boldsymbol{u}(\boldsymbol{x}, t) - \boldsymbol{U}(\boldsymbol{x}) = A(t)\boldsymbol{f}(\boldsymbol{x}) + c.c. \tag{2.36}$$

for some complex amplitude $A \propto e^{\lambda t}$, where $Re\ \lambda$ indicates the relative growth rate. Here all the values of λ are real. When $Ra < Ra_{cr}$ all disturbances are stable with $\lambda < 0$. When $Ra = Ra_{cr}$ there is just one normal mode, with $\lambda = \lambda_1 = 0$, which is marginally stable. As Ra increases above Ra_{cr}, $\lambda_1 > 0$ but $\lambda < 0$ for all the other modes. When Ra is sufficiently large these other modes also become unstable in turn.

In general,

$$\lambda_1 = k(Ra - Ra_{cr}) + O\left\{(Ra - Ra_{cr})^2\right\} \quad \text{as} \quad Ra \to Ra_{cr}, \tag{2.37}$$

where k is some positive constant. Thus if $0 < Ra - Ra_{cr} \ll 1$, the most unstable mode grows slowly but all other modes decay. However, linear theory shows that the most unstable mode becomes dominant very soon and the nonlinear self-interaction of the dominant mode generates harmonics and distorts the mean flow, thereby moderating the slow exponential growth (Drazin and Reid, 1981). This theory was developed by Landau (1944) and he described the instability by the equation

$$\frac{d|A|^2}{dt} = 2\lambda|A|^2 - l|A|^4, \tag{2.38}$$

where $|A|$ is the amplitude of the dominant mode and l is some constant. Later weakly nonlinear theories were developed by Malkus and Veronis (1958) and a summary can be found in Busse (1978). We carry out a weakly non-linear stability analysis for our problem and try to find out the amplitude of the dominant mode.

A multiple scale analysis will be needed as in Matkowsky (1970). The first scale is the initial time scale, denoted by t, in which the solution begins to develop from the initial perturbation. The linear theory is assumed to be valid here. The second region, denoted by τ, is one in which nonlinear effects become important, and the solution continues to evolve in time until it approaches the steady state which is the third region, reached in the limit as τ approaches ∞. Rewriting the nonlinear equations (2.22)-(2.25) in the form

$$\begin{aligned} \nabla^4\psi + Ra\theta_x &= 0, \\ \theta_t - \psi_x + \psi_x\theta_z - \psi_z\theta_x &= \nabla^2\theta, \end{aligned} \tag{2.39}$$

we substitute

$$\begin{aligned} Ra &= Ra_{cr} + s\epsilon^2, \\ \tau &= \epsilon^2 t, \\ \psi &= \epsilon\psi_1 + \epsilon^2\psi_2 + \epsilon^3\psi_3 + ..., \\ \theta &= \epsilon\theta_1 + \epsilon^2\theta_2 + \epsilon^3\theta_3 + ..., \end{aligned} \tag{2.40}$$

where $s = \pm 1$ distinguishes supercritical and subcritical bifurcations. We equate the coefficients of the like powers of ϵ from both sides to get

$$\text{At} \quad O(\epsilon) : \mathcal{L} \begin{pmatrix} \psi_1 \\ \theta_1 \end{pmatrix} = \begin{pmatrix} 0 \\ 0 \end{pmatrix}, \tag{2.41}$$

$$\text{At} \quad O(\epsilon^2) : \mathcal{L} \begin{pmatrix} \psi_2 \\ \theta_2 \end{pmatrix} = \begin{pmatrix} 0 \\ \psi_{1x}\theta_{1z} - \psi_{1z}\theta_{1x} \end{pmatrix}, \tag{2.42}$$

$$\text{At} \quad O(\epsilon^3) : \mathcal{L} \begin{pmatrix} \psi_3 \\ \theta_3 \end{pmatrix} = \begin{pmatrix} -s\theta_{1x} \\ \theta_{1\tau} - \psi_{2z}\theta_{1x} - \psi_{1z}\theta_{2x} + \psi_{2x}\theta_{1z} + \psi_{1x}\theta_{2z} \end{pmatrix}, \tag{2.43}$$

where the linear operator $\mathcal{L}$ is defined by

$$\mathcal{L} = \begin{pmatrix} \nabla^4 & Ra_{cr}\dfrac{\partial}{\partial x} \\ \dfrac{\partial}{\partial x} & \nabla^2 \end{pmatrix}. \tag{2.44}$$

The boundary conditions in (2.30) help us to choose ψ_1, θ_1 as

$$\begin{pmatrix} \psi_1 \\ \theta_1 \end{pmatrix} = A(\tau) \begin{pmatrix} \psi_1^* \\ \theta_1^* \end{pmatrix} e^{i\pi x} \sin \pi z + c.c., \tag{2.45}$$

where $A(\tau)$ is an amplitude function taken to be real and $(\psi_1^*, \theta_1^*)^T$ is an eigenvector in the nullspace of $\mathcal{L}$. We find

$$\begin{pmatrix} \psi_1^* \\ \theta_1^* \end{pmatrix} = \begin{pmatrix} -i \\ \dfrac{1}{2\pi} \end{pmatrix} \tag{2.46}$$

and hence by taking the real parts from (2.45), we get

$$\begin{aligned} \psi_1 &= A \sin \pi x \sin \pi z, \\ \theta_1 &= \frac{A}{2\pi} \cos \pi x \sin \pi z. \end{aligned} \tag{2.47}$$

Using (2.47) in (2.42), we obtain

$$\mathcal{L} \begin{pmatrix} \psi_2 \\ \theta_2 \end{pmatrix} = \begin{pmatrix} 0 \\ \dfrac{1}{4}\pi A^2 \end{pmatrix} \sin 2\pi z + c.c. \tag{2.48}$$

Now, if $\boldsymbol{v} = \begin{pmatrix} a \\ b \end{pmatrix} e^{ip\pi x} \sin q\pi z$, then $\boldsymbol{\mathcal{L}v} = L_{pq}\boldsymbol{v}$, where

$$L_{pq} = \begin{pmatrix} \pi^4(p^2+q^2)^2 & i\pi p Ra_{cr} \\ i\pi p & -\pi^2(p^2+q^2) \end{pmatrix}. \tag{2.49}$$

Therefore, we can write from (2.48)

$$\begin{pmatrix} \psi_2 \\ \theta_2 \end{pmatrix} = L_{02}^{-1} \begin{pmatrix} 0 \\ \dfrac{1}{4}\pi A^2 \end{pmatrix} \sin 2\pi z = \begin{pmatrix} 0 \\ -\dfrac{1}{16\pi} A^2 \end{pmatrix} \sin 2\pi z. \tag{2.50}$$

There is also an arbitrary multiple of $(\psi_1, \theta_1)^T$ on the right side of (2.50), but this term is irrelevant in calculating $A(\tau)$. The above calculations give (2.43) in the form

$$\mathcal{L}\begin{pmatrix} \psi_3 \\ \theta_3 \end{pmatrix} = \begin{pmatrix} -s\theta_{1x} \\ \theta_{1\tau} + \psi_{1x}\theta_{2z} \end{pmatrix} = \begin{pmatrix} \frac{1}{2}sA\sin\pi x \sin\pi z \\ \left(\frac{A'}{2\pi} + \frac{\pi A^3}{16}\right)\cos\pi x \sin\pi z - \frac{\pi A^3}{16}\cos\pi x \sin 3\pi z \end{pmatrix}. \tag{2.51}$$

In other words,

$$\mathcal{L}\begin{pmatrix} \psi_3 \\ \theta_3 \end{pmatrix} = \begin{pmatrix} -\frac{isA}{2} \\ \frac{A'}{2\pi} + \frac{\pi A^3}{16} \end{pmatrix} e^{i\pi x}\sin\pi z + c.c. + \text{higher harmonics.} \tag{2.52}$$

In general, (2.52) has no bounded solution; thus in order to obtain such a solution the secular term involving $e^{i\pi x}\sin\pi z$ must be suppressed, i.e. we must ensure that the right hand side of (2.52) is orthogonal to the null vector of the adjoint of the linear operator L. This is known as *solvability condition* or *Fredholm alternative*. The adjoint of L_{11} is given by

$$L_{11}^* = \begin{pmatrix} 4\pi^4 & -i\pi \\ -i\pi Ra_{cr} & -2\pi^2 \end{pmatrix} \tag{2.53}$$

and the null vector is $u = (i, 4\pi^3)$. Therefore the solvability condition for equation (2.52) is (because the inner product $\langle u, v\rangle$ is $\overline{u}^T v$)

$$\overline{(i, 4\pi^3)}\begin{pmatrix} -\frac{isA}{2} \\ \frac{A'}{2\pi} + \frac{\pi A^3}{16} \end{pmatrix} = 0, \tag{2.54}$$

$$\Rightarrow A' = \frac{1}{4\pi^2}sA - \frac{1}{8}\pi^2 A^3, \tag{2.55}$$

which we recognize as the Landau equation (2.38). The bifurcation is supercritical when $s = 1$ ($Ra = Ra_{cr} + \epsilon^2$) (Fowler, 1997) and the equilibrium amplitude is

$$A_{eq} = \frac{\sqrt{2}}{\pi^2}. \tag{2.56}$$

Finally, we can express the stream function and the temperature as

$$\psi \sim \frac{\sqrt{2}}{\pi^2}(Ra - Ra_{cr})^{\frac{1}{2}}\sin\pi x \sin\pi z, \tag{2.57}$$

$$\theta \sim \frac{1}{\sqrt{2}\pi^3}(Ra - Ra_{cr})^{\frac{1}{2}}\cos\pi x \sin\pi z. \tag{2.58}$$

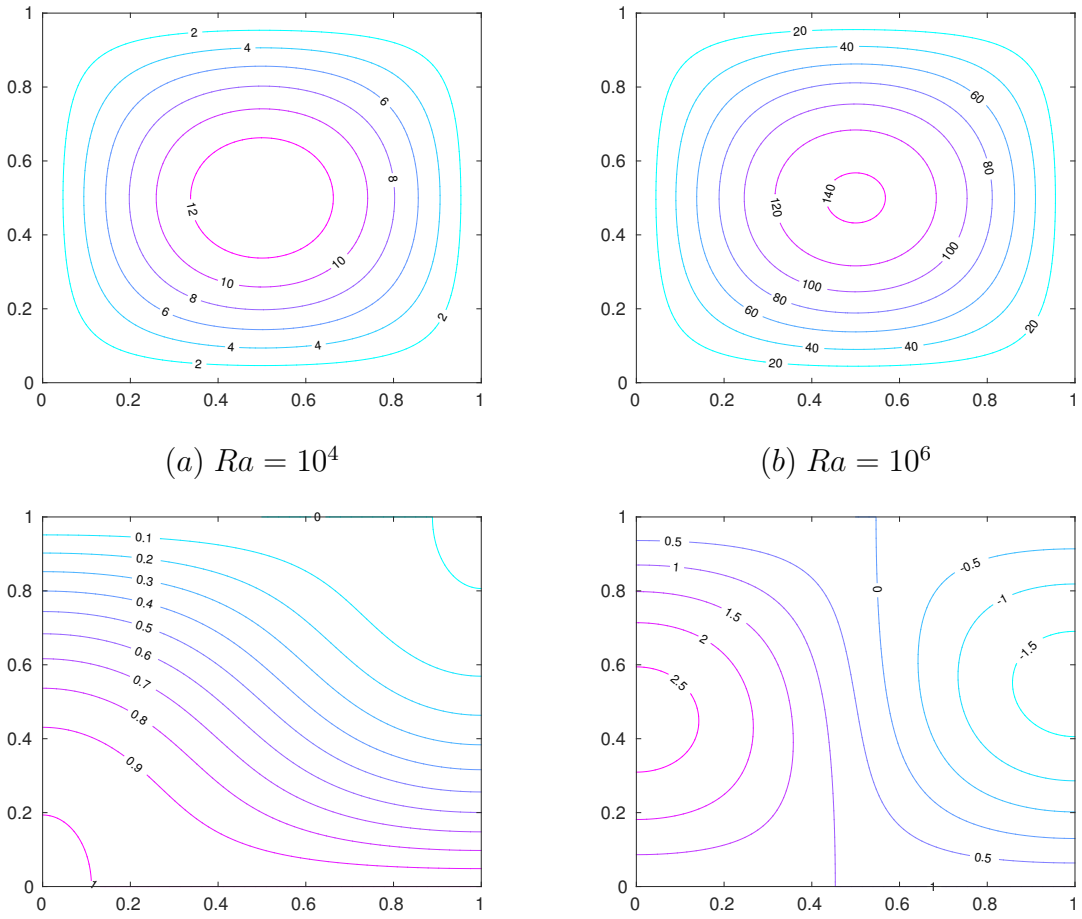

(a) $Ra = 10^4$ (b) $Ra = 10^6$

(c) $Ra = 10^3$ (d) $Ra = 10^4$

Figure 2.2: Weakly nonlinear stream function contours for (a) $Ra = 10^4$, (b) $Ra = 10^6$ and isothermal contours for (c) $Ra = 10^3$, (d) $Ra = 10^4$ given by equations (2.57) and (2.58).

Figure 2.2(a, b) show the stream function contours for $Ra = 10^4$ and 10^6 and Figure 2.2(c, d) display the temperature contours for $Ra = 10^3$ and 10^4 obtained using (2.57) and (2.58). Obviously the higher value of Ra is not of the form assumed in (2.40), as we can see from Figure 2.2(d) that when $Ra \gg Ra_{cr}$ the isothermal contours are completely absurd. However, it has already been mentioned in Table 2.1 that for mantle convection, the effective Rayleigh humber is very high $(10^7 - 10^9)$. Therefore we can not expect the weakly nonlinear theory to apply in this case. In fact, the flow for large Ra can be described using boundary layer theory. Before we discuss the boundary layer theory, some numerical solutions for high Rayleigh number convection will be presented.

2.5 Numerical investigation

In this thesis we use a finite element based PDE software COMSOL Multiphysics to solve numerically the dimensionless equations derived in section 2.3 and we present our results for temperature distributions, isotherms and streamlines below.

COMSOL Multiphysics is a general-purpose software platform, based on advanced numerical methods, for modeling and simulating physics-based problems. It is a particularly convenient tool for implementing the *finite element method (FEM)*. The essence of the finite element method is to state any constraints on the field variables in *weak* form. The weak formulation of partial differential equation (PDE) and basics of the finite element method are briefly described in appendix A. Once the system of equations are expressed in weak forms, then it can be written in a discrete, matrix form

$$L(U) = 0, \tag{2.59}$$

where U is a vector of unknowns u_i or simply, the solution vector and L_{ij} is comprised of integrals and derivatives of the basis functions (similar to a_{ij} as described in A.12).

To solve the system in (2.59) COMSOL Multiphysics has a built-in nonlinear solver which is based on Newton's method. If U_0 is the initial guess of the solution vector U, then the software forms the linearized model using U_0 as the linearization point and solves the discretized form of the linearized model

$$U = U_0 - J(U_0)^{-1}L(U_0), \tag{2.60}$$

where J is the Jacobian matrix of L, i.e.

$$J(U_0) = \frac{\partial L}{\partial U}(U_0). \tag{2.61}$$

According to fixed point theorem, (2.60) gives quadratic convergence to the solution of (2.59), provided that $J(U)$ is non-singular at the fixed point U_0 (Burden and Faires, 2011). (2.60) can also be written as

$$J(U_0)(U - U_0) = -L(U_0). \tag{2.62}$$

To avoid proceeding into a region where there is no solution, and to minimize the number of Newton steps taken, COMSOL uses a damping factor. Once it is solved for the Newton step $U - U_0$, it then computes the new iteration $U_1 = U_0 + \lambda(U - U_0)$, where λ is called the damping factor and has bounds $0 < \lambda \leq 1$. As $\lambda \to 0$, we say that the damping is increased, while $\lambda = 1$ means that the problem is undamped.

Next, the damped Newton correction estimates the error E for the new iteration U_1 by solving

$$J(U_0)E = -L(U_1). \tag{2.63}$$

If the relative error corresponding to E is larger than the relative error in the previous iteration, the algorithm reduces the damping factor λ and recomputes U_1. This algorithm repeats the damping-factor reduction until the relative error is less than in the previous iteration or until the damping factor underflows the minimum damping factor. When it has taken a successful step U_1, the algorithm proceeds with the next Newton iteration (Deuflhard, 1974). A value of $\lambda = 1$ results in Newton's method, and thus converges quadratically as mentioned. It happens only when the initial guess U_0 is sufficiently close to a solution. In order to enlarge the domain of attraction, the solver chooses the damping factors judiciously. Nevertheless, the success of a nonlinear solver depends heavily on a carefully selected initial guess.

Suppose we have some boundary conditions. In that case, using the weak formulation, a vector equation for the boundary constraints can be expressed as

$$M(U) = 0. \tag{2.64}$$

For the initial guess U_0, the above equation which is known as constraint residual equation, can be written similar to (2.62)

$$N(U_0)(U - U_0) = -M(U_0), \tag{2.65}$$

which often contains the same equation several times and where N is the Jacobian of M

$$N(U_0) = \frac{\partial M}{\partial U}(U_0). \tag{2.66}$$

Now the stiffness matrix equation is augmented by a vector of unknowns Λ, called the Lagrange multipliers, like

$$J(U_0)(U - U_0) + N(U_0)^T\Lambda = -L(U_0), \tag{2.67}$$

where N^T is the transpose of N. Before solving this system, the algorithm eliminates the Lagrange multipliers Λ. If the constraint (2.64) is satisfied, then there is a unique set of Lagrange multipliers satisfying (2.67). In other words, by a variational principle, Lagrange multipliers ensure that (2.64) is satisfied. However, (2.65) and (2.67) permit the simultaneous solution of more than just the boundary conditions. Any constraint that can be expressed in weak form can be treated by the Lagrange multiplier method. More details of the numerical method adopted by Comsol Multiphysics is described by Zimmerman (2006).

2.5.1 Building the model

There are several application modes like acoustics, chemical species transfer, fluid flow, heat transfer, structural mechanics, etc. based on physics in Comsol Multuphysics. To build our model we couple the physics of laminar fluid flow, heat transfer in fluids and Poisson's equation. The Poisson's equation is used to describe the stream-function - vorticity relation

$$-\nabla^2\psi = \omega, \tag{2.68}$$

where $\omega = u_z - w_x$ is the vorticity function.

After defining the geometry of the domain (i.e. the convection cell), we adjust the built-in equations and apply the boundary conditions according to our governing equations. Then we choose the appropriate meshing for the domain. In our case, we opt for free triangular meshing with some refinement near the boundaries which results in a complete mesh of $17,154$ elements. As the basis functions or shape functions, we select Lagrangian P2-P1 elements for laminar flow which means the shape functions for the velocity field and pressure are Lagrangian quadratic polynomials and Lagrangian linear polynomials, respectively. Thus for the velocity field we obtain six basis functions for each triangular element with nodes at the vertices and at the mid-points of the edges, whereas for the pressure variable, we get three basis functions per element. Similarly, we choose Lagrangian quadratic elements for both temperature in the heat equation and the streamfunction in Poisson's equation. For Lagrange elements, the values of all the variables at the node are called *degrees of freedom (dof)* and in this case, our specific discretization finally produces $150,216$ degrees of freedom (N_{dof}).

COMSOL Multiphysics has built-in 'stationary solver' and 'time-dependent solver' in solver setting for steady state (i.e. time-independent) problems and time-dependent problems respectively. As we are interested in steady state solutions, in solver settings, 'stationary solver' is our natural choice. However, to obtain an acceptable initial guess, we solve the problem in the time dependent solver with a low Rayleigh number Ra at first and allow it to evolve to a steady state. Then we use this solution as the initial guess in the stationary solver and ramp up Rayleigh number Ra gradually.

In the stationary solver, the computation terminates when the relative error computed as the weighted Euclidean norm satisfies

$$err = \frac{1}{\sqrt{M}} \left(\sum_{j=1}^{M} \frac{1}{N_{dof_j}} \sum_{i=1}^{N_{dof_j}} \left(\frac{|E_{i,j}|}{W_{i,j}} \right)^2 \right)^{\frac{1}{2}} < \epsilon, \tag{2.69}$$

where M is the number of fields (e.g. velocity, temperature, etc.), N_{dof_j} is the number of degrees of freedom in field j. The double subscript denotes degree of freedom index (i) and field (j) component. E is the estimated error calculated from (2.63), $W_{i,j} = max(|U_{i,j}|, S_j)$, where U is the current approximation to the solution vector, S_j is a scale factor that the solver determines from the scaling method. In our model S_j is the average of $|U_{i,j}|$ for all *dof*s i for fixed j. The relative tolerance is denoted by ϵ and we have chosen $\epsilon = 10^{-6}$. The default value for ϵ is 0.001 for the stationary solver and the results with $\epsilon = 10^{-3}$ and $\epsilon = 10^{-6}$ are practically indistinguishable.

Whilst the above describes the solution to the steady state, it also proved necessary to consider the associated time-dependent problem as a route to obtaining the solution to the steady problem. The convergence criterion at each time step is taken as

$$\frac{1}{\sqrt{M}} \left(\sum_{j=1}^{M} \frac{1}{N_{dof_j}} \sum_{i=1}^{N_{dof_j}} \left(\frac{|E_{Y_i}|}{A_{s,i} + R|Y_i|} \right)^2 \right)^{\frac{1}{2}} < 1, \tag{2.70}$$

where M is the number of fields, N_{dof_j} is the number of degrees of freedom in field j, E_Y is the solver's estimate of the (local) absolute error in Y, $A_{s,i}$ is the scaled absolute tolerance for the i-th *dof*, R is the relative tolerance, and $|Y_i|$ is the scaled solution vector corresponding to the solution at a certain time step. For our computations, $R = 0.001, A_i = 0.0005$ for $i = 1, ..., N_{dof}$ are used.

In the time-dependent solver, for time-stepping, we have used the implicit *generalized - α* method and, for both stationary and time-dependent solvers, the direct solver PARDISO is used to solve the linear system $Ax = B$, which uses LU factorization on the matrix A to compute the solution x. More specific details concerning the solvers can be found in the software manual (COMSOL Multiphysics, 2014).

2.5.2 Comparison with benchmark values

To validate our model, we have compared the values of Nusselt number Nu and root mean square velocity V_{rms} with the benchmark values from Blankenbach et al. (1989)[a] and Koglin Jr et al. (2005)[b]. Their values were computed for Ra up to 10^6 and 10^7 respectively. The comparison is shown in Table 2.2, where we can observe that the agreement is within a very good range. In this present work, we have successfully computed the values of Nu and V_{rms} for $Ra = 10^8$ and $Ra = 10^9$, and we present these also in Table 2.2.

Table 2.2: Comparison of computed Nusselt number Nu and RMS velocity V_{rms} with benchmark values from Blankenbach et al. (1989)[a] and Koglin Jr et al. (2005)[b]

	Nu			V_{rms}		
Ra	This work	Benchmark	Error(%)	This work	Benchmark	Error(%)
10^4	4.88447	4.884409[a]	0.001	42.86556	42.864947[a]	0.0016
10^5	10.53431	10.534095[a]	0.002	193.21859	193.21454[a]	0.002
10^6	21.97299	21.972465[a]	0.002	834.013189	833.98977[a]	0.0028
10^7	45.63939	45.62[b]	0.04	3633.38685	-	-
10^8	95.57220	-	-	16157.87730	-	-
10^9	201.31245	-	-	72930.10352	-	-

2.5.2.1 Nusselt number

The Nusselt number Nu is a ratio of the average surface heat flow from the convective solution to the heat flow due to conduction and is calculated in the present case of a square cell by the dimensionless relation

$$Nu = -\int_0^1 \frac{\partial T}{\partial z}(x,1)\, dx. \tag{2.71}$$

Nu is equal to unity for conduction and exceeds unity as soon as convection starts.

2.5.2.2 Root mean square (RMS) velocity

The non-dimensional RMS velocity V_{rms} is given in the present case of a square cell by the dimensionless relation

$$V_{rms} = \left[\int_0^1 \int_0^1 \left(u^2 + w^2\right) dxdz\right]^{\frac{1}{2}}, \tag{2.72}$$

where u is the horizontal component of velocity and w is the vertical component of velocity.

2.5.3 Numerical results

The steady-state two-dimensional solutions for temperature distributions, isothermal contours and streamlines for different Rayleigh numbers are presented in Figure 2.3, Figure 2.4 and Figure 2.5 respectively. As the Rayleigh number increases, convection starts to dominate the flow. In Figure 2.3, the colour blue indicates the cold region and red indicates the hot region. We can easily see that the analytic solutions from the weakly nonlinear stability analysis are acceptable for lower values of Ra (i.e. near the

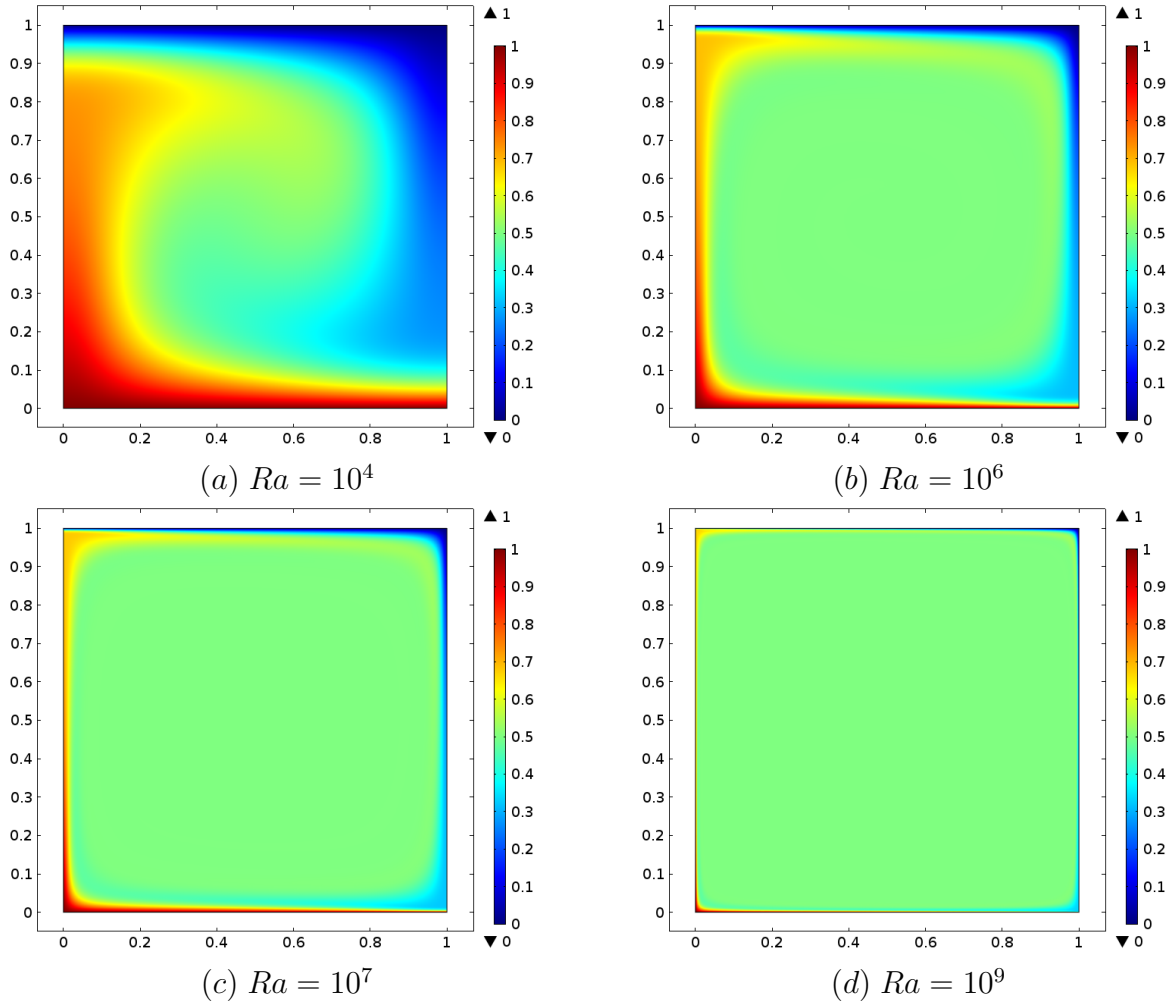

(a) $Ra = 10^4$ (b) $Ra = 10^6$

(c) $Ra = 10^7$ (d) $Ra = 10^9$

Figure 2.3: Temperature distributions for different Rayleigh numbers.

value of Ra_{cr}) but they do not give satisfactory solutions for high Rayleigh numbers relevant to mantle convection. It is also evident that as Ra is increased, the interior or core becomes isothermal and the extreme hot and cold regions become confined to the thin layers adjacent to the boundaries, thus creating thermal boundary layers. The thickness of the boundary layers also decrease gradually as Ra is increased. The values of ψ indicated on the contours in Figure 2.5 also indicate that the convection becomes more rigorous as Ra gets larger.

To understand the flow structure for high Rayleigh number better, the boundary layer theory will be discussed now.

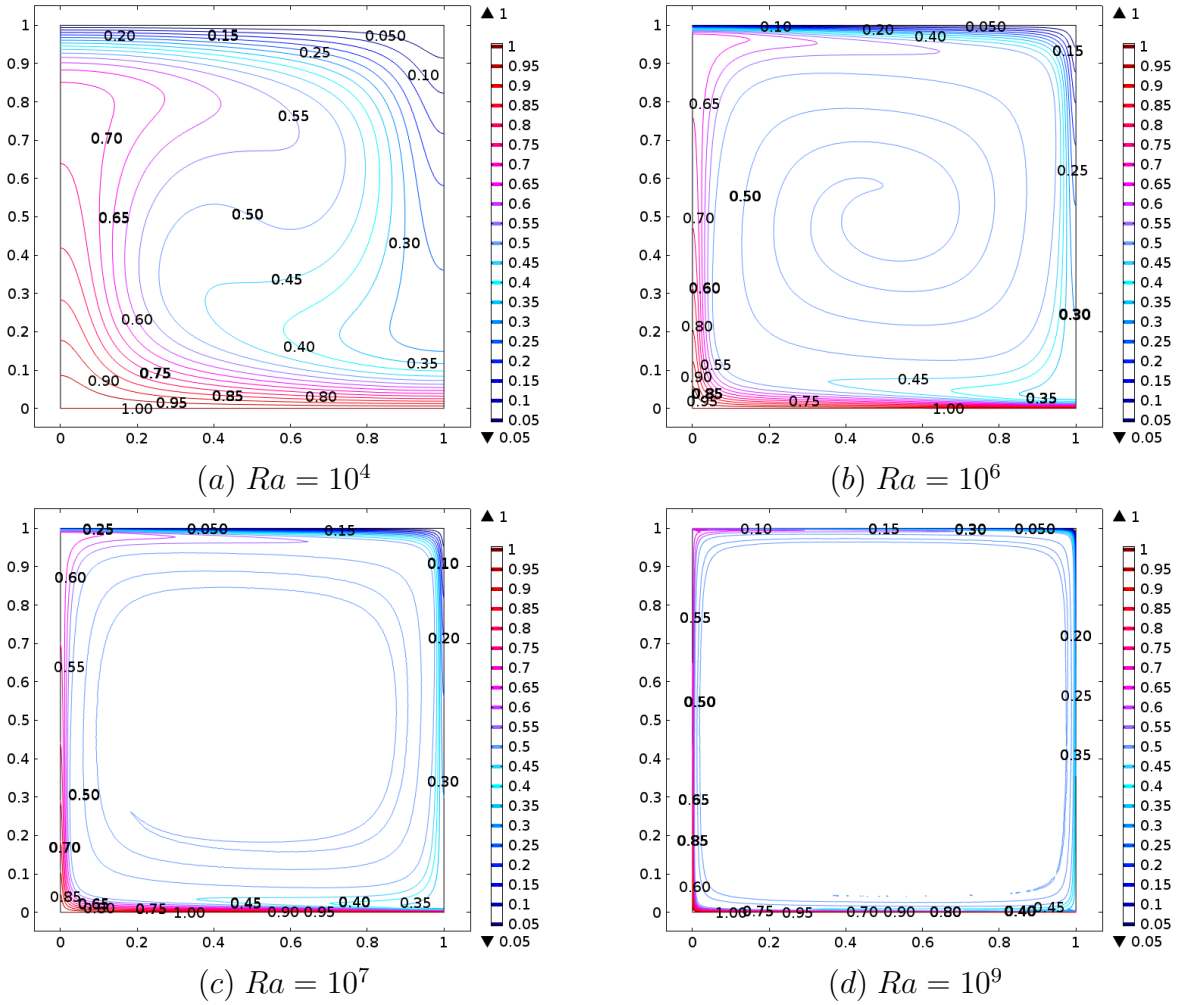

(a) $Ra = 10^4$ (b) $Ra = 10^6$

(c) $Ra = 10^7$ (d) $Ra = 10^9$

Figure 2.4: Isothermal contours for different Rayleigh numbers.

2.6 Boundary layer theory

A *boundary layer* is defined as a thin region in a flow field, usually adjoining an interface or boundary, where the gradients of some quantity transported by the fluid (e.g. vorticity, temperature, or chemical concentration) are large relative to those elsewhere in the flow (Bercovici, 2009). Physically, boundary layers arise when the boundary acts as a source of the transported quantity, which is then prevented from diffusing far from the boundary by strong advection.

Nonlinear stability theory, or weakly nonlinear theory, is useful when Ra is close to critical Ra_{cr}. The small amplitude theory is entirely satisfactory if $Ra - Ra_{cr} = O(1)$ (Fowler, 1997). However, it is inadequate for $Ra \gg 1$. The amount that the Rayleigh number of a convecting fluid exceeds Ra_{cr} is a measure of its convective vigour. While

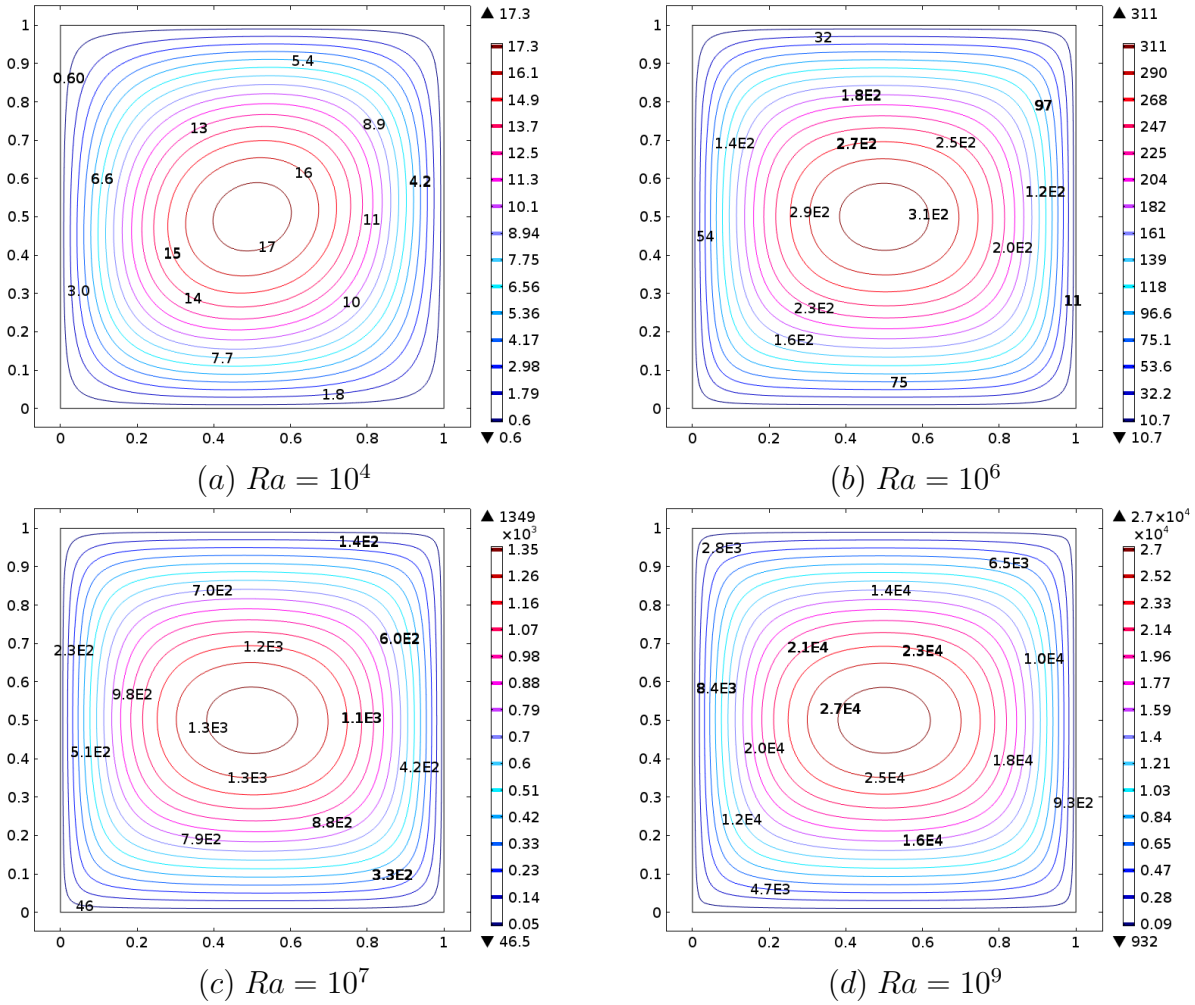

Figure 2.5: Stream function contours for different Rayleigh numbers.

Ra_{cr} for any fluid layer is of order 10^3, the present Rayleigh number of Earth's mantle is between 10^7 and 10^9. Thus, even though the mantle convects very slowly, it does so over great distances (thousands of kilometres) and against an extreme viscosity (10^{21} Pa s, as compared to, say, 10^2 Pa s for cold molasses), and therefore actually undergoes highly vigorous convection (Bercovici et al., 2000).

When basally heated convection is reasonably vigorous, it tends to stir the fluid until most of it is as homogeneous as possible, i.e. most of the fluid is at or near the average temperature of the top and bottom boundaries. However, directly adjacent to the top and bottom boundaries the fluid temperature must make a transition from the largely homogeneous interior value to the colder (at the top) or hotter (at the bottom) boundary value. As a result, in this transition region, temperature gradients along the horizontal direction are much smaller than across it and this gives rise to

thermal boundary layers. In effect, convection confines the gravitationally unstable parts of the fluid to these relatively thin boundary layers, keeping most of the rest of the fluid gravitationally stable (Bercovici et al., 2000). Because of their large vertical temperature gradients, the thermal boundary layers control, via thermal conduction, the influx and the efflux of heat. If the fluid is more vigorously stirred by convection then more of the fluid will be homogeneous, and thus the boundary layers will become thinner; and this results in even larger heat fluxes in to and/or out of the layer. As the gravitationally unstable material is confined to the thermal boundary layers, fluid in these layers must eventually either sink (if in the cold top boundary layer) or rise (if in the hot bottom boundary layer). This is exactly what we have found in our numerical solutions showed above. A very thin cold thermal boundary layer is formed at the upper boundary which can be related to the stagnant lid or lithosphere, the downwellings can be linked to subduction at an ocean trench. On the other hand, a thin hot thermal boundary adjoins the bottom boundary with upwellings at the side. The upwelling can be associated with the plumes.

Boundary layer analysis for steady cellular thermal convection with constant viscosity has been thoroughly studied by Turcotte and Oxburgh (1967), Roberts (1979), Olson and Corcos (1980), Jarvis and Peltier (1982), Jimenez and Zufiria (1987), Fowler (2011), Vynnycky and Masuda (2013). If the layer has thickness d and is unbounded in the horizontal direction, then the flow is divided into cellular two-dimensional rolls of width $\lambda/2$; alternate rolls rotate in opposite directions (Schubert et al., 2001). According to the studies cited above, the width of a cell corresponds to the linear stability value and can be taken as $\lambda = \sqrt{8}d$. The entire flow is highly viscous. On the cold upper boundary a thin cold thermal boundary layer forms. When the two cold boundary layers of adjacent cells meet, they separate from the boundary and form a cold descending sheet (plume). Similarly, a hot thermal boundary layer forms on the lower boundary of the cell. When two hot boundary layers from adjacent cells meet, they form a hot ascending sheet (plume). The buoyancy forces in the ascending and descending sheets drive the flow. The core or interior of each cell is nearly isothermal (Schubert et al., 2001). However, it should be noted here that the horizontal pressure gradients are the primary driving forces for thermal boundary layers (Bercovici et al., 2000).

Boundary layer analysis shows that vertical advection plays an important role in the energy balance within horizontal boundary layers at all Rayleigh numbers. Horizontal and vertical advection dominate the energy balance within vertical plumes while horizontal diffusion plays a very minor role (Jarvis and Peltier, 1982). The

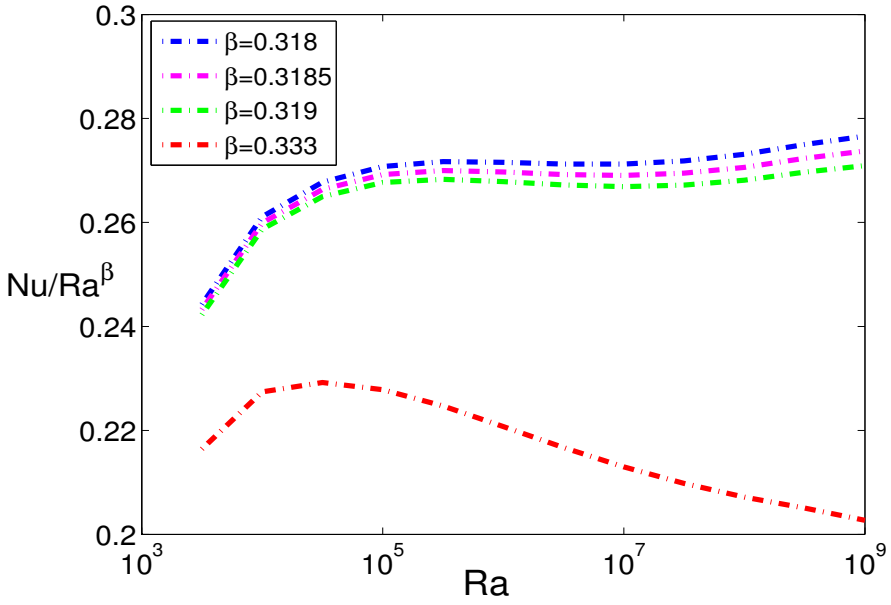

Figure 2.6: Nu/Ra^{β} versus Ra for different β values.

scaling analysis of boundary layer equations also reveals that for $Ra \gg 1$ and boundary layer thickness, $\delta_0 \ll 1$, if $\psi, \omega \sim \delta_0^{-2}$, where ψ is the stream-function and ω is the vorticity, then

$$\delta_0 \sim Ra^{-\frac{1}{3}} \quad \text{and} \quad Nu \sim \frac{1}{\delta_0} \sim Ra^{\frac{1}{3}}, \tag{2.73}$$

where Nu is the dimensionless heat transfer rate at the boundary (Fowler, 2011). The above relation implies that as Ra gets larger, the boundary layer thickness will decrease further. Our numerical results showed this behaviour quite clearly in the previous section.

2.7 Relation between Nusselt and Rayleigh numbers

The relationship between heat transfer coefficient, Nusselt number Nu and the Rayleigh number Ra from the boundary layer analysis is expressed usually as a power law form

$$Nu \sim cRa^{\beta} \quad \text{as} \quad Ra \to \infty. \tag{2.74}$$

Boundary layer theory yields $\beta = 1/3$ with the coefficient c depending on the cell width (Schubert et al., 2001). However, for square cells, calculations by Jarvis (1984) give

$$c = 0.29, \quad \beta = 0.318, \quad \text{for} \quad Ra \leq 8 \times 10^7, \tag{2.75}$$

while Schubert and Anderson (1985) obtain

$$c = 0.268, \quad \beta = 0.319 \quad \text{for} \quad Ra \leq 4 \times 10^8. \tag{2.76}$$

Later Olson (1987) found in the range $10^5 < Ra < 10^9$,

$$c = 0.1941 \quad \text{for} \quad \beta = 1/3, \tag{2.77}$$

and Jimenez and Zufiria (1987) estimated $c = 0.1968$ for $\beta = 1/3$. Christensen (1989) found that no single power law fit the Nusselt number for all Ra values. Near $Ra = 10^6$, his results give $c = 0.27, \beta = 0.3185$ and they slowly asymptote toward the $1/3$ power law at very large Ra.

Here we present the graphs of $c = Nu/Ra^\beta$ versus Ra for different β values in Figure 2.6. It shows that for $\beta = 0.333$, the curve for Nu/Ra^β converges to a constant value c more rapidly than the other curves for large Ra values. However, an oscillatory behaviour is quite prominent when $\beta = 0.318, 0.3185$ and 0.319. To predict the value of c theoretically in (2.74), we use the *Shanks transformation.*

We assume that the relation between Nu and Ra is of the form

$$\frac{Nu}{Ra^\beta} = c + \frac{a}{Ra^\gamma}, \tag{2.78}$$

where c is the proportionality constant and the final term is the decaying transient we wish to eliminate. We calculate the left-hand side numerically for equally-spaced values of large Ra, specifically for $Ra = 10^{4.5+n/2}, n = 1, 2, ...$ so that (2.78) takes the form

$$\left(\frac{Nu}{Ra^\beta}\right)_n = c + \frac{a}{10^{9\gamma/2+\gamma n/2}}, \tag{2.79}$$

which is of the required form for Shanks transformation (see appendix B) with

$$A_n = \left(\frac{Nu}{Ra^\beta}\right)_n, \quad A = c, \quad \alpha = \frac{a}{10^{4.5\gamma}}, \quad q = 10^{-\gamma/2}. \tag{2.80}$$

In Table 2.3 - 2.6, we have used iterated Shanks transformation on the columns to predict the value of c in (2.74), where $S1 = S(A_n)$, $S2 = S^2(A_n) = S[S(A_n)]$, $S3 = S^3(A_n) = SS[S(A_n)]$ and so on, and each column of S1, S2, S3, S4 gives estimates for c. In Table 2.3, we have taken $\beta = 1/3$ to generate the series and see that the Shanks transformation gives an accurate value of c just as Olson (1987) predicted. In Table 2.4, we have chosen $\beta = 0.318$ to calculate the values of $Nu/Ra^{0.318}$, and the Shanks transformation successfully predicts the value of c up to 3 decimal places. However, this value does not match the value that Jarvis (1984) gave. In Table 2.5 and Table 2.6, the Shanks transformation is used for $\beta = 0.3185$ and 0.319 and the values we obtain are quite close to the values given by Christensen (1989) and Schubert and Anderson (1985) respectively.

Table 2.3: Estimation of c in (2.74) using Shanks transformation for $\beta = 1/3$.

n	Nu/Ra^(1/3)	S1	S2	S3	S4
1	0.22695				
2	0.22376	0.23931			
3	0.21973	0.40676	0.30866		
4	0.21561	0.16986	0.18733	0.19372	
5	0.21184	0.18872	0.19407	0.19431	0.19416
6	0.20859	0.19289	0.1943	0.19411	
7	0.2059	0.19395	0.19286		
8	0.20371	0.23001			
9	0.20131				

Table 2.4: Estimation of c in (2.74) using Shanks transformation for $\beta = 0.318$.

n	Nu/Ra^(0.318)	S1	S2	S3	S4
1	0.27077				
2	0.27171	0.27159			
3	0.27157	0.27181	0.27165		
4	0.27123	0.27123	0.27123	0.27123	
5	0.27123	0.27123	0.27123	0.27123	0.27123
6	0.27183	0.27069	0.27156	0.27131	
7	0.27311	0.26924	0.27057		
8	0.27501	0.28539			
9	0.27661				

Table 2.5: Estimation of c in (2.74) using Shanks transformation for $\beta = 0.3185$.

n	Nu/Ra^(0.3185)	S1	S2	S3	S4
1	0.26922				
2	0.27	0.26978			
3	0.26971	0.27042	0.26998		
4	0.26921	0.26898	0.26915	0.26902	
5	0.26905	0.26917	0.26904	0.26912	0.26915
6	0.2695	0.26876	0.26937	0.26914	
7	0.2706	0.26751	0.26865		
8	0.27233	0.28077			
9	0.27376				

Table 2.6: Estimation of c in (2.74) using Shanks transformation for $\beta = 0.319$.

n	Nu/Ra^(0.319)	S1	S2	S3	S4
1	0.26767				
2	0.26829	0.26803			
3	0.26785	0.26929	0.26843		
4	0.26721	0.2666	0.26698	0.26687	
5	0.26689	0.26704	0.26688	0.26695	0.26698
6	0.26718	0.26677	0.26714	0.26697	
7	0.26812	0.26572	0.26668		
8	0.26968	0.2764			
9	0.27094				

2.8 Summary

In this chapter, we have set out the model equations to describe mantle convection with constant viscosity. The governing equations are simplified with the assumption of infinite Prandtl number and by neglecting the effects of viscous dissipation and internal heating. The dimensionless equations contain only one parameter, namely the Rayleigh number Ra. Linear stability analysis predicts the critical Rayleigh number Ra_{cr} for the onset of convection, and weakly nonlinear stability analysis describes the convection pattern which is quite satisfactory when Ra is close to Ra_{cr}. Since the effective Ra for mantle is very large compared to the critical Ra, we solve the model numerically for high values of Ra and compare our results with benchmark values which are found to be in very good agreement. Having our code validated, we are able to solve our model for extreme values of Ra up to 10^9. From our solutions we observe an isothermal core, plumes at the side walls and boundary layers at the top and bottom boundaries in the unit aspect-ratio convecting cell. The numerical investigation also helps us to calculate the proportionality constant c in the asymptotic relation between Nusselt number and Rayleigh number found from the boundary layer analysis as (2.74). The numerical result of this chapter reassures us that our code is working properly.

There are remarkable similarities and important differences between this model and mantle convection. To a good approximation the cold thermal boundary layer is the lithospheric plate or plate tectonics. As the convection cell has been assumed as a part of the periodic structure in an infinite horizontal layer, the boundaries between cells where hot material ascends and the cold thermal boundary layers form are analogous to mid-ocean ridges, and the cold descending sheets are analogous to

subduction zones. An important difference between this model and the mantle is that subduction in the simple boundary layer model is symmetric while subduction in the Earth is invariably asymmetric (Schubert et al., 2001). But the main difference between this model and mantle convection lies with the assumption of constant viscosity, because it is a well-established fact that the actual mantle viscosity is a variable which strongly depends on temperature, stress and pressure as well as characterized by brittle fracture, plastic yielding, elasticity. In the next chapter, we will consider the case where viscosity depends on temperature only.

Chapter 3

Convection with Temperature-dependent Viscosity

3.1 Introduction

Both numerical and analytic studies of mantle convection assuming a constant viscosity appear to give a satisfactory explanation for plate tectonic observations on the Earth; for example, the lithosphere plates are identified with thermal boundary layers of the convection cells. The studies of Turcotte and Oxburgh (1967), Roberts (1979), Jimenez and Zufiria (1987), Moore and Weiss (1973), Jarvis and Peltier (1982) provided good quantitative predictions of plate velocity and oceanic heat flux, but failed to explain the rigidity of the lithosphere. Hence, we now consider the rheology of mantle rocks in the convection model. Since the effective viscosity of the mantle strongly depends on temperature, pressure and stress (Kirby 1983, Karato and Wu 1993) as we have discussed in section 1.5, in this chapter we will introduce convection with variable viscosity and especially study the effects of temperature-dependent viscosity.

3.2 Governing equations

We consider classical Rayleigh-Bénard convection in a two-dimensional rectangular cell of depth d and width ad, with a fixed temperature difference between the horizontal boundaries. This convective cell, with aspect ratio a, is assumed to be a part of a periodic structure in an infinite horizontal layer. We adopt Cartesian coordinates (x, z) with the x-axis horizontal and the z-axis pointing vertically upwards. The governing equations ensure the conservation of mass, momentum and energy and are completed by a suitable thermodynamic equation of state. We make the Boussinesq

approximation and neglect the inertia terms in the Navier–Stokes equations (taking the limit of infinite Prandtl number) as in chapter 2, so that the governing equations read

$$\begin{aligned}
\frac{\partial u}{\partial x} + \frac{\partial w}{\partial z} &= 0, \\
\frac{\partial p}{\partial x} &= \frac{\partial \tau_1}{\partial x} + \frac{\partial \tau_3}{\partial z}, \\
\frac{\partial p}{\partial z} &= \frac{\partial \tau_3}{\partial x} - \frac{\partial \tau_1}{\partial z} - \rho g, \\
\tau_1 &= 2\eta \frac{\partial u}{\partial x}, \\
\tau_3 &= \eta \left(\frac{\partial u}{\partial z} + \frac{\partial w}{\partial x} \right), \\
\rho &= \rho_0 \left[1 - \alpha \left(T - T_b \right) \right], \\
\frac{\partial T}{\partial t} + \boldsymbol{u} \cdot \nabla T &= \kappa \nabla^2 T,
\end{aligned} \tag{3.1}$$

where u, w are the velocity components in the x and z directions, p is the pressure, τ_1 and τ_3 are the longitudinal and shear components of the deviatoric stress tensor respectively, ρ is the density, g is the constant gravitational acceleration, t is time, T is the absolute temperature and η is the viscosity. The parameters in the model are the gravitational acceleration g, thermal expansion coefficient α, thermal diffusivity κ, reference temperature T_b and ρ_0 is the reference density at T_b.

We use the constitutive relation (1.14) for the viscosity, namely

$$\eta = \frac{1}{2A||\tau||^{n-1}} \exp\left\{ \frac{E^* + pV^*}{RT} \right\}, \tag{3.2}$$

where A is the rate factor, n is the flow index, $||\tau||$ is the square root of the second invariant of the deviatoric stress tensor, E^* is the activation energy per mole, V^* is the activation volume per mole, $Q = E^* + pV^*$ is the activation enthalpy (basically the height of the potential-well of the lattice site out of which the mobilized atom must jump), R is the gas constant and RT represents the average kinetic energy of the atoms in the lattice sites. The second stress invariant is given by

$$||\tau|| = \sqrt{\tau_1^2 + \tau_3^2}. \tag{3.3}$$

We impose free-slip boundary conditions on all boundaries and thermal insulation on the vertical sides. The base and top of the cell are assumed to be at specified

temperatures T_b and T_s respectively, so the boundary conditions are

$$\begin{aligned} w = 0, \quad \tau_3 = 0, \quad T = T_b \qquad &\text{on} \quad z = 0, \\ w = 0, \quad \tau_3 = 0, \quad T = T_s \qquad &\text{on} \quad z = d, \\ u = 0, \quad \tau_3 = 0, \quad \frac{\partial T}{\partial x} = 0 \qquad &\text{on} \quad x = 0, ad. \end{aligned} \tag{3.4}$$

In addition to the assumptions noted above, we have neglected internal heating and compressibility, and thermal diffusivity is taken as a constant as in chapter 2.

3.2.1 Non-dimensionalisation

We use the same scaling variables to non-dimensionalize the equations as in chapter 2, except now η_0 is unknown and the temperature is scaled with the basal temperature T_b as follows:

$$\begin{aligned} &(x, z) = d(x^*, z^*), \qquad T = T_b T^*, \qquad u = \frac{\kappa}{d}\, u^*, \quad \eta = \eta_0 \eta^*, \\ &\tau = \frac{\eta_0 \kappa}{d^2}\, \tau^* \equiv \tau_0\, \tau^*, \qquad t = \frac{d^2}{\kappa} t^*, \qquad p = \rho_0 g d(1 - z^*) + \frac{\eta_0 \kappa}{d^2} p^*. \end{aligned} \tag{3.5}$$

Using these in (3.1) and dropping the asterisk decorations, we find that the dimensionless equations are

$$\begin{aligned} \frac{\partial u}{\partial x} + \frac{\partial w}{\partial z} &= 0, \\ \frac{\partial p}{\partial x} &= \frac{\partial \tau_1}{\partial x} + \frac{\partial \tau_3}{\partial z}, \\ \frac{\partial p}{\partial z} &= \frac{\partial \tau_3}{\partial x} - \frac{\partial \tau_1}{\partial z} - Ra(1 - T), \\ \tau_1 &= 2\eta \frac{\partial u}{\partial x}, \\ \tau_3 &= \eta \left(\frac{\partial u}{\partial z} + \frac{\partial w}{\partial x} \right), \\ \frac{\partial T}{\partial t} + \boldsymbol{u} \cdot \nabla T &= \nabla^2 T, \\ \eta &= \frac{1}{\tau^{n-1}} \exp \left[\frac{1 - T + \mu \left\{ 1 - z - T + \overline{B} p / Ra \right\}}{\varepsilon T} \right], \end{aligned} \tag{3.6}$$

where the parameters are defined as

$$\begin{aligned} Ra = \quad & \frac{\alpha \rho_0 g T_b d^3}{\eta_0 \kappa}, \qquad \varepsilon = \frac{R T_b}{E^*}, \\ \mu = \quad & \frac{\rho_0 g d V^*}{E^*}, \qquad \overline{B} = \alpha T_b, \end{aligned} \tag{3.7}$$

Table 3.1: Typical parameter values for numerical models of mantle convection.

Parameter	Symbol	Value	Units
Depth	d	3×10^6	m
Thermal expansion coefficient	α	2×10^{-5}	K^{-1}
Reference density	ρ_0	4×10^3	$\mathrm{kg\,m}^{-3}$
Gravitational acceleration	g	10	$\mathrm{m\,s}^{-2}$
Temperature at the top	T_s	300	K
Temperature at the base	T_b	3000	K
Activation energy	E^*	$300 - 540$	$\mathrm{kJ\,mol}^{-1}$
Activation volume	V^*	$6 \times 10^{-6} - 2 \times 10^{-5}$	$\mathrm{m}^3\,\mathrm{mol}^{-1}$
Gas law constant	R	8.31	$\mathrm{J\,mol}^{-1}\,\mathrm{K}^{-1}$
Viscous rate constant	A	10^5	$\mathrm{MPa}^{-1}\mathrm{s}^{-1}$

and η_0 is chosen as

$$\eta_0 = \frac{1}{2A\tau_0^{n-1}} \exp\left(\frac{1+\mu}{\varepsilon}\right). \tag{3.8}$$

The dimensionless boundary conditions (3.4) are

$$\begin{aligned}
&w = 0, \quad \tau_3 = 0, \quad \frac{\partial u}{\partial z} = 0, \quad T = 1 \quad \text{on} \quad z = 0, \\
&w = 0, \quad \tau_3 = 0, \quad \frac{\partial u}{\partial z} = 0, \quad T = \frac{T_s}{T_b} = T_0 \quad \text{on} \quad z = 1, \\
&u = 0, \quad \tau_3 = 0, \quad \frac{\partial w}{\partial x} = 0, \quad \frac{\partial T}{\partial x} = 0 \quad \text{on} \quad x = 0, a.
\end{aligned} \tag{3.9}$$

The typical values of the parameters for the Earth are given in Tables 3.1 and 3.2. The values of activation energy E^* and activation volume V^* given above are good estimates for dry upper mantle, the lowest values being for diffusion creep and the highest for the dislocation creep (Schubert et al., 2001). However, Ammann et al. (2009) found that the activation volume V^* can be as small as 1.49×10^{-6} m^3 mol^{-1} in the lower mantle due to high pressure.

For $Ra \gg 1$, we can see that $\overline{B}/Ra$ can be easily ignored. Moreover, we neglect the stress dependence by choosing $n = 1$ and this gives us a Newtonian viscosity in the following form

$$\eta = \exp\left[\frac{1 - T + \mu\,(1 - z - T)}{\varepsilon T}\right]. \tag{3.10}$$

When viscosity is purely *temperature-dependent* i.e. $\mu = 0$ and $\varepsilon \neq 0$, then (3.10) has the form

$$\eta = \exp\left(\frac{1-T}{\varepsilon T}\right), \tag{3.11}$$

Table 3.2: Dimensionless parameter values.

Parameter	Symbol	Value
Rayleigh number	Ra	$10^7 - 10^9$
Surface temperature	T_0	0.1
Boussinesq number	$\overline{B}$	0.06
Viscous temperature number	ε	$0.046 - 0.083$
Viscous pressure number	μ	$1.3 - 2.4$

where ε is the only parameter that controls the viscosity variation across the mantle. Our complete dimensionless model for the temperature-dependent viscosity case consists of the governing equations (3.6), the constitutive relation (3.11) and the boundary conditions (3.9).

3.2.2 Viscosity contrast, Nusselt number and RMS velocity

We now define three useful diagnostic quantities which will be used to characterise the numerical results found below. First, we define the viscosity contrast $\Delta\eta$ to be the ratio between the surface and basal values of the viscosity, that is

$$\Delta\eta = \exp\left(\frac{1 - T_0}{\varepsilon T_0}\right). \tag{3.12}$$

Second, the Nusselt number Nu in this case is calculated by

$$Nu = -\frac{1}{a(1 - T_0)} \int_0^a \frac{\partial T}{\partial z}(x, 1)\, \mathrm{d}x. \tag{3.13}$$

Finally, the vigour of the circulating flow is characterised by the non-dimensional RMS (root mean square) velocity which is defined here by

$$V_{rms} = \left[\int_0^1 \int_0^a \left(u^2 + w^2\right)\, \mathrm{d}x\, \mathrm{d}z\right]^{1/2}. \tag{3.14}$$

3.3 Numerical investigation

With the inverse dependence on T in the exponent of (3.11), viscosity is highly sensitive to temperature fluctuations at lower temperatures. As a result, the viscosity versus temperature curve is steepest at low T as shown in Figure 3.1. This implies that in the coldest region of the mantle, i.e. the lithosphere, the viscosity undergoes drastic changes. Thus the effect of temperature-dependent viscosity on mantle convection is to make the top colder thermal boundary layer much stronger than the rest of the

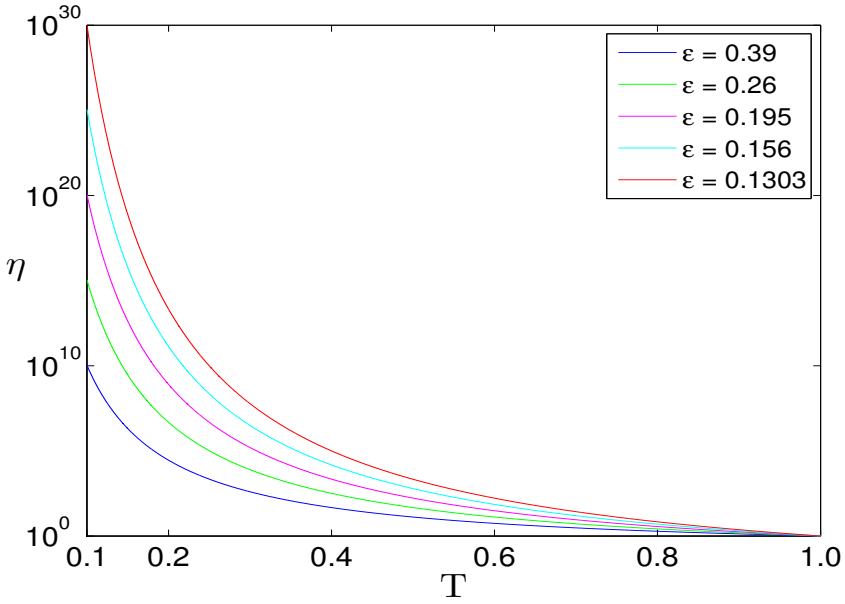

Figure 3.1: Viscosity variation with temperature in the range $0.1 \leqslant T \leqslant 1.0$ for different ε values.

mantle. This phenomenon helps make thermal convection in the mantle plate-like at the surface in some respects (Bercovici et al., 2000).

Convection with temperature-dependent viscosity has been investigated by various authors (Christensen, 1984a, Kameyama and Ogawa, 2000, Trompert and Hansen, 1998) where the viscosity contrast was taken up to 10^8 only. Experimental studies of convection in fluids with temperature-dependent viscosity reached viscosity contrasts of the order of 10^5. Moresi and Solomatov (1995) used a finite element multigrid scheme (CITCOM) to investigate convection with viscosity variation up to 10^{14} for the first time. Here we build our model using the finite element method based PDE solver Comsol Multiphysics in a similar way to that described in chapter 2 for the dimensionless governing equations (3.6), (3.9) and (3.11) and study thermal convection with a viscosity contrast of order up to 10^{30} in a unit aspect-ratio convection cell ($a = 1$). Even though we are interested with high Rayleigh number convection with extreme viscosity contrast, COMSOL Multiphysics can not find a solution for $Ra = 10^7$ directly. For the convergence to a solution, Newton's method must start near a solution. For a nonlinear problem, the initial condition may not be in the 'basin of attraction' for the desired solution. That is why, we start by solving the system for a low Ra with relatively large value of ε and then restart the simulation with a slightly larger value of Ra but this time we use the solution of the low Ra

convection as the initial condition. In this way, we gradually increase the value of Ra by using the solution of the previous simulation as the initial guess. When we achieve the solution of the high Ra convection, we decrease the value of temperature dependence parameter ε to increase the viscosity across the layer. The process can be termed as the 'parametric continuation'. Because the solution at the new parameter values is not expected to be much different than at the old parameter values, the Newton solver should converge rapidly. This methodology only fails if the new parameter is close to a bifurcation point - in which case multiple solutions are possible. The Jacobian used by Newton's method is then very close to singular, so convergence may not be achieved. Or if it is, which of the multiple solutions that is selected may not be *a priori* predictable (Zimmerman, 2006). It should be mentioned that we use both the stationary solver and the time-dependent solver in this process of parametric continuation. For each simulation, the steady solution is found from the stationary solver first and then this solution is used in the time-dependent solver as the initial guess with the same parameters. Again, the steady state is found by solving the time-dependent version and allowing it to evolve to a steady state in time-dependent solver. Comparison of the Nusselt number and root mean square velocity from both solvers ensures the equality of the solutions.

3.3.1 Comparison with benchmark values

We tested our model according to the benchmark published by King (2009) and found good agreement with the Nusselt number Nu and root mean square velocity V_{rms} values shown in Table 3.3. King (2009) shows that for viscosity contrast $\Delta\eta = 10^3$, Nu and V_{rms} decrease significantly as the grid is changed from 50×50 to 500×500, but as the viscosity contrast gets larger, Nu and V_{rms} give the same value for every grid choice. Our mesh is created using the free triangular elements predefined by 'general physics', which is the default Comsol Multiphysics solver setting. However, we used Comsol's 'extra fine' setting with refinement near the boundaries (200×200) and the mesh is composed of 17,154 elements with a total number of degrees of freedom 150,437. Here we present our result along with the benchmark values that were calculated for grid size 200×200. Clearly, our mesh is coarser than the benchmark model but still we get good results. It should be mentioned here that we set $T_0 = 0.12$ and $Ra = 1.136 \times 10^7$ and accordingly adjusted our parameter values of ε to compare with King (2009).

Table 3.3: Comparison with benchmark values for $Ra = 1.136 \times 10^7$.

		Nu		V_{rms}	
$\Delta\eta$	ε	This work	Benchmark	This work	Benchmark
10^3	1.06	19.302	19.80	1559.69	1572.76
10^5	0.637	9.289	9.29	1035.316	1034.87
10^7	0.455	7.689	7.69	885.329	884.89

3.3.2 Results

Having validated our code with benchmark values, we proceed to solve the system of equations described in (3.6), (3.9) and (3.11) and we fix the dimensionless surface temperature $T_0 = 0.1$ throughout. Figure 3.2 shows the variation of Nu and V_{rms} with ε for different Rayleigh numbers Ra. The larger values of Nu and V_{rms} for $Ra = 10^7$ compared to $Ra = 10^6$ gives evidence that when Ra gets larger, the vigour of convection becomes stronger as expected. It also shows that stronger temperature-dependence, induced by smaller ε values, makes the convection weaker and that is why Nu and V_{rms} decrease with high viscosity contrasts. The subplot of Nu versus ε gives an indication that there might be an asymptotic relation between Nu, Ra and ε, and this will be discussed in the next section.

Figure 3.3 and Figure 3.4 show the temperature distributions and equally spaced isothermal contours for different viscosity contrasts $\Delta\eta = 10^3, 10^5, 10^{10}, 10^{20}, 10^{25}, 10^{30}$ at $Ra = 10^7$. As before, the colour blue indicates the cold thermal boundary layer and red indicates the hot thermal boundary layer. So, it is evident from the figures that as the viscosity contrast gets larger, i.e. the value of ε decreases, the cold upper thermal boundary layer thickness increases. Also, the temperature of the interior of the cell increases significantly with the increase of viscosity variation.

The streamlines corresponding to $\varepsilon = 0.39$ and $\varepsilon = 0.1303$ are presented in Figure 3.5. These are defined as contours of the streamfunction $\psi(x, z)$, defined as usual such that

$$u = -\psi_z, \qquad w = \psi_x. \tag{3.15}$$

The absence of streamlines at the top indicates the presence of a stagnant lid which can explain the existence of the lithosphere as well.

Figure 3.6 displays how the temperature profiles at the mid-cell (i.e. $x = 0.5$) change with depth at different viscosity contrasts. It is interesting to note that most of the temperature change across the fluid occurs in the relatively narrow thermal

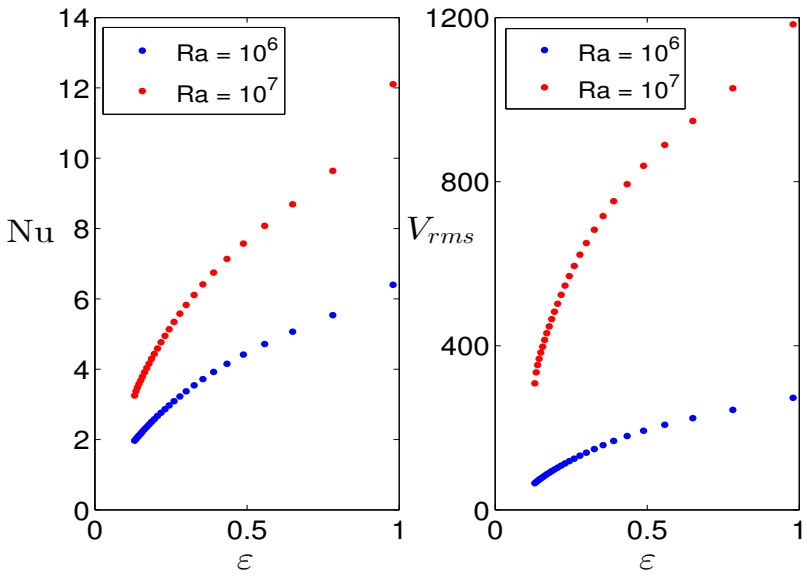

Figure 3.2: Nusselt number Nu and root mean square velocity V_{rms} versus ε for $T_0 = 0.1$ and different values of Ra. The viscosity variation $\Delta\eta$ is between 10^4 and 10^{30}.

boundary layers near the top and bottom surfaces. In between these two layers, the fluid temperature is almost constant.

The cold thermal boundary layer at the top is mechanically much stronger and less mobile than the hot boundary layer at the base. This can be supported by Figure 3.7 which shows the viscosity distributions at $\varepsilon = 0.39$ and $\varepsilon = 0.1303$ in log scale. It can be easily seen that viscosity changes abruptly at the top and the rest of the mantle is almost isoviscous. In fact, the less mobile upper boundary induces something like a heat plug that forces the fluid interior to warm up; this in turn causes the temperature contrast between the fluid interior and the surface to increase, and the contrast between the fluid interior and underlying medium (the core in the Earth's case) to decrease. This effect leads to a larger temperature jump across the top boundary layer and a smaller one across the bottom boundary layer (Bercovici et al., 2000). It is also evident from Figure 3.6 that the interior of the mantle gets warmer as the viscosity variation gets larger.

3.4 Boundary layer theory and scaling analysis

According to Stengel et al. (1982), when the fluid viscosity can be well-approximated by an exponential function with a steeper viscosity gradient at low temperatures,

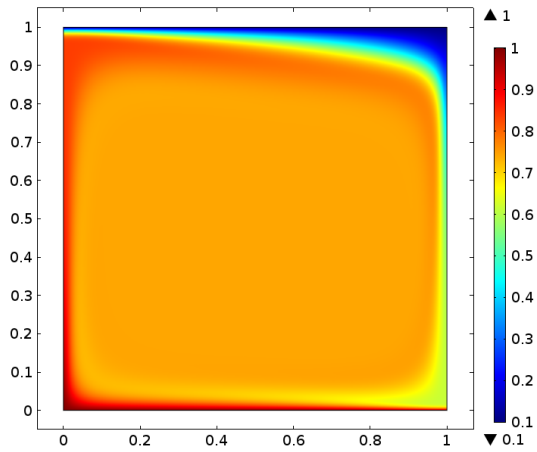

$(a)\ \Delta\eta = 10^3,\ \varepsilon = 1.3$

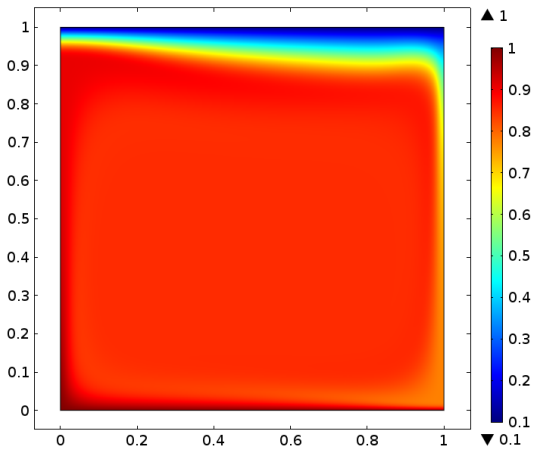

$(b)\ \Delta\eta = 10^5,\ \varepsilon = 0.782$

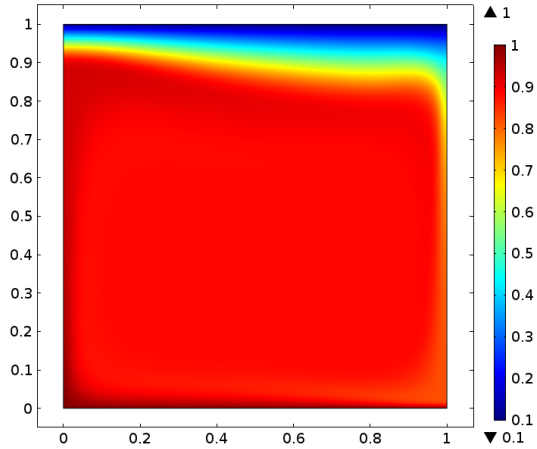

$(c)\ \Delta\eta = 10^{10},\ \varepsilon = 0.39$

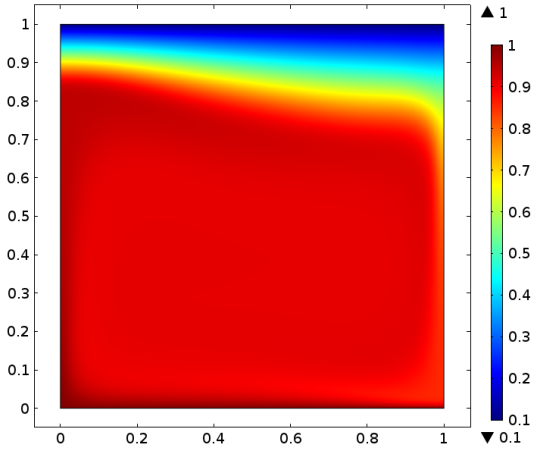

$(d)\ \Delta\eta = 10^{20}\ \varepsilon = 0.195$

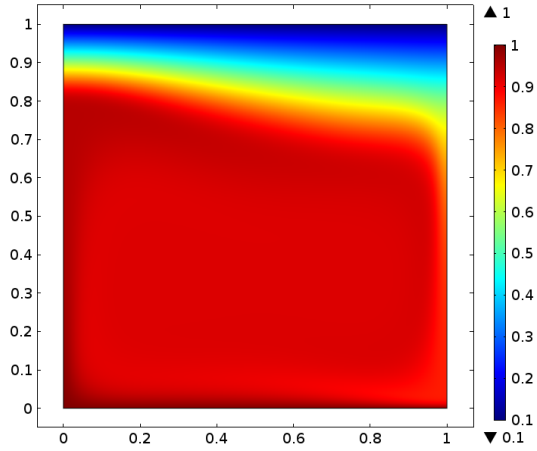

$(e)\ \Delta\eta = 10^{25},\ \varepsilon = 0.156$

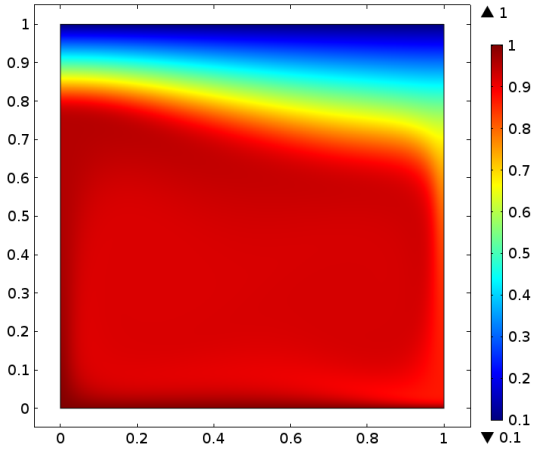

$(f)\ \Delta\eta = 10^{30},\ \varepsilon = 0.1303$

Figure 3.3: Thermal distributions of a temperature-dependent viscosity convection at different viscosity variations for $T_0 = 0.1$ and $Ra = 10^7$.

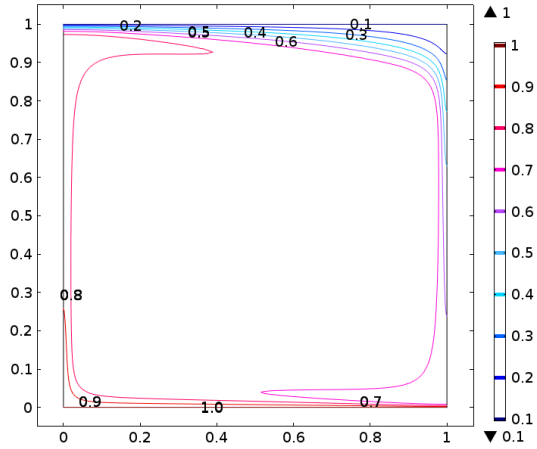

$(a)\ \Delta\eta = 10^3,\ \varepsilon = 1.3$

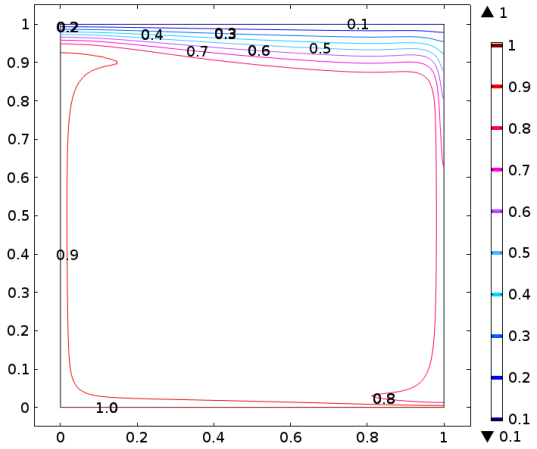

$(b)\ \Delta\eta = 10^5,\ \varepsilon = 0.782$

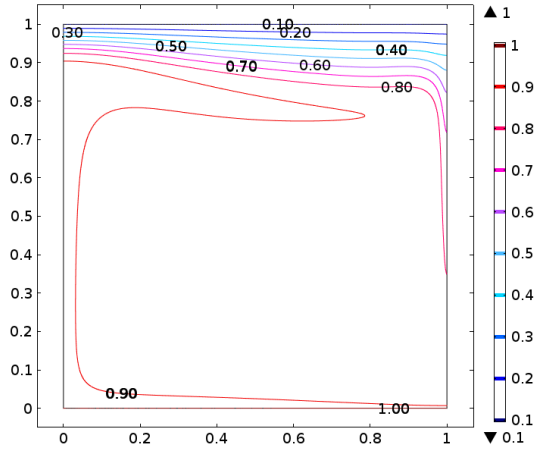

$(c)\ \Delta\eta = 10^{10},\ \varepsilon = 0.39$

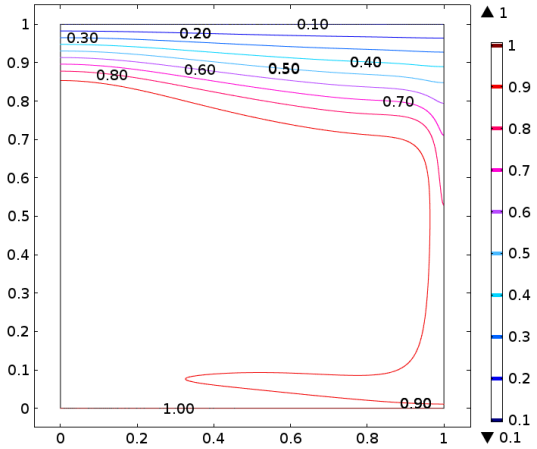

$(d)\ \Delta\eta = 10^{20}\ \varepsilon = 0.195$

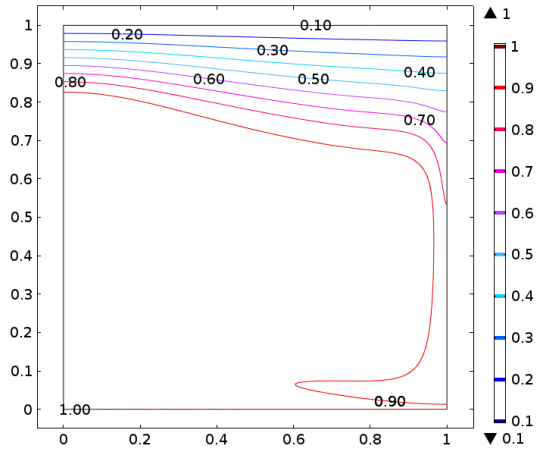

$(e)\ \Delta\eta = 10^{25},\ \varepsilon = 0.156$

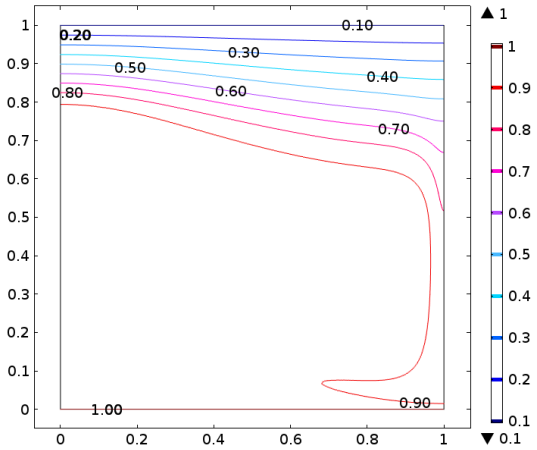

$(f)\ \Delta\eta = 10^{30},\ \varepsilon = 0.1303$

Figure 3.4: Isothermal contours of a temperature-dependent viscosity convection at different viscosity variations for $T_0 = 0.1$ and $Ra = 10^7$.

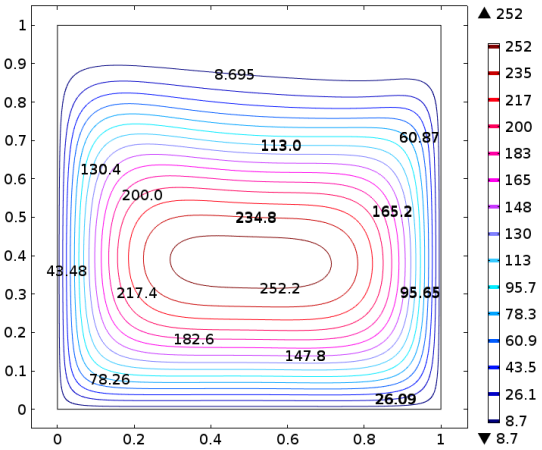

(*a*) $\Delta\eta = 10^{10}$, $\varepsilon = 0.39$

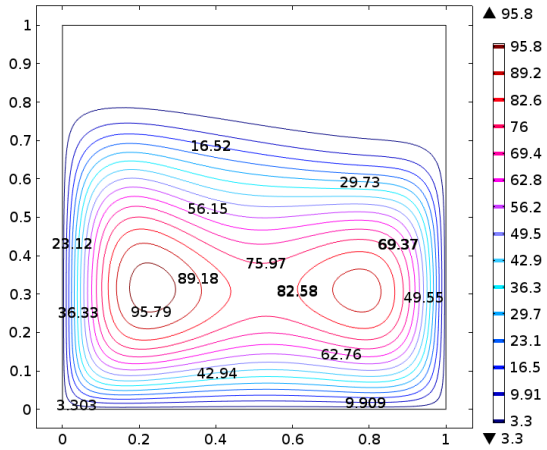

(*b*) $\Delta\eta = 10^{30}$, $\varepsilon = 0.1303$

Figure 3.5: Stream function contours of a temperature-dependent viscosity convection at different viscosity variations for $T_0 = 0.1$ and $Ra = 10^7$.

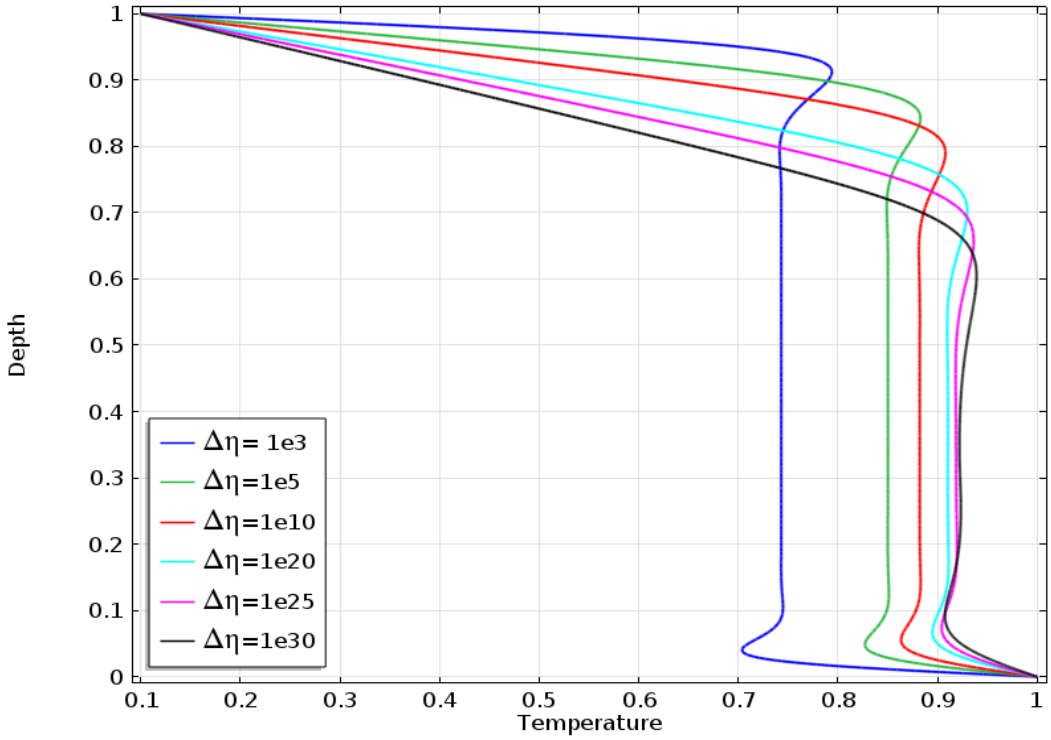

Figure 3.6: Temperature profiles at the mid-cell ($x = 0.5$) at different ε values for different viscosity contrasts for convection with temperature-dependent viscosity at $T_0 = 0.1$ and $Ra = 10^7$.

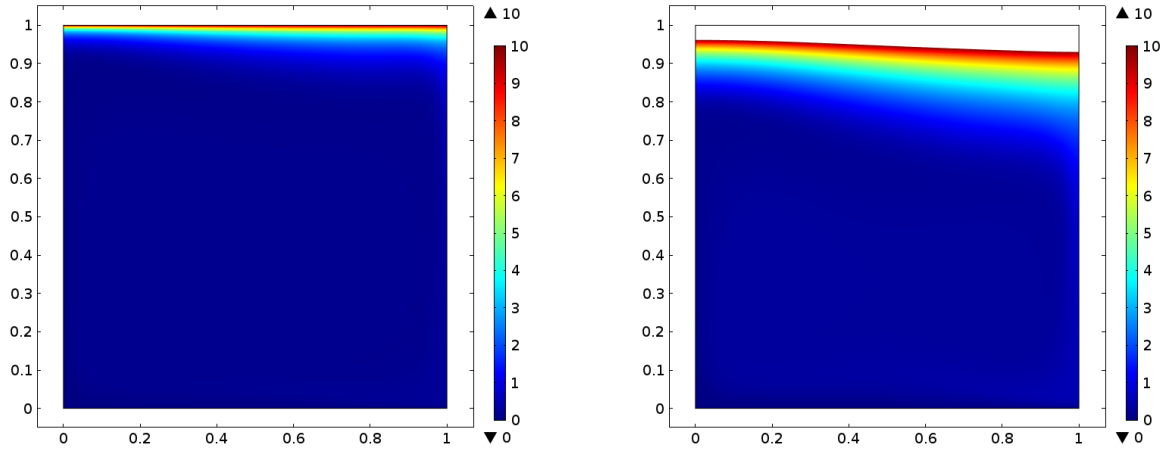

(*a*) $\Delta\eta = 10^{10},\ \varepsilon = 0.39$ (*b*) $\Delta\eta = 10^{30},\ \varepsilon = 0.1303$

Figure 3.7: Log viscosity contours of a temperature-dependent viscosity convection at different ε values for $T_0 = 0.1$ and $Ra = 10^7$. In (b) the upper part of the range of viscosity variation is excised.

the theoretical critical Rayleigh number Ra_{cr} based on the viscosity at the mean of the boundary temperatures increases as the ratio between the boundary viscosities initially increases. If the logarithmic temperature derivative of the viscosity is sufficiently negative, Ra_{cr} reaches a maximum at a critical viscosity ratio. In the large viscosity-ratio regime above this critical viscosity ratio, Ra_{cr} decreases, and the onset of convection is governed by a sublayer that is more unstable than the full layer.

Three different regimes of convection with temperature-dependent viscosity were first noted by Christensen (1984a) and later analysed by Solomatov (1995) with a basic scaling analysis. At small viscosity contrasts (when $\Delta\eta$ is less than about 10^2), the cold fluid near the upper boundary is entirely mobile and participates freely in the convective motions. This is the small viscosity contrast regime. As the viscosity contrast grows larger ($\Delta\eta$ in the range $10^2 - 10^3$), cold fluid near the upper boundary becomes increasingly viscous and is less able to participate in convective overturning. This is known as sluggish-lid convection or the transitional regime. When the viscosity contrast is increased further (about 10^4), the top boundary layer becomes effectively rigid and immobile, and convection assumes much of the appearance of isoviscous convection beneath a rigid lid. This is known as the stagnant-lid mode of convection. Since the viscosity variation across the mantle is significantly larger than 10^4, the convection in the mantle is regarded as 'stagnant-lid convection'.

Fowler (1985a) and Morris and Canright (1984) did a detailed asymptotic boundary layer analysis and found an asymptotic relation between Nusselt number Nu,

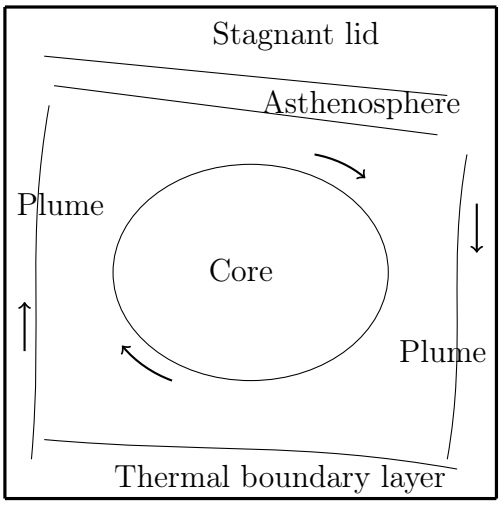

Figure 3.8: Asymptotic structure of convection with temperature-dependent viscosity in a square cell in mantle.

sensitivity parameter ε, aspect ratio a and Rayleigh number Ra namely,

$$Nu \sim Ca^{-2/5}\varepsilon Ra^{1/5}, \quad \text{as} \quad \varepsilon \to 0 \quad \text{and} \quad \varepsilon^5 Ra \to \infty, \tag{3.16}$$

where C is some constant. Fowler (1985a) chose the dimensionless viscosity as

$$\eta = \exp\left[-T/\varepsilon\right], \tag{3.17}$$

whereas we have defined the dimensionless viscosity as (3.11). Here we will show that the relation (3.16) is also valid for our choice of η. We assume that there is a thick, cold, stagnant lid at the top of the cell. This lid is of variable thickness, and the bulk of the temperature drop across the cell is taken up by it. The flow below is analogous to constant-viscosity convection, having an isothermal (hence isoviscous) interior which is driven by vorticity generated by (weak) buoyancy in the upwelling and downwelling plumes. The temperature difference in these plumes is small so that the viscosity change from the interior is small. Connecting the stagnant lid to the isothermal interior is a shear layer in which the temperature is adjusted, which is the analogue of the thermal boundary layer beneath the lithosphere as described by Parsons and McKenzie (1978) which is also known as asthenosphere. A schematic of the regions is shown in Figure 3.8.

In the shear layer, the shear stress is larger than in the interior or in the plumes, the temperature jump is small, and the velocity is small. The layer is self-determining, independent of the details of the rest of the flow (Fowler, 1986). Because the temperature drop across the lid is so large, and because it is of variable thickness, the

buoyancy term in the momentum equation is very large, and so a very large (shear) stress is generated within the lid. An even larger longitudinal stress occurs in a thin skin at the top of the lid, whose function is to enable shear stress to decrease to zero at the top surface. Thus the dominant features of the system are the thick lid, with its large stresses, and the adjoining shear-thermal layer (Fowler, 1986).

Following Fowler (2011), we assume that the cold, rigid lid is of thickness $\nu s(x)$, where $\nu \ll 1$ and $s = O(1)$, and in which $T < 1$ and η is exponentially large. Hence, $\psi \approx 0$ there and $\nabla^2 T = 0$, and since ν is small the temperature profile is approximately linear with depth. We suppose that in the rapidly convecting region, $T \approx 1$ and in the thermal boundary layers, $T = 1 + O(\varepsilon)$ (otherwise, η would be exponentially small, and ψ exponentially large) which we can write as

$$T = 1 + \varepsilon\theta. \tag{3.18}$$

Let us suppose that the thermal boundary layer thickness beneath the lid is of order $\delta \ll 1$. Continuity of heat flux into the lid implies $T_z \sim 1/\nu \sim \varepsilon/\delta$, so we choose

$$\nu = \delta/\varepsilon. \tag{3.19}$$

We further assume that δ_p is the width of the thermal plumes and $\theta \sim \theta_p$ there. The base and the sides of the convecting zone are free, not rigid, suggesting $\delta_p \ll \delta$, since heat is advected round the corners (Roberts, 1979). In fact, advection round the corner implies

$$\theta_p = \delta_p/\delta. \tag{3.20}$$

Balance of advection and conduction in the shear layer implies $\psi \sim 1/\delta$ there, where ψ is a a stream-function for the flow, so that $\psi \sim 1/\delta_p$ in the plumes due to conservation of $\int \theta d\psi$ round corners (Roberts, 1979). By matching this plume value of ψ to the interior flow, we see that $\psi \sim 1/\delta_p^2$ in the interior. Since the interior is almost isoviscous, $p, \tau_1, \tau_3, \psi \sim 1/\delta_p^2$ in the core and a balance of shear stress with buoyancy in the plumes gives (i.e. balancing $\tau_{3,x}$ and $Ra(1-T)$ in $(3.6)_3$)

$$\frac{1}{\delta_p^3} = Ra\,\varepsilon\theta_p, \tag{3.21}$$

which implies with the help of (3.20)

$$\delta = Ra\,\varepsilon\delta_p^4. \tag{3.22}$$

Now if the lid base slope is expressed as $\lambda \sim \nu s'$, then the balance of shear stress with buoyancy in the shear layer gives

$$\tau_{3,zz} \sim Ra\varepsilon\theta_x. \tag{3.23}$$

Together with $\psi \sim 1/\delta$, $\partial/\partial z \sim 1/\delta$, the definition $\tau_3 \approx \eta\psi_{zz} (\gg \tau_1)$ implies $\tau_3 \sim \eta/\delta^3 \sim 1/\delta^3$ (since $\eta \sim 1/\tau^{n-1}$ with $n = 1$) and so we obtain

$$\delta^4 Ra\, \varepsilon\lambda = 1. \tag{3.24}$$

According to Fowler (1985a), when the slope of the lid base is comparable to its thickness, we have $\lambda \sim \nu$ and this yields from (3.19) and (3.24)

$$\delta = Ra^{-1/5} \quad \text{and} \quad \nu = \frac{Ra^{-1/5}}{\varepsilon}. \tag{3.25}$$

The Nusselt number Nu is defined by (3.13). Here since the temperature drops from ≈ 1 in the bulk to T_0 at the surface across the lid of thickness $= O(\nu)$, we have $-\left.\dfrac{\partial T}{\partial z}\right|_{z=1} \sim \dfrac{1 - T_0}{\nu}$ and hence $Nu \sim \dfrac{1}{\nu}$ so that

$$Nu \sim C\varepsilon Ra^{1/5}. \tag{3.26}$$

This shows that the asymptotic relation (3.16) between Nu, Ra and ε is also valid for the viscosity function defined in (3.11).

Now we compute C for different values of ε with the help of the Shanks transformation which was introduced in chapter 2. There were some previous attempts at calculating C in different cases, but most were done where the viscosity was defined in a Frank-Kamenetskii form (Moresi and Solomatov, 1995, Reese et al., 1998). Here we will use the numerical values that are found from our model which is based on the Arrhenius form of viscosity (3.11). We assume that the relation between Nu and Ra is of the form

$$\frac{Nu}{\varepsilon Ra^{1/5}} = C + \frac{\Lambda}{Ra^{\gamma}}, \tag{3.27}$$

where C is the proportionality constant and the final term is the decaying transient we wish to eliminate. We calculate the left-hand side numerically for equally-spaced values of large $\log Ra$, specifically for $Ra = 10^{\xi+n/4}, n = 1, 2, ...$ and ξ is chosen in a way that satisfies $Ra\,\varepsilon^5 \gg 1$. Finally (3.27) takes the form

$$\left(\frac{Nu}{\varepsilon Ra^{1/5}}\right)_n = C + \frac{\Lambda}{10^{\xi\gamma+\gamma n/4}}, \tag{3.28}$$

which is of the required form for Shanks transformation (see appendix B) with

$$A_n = \left(\frac{Nu}{\varepsilon Ra^{1/5}}\right)_n, \quad A = C, \quad \alpha = \frac{\Lambda}{10^{\xi\gamma}}, \quad q = 10^{-\gamma/4}. \tag{3.29}$$

Table 3.4: Estimation of C in (3.26) using Shanks transformation for $\varepsilon = 0.26$.

n	$Nu/\varepsilon Ra^{1/5}$	$S1$	$S2$	$S3$	$S4$
1	0.68919				
2	0.71622	0.74164			
3	0.72932	0.76753	0.74565		
4	0.73908	0.6262	0.68051	0.69846	
5	0.74976	0.7144	0.7053	0.71847	0.71042
6	0.76505	0.70425	0.7139	0.70501	0.71713
7	0.78549	0.90002	0.98069	0.82651	
8	0.80284	0.95715	0.61544		
9	0.81843	1.0258			
10	0.83293				

Table 3.5: Estimation of C in (3.26) using Shanks transformation for $\varepsilon = 0.195$.

n	$Nu/\varepsilon Ra^{1/5}$	$S1$	$S2$	$S3$	$S4$
1	0.65366				
2	0.81395	0.82618			
3	0.82532	0.86526	0.83781		
4	0.83416	0.77307	0.80133	0.81493	
5	0.84451	0.81381	0.82302	0.81635	0.81454
6	0.86011	0.82132	0.8134	0.82288	
7	0.88621	0.96335	1.4633		
8	0.90571	1.074			
9	0.92319				

Table 3.6: Estimation of C in (3.26) using Shanks transformation for $\varepsilon = 0.156$.

n	$Nu/\varepsilon Ra^{1/5}$	$S1$	$S2$	$S3$
1	0.87052			
2	0.89092	0.90723		
3	0.89999	0.98468	0.93757	
4	0.90817	0.86443	0.88532	0.90779
5	0.91825	0.88971	0.92474	0.90562
6	0.93381	0.90439	0.8876	
7	0.96688	1.0214		
8	0.98746			

Table 3.7: Estimation of C in (3.26) using Shanks transformation for $\varepsilon = 0.1303$.

n	$Nu/\varepsilon Ra^{1/5}$	$S1$	$S2$
1	0.95222		
2	0.95947	0.87215	
3	0.96738	0.92597	0.98074
4	0.97715	0.95312	0.97673
5	0.99363	0.96574	
6	1.0339		

In Table 3.4 to Table 3.7, we have chosen $\xi = 5, 5.25, 5.5, 6$ respectively so that they satisfy the relation $Ra\,\varepsilon^5 \gg 1$ even for $n = 1$. It may be noted here that for $\varepsilon = 0.26, 0.195, 0.156, 0.1303$, we have viscosity contrasts of $\Delta\eta = 10^{15}, 10^{20}, 10^{25}, 10^{30}$ respectively across the mantle. The last column in the Tables 3.4 – 3.7 predict the value of C in (3.26). Even though the theory suggests that C should be independent of ε, we observe that the tables predict different values of C for different values of ε.

3.5 Low temperature cut-off viscosity

To investigate the convection with ultra-high viscosity contrasts, we propose a low-temperature cut-off viscosity of the form

$$\eta = \begin{cases} \exp\left[M/\varepsilon\right] & M \leq \varepsilon \log 10^r; \\ 10^r & M > \varepsilon \log 10^r, \end{cases} \tag{3.30}$$

Table 3.8: Nusselt number Nu and RMS velocity V_{rms} computed for convection with full-form temperature-dependent viscosity function (3.11) and with cut-off viscosity function (3.30) at $Ra = 10^7$ and $T_0 = 0.1$.

		Full form η		Cut-off η	
$\Delta\eta$	ε	Nu	V_{rms}	Nu	V_{rms}
10^{10}	0.39	6.7485	752.6427	6.7512	753.1202
10^{15}	0.26	5.3451	594.5200	5.3473	594.7689
10^{20}	0.195	4.4363	483.0021	4.4386	483.1459
10^{25}	0.156	3.7888	397.7411	3.7913	397.8065
10^{30}	0.1303	3.2521	308.5344	3.2549	308.4688
10^{40}	0.0977	-	-	2.6020	224.5620
10^{50}	0.0782	-	-	2.1887	175.2569
10^{60}	0.0651	-	-	1.8945	139.7176

where

$$M = \frac{(1-T)}{T}, \tag{3.31}$$

and the cut-off viscosity value 10^r is to be chosen appropriately; in numerical experiments, we choose $r = 6$. This type of Arrhenius law with an imposed cut-off viscosity was applied by Huang et al. (2003), Huang and Zhong (2005) and King (2009). To validate this proposed approximate solution approach, we compare in Table 3.8 values of the Nusselt number and the root mean square velocity calculated using the full viscosity function (3.11) and using the cut-off viscosity function (3.30). The comparison shows that the relative error is less than 0.1% throughout.

With this new piecewise viscosity function, we are able to solve the system comprised of (3.6), (3.11) and (3.30) for viscosity contrasts up to $\Delta\eta = 10^{60}$, corresponding to $\varepsilon = 0.0651$. In Figure 3.9, we present the thermal distribution and the corresponding stream function contours for $\varepsilon = 0.0977, 0.0782, 0.0651$. The thermal distributions and the flow patterns are consistent with the ones we found with the full-viscosity function in Figures 3.3 and 3.5. The absence of streamlines in the upper part of Figure 3.9 (b, d, f) indicates that the stagnant lid becomes thicker as the viscosity contrast gets larger, as expected.

To get a better understanding of the asymptotic relation between Nu, Ra and ε, we plot $Nu/\varepsilon\, Ra^{1/5}$ versus ε in log scale in Figure 3.10. It is clear from the figure that $\dfrac{Nu}{\varepsilon Ra^{1/5}}$ has not reached any asymptotic limit within the range of values of ε and Ra we considered here. It might be worth mentioning that Fowler (1985a) suggested

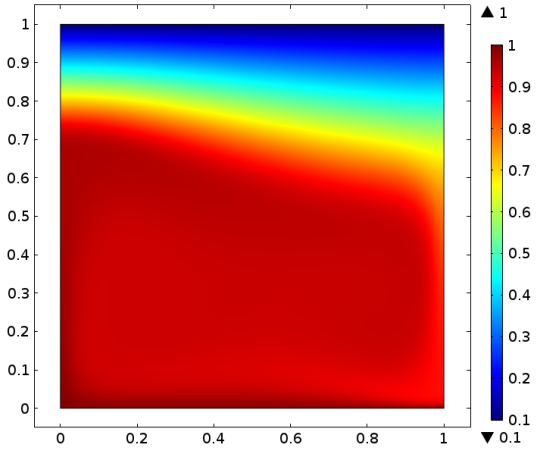

$(a)\ \Delta\eta = 10^{40},\ \ \varepsilon = 0.0977$

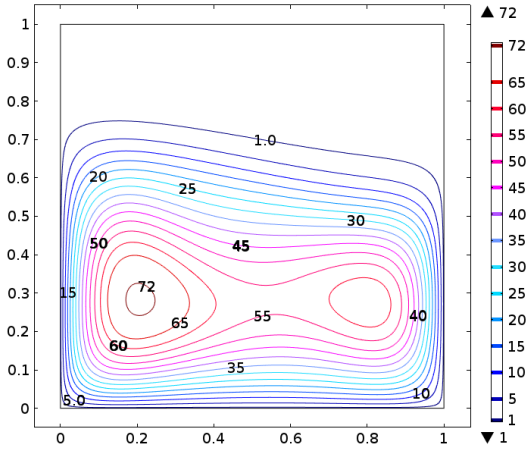

$(b)\ \Delta\eta = 10^{40},\ \ \varepsilon = 0.0977$

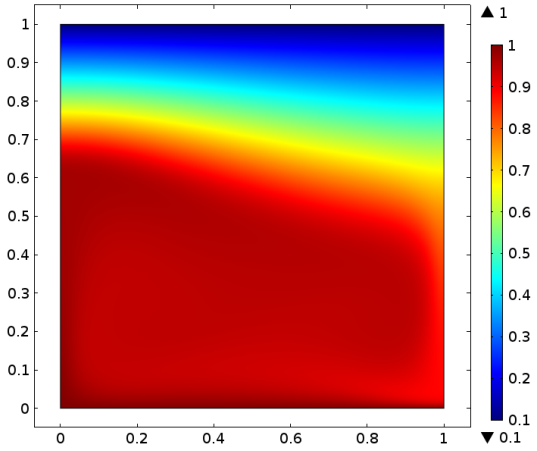

$(c)\ \Delta\eta = 10^{50},\ \ \varepsilon = 0.0782$

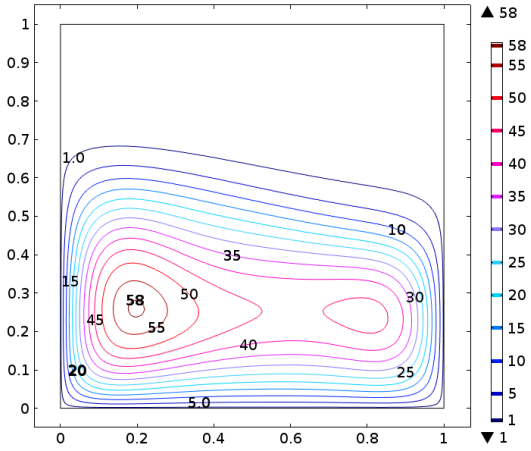

$(d)\ \Delta\eta = 10^{50},\ \ \varepsilon = 0.0782$

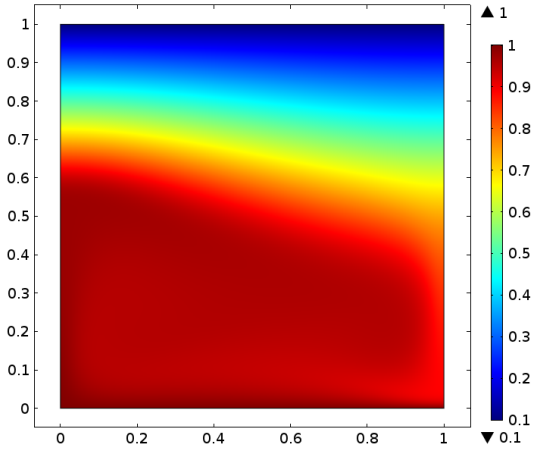

$(e)\ \Delta\eta = 10^{60},\ \ \varepsilon = 0.0651$

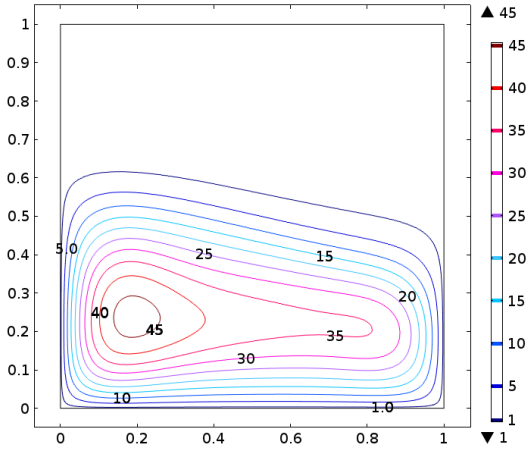

$(f)\ \Delta\eta = 10^{60},\ \ \varepsilon = 0.0651$

Figure 3.9: Thermal distributions (a, c, e) and corresponding stream function contours (b, d, f) with different viscosity contrasts $\Delta\eta = \ 10^{40},\ 10^{50},\ 10^{60}$ in a square cell with piecewise temperature dependent viscosity function for $T_0 = 0.1$, $Ra = 10^7$.

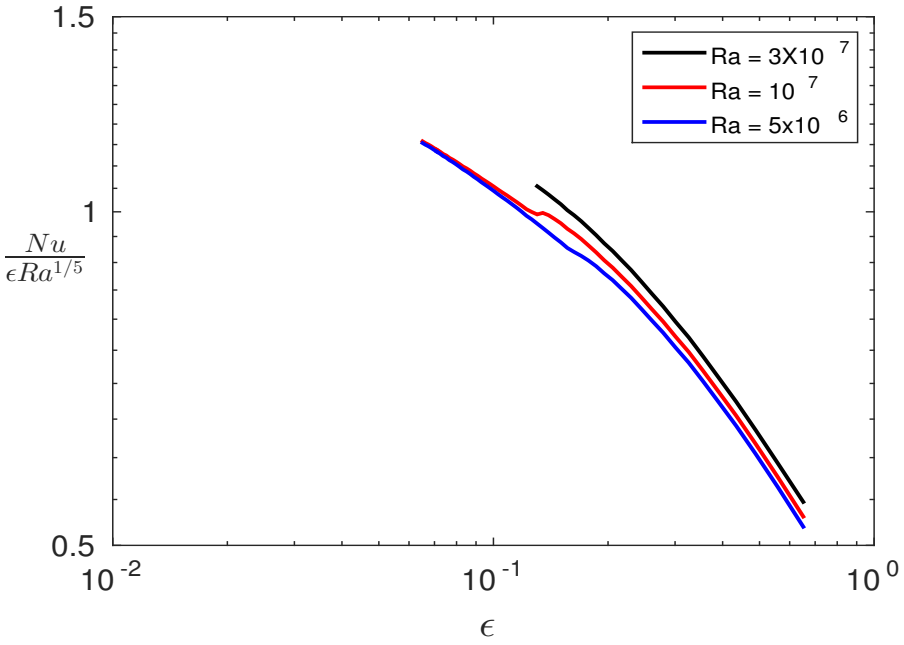

Figure 3.10: Log-log plot of $Nu/\varepsilon Ra^{1/5}$ vs ε with cut-off temperature dependent viscosity function (3.30).

that for a temperature-dependent viscosity case,

$$Nu \sim C\varepsilon Ra^{1/5}\left[1 + O(Ra^{-1/10}\varepsilon^{-1/4}, \varepsilon^{1/2}, Ra^{-2/5}\varepsilon^{-2}, Ra^{-1/20}\varepsilon^{-1/24})\right], \tag{3.32}$$

and one should not expect high precision at moderate viscosity contrasts and Rayleigh numbers, where moderate means $Ra < 10^{10}$ and $\varepsilon > 0.067$. We can easily see that in our case, max $Ra = 3 \times 10^7$ and min $\varepsilon = 0.0651$, which are undoubtedly not in the required extreme region. Hence, this may also explain why Shanks transformation could not remove the transient behaviour and predict a consistent asymptotic limit for $Nu/\varepsilon Ra^{1/5}$ for different ε values in section 3.4.

3.6 Summary

In this chapter, we introduced the mathematical model of mantle convection with variable viscosity. Even though the Frank-Kamenetskii form is a widely used function for variable viscosity, we choose the correct Arrhenius form of the viscosity function for our numerical computations.

Since convection with temperature-dependent viscosity is a thoroughly studied area, we checked our numerical model with benchmark values and found good agree-

ment between them. This leads us to study convection with high viscosity contrast up to 10^{30} successfully for the first time. With these new computational results, we attempt to calculate the proportionality constant C in the predicted asymptotic relation between Nu, Ra and ε,

$$Nu \sim C\varepsilon Ra^{1/5},$$

by applying Shanks transformation. However, our attempt did not predict anything conclusive like the constant viscosity case in chapter 2. Then we adopt a familiar technique to ease the computational complexity by defining a low-temperature cut-off viscosity function. This new form of viscosity function enabled us to perform simulations for viscosity contrasts up to 10^{60} and gave us the indication that the appropriate region of the asymptotic relation lies with very high values of Rayleigh number and extremely low values of ε.

Inclusion of a variable viscosity for mantle convection is a logical approach. We show that at a reasonably high viscosity contrast, the interior of the mantle becomes isothermal and hence isoviscous. Also we observe the presence of a cold and stiff thermal boundary layer at the top surface which is more akin to the rigid lithosphere that we witness in the real Earth. This is a significant improvement of the convecting cell over the one with constant viscosity considered in chapter 2. Numerical simulations of mantle convection in a three-dimensional Cartesian box geometry with wide aspect ratios (Tackley, 1996, Trompert and Hansen, 1998) and in a spherical shell geometry (Ratcliff et al., 1997, 1996, Reese et al., 1999) also found a highly viscous lid with temperature-dependent viscosity as well as convection under the stagnant lid characterized by numerous small-scale cylindrical upwelling plumes surrounded by sheet-like downwellings.

For a typical value of ε, we find that the viscosity contrast would be of order 10^{50} or more, and with such strong temperature-dependent viscosity, the top thermal boundary layer can become completely immobile. But that does not happen in the Earth. On the real Earth, the lithosphere is rigid but broken into tectonic plates separated by weak boundaries. Without mechanisms other than the simple temperature-dependence of viscosity, the Earth would be in a stagnant-lid regime which fails to explain the presence of plate margins in plate tectonics. Hence to get a better understanding of a mantle-like convection, we are interested to consider the other effects on viscosity.

Chapter 4

Convection with Temperature and Pressure-dependent Viscosity

4.1 Introduction

The dynamical effects of a stratified viscosity profile on the mantle convection without lateral viscosity variations have been studied by Hansen et al. (1993), Zhang and Yuen (1995), and Bunge et al. (1996) in Cartesian 2D or 3D or in a spherical model. Bunge et al. (1996) have shown that a modest increase in the mantle viscosity with depth has a remarkable effect on the convection pattern, resulting in a long-wavelength structure. However, another important factor for the mantle viscosity, i.e., a strong dependence on temperature, was absent in their models. Some numerical experiments have been done for convection with temperature and depth-dependent viscosity by Christensen (1984b), Fleitout and Yuen (1984), Doin et al. (1997), Stemmer et al. (2006) in a 2D model, whereas Yoshida and Kageyama (2006) have done some work in spherical shells. Nevertheless, the simultaneous effect of temperature and pressure-dependent rheology on mantle convection does not appear to have attracted the attention it deserves, either analytically or computationally.

Here our aim is to use the Arrhenius form of viscosity in Cartesian coordinates and to investigate the convection pattern with very high viscosity variation. For our problem, when viscosity depends on temperature and pressure, i.e. $\mu \neq 0$ and $\varepsilon \neq 0$, then it has the form as described in (3.10),

$$\eta = \exp\left[\frac{1 - T + \mu(1 - z - T)}{\varepsilon T}\right], \tag{4.1}$$

where ε and μ are the parameters that control the viscosity variation across the layer. Although the temperature sensitivity in Arrhenius rheology is greater than the

pressure sensitivity, the latter becomes more critical in the lower mantle. However, the pressure-dependence of flow in the lower mantle is quite complex.

4.2 Governing equations

The dimensionless governing equations are derived as described in chapter 3. Hence, the dimensionless set of equations with temperature and pressure-dependent viscosity are

$$\begin{aligned} u_x + w_z &= 0, \\ p_x &= \tau_{1x} + \tau_{3z}, \\ p_z &= \tau_{3x} - \tau_{1z} - Ra(1-T), \\ \tau_1 &= 2\eta u_x, \\ \tau_3 &= \eta\left(u_z + w_x\right), \\ T_t + \boldsymbol{u}\cdot\nabla T &= \nabla^2 T, \\ \eta &= \exp\left[\frac{1-T+\mu(1-z-T)}{\varepsilon T}\right], \end{aligned} \tag{4.2}$$

and the dimensionless free-slip boundary conditions are

$$\begin{aligned} w = 0, \quad u_z = 0, \quad T = 1 \quad \text{on} \quad z = 0, \\ w = 0, \quad u_z = 0, \quad T = T_0 \quad \text{on} \quad z = 1, \\ u = 0, \quad w_x = 0, \quad T_x = 0 \quad \text{on} \quad x = 0, a, \end{aligned} \tag{4.3}$$

where a is the aspect ratio.
The typical parameter values are those given in Tables 3.1 – 3.2.

4.2.1 Viscosity contrast, Nusselt number and RMS velocity

For our convenience, we mention the useful diagnostic quantities for the convection with temperature and pressure-dependent viscosity that will be used to characterise the numerical results in the following sections. The viscosity contrast $\Delta\eta$ is defined as the ratio between the surface and basal values of the viscosity, that is

$$\Delta\eta = \exp\left(\frac{1-T_0-\mu T_0}{\varepsilon T_0}\right), \tag{4.4}$$

which is slightly different from the temperature-dependent case in chapter 3.

The Nusselt number Nu and the non-dimensional RMS (root mean square) velocity V_{rms} are calculated in a similar manner as in (3.13) and (3.14) respectively.

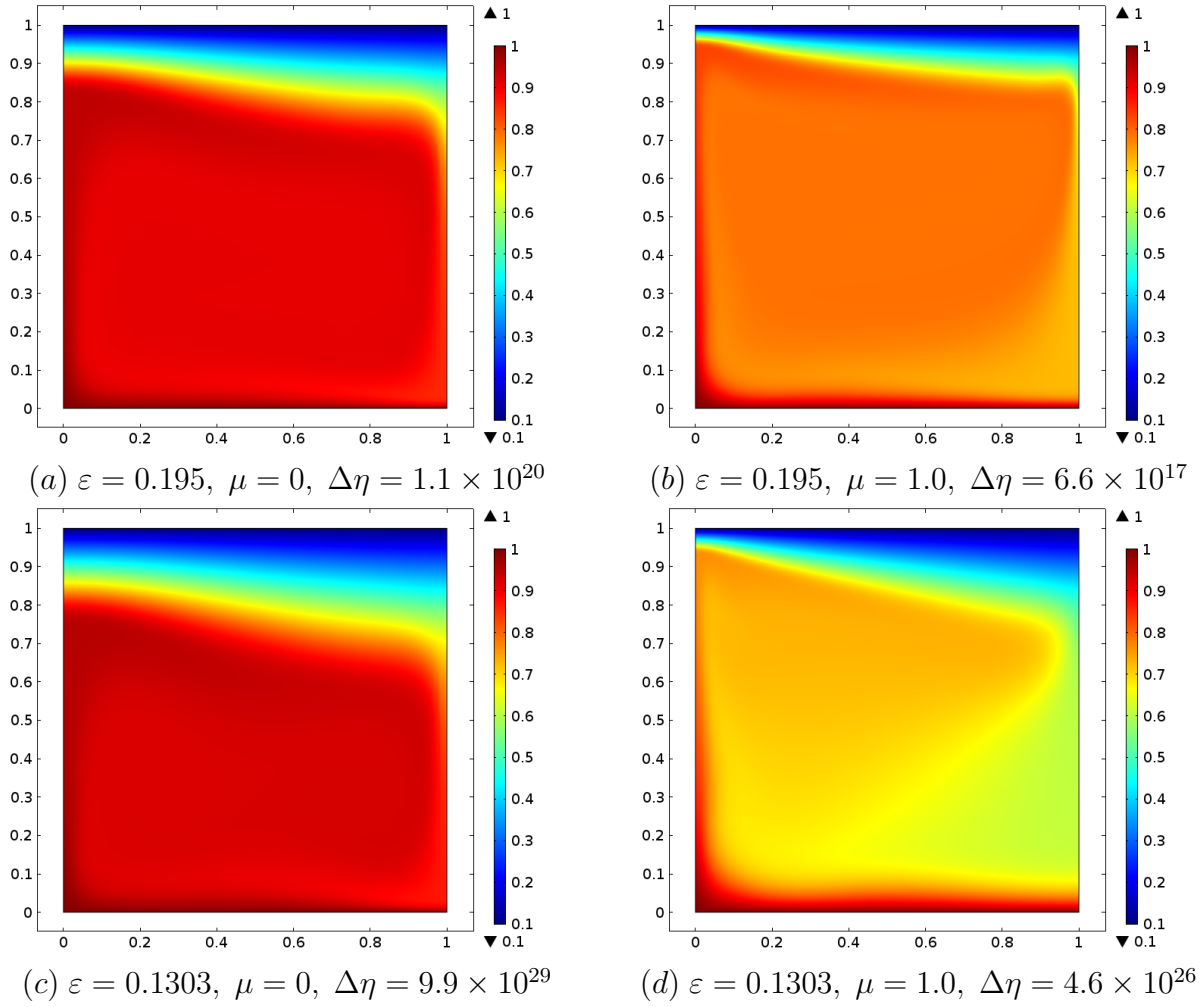

(a) $\varepsilon = 0.195,\ \mu = 0,\ \Delta\eta = 1.1 \times 10^{20}$

(b) $\varepsilon = 0.195,\ \mu = 1.0,\ \Delta\eta = 6.6 \times 10^{17}$

(c) $\varepsilon = 0.1303,\ \mu = 0,\ \Delta\eta = 9.9 \times 10^{29}$

(d) $\varepsilon = 0.1303,\ \mu = 1.0,\ \Delta\eta = 4.6 \times 10^{26}$

Figure 4.1: Thermal distributions of a temperature-dependent viscosity convection (a,c) and a temperature- and pressure-dependent viscosity convection (b,d) at different viscosity variations for $T_0 = 0.1$ and $Ra = 10^7$.

4.3 Numerical investigation

We solve the system of dimensionless equations (4.2)–(4.3) in a unit aspect ratio cell in Comsol Multiphysics. The computational model is set up with the same criteria as described in chapter 3 and the results are presented here. The only difference with chapter 3 is that here we have three dimensionless parameters instead of two and we change each of the parameters slowly to achieve our results. We set $T_0 = 0.1$ throughout.

4.3.1 Results

In Figure 4.1, we demonstrate the significant effects of including pressure dependence in the viscosity relation (4.1). The left-hand panels (a) and (c) show temperature profiles in the convecting cell with $\mu = 0$ so that the viscosity depends only on the temperature. In the right-hand panels (b) and (d) we show the corresponding results when pressure dependence is included, with $\mu = 1$. In each plot, the blue region indicates a cold thermal boundary layer at the top of the cell, where the fluid is extremely viscous and forms an effectively rigid lid. Both with and without pressure dependence, the thickness of the lid increases as the viscosity contrast gets larger. However, in the rest of the cell the differences between the left and right-hand panels are striking.

When $\mu = 0$, so the viscosity depends only on temperature, the fluid is roughly isothermal outside the lid and thin thermal boundary layers are present on the base and sides of the cell. The presence of an isothermal core eliminates the extreme viscosity contrast in the bulk flow. However, when $\mu = 1$ it is no longer possible for the bulk flow to be both isothermal and isoviscous. Instead, we observe in panels (b) and (d) the emergence of a quite different characteristic flow structure, with relatively warm (yellow) upper core separated from a cooler (green) lower core. The upper core is fed by hot fluid from a thermal boundary layer at the base of the cell, while the lower core is fed by cooler fluid from the lid. The average temperature in the cell is significantly lower when pressure-dependence is included, with hot fluid confined to the basal thermal boundary layer and the plume on the left boundary $x = 0$.

In Figure 4.2, the temperature profiles at the mid-cell (i.e. $x = 0.5$) for different viscosity contrasts are shown. In each case, $\mu = 1.0$ and $Ra = 10^7$. Clearly, for the temperature and pressure-dependent viscosity case, the mantle has a lower temperature than for the purely temperature-dependent viscosity convection and the interior temperature decreases whereas for the temperature-dependent case, the interior temperature is increased as viscosity contrast becomes larger across the layer (cf. section 3.3). These temperature profiles also confirm that the interior is not isothermal anymore.

In Figures 4.3 and 4.4, we illustrate the effects of varying the sensitivity of the viscosity to pressure while choosing the value of ε to keep the net viscosity contrast constant. In Figure 4.3 we plot the temperature distributions at viscosity contrasts of 10^{20}, 10^{25} and 10^{30} with $\mu = 0.5$ and $\mu = 1.0$. Panels (a), (c) and (e) show the distributions for $\mu = 0.5$, which appear very similar to those for the purely temperature-dependent viscosity, although one can detect an emergent cold plume

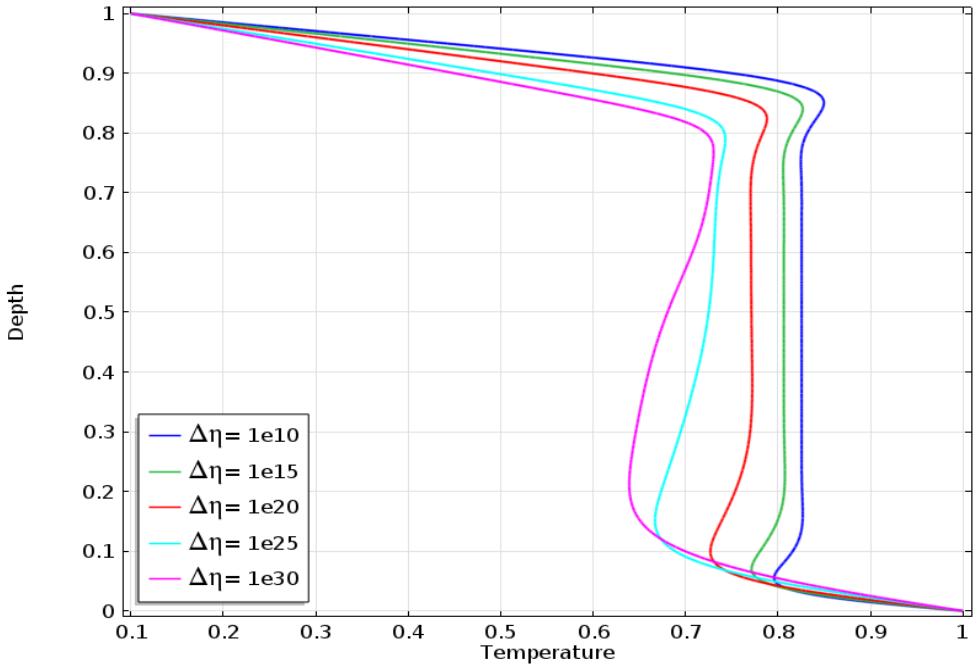

Figure 4.2: Temperature profiles of mid-cell at different viscosity contrasts due to varying ε for convection with temperature and pressure-dependent viscosity with $\mu = 1.0$ and $Ra = 10^7$.

descending on the right boundary $x = 1$. With $\mu = 1.0$, this plume has developed into a relatively cold lower core near the bottom right-hand corner of the cell, while the effect of relatively warm fluid from the base is confined to an upper core region near the top left corner of the cell. Both of these features become increasingly pronounced as the viscosity contrast increases, as seen by comparing panels (b), (d) and (f).

The corresponding streamlines are presented in Figure 4.4. These are defined as in §3.3.2 as contours of the streamfunction $\psi(x, z)$. In each case, the absence of streamlines at the top indicates the presence of a stagnant lid, but the overall convection pattern changes markedly as the pressure dependence of the viscosity becomes more important. In panel (a), where the pressure sensitivity and the net viscosity contrast are both relatively small, the flow resembles the purely temperature-dependent case, with a single large convection cell and corresponding approximately isothermal core. In contrast, panels (d) and (f) show that with significant pressure dependence, the convective flow is concentrated in the upper core region. The values of ψ indicated on the contours indicate that the convection is much less vigorous in panel (f) than in panel (a), especially in the lower core region near the bottom right corner.

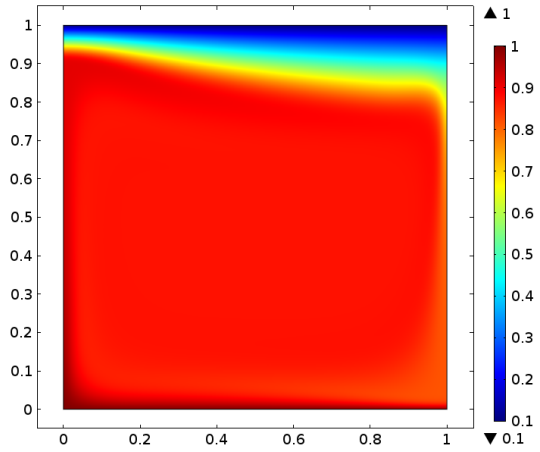

(a) $\Delta\eta = 10^{20},\ \mu = 0.5,\ \varepsilon = 0.1846$

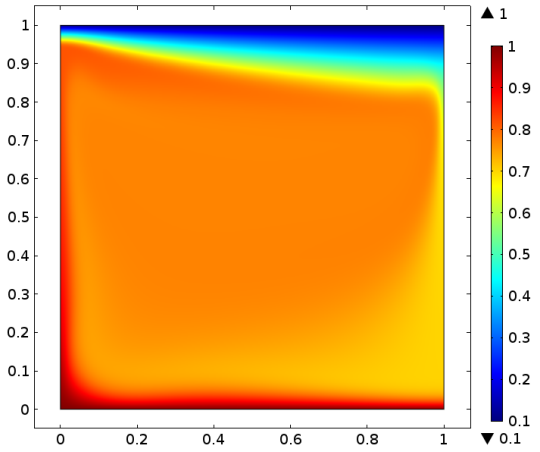

(b) $\Delta\eta = 10^{20},\ \mu = 1.0,\ \varepsilon = 0.1737$

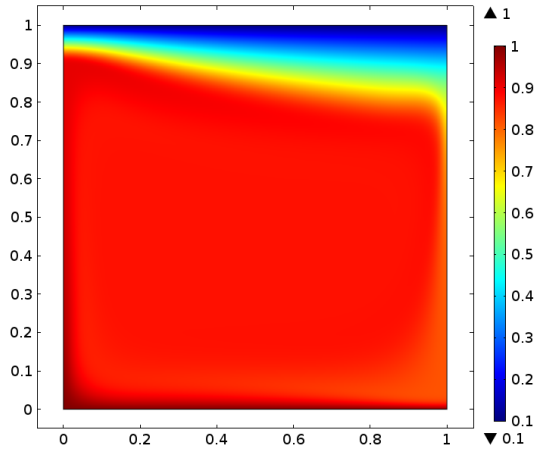

(c) $\Delta\eta = 10^{25},\ \mu = 0.5,\ \varepsilon = 0.1477$

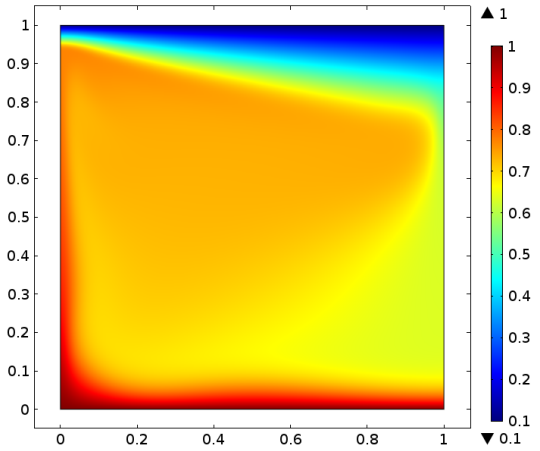

(d) $\Delta\eta = 10^{25},\ \mu = 1.0,\ \varepsilon = 0.139$

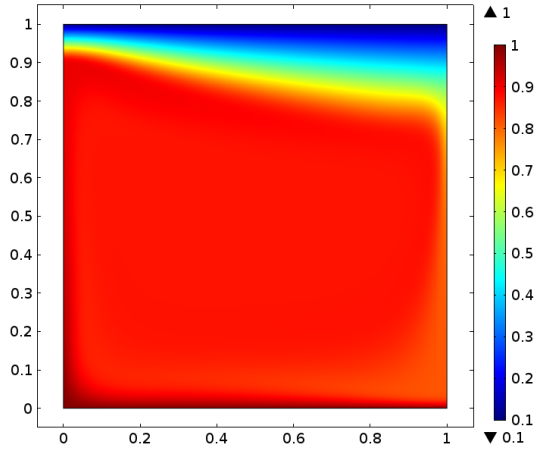

(e) $\Delta\eta = 10^{30},\ \mu = 0.5,\ \varepsilon = 0.123$

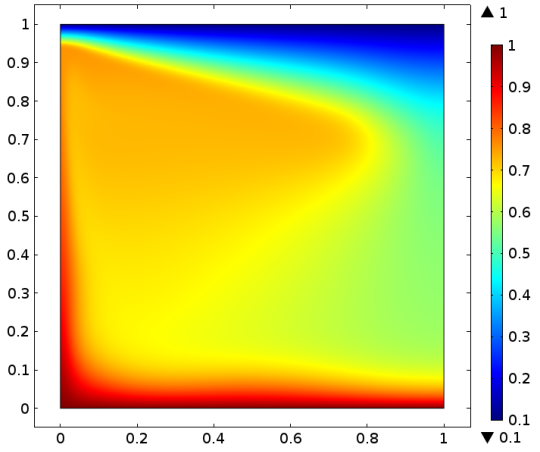

(f) $\Delta\eta = 10^{30},\ \mu = 1.0,\ \varepsilon = 0.1158$

Figure 4.3: Thermal distributions with different viscosity contrasts $\Delta\eta = 10^{20},\ 10^{25},\ 10^{30}$ and different pressure sensitivities $\mu = 0.5,\ 1.0$, in a square cell with $T_0 = 0.1$ and $Ra = 10^7$.

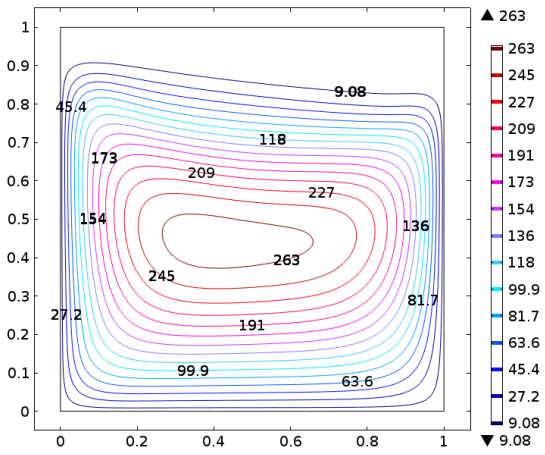

$(a)\ \Delta\eta = 10^{20},\ \mu = 0.5,\ \varepsilon = 0.1846$

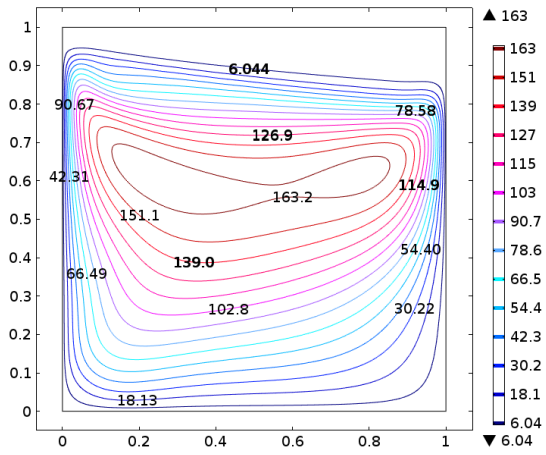

$(b)\ \Delta\eta = 10^{20},\ \mu = 1.0,\ \varepsilon = 0.1737$

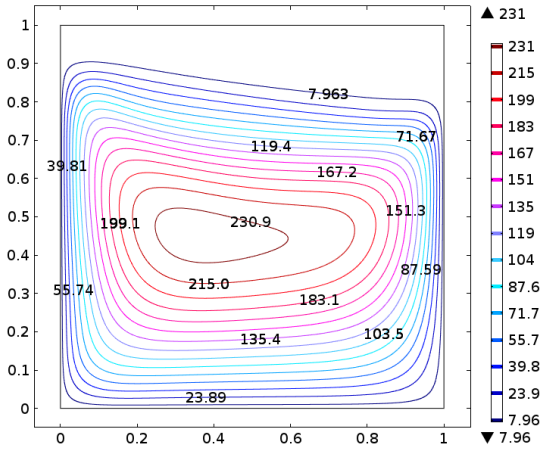

$(c)\ \Delta\eta = 10^{25},\ \mu = 0.5,\ \varepsilon = 0.1477$

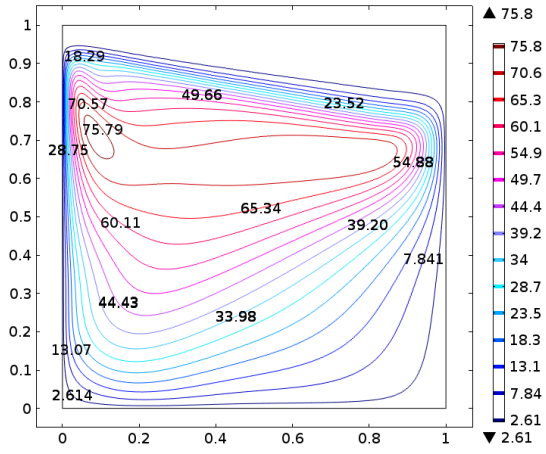

$(d)\ \Delta\eta = 10^{25},\ \mu = 1.0,\ \varepsilon = 0.139$

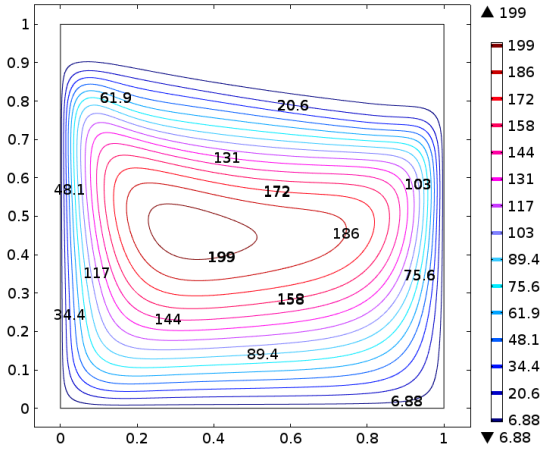

$(e)\ \Delta\eta = 10^{30},\ \mu = 0.5,\ \varepsilon = 0.123$

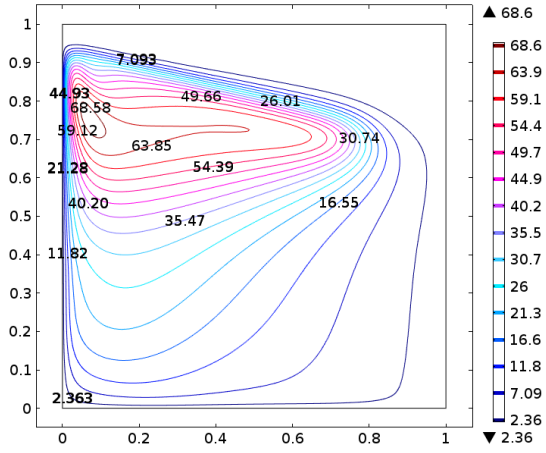

$(f)\ \Delta\eta = 10^{30},\ \mu = 1.0,\ \varepsilon = 0.1158$

Figure 4.4: Flow streamlines with different viscosity contrasts $\Delta\eta = 10^{20},\ 10^{25},\ 10^{30}$ and different pressure sensitivities $\mu = 0.5,\ 1.0$, in a square cell with $T_0 = 0.1$ and $Ra = 10^7$.

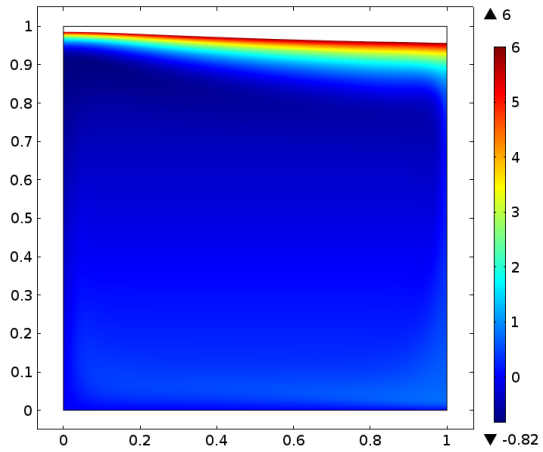

$(a)\ \Delta\eta = 10^{20},\ \mu = 0.5,\ \varepsilon = 0.1846$

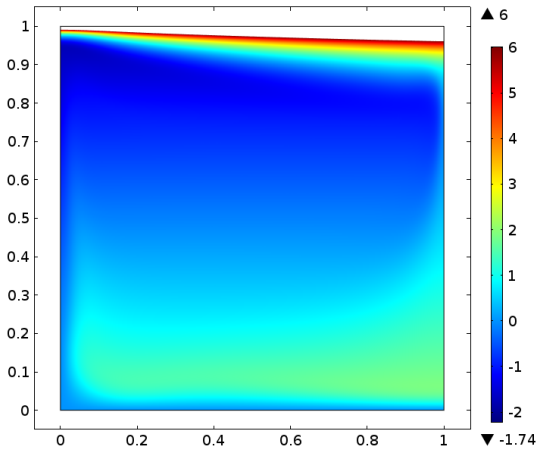

$(b)\ \Delta\eta = 10^{20},\ \mu = 1.0,\ \varepsilon = 0.1737$

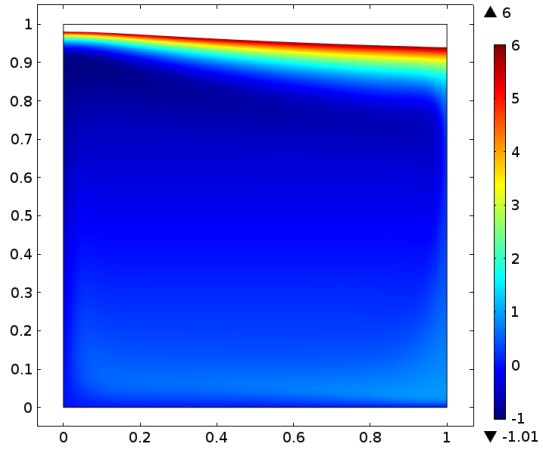

$(c)\ \Delta\eta = 10^{25},\ \mu = 0.5,\ \varepsilon = 0.1477$

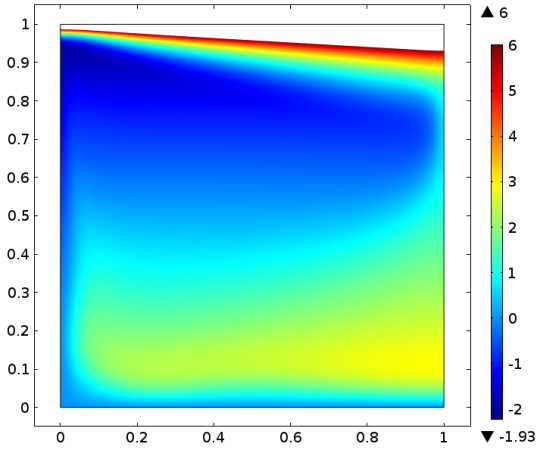

$(d)\ \Delta\eta = 10^{25},\ \mu = 1.0,\ \varepsilon = 0.139$

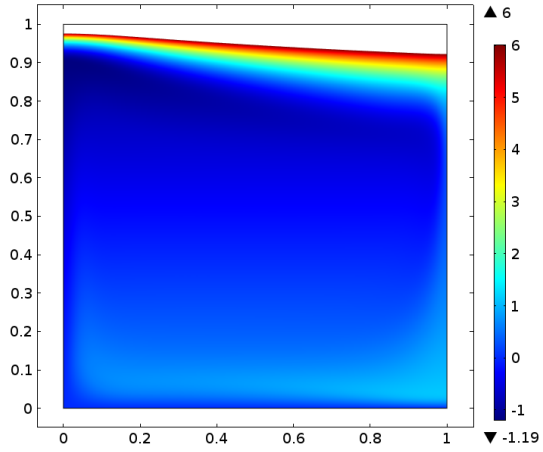

$(e)\ \Delta\eta = 10^{30},\ \mu = 0.5,\ \varepsilon = 0.123$

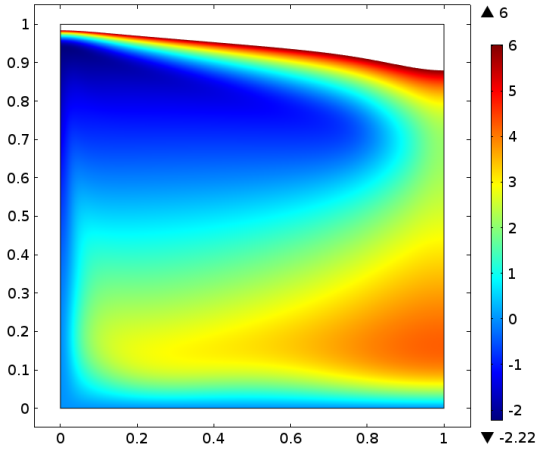

$(f)\ \Delta\eta = 10^{30},\ \mu = 1.0,\ \varepsilon = 0.1158$

Figure 4.5: Viscosity distributions (logarithm plots) with different viscosity contrasts $\Delta\eta = 10^{20},\ 10^{25},\ 10^{30}$ and different pressure sensitivities $\mu = 0.5,\ 1.0$, in a square cell with $T_0 = 0.1$ and $Ra = 10^7$. White regions at the top indicate dimensionless viscosities $> 10^6$.

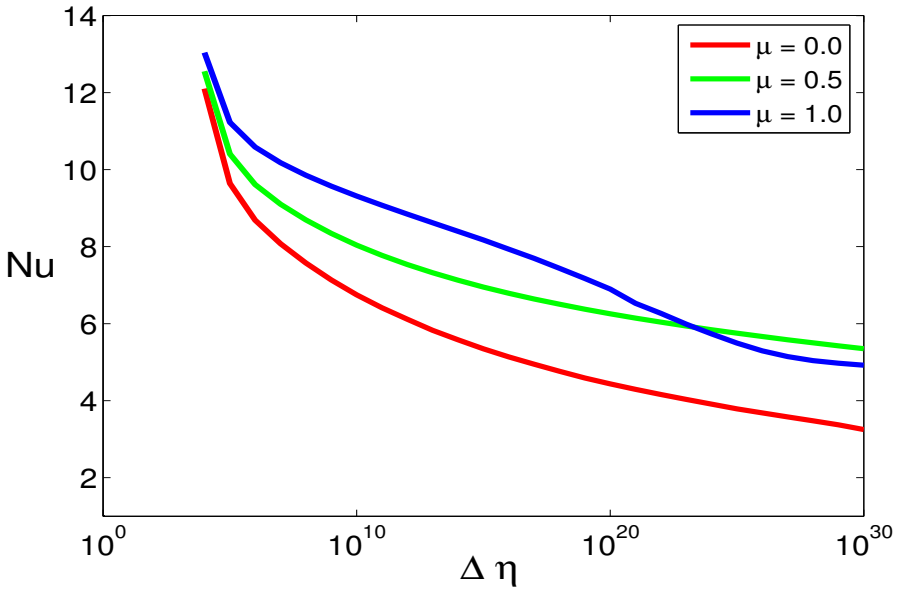

Figure 4.6: Variation of Nusselt number Nu with viscosity contrast $\Delta\eta$ for fixed values of μ in a unit aspect-ratio cell with $T_0 = 0.1$ and $Ra = 10^7$.

In Figure 4.5, the viscosity variation from top to bottom is indicated; the upper part of the range is excised (in the lid) and the resulting colour indicates a variation from the lowest value (blue) to 10^6 (red). It is clear from this figure that for $\mu = 0.5$, the interior is almost isoviscous, whereas for $\mu = 1.0$, the interior is no longer isoviscous. We can see that as the viscosity contrast across the mantle grows from 10^{20} to 10^{30}, the pressure dependence increases the viscosity quite significantly in the lower mantle. In fact, we can observe a relative increase in viscosity from the 'upper mantle' to the 'lower mantle' by a factor ranging from 10^2 at the left to 10^6 at the right. Such a result is consistent with observationally derived inferences of upper mantle/lower mantle viscosity contrast (Mitrovica and Forte, 2004). The difference between the viscosity distributions for purely temperature-dependent viscosity function and the strongly temperature and pressure-dependent viscosity function is really striking and hence we can say that this dramatic viscosity variation and the corresponding temperature distribution must be related.

Next in Figure 4.6, we plot the variation of the Nusselt number Nu versus viscosity contrast $\Delta\eta$ for $\mu = 0.0, 0.5$ and 1.0. Inclusion of pressure dependence (i.e. $\mu \neq 0$) on viscosity clearly affects the heat transfer rate on the upper boundary. For a fixed value of μ, as viscosity contrast across the layer is increased (i.e. ε is decreased), the con-

Table 4.1: Nu and V_{rms} values at different viscosity contrasts for the temperature and pressure-dependent viscosity convection at $Ra = 10^7$.

$\Delta\eta$	μ	ε	Nu	V_{rms}
10^3	0.0	1.3	19.6878	1540.9737
10^3	0.5	1.23	19.8059	1599.4749
10^3	1.0	1.158	19.6077	1634.3531
10^3	1.5	1.0857	19.1912	1635.3958
10^5	0.0	0.782	9.6414	1027.7597
10^5	0.5	0.738	10.4051	1181.8249
10^5	1.0	0.695	11.2272	1338.9623
10^5	1.5	0.651	12.0013	1458.4684
10^{10}	0.0	0.39	6.7485	752.6427
10^{10}	0.5	0.37	8.0484	1000.4599
10^{10}	1.0	0.3474	9.3134	1186.3642
10^{10}	1.5	0.326	9.6452	1037.256
10^{15}	0.0	0.26	5.3451	594.5200
10^{15}	0.5	0.246	6.9510	892.7172
10^{15}	1.0	0.2316	8.1724	956.3948
10^{20}	0.0	0.195	4.4363	483.0021
10^{20}	0.5	0.1846	6.2569	804.5098
10^{20}	1.0	0.1737	6.8865	611.7843
10^{25}	0.0	0.156	3.7888	397.7411
10^{25}	0.5	0.1477	5.7526	720.3409
10^{25}	1.0	0.139	5.4966	317.9041
10^{30}	0.0	0.1303	3.2521	308.5344
10^{30}	0.5	0.123	5.3491	634.4470
10^{30}	1.0	0.1158	4.9213	273.3209

vection becomes less vigorous and Nu gets gradually smaller. However, as expected, when μ is included, to maintain the same viscosity contrast, ε is decreased and this results in a higher Nusselt number value. For both the cases $\mu = 0.0$ (temperature-dependent viscosity) and $\mu = 0.5$, Nu decreases steadily with the increase of viscosity contrast (i.e. with the decrease of ε). But, a noteworthy feature can be seen for the case $\mu = 1.0$. When $\Delta\eta$ crosses the value of $\sim 10^{19}$, Nu starts to decrease quite rapidly and for smaller values of ε the value of Nu with $\mu = 1.0$ is unexpectedly less than the corresponding value with $\mu = 0.5$. This unexpected behaviour may be explained by comparing the figures of thermal distributions given in Figure 4.1, Figure 4.3 and also the temperature profiles given in Figure 3.6 and Figure 4.2. For convection with purely temperature dependent viscosity, the core is isothermal and

has higher temperature than the temperature and pressure-dependent case at the same viscosity contrast. For the temperature and pressure-dependent viscosity case, the core is cooler, the convection is less vigorous and the lid is comparatively thinner. This may be the primary reason why Nu is greater with $\mu = 1$ compared to $\mu = 0, 0.5$ in the region $\Delta\eta < 10^{20}$. But at high viscosity contrast, the convection pattern changes dramatically and the lid gets considerably thicker at $\Delta\eta = 10^{30}$ (cf. Figure 4.3(d) and 4.3(f)) and Nu values fall sharply. It seems that the strong influence of pressure dependence creates a competition between the dominance of the temperature parameter ε and the pressure sensitivity parameter μ and this results in a drastic change in Nu values at high viscosity contrast.

In Table 4.1 we present the values of the Nusselt number Nu and the root mean square velocity V_{rms} at different viscosity variations for convection with temperature and pressure-dependent viscosity at $Ra = 10^7$. At a fixed viscosity contrast, we are interested to see how Nusselt number Nu and root mean square velocity V_{rms} change with the increase of the pressure dependence parameter μ, and in order to keep the viscosity contrast $\Delta\eta$ fixed, we adjusted the temperature dependence parameter ε accordingly. It is clear that both Nu and V_{rms} decrease as viscosity variation gets larger and at a fixed viscosity contrast, the inclusion of μ and gradual increase of μ result in an increase in both Nu and V_{rms}. However, there is a difference in this trend around $\Delta\eta = 10^{20}$ when Nu and V_{rms} show a sudden decrease with $\mu = 1.0$.

4.4 Low temperature cut-off viscosity

The computational problem becomes prohibitively stiff with further increase of the viscosity contrast. However, to obtain simulations relevant to the Earth, extremely high viscosity contrasts are necessary: the representative parameter values given in Table 3.2 suggest that $\Delta\eta$ may be 10^{50} or larger. Computations have been performed previously for variable viscosity contrasts up to 10^{15} (Moresi and Solomatov, 1995, Reese et al., 1999, Reese and Solomatov, 2002, Solomatov and Moresi, 1996), but surprisingly, this is not sufficient to establish a clear asymptotic limit for the flow. Figures 4.3 and 4.4 illustrate how, when the Rayleigh number is large and pressure dependence is included, a distinctive flow structure emerges as the viscosity contrast $\Delta\eta$ increases; however, this new regime only starts to become fully evident when $\Delta\eta$ is as large as 10^{30}. As will be demonstrated below, significant qualitative changes to the flow structure continue to occur as the viscosity contrast is increased yet further.

Table 4.2: Nusselt number Nu and RMS velocity V_{rms} computed for convection with full-form viscosity function (4.1) and with cut-off viscosity function (4.5) at $Ra = 10^7$ and $T_0 = 0.1$.

			Full form η		Cut-off η	
$\Delta\eta$	μ	ε	Nu	V_{rms}	Nu	V_{rms}
10^{10}	0.5	0.369	8.04068	999.7775	8.04491	999.9255
	1.0	0.3474	9.31342	1186.3642	9.31593	1186.3094
10^{15}	0.5	0.246	6.95103	892.7172	6.95366	892.7446
	1.0	0.2316	8.17241	956.3948	8.17339	956.18565
10^{20}	0.5	0.1846	6.25693	804.5098	6.25907	804.45323
	1.0	0.174	6.89653	614.43714	6.89670	614.08143
10^{25}	0.5	0.1477	5.75259	720.3409	5.75448	720.1903
	1.0	0.139	5.49656	317.90407	5.49674	317.69797
10^{30}	0.5	0.123	5.34914	634.4470	5.35085	634.18688
	1.0	0.1158	4.92133	273.3243	4.92340	273.45468

To overcome the difficulties associated with such extreme viscosity contrasts, we employ a trick based on the fact that, as in strongly temperature-dependent viscous convection, most of the viscosity variation occurs in a stagnant lid in which the velocity is essentially zero. We can thus calculate the sub-lid convection field accurately (but not the stress field) by cutting off the dimensionless viscosity at a sufficiently high value that the lid thickness, which essentially only depends on the interaction of the lid temperature with the underlying convecting flow, is unaffected.

We therefore propose a low temperature cut-off viscosity of the form

$$\eta = \begin{cases} \exp\left[M/\varepsilon\right] & M \leq \varepsilon \log 10^r; \\ 10^r & M > \varepsilon \log 10^r, \end{cases} \tag{4.5}$$

where

$$M = \frac{(1+\mu)(1-T) - \mu z}{T}, \tag{4.6}$$

and the cut-off viscosity value 10^r is to be chosen appropriately; in numerical experiments we found that $r = 6$ gives a good compromise between accuracy and stiffness. This type of Arrhenius law with an imposed cut-off viscosity was applied by Huang et al. (2003), Huang and Zhong (2005), King (2009) but none of them was for a temperature- and pressure-dependent viscosity. We emphasise that this trick enables numerical solution of the model, without compromising the extreme viscosity sensitivity which we seek. Its only drawback is that it does not allow accurate computation of the very high stresses in the lid.

4.4.1 Results and comparison

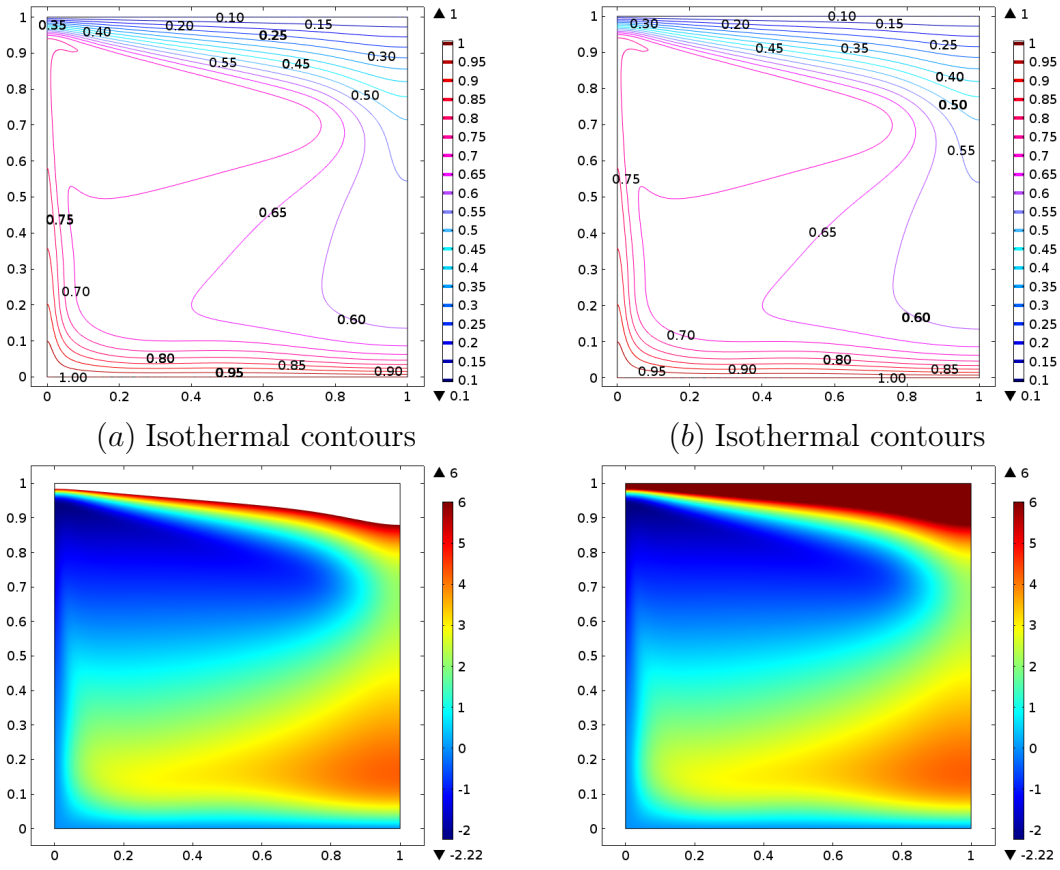

(*a*) Isothermal contours (*b*) Isothermal contours

(*c*) Distribution of $\log_{10}\eta$ (*d*) Distribution of $\log_{10}\eta$

Figure 4.7: Comparison of solutions from full-form viscosity model (a, c) and cut-off viscosity model (b, d) for $T_0 = 0.1$, $Ra = 10^7, \varepsilon = 0.1158$ and $\mu = 1.0$.

To validate this proposed approximate solution approach, we compare in Table 4.2 values of the Nusselt number and the RMS velocity calculated using the full viscosity function (4.1) and using the cut-off viscosity function (4.5). It is evident that the agreement is uniformly excellent, with a relative error less than 0.06% throughout. Further validation is provided in Figure 4.7, where we show computed isothermal contours and viscosity distributions for the parameter values $T_0 = 0.1$, $Ra = 10^7$, $\varepsilon = 0.1158$ and $\mu = 1.0$, corresponding to a viscosity contrast $\Delta\eta = 10^{30}$. Panels (a) and (c) show the results computed using the full viscosity function (4.1), while panels (b) and (d) show the corresponding results when the piecewise viscosity function (4.5) is used. The qualitative and quantitative agreement are again excellent. Although the full viscosity increases to 10^{30} in the lid, the cut-off value of 10^6 is already high

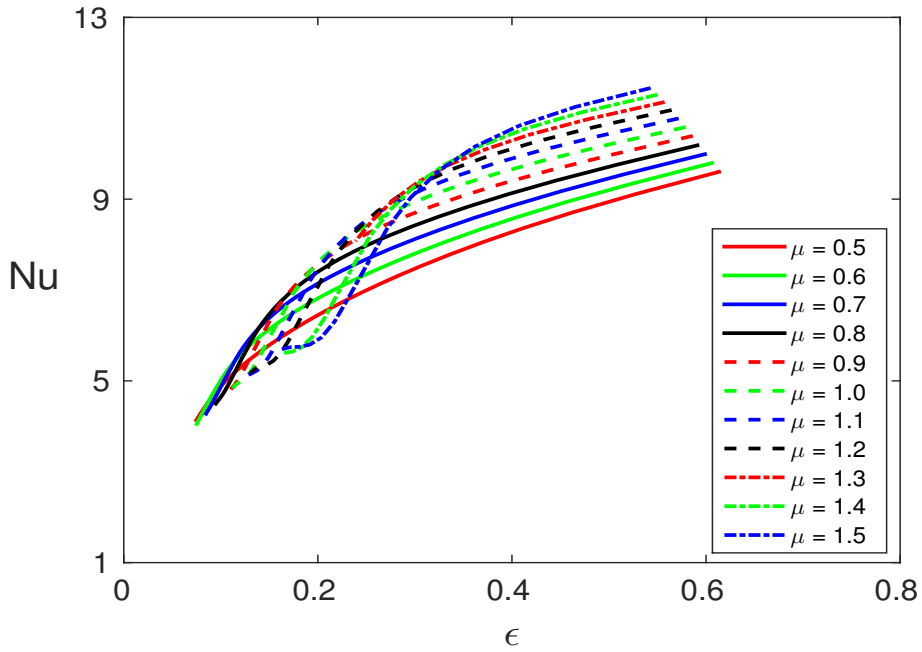

Figure 4.8: Variation of Nusselt number Nu with temperature parameter ε at different pressure sensitivity μ values in a square cell with $T_0 = 0.1$ and $Ra = 10^7$.

enough for the fluid to become effectively rigid and therefore immobile.

It is again worth emphasising that, although our solution method has effectively limited the computed dimensionless viscosity to a maximum value of 10^6, the solutions shown in Figure 4.7 are completely different from what would be obtained with an actual surface to base ratio of $\Delta\eta = 10^6$. At small values of ε, it is the extreme sensitivity of η to variations in T and z in the bulk flow that determines the observed structure, while the very high values of the viscosity attained in the lid are found to be unimportant (except for the calculation of stresses). For example, it is clear in Figure 4.7 that the bulk fluid is far from isoviscous, and this occurs only when ε is sufficiently small, regardless of the cut-off chosen to limit the value of η in the stagnant lid.

4.5 Variation of pressure dependence parameter μ

With this new form of viscosity function, we are able to run simulations for a larger range of μ values. In Figure 4.8, the Nusselt number Nu is plotted against ε for various μ values. For a fixed value of μ, Nu decreases as ε decreases. This is expected as decrease of ε corresponds to increase of viscosity contrast across the mantle. It

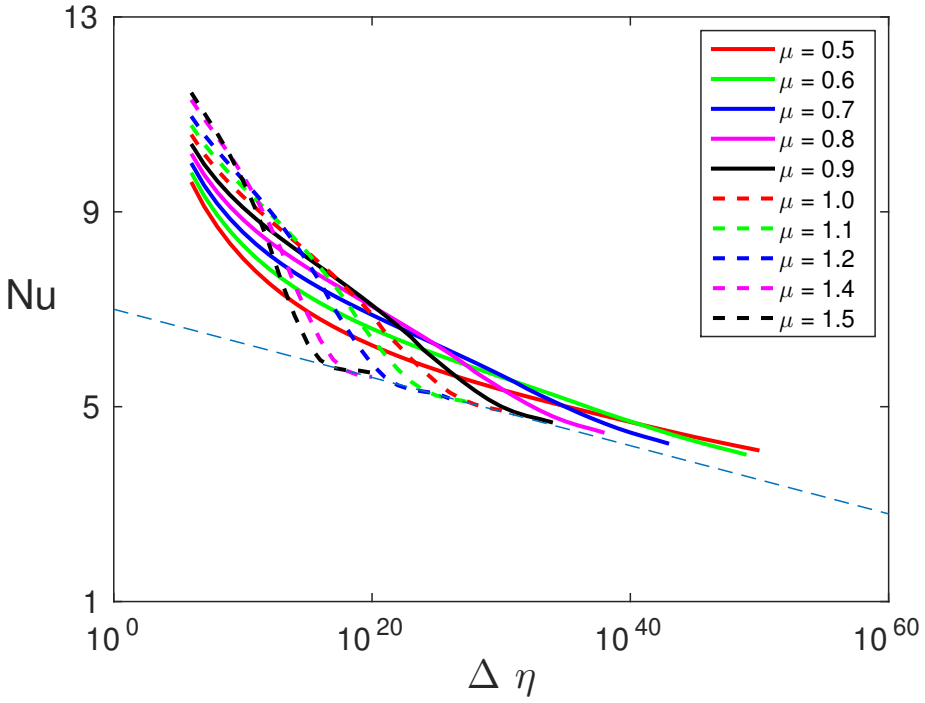

Figure 4.9: Variation of Nusselt number Nu with viscosity contrast $\Delta\eta$ at different pressure sensitivity μ values in a square cell with $T_0 = 0.1$ and $Ra = 10^7$. The dashed line is the envelope approximation given by (4.7).

should be noted that for the same viscosity contrast where $\Delta\eta < 10^9$ or $\varepsilon > 0.35$, Nu gets large with the increase of μ. However, the qualitative behaviour of the curves exhibits a significant change with the increase of μ. To get a better understanding, we also plotted Nu versus $\Delta\eta$ for various values of μ in Figure 4.9. When μ is around $0.5 \sim 0.6$, the value of Nu decreases steadily with the increase of viscosity variation. However, as μ increases, there comes a point where the curve changes its behaviour quite abruptly, i.e. Nu undergoes a rapid decrease and becomes a decreasing function of μ for very small values of ε (or for large viscosity contrasts $\Delta\eta$). Also for bigger values of μ, this point of sudden change comes at larger values of ε, i.e. at smaller viscosity variations. From Figure 4.9, we observe that the highest values of Nu at a certain viscosity contrast creates a type of envelope. Similarly, we also observe that the lowest values of Nu when strong pressure dependence is present, creates a log-linear relation with $\Delta\eta$. The line can be best approximated by

$$Nu = 7 - 0.07\log(\Delta\eta), \tag{4.7}$$

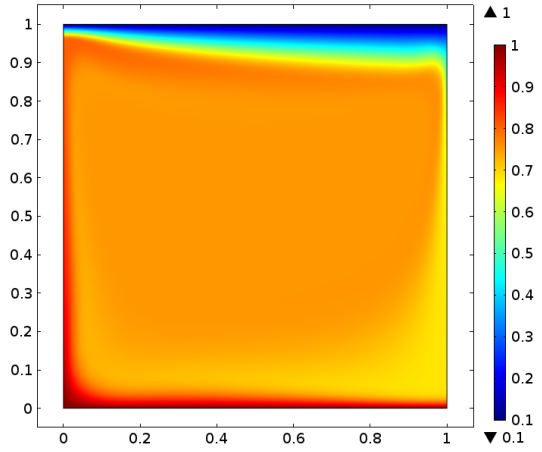

(a) $\Delta\eta = 10^{10},\ \mu = 1.5,\ \varepsilon = 0.326$

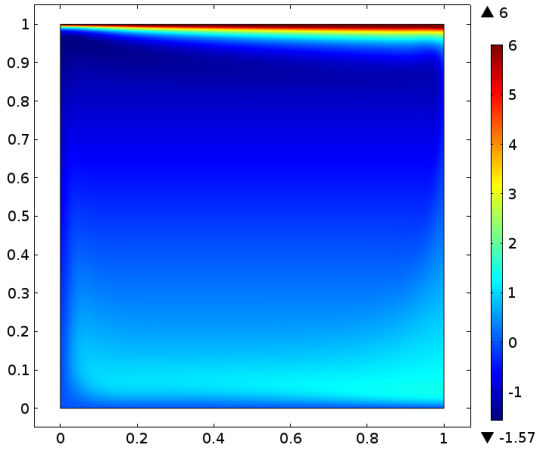

(b) $\Delta\eta = 10^{10},\ \mu = 1.5,\ \varepsilon = 0.326$

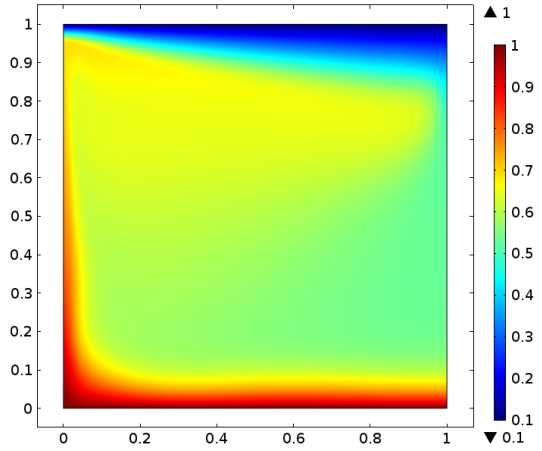

(c) $\Delta\eta = 10^{16},\ \mu = 1.5,\ \varepsilon = 0.2036$

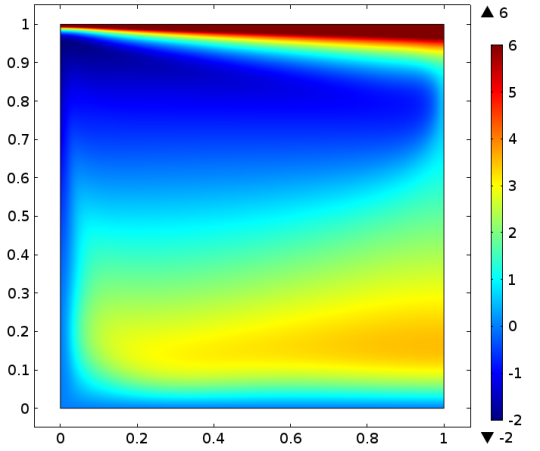

(d) $\Delta\eta = 10^{16},\ \mu = 1.5,\ \varepsilon = 0.2036$

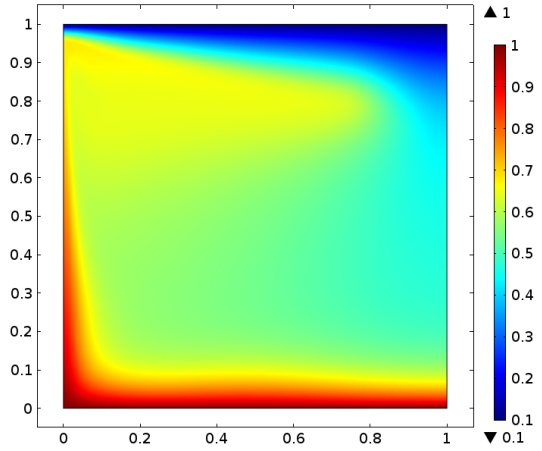

(e) $\Delta\eta = 10^{20},\ \mu = 1.5,\ \varepsilon = 0.163$

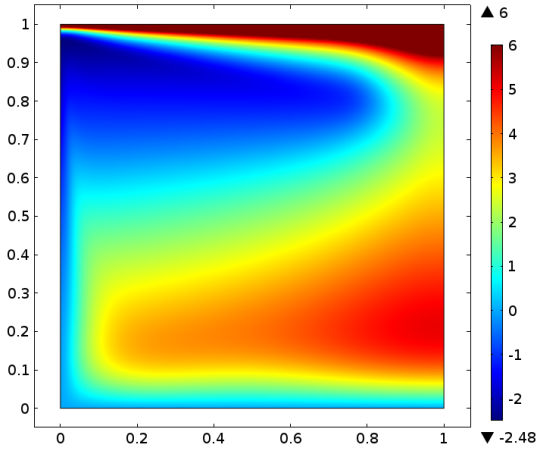

(f) $\Delta\eta = 10^{20},\ \mu = 1.5,\ \varepsilon = 0.163$

Figure 4.10: Temperature distributions (a, c, e) and the corresponding viscosity distributions (logarithm plots) (b, d, f) with different viscosity contrasts at a fixed pressure sensitivity $\mu = 1.5$, in a square cell with $T_0 = 0.1$ and $Ra = 10^7$.

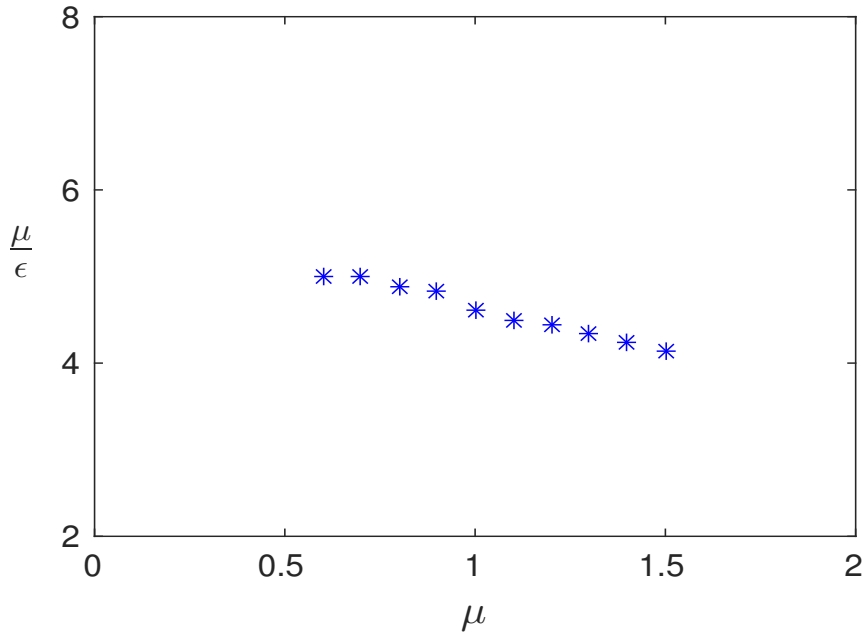

Figure 4.11: Variation of the ratio μ/ε with μ. The values of ε are chosen from Figure 4.8 where the Nusselt number Nu starts to decrease rapidly.

which is shown in Figure 4.9. The variation of Nu with ε and μ is quite extraordinary in qualitative manner. It is difficult to explain the exact reason behind this behaviour. However, to make a comment on it, we have presented some results of thermal distributions and logarithmic viscosity distributions at viscosity contrasts of 10^{10}, 10^{16} and 10^{20} for a fixed value of $\mu = 1.5$ in Figure 4.10. We observe that at $\Delta\eta = 10^{10}$, $\varepsilon = 0.326$, the interior is quite warm, isothermal and almost isoviscous, however, when $\Delta\eta = 10^{16}$, $\varepsilon = 0.2036$, the interior gets significantly cooler and the stagnant lid becomes thicker. Also there is a clear emergence of a high viscosity region in the lower mantle and this behaviour persists and becomes more prominent when $\Delta\eta = 10^{20}$ with $\varepsilon = 0.163$. We assume that all these remarkable changes in the thermal distribution might explain the significant change in the values of Nu. We believe this indicates that the transition in the curves in Figure 4.8 is from a thermoviscous $\eta(T)$ regime of $\mu \sim \varepsilon$ to a thermobaroviscous regime $\mu \gg \varepsilon$. In Figure 4.11, we have plotted the values of μ/ε versus μ, where the values of ε for each μ are chosen from Figure 4.8 at which the value of Nu starts to decrease rapidly. The graph is consistent with the idea that the transition in behaviour is associated with going from $\mu = O(1)$ to $\mu = O(\varepsilon)$ or vice-versa.

4.6 Narrower convecting cells

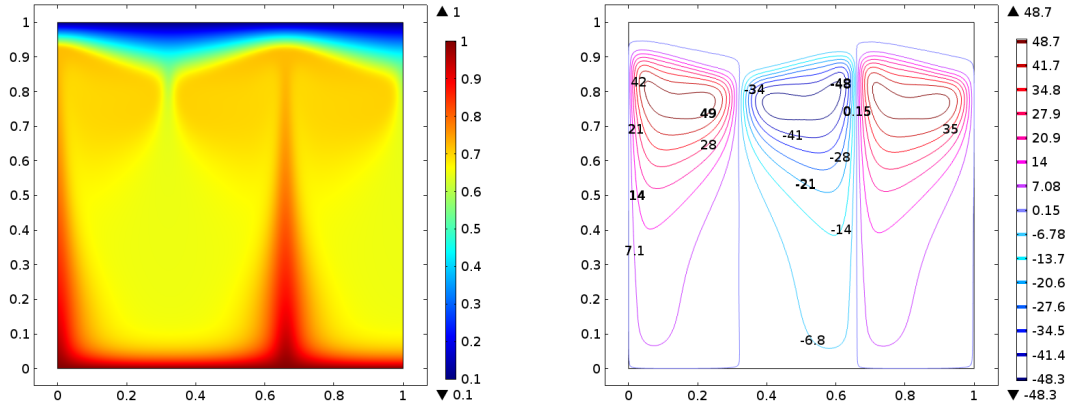

(*a*) Temperature distribution (*b*) Streamfunction contours

Figure 4.12: Three-cell convection pattern with $T_0 = 0.1$, $Ra = 10^7$, $\varepsilon = 0.1105$ and $\mu = 1.0$.

Reassured that computations with the cut-off viscosity function (4.5) accurately describe the convective flow, we are now able to compute solutions with higher viscosity contrasts corresponding to smaller values of ε. We performed a series of computations in which ε was gradually decreased while holding the other parameter values constant at $T_0 = 0.1$, $Ra = 10^7$ and $\mu = 1.0$. These numerical experiments revealed that convection in a square cell becomes unstable at a critical value of $\varepsilon \approx 0.1105$, corresponding to a viscosity contrast $\Delta\eta \approx 2.77 \times 10^{31}$. As ε decreases through this critical value, the convective flow breaks into a three-cell structure. Here unstable means that the stationary solver did not converge for this particular set of parameters. However, when the time-dependent solver was applied, the three-cell steady pattern emerged. As discussed earlier in section 3.3, this can happen when the new parameter is close to a bifurcation point - in which case multiple solutions are possible. The resulting temperature distribution and streamlines at $\varepsilon = 0.1105$ are shown in Figure 4.12, and we found that this three-cell pattern persists and is stable as ε is decreased further.

In Figure 4.13, we show the variation of Nu with viscosity contrast $\Delta\eta$ in a unit aspect ratio cell with $\mu = 1.0$, $T_0 = 0.1$ and $Ra = 10^7$. The blue dashed line gives the values of Nu when ε is decreased gradually. There is a sudden jump in Nu, when the convection cell breaks into a three-cell pattern. The red line shows the value of Nu as ε is increased. The convection starts with a three-cell pattern but when ε is large enough, i.e. viscosity contrast is small enough, it undergoes a transition back to a

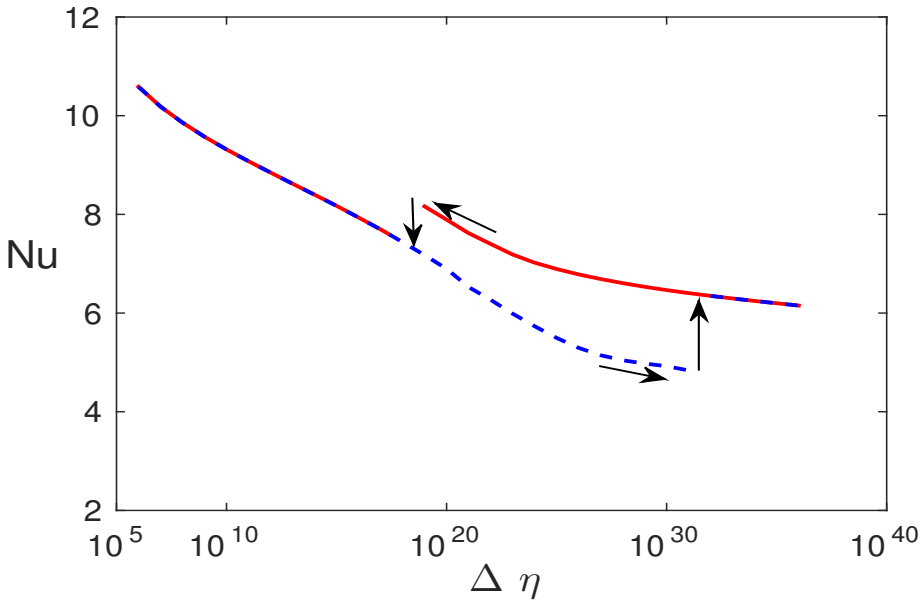

Figure 4.13: Variation of Nu as viscosity contrast $\Delta\eta$ is increased (i.e. ε is decreased) (blue dashed line) and as $\Delta\eta$ is decreased (i.e. ε is increased) (red solid line) in a unit aspect ratio cell with $\mu = 1.0$ and $Ra = 10^7$.

one-cell pattern. Hence there is a sharp fall in the numerical value of Nu at $\varepsilon = 0.2$, $\Delta\eta \sim 10^{19}$ and then it increases again as ε gets larger. Clearly Figure 4.13 shows the existence of a hysteresis loop as viscosity contrast gets larger and then smaller (or, ε is decreased and then increased). The hysteresis loop suggests that the system loses its stability at a saddle node bifurcation point. It also establishes the fact that there is a range of values of ε where both 1-cell (say, $n = 1$) and 3-cell (say, $n = 3$) solutions exist and are stable. There may be other stable branches for higher values of n, but it seems natural and convenient to go to a 3-cell pattern equilibrium solution because of the initial conditions.

Altogether, the revelation of three-cell structure leads us to hypothesise that the system copes with increasing sensitivity of the viscosity to temperature and pressure by restricting the flow to increasingly narrow convection cells. Following this idea, we were able to decrease ε even further and compute solutions with even higher viscosity contrasts by simultaneously decreasing the aspect ratio of the cell. Again fixing $T_0 = 0.1$, $Ra = 10^7$ and $\mu = 1.0$, we found that in a 1:3 cell, stable steady solutions could be computed for ε as low as 0.085, corresponding to a viscosity contrast $\Delta\eta \approx 7.5 \times 10^{40}$. For yet smaller values of ε, stable solutions could only be found by further decreasing the cell aspect ratio. In a 1:4 cell, for example, we solved the

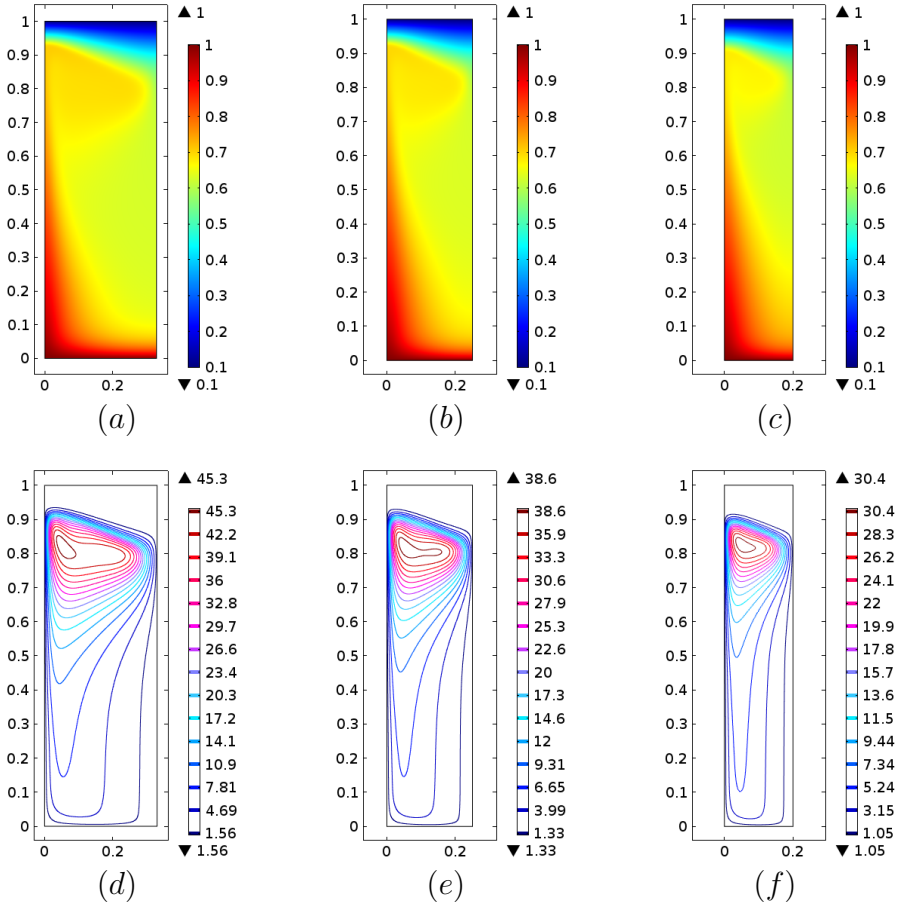

Figure 4.14: Temperature distribution and streamfunction contours in cells with different aspect ratios. The parameter values are $T_0 = 0.1$, $Ra = 10^7$, $\mu = 1.0$ and (a, d) 1:3 cell with $\varepsilon = 0.085$; (b, e) 1:4 cell with $\varepsilon = 0.077$; (c, f) 1:5 cell with $\varepsilon = 0.065$.

problem for values of ε down to 0.077 (corresponding to $\Delta\eta \approx 1.3 \times 10^{45}$), and in a 1:5 cell, we obtained solutions for $\varepsilon = 0.065$ ($\Delta\eta \approx 2.8 \times 10^{53}$).

The resulting temperature profiles and streamlines in cells of aspect ratio 1:3, 1:4 and 1:5 are plotted in Figure 4.14. Other than being compressed in the x-direction, the flow patterns in each case are strikingly similar to the 1:1 cell patterns observed above in Figures 4.3(f) and 4.4(f), for example. Below a stagnant and noticeably sloping lid, there is a rapidly circulating and relatively warm upper core, fed by a hot plume climbing the left-hand boundary of the cell. The somewhat cooler lower core is in turn fed by a descending plume from the cold lid. In all cases, the bulk fluid is neither isothermal nor isoviscous, and the flow patterns are completely different from results for purely temperature-dependent viscosity, as shown in Figures 4.1(a) and 4.1(c).

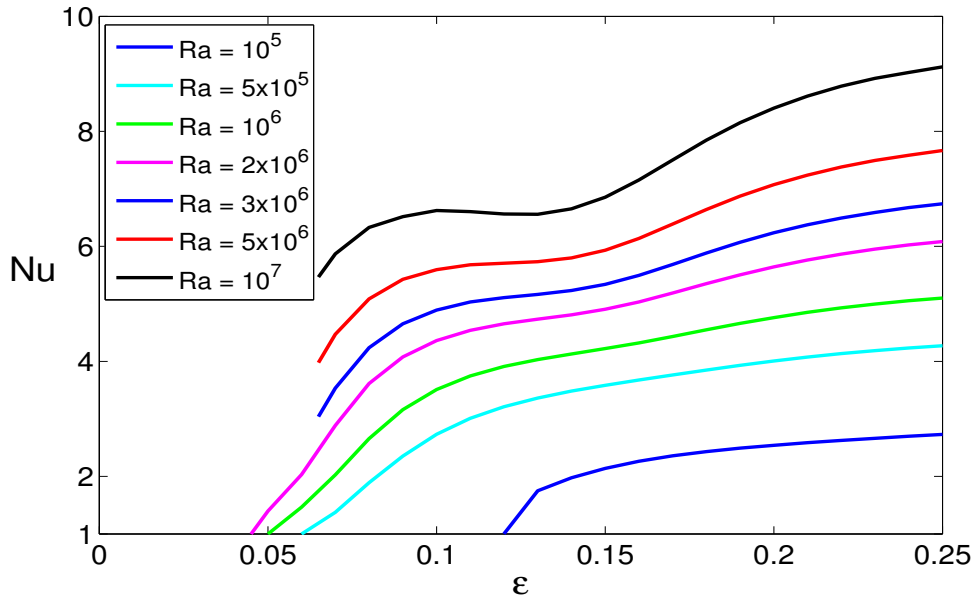

Figure 4.15: Variation of Nu with ε at fixed Ra with $T_0 = 0.1$, $a = 3\varepsilon$ and $\mu = 1.0$.

These results demonstrate that the preferred convection cell aspect ratio decreases as ε decreases, and the values found suggest that the cell width a (given unit cell height) should scale with ε. We recall that the initial breakdown of a unit aspect ratio cell occurs at $\varepsilon \approx 0.1105$, and that a three-cell pattern is then preferred, corresponding to $a = 1/3 \approx 3\varepsilon$. This scaling law is also approximately obeyed in the solutions found above with $a = 1/4$ and $a = 1/5$. We therefore hypothesise that, everything else being equal, the system prefers to adopt convection cells of width $a \propto \varepsilon$ when $\varepsilon \ll 1$, and that the constant of proportionality is around 3 when the other parameter values are $T_0 = 0.1$, $Ra = 10^7$ and $\mu = 1.0$.

Some numerical results obtained by varying Rayleigh number Ra and ε while maintaining $a = 3\varepsilon$ are summarised in Figure 4.15 and Figure 4.16. In Figure 4.15, we present the variation of Nusselt number Nu with ε at different Rayleigh number Ra with other parameter values fixed at $T_0 = 0.1$ and $\mu = 1.0$. As expected, the higher the Ra, the larger is Nu at a fixed ε (i.e. at a fixed viscosity contrast across the layer), since large Ra ensures vigorous convection. Figure 4.15 shows that for a fixed value of Ra, the general trend is that Nu increases with the increase of ε. However, there is no consistent pattern for the curves. We associate this with the fact computations can not reach the combined limit of $Nu \gg 1$ and $\varepsilon \ll 1$, where an asymptotic limit might be expected. Only at the left of the upper three curves is there an indication of asymptotic behaviour.

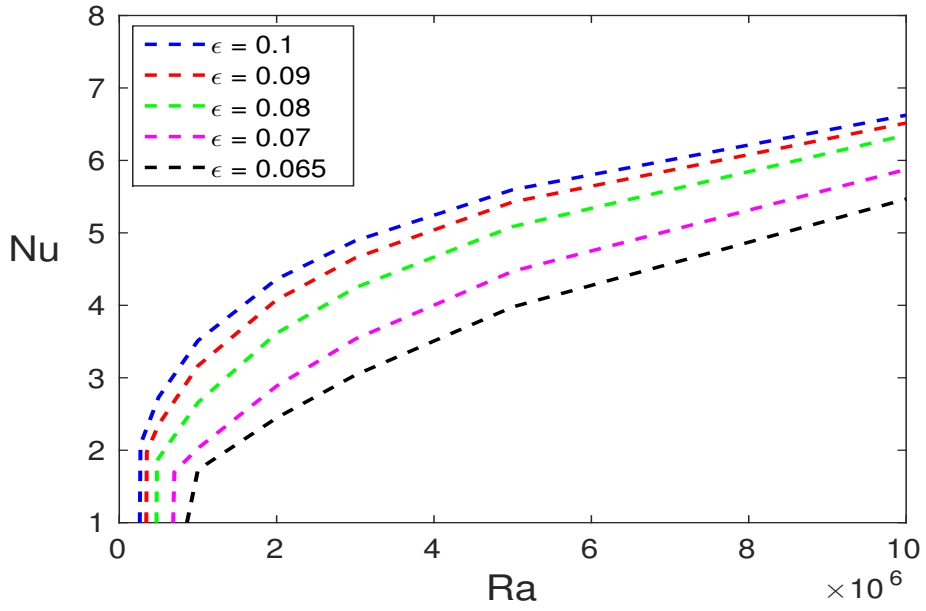

Figure 4.16: Variation of Nusselt number Nu with Rayleigh number Ra at various fixed values of ε with $T_0 = 0.1$, $\mu = 1.0$. In each case the cell aspect ratio is $a = 3\varepsilon$.

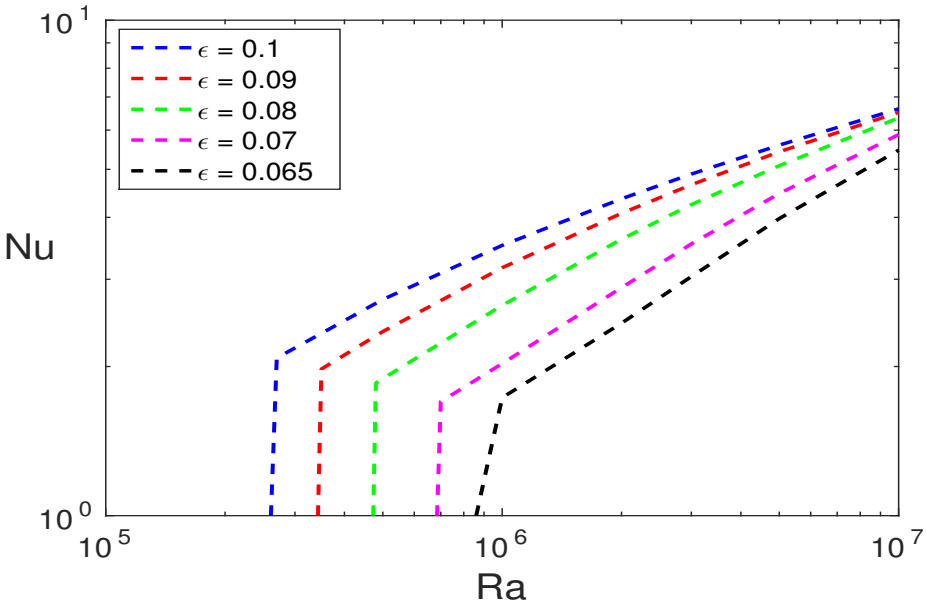

Figure 4.17: Log-log plot of variation of Nusselt number Nu with Rayleigh number Ra at various fixed values of ε with $T_0 = 0.1$, $\mu = 1.0$. In each case the cell aspect ratio is $a = 3\varepsilon$.

In Figure 4.16, we plot the Nusselt number Nu versus the Rayleigh number Ra for various fixed values of ε while the other parameter values are fixed at $T_0 = 0.1$, $\mu = 1.0$ and $a = 3\varepsilon$. It is worth mentioning that with these values of ε, the viscosity contrast across the layer is quite extreme (i.e. $\Delta\eta = 10^{34} - 10^{53}$). The figure exhibits that at these high viscosity contrasts, Nu increases rather weakly with Ra; compare with the constant viscosity values given in Table 2.2. We observe from the log-log plot of Nu versus Ra in Figure 4.17 that no asymptotic limit is evident for a convecting cell $a = 3\varepsilon$. From Figure 4.16 we observe that Nu reaches the value 1, implying that the flow is completely suppressed, at a finite critical value of the Rayleigh number $Ra_{\rm cr}$ which is tabulated in Table 4.3. To obtain further support for both this switching off of the convective flow and the scaling of the cell width a with ε, we next consider a linear stability analysis.

4.7 Linear stability analysis

Here we briefly summarise a linear stability analysis which predicts the critical Rayleigh number $Ra_{\rm cr}$ for the onset of convection and the resulting selected wavelength. Eliminating p by cross-differentiation, the governing equations (4.2) can be written as

$$\nabla^2(\eta\nabla^2\psi) - 4(\eta\psi_{xz})_{xz} - 2(\eta\psi_{xx})_{xx} - 2(\eta\psi_{zz})_{zz} = RaT_x, \tag{4.8}$$

$$T_t + \psi_x T_z - \psi_z T_x = \nabla^2 T, \tag{4.9}$$

where ψ is the streamfunction and η is given by (4.1). The boundary conditions are

$$\begin{aligned} \psi = \psi_{zz} = 0, \quad T = 1 \quad \text{at} \quad z = 0, \\ \psi = \psi_{zz} = 0, \quad T = T_0 \quad \text{at} \quad z = 1, \\ \psi = \psi_{xx} = 0, \quad T_x = 0 \quad \text{at} \quad x = 0, a, \end{aligned} \tag{4.10}$$

where a is the aspect ratio.

Now the base state is

$$\begin{aligned} \psi &= 0, \\ \theta_0(z) &= 1 - (1 - T_0)z, \\ \eta = \eta_0(z) &= \exp\left(\frac{(1 - T_0 - \mu T_0)z}{\varepsilon(1 - (1 - T_0)z)}\right), \end{aligned} \tag{4.11}$$

where we have written $T = \theta_0(z)$ as the notation T_0 is already used.
To linearize about this state, we set

$$\begin{aligned} \psi(x, z, t) &= f(z)e^{\lambda t}\sin kx, \\ T(x, z, t) &= \theta_0(z) + g(z)e^{\lambda t}\cos kx, \end{aligned} \tag{4.12}$$

where λ is the linear growth rate and $k = \pi/a$ is the wavenumber. Then f and g satisfy the ODEs

$$\eta_0(f'''' - 2k^2 f'' + k^4 f) + 2\eta_0'(f''' - k^2 f') + \eta_0''(f'' + k^2 f) = Ra\, k g, \tag{4.13}$$

$$g'' - (\lambda + k^2)g = -(1 - T_0)kf, \tag{4.14}$$

with the boundary conditions

$$f(0) = f''(0) = f(1) = f''(1) = g(0) = g(1) = 0. \tag{4.15}$$

In the limit $\varepsilon \to 0$, we hypothesize that $k = O(1/\varepsilon)$ and hence let $\varepsilon k = \kappa$. The viscosity $\eta_0(z)$ is exponentially large, and hence we expect $f(z)$ and $g(z)$ to be exponentially small outside a neighbourhood of $z = 0$. We therefore focus on a boundary layer near $z = 0$ by setting $z = \varepsilon Z$. The governing equations (4.13) and (4.14) then become

$$\eta_0(f_{ZZZZ} - 2\kappa^2 f_{ZZ} + \kappa^4 f) + 2\eta_{0Z}(f_{ZZZ} - \kappa^2 f_Z) + \eta_{0ZZ}(f_{ZZ} + \kappa^2 f) = Ra\, \varepsilon^3 \kappa g, \tag{4.16}$$

$$g_{ZZ} - (\varepsilon^2\lambda + \kappa^2)g = -(1 - T_0)\varepsilon\kappa f, \tag{4.17}$$

subject to

$$f = f_{ZZ} = g = 0 \quad \text{at} \quad Z = 0, \qquad f, g \to 0 \quad \text{as} \quad Z \to \infty. \tag{4.18}$$

The viscosity in this boundary layer takes the form

$$\eta_0 = \exp\left(\frac{(1 - T_0 - \mu T_0)Z}{1 - (1 - T_0)\varepsilon Z}\right) \sim e^{\beta Z} + O(\varepsilon), \tag{4.19}$$

where

$$\beta = 1 - (1 + \mu)T_0 \in (0, 1), \tag{4.20}$$

assuming $T_0 < \dfrac{1}{1 + \mu}$.

The problem may be normalized by setting

$$Z = \frac{y}{\beta}, \qquad \kappa = \beta m, \qquad \lambda = \frac{\beta^2}{\varepsilon^2}\sigma, \qquad g = \frac{\beta^3}{\varepsilon^3 Ra\, m}h. \tag{4.21}$$

Then to leading order in ε we get

$$f_{yyyy} + 2f_{yyy} + (1 - 2m^2)f_{yy} - 2m^2 f_y + m^2(1 + m^2)f = e^{-y}h, \tag{4.22}$$

$$h_{yy} - (\sigma + m^2)h = -R^* m^2 f, \tag{4.23}$$

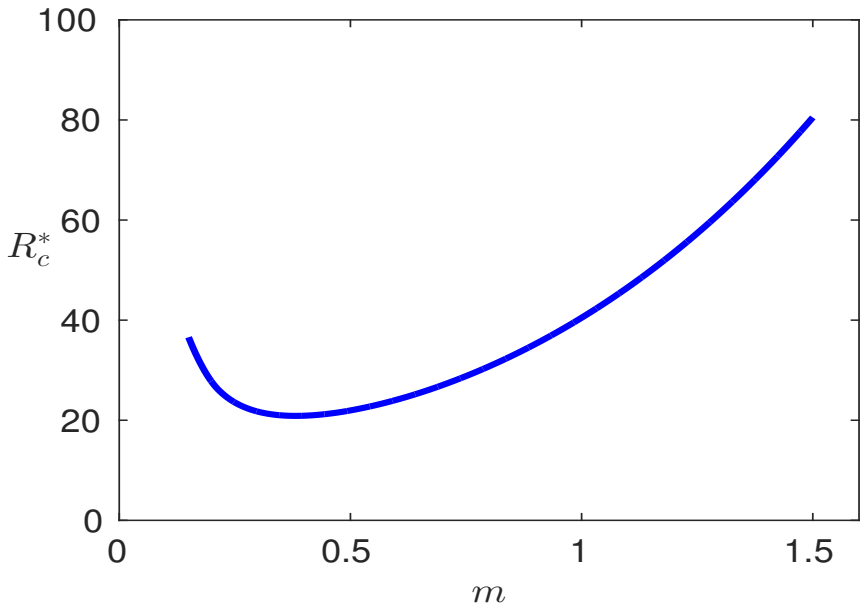

Figure 4.18: Critical normalized Rayleigh number R^* versus normalized wave number m. Here truncation length is $L = 15$.

where

$$R^* = \frac{(1 - T_0)\varepsilon^4 Ra}{\beta^4} \tag{4.24}$$

and the boundary conditions are

$$f = f_{yy} = h = 0 \quad \text{at} \quad y = 0, \qquad f, h \to 0 \quad \text{as} \quad y \to \infty. \tag{4.25}$$

We can verify that there are sufficient degrees of freedom to satisfy the conditions as $y \to \infty$ by seeking solutions where $h(y) \propto e^{ly}$ as $y \to \infty$. For all positive values of m and R^*, provided $\sigma > -m^2$, there is a three-parameter family of decaying solutions, with $\mathrm{Re}\, l < 0$. The first is a pure decaying mode, with

$$f(y) \sim Ae^{(l-1)y}, \qquad h(y) \sim (m^2 + (l^2 - l - m^2)^2)Ae^{ly}, \tag{4.26}$$

where

$$l = -\sqrt{\sigma + m^2}. \tag{4.27}$$

There is also a two-parameter family of modes which oscillate and decay, with

$$f(y) \sim (l^2 - \sigma - m^2)Ae^{ly}, \qquad h(y) \sim -m^2 R^* Ae^{ly}, \tag{4.28}$$

where

$$l = \frac{1}{2}(-1 - \gamma \pm \frac{2mi}{\gamma}), \tag{4.29}$$

and γ is given by

$$\gamma = \sqrt{\frac{1 + 4m^2 + \sqrt{1 + 24m^2 + 16m^4}}{2}} \in (1, \infty). \tag{4.30}$$

Hence, on the marginal curve where $\sigma = 0$, the general far-field behaviour of the solution is

$$f(y) \sim Ae^{-(m+1)y} + (1+\gamma)Be^{-(1+\gamma)y/2}\left\{\gamma \sin\left(\frac{my}{\gamma} + c\right) - 2m\cos\left(\frac{my}{\gamma} + c\right)\right\}, \tag{4.31}$$

$$h(y) \sim 2m^2 Ae^{my} - 2\gamma m^2 R^* Be^{-(1+\gamma)y/2}\sin\left(\frac{my}{\gamma} + c\right), \tag{4.32}$$

as $y \to \infty$, where A, B, c are arbitrary constants.
In practice, we solve numerically by truncating at a large but finite length $L \gg 1$ and replace (4.25) by

$$f = f_{yy} = h = 0 \quad \text{at} \quad y = 0, L. \tag{4.33}$$

Then the ODEs (4.22), (4.23) (with $\sigma = 0$) and boundary conditions (4.33) give us an eigenvalue problem for R^* as a function of m. We solve this eigenvalue problem using *chebop* in MATLAB. The smallest eigenvalue R^* is plotted against scaled wavenumber m in Figure 4.18. Evidently, R^* tends to infinity as $m \to 0$ and as $m \to \infty$, and takes its minimum $R^*_{cr} \sim 20.8724$ when $m \sim 0.3818$. These improve the approximate values of $R^*_{\rm cr} \approx 20.9$ and $m_{\rm c} \approx 0.395$ given by Stengel et al. (1982).

By reversing the scalings, we deduce that the base state (4.11) becomes unstable when the Rayleigh number exceeds a critical value.

$$Ra_{cr} \sim \frac{R^*_{cr}}{1 - T_0}\left(\frac{\beta}{\varepsilon}\right)^4. \tag{4.34}$$

As this threshold is crossed, disturbances of half-wavelength

$$a = \frac{\pi\varepsilon}{m\beta} \sim 8.2284\frac{\varepsilon}{\beta} \tag{4.35}$$

are excited. In our problem, $\mu = 1.0$ and $T_0 = 0.1$, and so we have $\beta = 0.8$. If $a = 3\varepsilon$, then from (4.35), we get

$$m = \frac{\pi}{3\beta} = 1.309. \tag{4.36}$$

From Figure 4.18, this value of m corresponds to $R^*_c = 62.218$. In Table 4.3, we present the critical Rayleigh number for different ε values when half wavelength $a = 3\varepsilon$.

In summary, the linear stability analysis supports our hypothesis that the preferred convection cell width a should scale with ε when $\varepsilon \ll 1$. Admittedly the constant

Table 4.3: Critical Rayleigh number, Ra_{cr} and half wavelength a for different ε from linear stability analysis and numerical computation.

	Stability analysis	Numerical model
ε	Ra_{cr} $\times 10^6$	Ra_{cr} $\times 10^6$
0.1	0.283	0.261
0.09	0.431	0.344
0.08	0.691	0.473
0.07	1.179	0.685
0.065	1.586	0.860
0.06	2.185	-
0.05	4.531	-

of proportionality predicted by equation (4.35) with $\beta = 0.8$ is approximately 10.3 rather than the value 3 proposed in section 4.6. However, we should not expect the critical wavelength at onset of instability to be necessarily close to the preferred value at much larger values of the Rayleigh number. We also recall from Figure 4.16 that our numerical calculations predict a critical Rayleigh number $Ra_{\rm cr} \approx 8.6007 \times 10^5$ when $\varepsilon = 0.065$, while equation (4.34) predicts $Ra_{\rm cr} \approx 5.3 \times 10^5$. The linear stability analysis therefore produces the correct order of magnitude for Ra_{cr} despite the fact that we had used a wavelength $a = 3\varepsilon$ rather than (4.35) in our simulations.

4.8 Discussion

The results we have found have serious implications for the style of convection in the mantle of the Earth and other terrestrial planets. The paradigm which has emerged over the last fifty years is one of large scale convection cells. The various phase transitions in the mantle, most notably that at 670 km, raised an early controversy on layered versus whole mantle convection, one whose resolution depends on the nature of the spinel–perovskite phase change (Christensen, 1995). The discussion was spiced by geochemical arguments concerning different long-lived mantle reservoirs (van Keken and Ballentine, 1998), and this led to various cartoons concerning mantle convection style (Ogawa, 2008, Tackley, 2009). One notable suggestion regarding narrow convection cells was made by Solomatov (2004) when he studied the initiation of subduction. Apart from this, the nearest comparable suggestion was that of Parsons and McKenzie (1978) and Huang et al. (2003), who suggested that small scale convection in the form of transverse rolls might occur below the lithosphere.

Our thesis is that the strong pressure dependence of mantle rheology will cause, in stagnant lid convection, convection cells to be narrow, and to be segregated into a vigorous upper cell with a more sluggish flow below this. This might apply on Venus, for example. What implications might there be for the Earth?

The active style of plate tectonics on the Earth, driven by the subduction of the oceanic lithosphere at plate boundaries, mitigates against the structure suggested here, at least in the upper mantle. There we would suppose that the oceanic plates drive a vigorous shallow return flow on the scale of the plates. But we suggest that the structure of the lower mantle must be similar to that shown here. The viscosity increases, and convection takes the form of narrow, sluggish fingers. The details of how this might occur remain to be investigated.

4.9 Summary

In this chapter we study numerically the Rayleigh-Bénard convection of a fluid whose viscosity depends strongly upon both temperature and pressure. Our computations are facilitated by the use of the cut-off viscosity function (4.5), which allows us to access very large and previously unexplored viscosity contrasts. This approach exploits the fact that the most extreme changes in viscosity occur in the cold lid region where the flow velocity is essentially zero; without the cut-off, one ends up expending the majority of the computational effort endeavouring to resolve this stagnant region where there is very little motion. By decreasing ε, we are able to study viscosity contrasts up to 10^{53}, while using the cut-off trick to limit the actual viscosity ratio in the computations to 10^6. We find that this absolute maximum value of η achieved in the lid is unimportant: the key consequence of decreasing ε is to enhance the sensitivity of the viscosity to variations in temperature and pressure in the bulk flow.

We find that pressure dependence of the viscosity results in a new flow regime, shown for example in Figures 4.3(f) and 4.4(f), which is completely different from the flow profile when only temperature dependence is included. Rather than a single approximately isothermal convection cell filling the whole core, we observe a warm upper core, and a quite distinct cooler lower core, fed by cold fluid from the lid. In the resulting flow profile, the fluid in the bulk is neither isothermal nor isoviscous, as suggested by Fowler (1993a). It would be impossible to explore computationally the extremely high viscosity contrasts needed to observe this new flow regime without using our cut-off viscosity trick.

As ε is decreased further, a second unexpected phenomenon is observed, namely that flow in a single square cell becomes unstable, and instead the flow breaks up into increasingly narrow convection cells. As shown in Figure 4.14, the flow structure appears self-similar if the aspect ratio of the cell is decreased in line with ε. This observation leads us to hypothesise that the limiting flow structure as $\varepsilon \to 0$ consists of convection cells of width $a \propto \varepsilon$. This hypothesis is supported by a linear stability calculation. The detailed asymptotic analysis in chapter 5 and 6 will provide further justification of this hypothesis and a detailed description of the flow structures observed in our simulations.

Chapter 5

Asymptotic Analysis: Upper Mantle

5.1 Introduction

In the previous chapters, we have demonstrated through numerical simulation that convection of a fluid with temperature- and pressure- dependent viscosity adopts a distinct structure when the sensitivity parameter ε is small and the Rayleigh number Ra is very high. The aim of this chapter and the next chapter is to study the structure using asymptotic analysis. The theoretical study of high Rayleigh number convection has come a long way since the final acceptance of the theory of plate tectonics in the 1960s. However, very little attention has been paid to the pressure dependence of viscosity, despite the fact that it can affect the behaviour profoundly, and the apparent reason for this is that it is computationally difficult to do.

The numerical solutions obtained in chapter 4, and the previous studies of Fowler (1985a), indicate that we should consider the convection in different parts separately and then match between them to complete the asymptotic analysis. If we look back at Figure 3.8 in section 3.4, then we can see that for the case of temperature-dependent viscosity, the unit aspect ratio convection cell can be decomposed into different regions, namely (i) the stagnant lid or lithosphere, (ii) the asthenosphere or delamination layer, (iii) the plumes, (iv) the core and (v) the basal thermal boundary layer. The primary feature of high Rayleigh number convection with purely temperature-dependent viscosity is that the cold boundary layer at the surface is so rigid that it will not deform, and remains stagnant on top of a vigorous convection beneath. The fact that it is buoyantly unstable is far outweighed by its extreme reluctance to move. Conversely, large temperature excesses would lead to very small viscosity, and therefore rapid movement. To prevent this the flow only allows a small temperature jump at its base. Just beneath the stagnant lid, there is a thin shear layer which we call the asthenosphere which connects the stagnant lid to the isothermal interior and

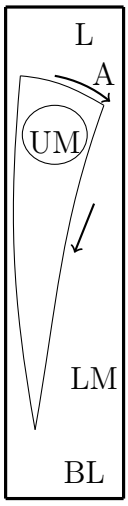

L: Stagnant lid
A: Asthenosphere
UM: Upper mantle
LM: Lower mantle
BL: Core-mantle thermal boundary layer

Figure 5.1: Schematic diagram of different regions or asymptotic structure of convection with temperature and pressure-dependent viscosity in a narrower cell, shown with two streamlines of the convective flow.

in which the temperature is adjusted. The flow below this shear layer is isothermal and also isoviscous, and is driven by the buoyancy in the plumes at the vertical walls. One of the challenging task is to identify the lid base profile which was studied by Fowler (1985a) extensively.

However, for the case of temperature and pressure-dependent viscosity, the structure is quite different, as illustrated in Figure 5.1. We have shown that the convection cell becomes increasingly narrow as ε decreases, and that the convection occurs predominantly in the "upper mantle" region, which lies above a relatively slow-moving "lower mantle". In the upper mantle, the uppermost part, i.e. the region attached to the surface of the Earth, is also identified as the stagnant lid or lithosphere. Below the stagnant lid, lies the thin shear layer i.e. asthenosphere. The rest of the upper mantle can be identified as the upper mantle core. The lower mantle can be divided into two parts, the basal thermal boundary layer which is situated at the core-mantle boundary, and just above this boundary layer, the rest of the lower mantle can be identified as lower mantle core. In between the upper and the lower mantle, we expect there to be a transition zone. It is worth mentioning that the word 'core' means the central part of the mantle in this dissertation and it has no relevance to the core of the Earth.

In this chapter, we will discuss the asymptotic behaviour of the upper mantle which is somewhat similar to that of purely temperature dependent viscous convection. Thus in a similar manner to temperature dependent viscosity convection, we will try to identify the lid base profile. We assume that the lid base can be determined by

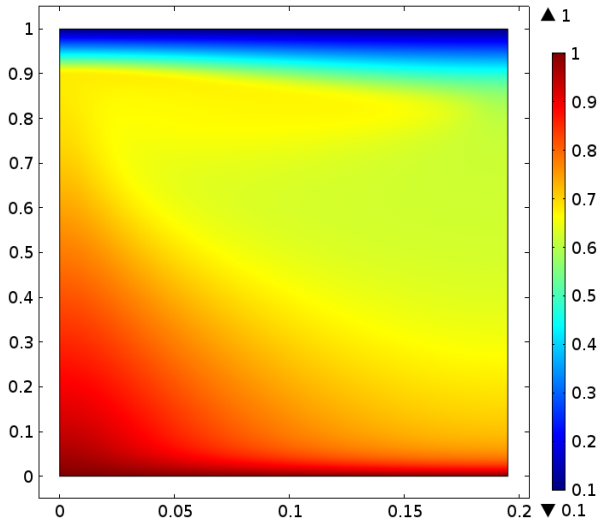

Figure 5.2: Thermal distribution in a cell of width 3ε at values $Ra = 10^7, \mu = 1$ and $\varepsilon = 0.065$ and with $T_0 = 0.1$. The top to bottom viscosity contrast for these values is 2.8×10^{53}. The calculations were done using a cut-off viscosity (defined in (4.5)), with the cut-off at $\eta = 10^6$.

an isothermal contour, but the temperature is unknown at the lid base or in the asthenosphere. So, an appropriate temperature needs to be determined for the lid base by matching to the layers below. Besides this, we will see that the upper mantle core is no longer driven by the plumes like isothermal core in temperature-dependent flow, but driven by the lid.

5.2 Rescaling for narrow cells

To facilitate the asymptotic analysis, it is helpful to re-define the normalized pressure in the governing equations (4.2)-(4.3) as follows:

$$p(x, z, t) = \tilde{p}(x, z, t) - Ra(1 - T_a)z, \tag{5.1}$$

where T_a is a constant. Then the dimensionless governing equations become (with tilde dropped)

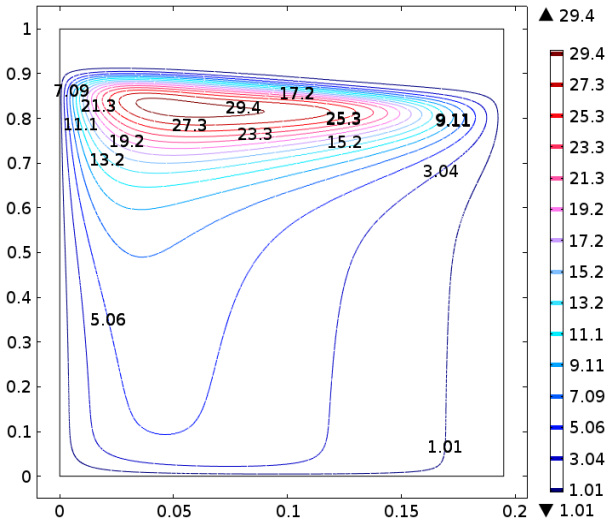

Figure 5.3: Flow streamlines corresponding to the Figure 5.2.

$$
\begin{aligned}
u_x + w_z &= 0, \\
p_x &= \tau_{1x} + \tau_{3z}, \\
p_z &= \tau_{3x} - \tau_{1z} - Ra(T_a - T), \\
\tau_1 &= -2\eta\psi_{xz}, \\
\tau_3 &= \eta\left(\psi_{xx} - \psi_{zz}\right), \\
T_t + \psi_x T_z - \psi_z T_x &= \nabla^2 T, \\
\eta &= \exp\left[\frac{1 - T + \mu(1 - z - T)}{\varepsilon T}\right],
\end{aligned}
\tag{5.2}
$$

and the free slip boundary conditions are

$$
\begin{aligned}
&\psi = \tau_3 = 0, \quad T = 1 \quad \text{on} \quad z = 0, \\
&\psi = \tau_3 = 0, \quad T = \frac{T_s}{T_b} = T_0 \quad \text{on} \quad z = 1, \\
&\psi = \tau_3 = T_x = 0 \quad \text{on} \quad x = 0, a,
\end{aligned}
\tag{5.3}
$$

where the symbols have their usual meaning described in previous chapters. We will identify T_a with the dimensionless temperature in the asthenosphere, which is to be determined as part of the solution. In the core flow, the buoyancy term proportional to Ra is dominant when $Ra \gg 1$. However, in the lid, where η is extremely large, the viscous stress terms dominate. Our definition of T_a ensures that the buoyancy term is zero in the transition region between these two extremes.

Figures 5.2, 5.3, 5.4 show an example of a computation with a viscosity contrast of $\sim 3 \times 10^{53}$ in a box with an aspect ratio $a = 3\varepsilon$ with $\varepsilon = 0.065, \mu = 1.0$ and

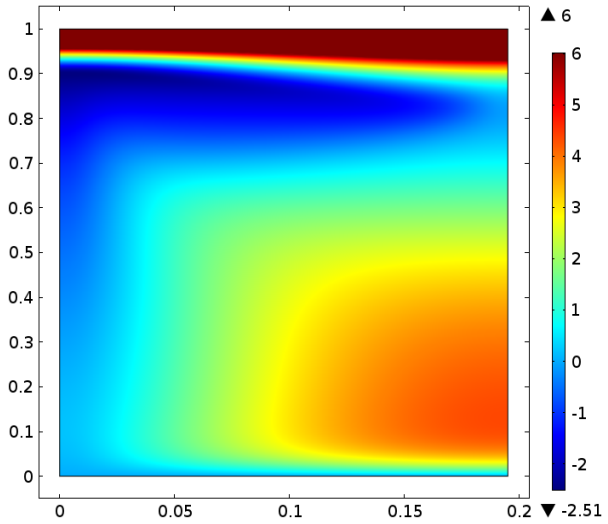

Figure 5.4: Viscosity distributions ($\log_{10}\eta$) corresponding to the Figure 5.2. The colour scale gives $\log_{10}\eta$. The values at 10^6 in the lid indicate actual values $\geqslant 10^6$ (via the cut-off).

$Ra = 10^7$; the horizontal coordinate is stretched to illuminate the flow structure. These figures are discussed further below. While there is clearly a stagnant lid in the cell, it is clear that the convecting part of the flow is neither isothermal nor isoviscous. In fact, there is a viscosity increase of a few orders of magnitude with depth as well as horizontally from left to right. In addition to these, it is fairly clear from Figure 5.2 that for temperature and pressure dependent viscosity, there is no equivalent thermal plume driving the upper core flow. The flow in the lower core is sufficiently sluggish that the excess heat from the lower boundary is simply conducted away, and the rapid flow in the upper core is driven by the buoyancy induced by the sloping lid roof.

Based on these results and others in chapter 4, our presumption is that the preferred width for the convection cell is of order ε, and the essence of our discussion follows from the assertion that the flow consists of two parts, an 'upper mantle' flow in which $1 - z = O(\varepsilon)$, and a 'lower mantle' part in which $z = O(1)$. In this chapter, we will concentrate on the structure of the upper mantle.

5.3 Upper mantle

The scaling for the upper mantle is given by

$$x = \varepsilon X, \qquad z = 1 - \varepsilon Z, \qquad t \sim \varepsilon^2. \tag{5.4}$$

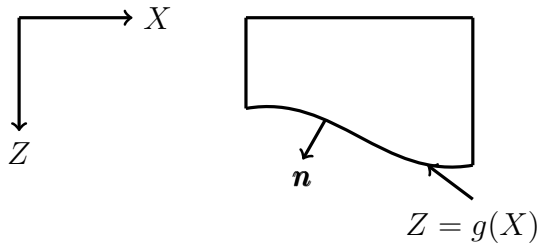

Figure 5.5: Schematic of the region S.

In terms of these, the scaled upper mantle system is

$$\begin{aligned} p_X &= \tau_{1,X} - \tau_{3,Z}, \\ -p_Z &= \tau_{3,X} + \tau_{1,Z} - \varepsilon Ra(T_a - T), \\ \tau_1 &= \frac{2\eta}{\varepsilon^2}\psi_{XZ}, \\ \tau_3 &= \frac{\eta}{\varepsilon^2}(\psi_{XX} - \psi_{ZZ}), \\ T_t + \psi_Z T_X - \psi_X T_Z &= \nabla^2 T, \end{aligned} \tag{5.5}$$

and the viscosity takes the form

$$\eta = \eta_a \exp\left[\frac{\mu Z}{T} + \frac{1}{\varepsilon}\left(\frac{1}{T} - \frac{1}{T_a}\right)\right], \tag{5.6}$$

where

$$\eta_a = \exp\left[\frac{1 - (1+\mu)T_a}{\varepsilon T_a}\right]. \tag{5.7}$$

It is to be noted that the other dimensionless variables have yet to be scaled properly. The boundary conditions are

$$\begin{aligned} \psi = \tau_3 = 0, \quad T = T_0 \quad \text{on} \quad Z = 0, \\ \psi = \tau_3 = T_X = 0 \quad \text{on} \quad X = 0, b, \end{aligned} \tag{5.8}$$

where $X = b = \dfrac{a}{\varepsilon}$ is the scaled width of the convection cell and in our case, $b = 3$.

5.3.1 Heat flux

At the beginning, we derive a useful condition on the surface heat flux. We recall the definition of (3.13) of the Nusselt number namely.

$$Nu = \frac{1}{(1-T_0)a}\int_0^a \left(-\left.\frac{\partial T}{\partial z}\right|_{z=1}\right) dx = \frac{1}{\varepsilon(1-T_0)b}\int_0^b \left(\left.\frac{\partial T}{\partial Z}\right|_{Z=0}\right) dX. \tag{5.9}$$

In a steady state flow, the energy equation from (5.5) can be written as

$$\nabla \cdot (T\boldsymbol{u}) = \nabla^2 T, \quad \text{where} \quad \boldsymbol{u} = (\psi_Z, -\psi_X). \tag{5.10}$$

If S is a region in the plane with boundary ∂S as shown in Figure 5.5, where the bottom boundary is an arbitrary curve $Z = g(X)$, then S can be considered as an upper part of the rescaled narrow cell. An integration of (5.10) then gives

$$0 = \int_S \left(\nabla \cdot (T\boldsymbol{u}) - \nabla^2 T\right) dX\, dZ = \int_{\partial S} (T\psi_Z - T_X)\, dZ + (T\psi_X + T_Z)\, dX. \tag{5.11}$$

Applying the free-slip condition and the zero heat-flux condition on the vertical walls, we obtain

$$\int_{Z=g(X)} (T\psi_Z - T_X)\, dZ + (T\psi_X + T_Z)\, dX = \int_0^b \left.\frac{\partial T}{\partial Z}\right|_{Z=0} dX, \tag{5.12}$$

since $u_n = 0$ at the top. Thus (5.9) and (5.12) yield

$$Nu = \frac{1}{\varepsilon b(1 - T_0)} \int_C \left(T\, d\psi - T_X\, dZ + T_Z\, dX\right), \tag{5.13}$$

where the integral is along any curve C from $X = 0$ to $X = b$.
If C is a streamline on which ψ is a constant, then we obtain

$$Nu = \frac{1}{\varepsilon b(1 - T_0)} \int_C \left(-T_X\, dZ + T_Z\, dX\right). \tag{5.14}$$

Now let us take a look at Figure 5.3 and consider the top streamline as the curve C. Clearly, this closed streamline does not reach the side walls of the cell. So, if we want to replace $g(X)$ by this streamline C, at both ends we still need to calculate $\int T d\psi$ on $g(X)$. However, we can see that the value of the streamfunction is very small on the top streamline (Figure 5.3) and $\psi = 0$ on the side boundaries. As a result $d\psi$ must be very small at both ends and (5.13) may reduce to (5.14).
In the particular case where $g(X)$ is constant, (5.13) becomes

$$Nu = \frac{1}{\varepsilon b(1 - T_0)} \int_0^b (\psi_X T + T_Z) dX. \tag{5.15}$$

5.3.2 Stagnant lid

Our analysis follows the reasoning of Fowler (1985a) in making an effort to determine the appropriate scales. This is facilitated by the fact that in the upper mantle core, the circulation mimics that of temperature dependent viscous convection, and so we follow a similar sequence of arguments.

We assume that there is a cold, rigid lid of thickness $\gamma s(X)$ adjoining the top surface in which $T < 1$ and η is exponentially large. The region $0 < Z < \gamma s(X)$ is known as the *stagnant lid* or *lithosphere*, where $s(X)$ identifies the lid profile and we denote the lid base by

$$Z = \gamma s(X). \tag{5.16}$$

We presume that $\varepsilon\gamma \ll 1$, so that the lid is thin, relative to the cell depth. In the lid, $\psi \ll 1$ and the temperature is determined by solving the heat conduction equation because thermal advection is negligible. Thus, we have

$$\nabla^2 T = 0, \tag{5.17}$$

with boundary conditions

$$\begin{aligned} T &= T_0, \quad \text{on} \quad Z = 0, \\ T &= T_a, \quad \text{on} \quad Z = \gamma s(X), \end{aligned} \tag{5.18}$$

where T_a is the asthenospheric temperature at the base of the lid. We take T_a to be constant as we suppose the base of the lid is essentially determined by an isotherm, which will be confirmed by matching to the asthenosphere.

The unknown lid base is determined by an extra condition on T_Z there which will be derived below. Note that for $Z = \gamma s(X)$, we have $T = T_a$, $\psi \approx 0$, and so

$$T_X + \gamma s' T_Z = 0. \tag{5.19}$$

Hence the integration in (5.14) over the lid base implies that

$$\begin{aligned} Nu &= \frac{1}{\varepsilon b(1-T_0)} \int_C \left(\gamma^2 s'^2 T_Z \, dX + T_Z \, dX\right), \\ &= \frac{1}{\varepsilon b(1-T_0)} \int_0^b \left(1 + \gamma^2 s'^2\right) T_Z \Big|_{Z=\gamma s(X)} dX. \end{aligned} \tag{5.20}$$

5.3.3 Asthenosphere

Below the stagnant lid there is a shear layer, in which the temperature switches from its conductive profile to an adiabatic profile. The lithosphere remains rigid during long intervals of geologic time. In contrast, because of the higher temperature, rocks beneath the lithosphere can flow by subsolidous viscous creep. We term this layer the *asthenosphere*, which is its dynamical counterpart in plate tectonic models of mantle convection. It was referred to by Fowler (1985a) as a delamination layer. This layer

joins the rigid lid to the rapidly convecting core and has dimensionless thickness δ ($\delta \ll 1$).

In this layer we introduce the scales

$$T = T_a + \varepsilon\theta, \qquad Z = \gamma s(X) + \delta\zeta, \quad \psi \sim \Lambda, \quad \eta \sim \eta_a, \tag{5.21}$$

where η_a is defined in (5.7), and hence it is related to T_a by

$$T_a = \frac{1}{1 + \mu + \varepsilon \ln \eta_a}. \tag{5.22}$$

The chain rule for transformation from (X, Z) to (X, ζ) is

$$\partial_X = \partial_X - \frac{\gamma s'}{\delta}\partial_\zeta \quad \text{and} \quad \partial_Z = \frac{1}{\delta}\partial_\zeta. \tag{5.23}$$

The continuity of heat flux into the lid then implies $T_Z \sim 1/\gamma \sim \varepsilon/\delta$, and so we choose

$$\gamma = \frac{\delta}{\varepsilon}. \tag{5.24}$$

Using the above scales, the steady-state scaled upper mantle system of equations (5.5) becomes

$$p_X - \frac{\gamma s'}{\delta}p_\zeta = \tau_{1,X} - \frac{\gamma s'}{\delta}\tau_{1,\zeta} - \frac{1}{\delta}\tau_{3,\zeta}, \tag{5.25a}$$

$$-\frac{1}{\delta}p_\zeta = \tau_{3,X} - \frac{\gamma s'}{\delta}\tau_{3,\zeta} + \frac{1}{\delta}\tau_{1,\zeta} + \varepsilon^2\theta Ra, \tag{5.25b}$$

$$\tau_1 = \frac{2\eta_a\eta\Lambda}{\varepsilon^2\delta}(\psi_{X\zeta} - \frac{\gamma s'}{\delta}\psi_{\zeta\zeta}), \tag{5.25c}$$

$$\tau_3 = \frac{\eta_a\eta\Lambda}{\varepsilon^2}\left[\psi_{XX} - \frac{2\gamma s'}{\delta}\psi_{\zeta X} - \frac{\gamma s''}{\delta}\psi_\zeta + \frac{\gamma^2 s'^2}{\delta^2}\psi_{\zeta\zeta} - \frac{1}{\delta^2}\psi_{\zeta\zeta}\right], \tag{5.25d}$$

$$\frac{\Lambda}{\delta}\left[\psi_\zeta\theta_X - \psi_X\theta_\zeta\right] = \theta_{XX} - \frac{2\gamma s'}{\delta}\theta_{X\zeta} - \frac{\gamma s''}{\delta}\theta_\zeta + \frac{\gamma^2 s'^2}{\delta^2}\theta_{\zeta\zeta} + \frac{1}{\delta^2}\theta_{\zeta\zeta}. \tag{5.25e}$$

Balancing the terms in (5.25e) leads to

$$\Lambda = \frac{1}{\delta}. \tag{5.26}$$

From (5.25b), we deduce that

$$p, \tau_1, \tau_3 \sim \varepsilon^2\delta Ra, \tag{5.27}$$

and to balance (5.25c)-(5.25d), we choose

$$\eta_a = \varepsilon^4\delta^4 Ra. \tag{5.28}$$

It might be useful to mention here that η_a from (5.28) helps to determine T_a using (5.22) if δ is known. Also from the scaled viscosity relation (5.6), we have

$$\eta = \exp\left[\frac{1+\mu\varepsilon Z}{\varepsilon T_a\left(1+\dfrac{\varepsilon\theta}{T_a}\right)} - \frac{1}{\varepsilon T_a}\right] = \exp\left[-\frac{\theta}{T_a^2} + \frac{\mu\gamma s}{T_a}\right] + O(\varepsilon). \tag{5.29}$$

Thus the scalings in (5.26), (5.27), (5.28) lead us to the approximate governing equations in the asthenosphere (assuming steady state)

$$\begin{aligned}
\gamma s' p_\zeta &= \gamma s' \tau_{1,\zeta} + \tau_{3,\zeta}, && (5.30a)\\
-p_\zeta &= -\gamma s' \tau_{3,\zeta} + \tau_{1,\zeta} + \theta, && (5.30b)\\
\tau_1 &= -2\eta\gamma s' \psi_{\zeta\zeta}, && (5.30c)\\
\tau_3 &= \eta(\gamma^2 s'^2 - 1)\psi_{\zeta\zeta}, && (5.30d)\\
\psi_\zeta \theta_X - \psi_X \theta_\zeta &= \left(\gamma^2 s'^2 + 1\right)\theta_{\zeta\zeta}, && (5.30e)\\
\eta &= \exp\left[-\frac{\theta}{T_a^2} + \frac{\mu\gamma s}{T_a}\right]. && (5.30f)
\end{aligned}$$

We deduce suitable boundary conditions for these equations as follows. As we enter the lid, i.e. as $\zeta \to -\infty$, the viscosity increases exponentially and we expect negligible flow and a conductive temperature gradient. Thus

$$\psi \to 0, \quad \theta_\zeta \sim (T_a - T_0)G(X) \quad \text{as} \quad \zeta \to -\infty, \tag{5.31}$$

where G is an unknown function to be determined. We also assume for the moment that the upper mantle core is isothermal. This will be verified a posteriori below. So, to match with the upper mantle core, we propose

$$\tau_3 \to 0, \quad \theta \to 0 \quad \text{as} \quad \zeta \to \infty. \tag{5.32}$$

The choice of $\tau_3 \to 0$ will be justified in due course.

Some algebraic simplification of (5.30c) and (5.30d) produces

$$\tau_1 = \frac{2\gamma s' \tau_3}{1 - \gamma^2 s'^2}, \tag{5.33}$$

which leads to

$$\tau_{3,\zeta} = -\frac{\gamma s'(1 - \gamma^2 s'^2)}{(1 + \gamma^2 s'^2)^2}\theta. \tag{5.34}$$

Hence the governing equations in the asthenosphere reduce to

$$\begin{aligned} \tau_{3,\zeta} &= -\frac{\gamma s'(1-\gamma^2 s'^2)}{(1+\gamma^2 s'^2)^2}\theta, \\ \frac{\tau_3}{(1-\gamma^2 s'^2)} &= -\psi_{\zeta\zeta}\exp\left[-\frac{\theta}{T_a^2}+\frac{\mu\gamma s}{T_a}\right], \\ \psi_\zeta\theta_X - \psi_X\theta_\zeta &= \left(1+\gamma^2 s'^2\right)\theta_{\zeta\zeta}, \end{aligned} \tag{5.35}$$

with the boundary conditions in (5.31)-(5.32). The set of equations (5.35) admit a similarity solution which we now find following a similar procedure to that described by Fowler (1985a).

If we define

$$\begin{aligned} \xi = \frac{(T_a-T_0)}{T_a^2}G(X)\zeta, \qquad \psi = \frac{T_a^8\gamma s'}{(T_a-T_0)^3 G^3(1+\gamma^2 s'^2)^2}\exp\left[-\frac{\mu\gamma s}{T_a}\right]f(\xi), \\ \theta = T_a^2 g(\xi), \qquad \tau_3 = \frac{T_a^4\gamma s'(1-\gamma^2 s'^2)}{(T_a-T_0)G(1+\gamma^2 s'^2)^2}h(\xi), \end{aligned} \tag{5.36}$$

then the system (5.35) becomes

$$h_\xi + g = 0, \tag{5.37a}$$

$$f_{\xi\xi} + h\exp(g) = 0, \tag{5.37b}$$

$$g_{\xi\xi} + Afg_\xi = 0, \tag{5.37c}$$

where A is to be found, and s satisfies

$$\frac{1}{G(1+\gamma^2 s'^2)}\left[\frac{\gamma s'}{G^3(1+\gamma^2 s'^2)^2}\exp\left(-\frac{\mu\gamma s}{T_a}\right)\right]' = \frac{A(T_a-T_0)^4}{T_a^{10}} = \beta, \text{(say)} \tag{5.38}$$

and the corresponding boundary conditions are

$$g(\xi),\ h(\xi) \to 0, \quad \text{as} \quad \xi \to \infty \quad \text{(in the core)}, \tag{5.39a}$$

$$f(\xi) \to 0, \quad g'(\xi) \to 1, \quad \text{as} \quad \xi \to -\infty \quad \text{(in the lid)}. \tag{5.39b}$$

To use a shooting method to solve the problem (5.37)-(5.39), we introduce a new variable χ and use the transformation (as in Fowler (2011))

$$\begin{aligned} \chi = \frac{\xi}{c}, \qquad g = \hat{g}(\chi), \\ h = c\hat{h}(\chi), \qquad f = c^3\hat{f}(\chi), \end{aligned} \tag{5.40}$$

where c is to be determined. This gives a new system, dropping ($\hat{}$),

$$h_\chi + g = 0, \tag{5.41a}$$

$$f_{\chi\chi} + h\exp(g) = 0, \tag{5.41b}$$

$$g_{\chi\chi} + fg_\chi = 0, \tag{5.41c}$$

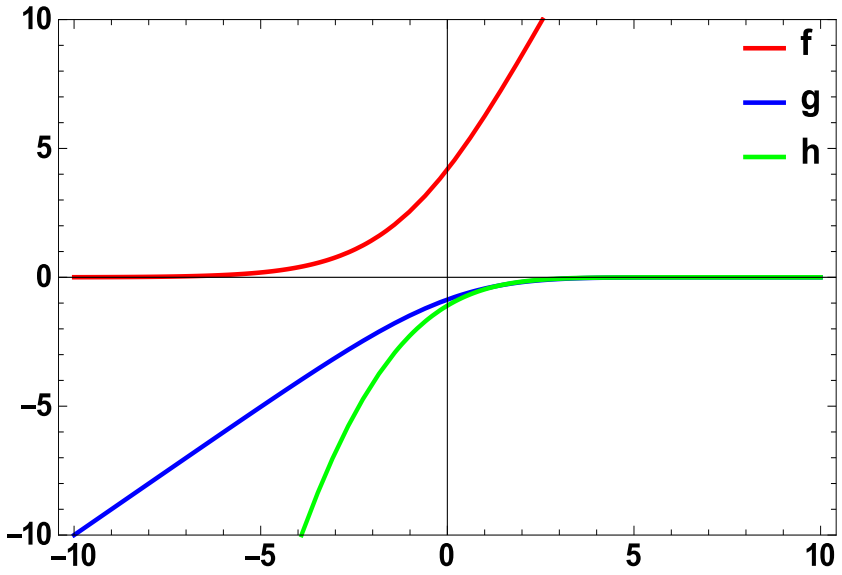

Figure 5.6: The profiles of f, g, h in the asthenosphere.

where A and c are related by

$$A = \frac{1}{c^4}. \tag{5.42}$$

The infinite domain $(-\infty, \infty)$ is truncated to $[-M, M]$, where M is chosen to be sufficiently large. The appropriate initial conditions are then

$$f = f' = 0, \quad g' = c, \quad g = -cM, \quad h = h_0 - \frac{1}{2}cM^2 \quad \text{at} \quad \chi = -M, \tag{5.43}$$

and the values of c and h_0 are adjusted until

$$g = h = 0 \quad \text{at} \quad \chi = M. \tag{5.44}$$

The initial conditions for g and h are chosen in a way so that they satisfy (5.41a). Numerical solution shows that $M = 20$ is large enough and gives $c = 1.843$, which yields

$$A = 0.08667. \tag{5.45}$$

The solutions for f, g, h are shown in Figure 5.6.

5.3.4 Upper mantle core

Emerging from the asthenosphere, $f \sim \zeta$, and it follows that we should rescale

$$\psi \sim \frac{1}{\delta}, \tag{5.46}$$

and hence also

$$p, \tau_1, \tau_3 \sim \delta, \tag{5.47}$$

thus verifying the choice of boundary condition for τ_3 in (5.32). In terms of the unscaled variables in (5.5), this suggests

$$\begin{aligned} \tau_1, \tau_3, p &\sim \varepsilon^2 \delta^2 Ra, \\ \psi &\sim \frac{1}{\delta^2}, \\ T &= T_a + \varepsilon\theta, \\ \eta &\sim \eta_a. \end{aligned} \tag{5.48}$$

Using these scalings in the system of equations (5.5)-(5.6), we get

$$\begin{aligned} p_X &= \tau_{1,X} - \tau_{3,Z}, \\ -p_Z &= \tau_{3,X} + \tau_{1,Z} + \frac{\theta}{\delta^2}, \\ \tau_1 &= 2\eta\psi_{XZ}, \\ \tau_3 &= \eta(\psi_{XX} - \psi_{ZZ}), \\ \delta^2\theta_t + \psi_Z\theta_X - \psi_X\theta_Z &= \delta^2\nabla^2\theta, \\ \eta &= \exp\left[\frac{\mu Z}{T} + \frac{1}{\varepsilon}\left(\frac{1}{T} - \frac{1}{T_a}\right)\right], \\ T &= T_a + \varepsilon\theta. \end{aligned} \tag{5.49}$$

We use this scaled set of equations as the basic reference set henceforth.

In conventional boundary layer theory for temperature-dependent viscous convection, $\theta = 0$ to all orders of δ. The reason for this is essentially the same as in the application of the Prandtl-Batchelor theorem, where the closed streamlines force a constant temperature in a steady flow (Fowler, 1985b). Although Figure 5.3 suggests that at least some of the streamlines invade the lower core (and thus not closed within the upper core), these are for low values of ψ, and the streamlines having $\psi \sim O(1)$ are closed. Approximately then, we have $\theta \approx 0$, and the model (5.49) reduces to a modified Stokes flow problem

$$\begin{aligned} p_X &= \tau_{1,X} - \tau_{3,Z}, \\ -p_Z &= \tau_{3,X} + \tau_{1,Z}, \\ \tau_1 &= 2\eta\psi_{XZ}, \\ \tau_3 &= \eta(\psi_{XX} - \psi_{ZZ}), \\ \eta &= \exp\left[\frac{\mu Z}{T_a}\right]. \end{aligned} \tag{5.50}$$

The fact that $\theta = 0$ to the lowest order leads to a self-consistent scaling that supports our earlier assumption that the upper core is approximately isothermal in the matching condition (5.32).

Before we move on to the lower mantle analysis, we will investigate the behaviour of the stagnant lid base profile.

5.4 Lid base profile computation

To identify the lid base profile $Z = \gamma s(X)$, a self-consistent determination of γ is one of the challenging parts of this theory. Following the analysis of the temperature-dependent viscosity case as in Fowler (1985a), we initially presume $\gamma \ll 1$.

5.4.1 Case I: $\gamma \ll 1$

Under this assumption, the temperature is essentially linear in the stagnant lid and (5.17)-(5.18) give

$$T = T_0 + \frac{T_a - T_0}{\gamma s} Z, \tag{5.51}$$

which implies

$$T_Z = \frac{T_a - T_0}{\gamma s}. \tag{5.52}$$

Using (5.52) in (5.20), leads us to

$$Nu = \frac{(T_a - T_0)}{\varepsilon \gamma b \, (1 - T_0)} \int_0^b \frac{dX}{s}. \tag{5.53}$$

We recall from (5.24) that $\gamma = \dfrac{\delta}{\varepsilon}$. Hence $\gamma \ll 1$ is equivalent to $\delta \ll \varepsilon$. If we ignore the higher order terms of γ in (5.35), then we obtain

$$\begin{aligned} \tau_{3,\zeta} &= -\gamma s' \theta, \\ \tau_3 &= -\psi_{\zeta\zeta} \exp\left[-\frac{\theta}{T_a^2}\right], \\ \psi_\zeta \theta_X - \psi_X \theta_\zeta &= \theta_{\zeta\zeta}, \end{aligned} \tag{5.54}$$

where the boundary conditions are

$$\psi \to 0, \quad \theta_\zeta \sim \frac{T_a - T_0}{s} \quad \text{as} \quad \zeta \to -\infty, \tag{5.55a}$$

$$\tau_3 \to 0, \quad \theta \to 0 \quad \text{as} \quad \zeta \to \infty. \tag{5.55b}$$

Comparing the conditions of (5.55) and (5.31), we see that the a priori unknown function $G(X)$ in this limit is given by

$$G(X) = \frac{1}{s(X)}. \tag{5.56}$$

To find the similarity solution, this time we choose

$$\begin{aligned} \xi &= \frac{(T_a - T_0)}{T_a^2}\frac{\zeta}{s}, \qquad & \psi &= \frac{T_a^8 \gamma s^3 s'}{(T_a - T_0)^3} f(\xi), \\ \theta &= T_a^2 g(\xi), & \tau_3 &= \frac{T_a^4 \gamma s s'}{(T_a - T_0)} h(\xi). \end{aligned} \tag{5.57}$$

This produces exactly the same problem (5.37), (5.39) for $f,\ g,\ h$, where now A satisfies

$$\gamma s (s^3 s')' = \frac{A(T_a - T_0)^4}{T_a^{10}} = \beta. \tag{5.58}$$

A shooting method will again produce $A = \ 0.08667$, and one can easily verify that (5.58) is consistent with (5.38) with $\gamma \to 0$ and $G = \dfrac{1}{s}$. With A and T_a known, we may calculate β, but γ is still unknown. So, there is no way we can solve the differential equation given in (5.58).

However, under the assumption of $\gamma \ll 1$, we can impose some further simplifications. Balancing the shear stress with buoyancy in (5.25b) and ignoring τ_1 at leading order yields

$$-\frac{s'}{\varepsilon} p_\zeta \approx -\frac{1}{\delta}\tau_{3,\zeta}, \tag{5.59a}$$

$$-p_\zeta \approx \varepsilon^2 \delta Ra\, \theta, \tag{5.59b}$$

$$\tau_1 \approx -\frac{2\eta_a \eta \Lambda}{\varepsilon^3 \delta} s' \psi_{\zeta\zeta}, \tag{5.59c}$$

$$\tau_3 \approx -\frac{\eta_a \eta \Lambda}{\varepsilon^2 \delta^2} \psi_{\zeta\zeta}, \tag{5.59d}$$

$$\frac{\Lambda}{\delta}(\psi_\zeta \theta_X - \psi_X \theta_\zeta) \approx \frac{1}{\delta^2}\theta_{\zeta\zeta}. \tag{5.59e}$$

Then the appropriate scalings for p, τ_1, τ_3, ψ and η_a are chosen as

$$\begin{aligned} p &\sim \varepsilon^2 \delta Ra, \\ \tau_1 &\sim \delta^3 Ra, \\ \tau_3 &\sim \varepsilon \delta^2 Ra, \\ \eta_a &\sim \varepsilon^3 \delta^5 Ra, \\ \Lambda &\sim \frac{1}{\delta}. \end{aligned} \tag{5.60}$$

Using the above scalings in (5.59), we obtain

$$
\begin{aligned}
s' p_\zeta &= \tau_{3,\zeta}, && \text{(5.61a)}\\
-p_\zeta &= \theta, && \text{(5.61b)}\\
\tau_1 &= -2\eta s' \psi_{\zeta\zeta}, && \text{(5.61c)}\\
\tau_3 &= -\eta \psi_{\zeta\zeta}, && \text{(5.61d)}\\
\psi_\zeta \theta_X - \psi_X \theta_\zeta &= \theta_{\zeta\zeta}, && \text{(5.61e)}\\
\eta &= \exp\left[-\frac{\theta}{T_a^2}\right]. && \text{(5.61f)}
\end{aligned}
$$

As a consequence, the approximate governing equations in the asthenosphere can be written as

$$
\begin{aligned}
\tau_{3,\zeta} &= -s'\theta, && \text{(5.62a)}\\
\psi_{\zeta\zeta} &= -\tau_3 \exp\left[\frac{\theta}{T_a^2}\right], && \text{(5.62b)}\\
\psi_\zeta \theta_X - \psi_X \theta_\zeta &= \theta_{\zeta\zeta}, && \text{(5.62c)}
\end{aligned}
$$

where the boundary conditions are as same as (5.55) and the a priori unknown function $G(X)$ is again

$$
G(X) = \frac{1}{s(X)}. \tag{5.63}
$$

For the similarity solution, we choose

$$
\begin{aligned}
\xi = \frac{(T_a - T_0)}{T_a^2}\frac{\zeta}{s}, \qquad & \psi = \frac{T_a^8 s^3 s'}{(T_a - T_0)^3} f(\xi),\\
\theta = T_a^2 g(\xi), \qquad & \tau_3 = \frac{T_a^4 s s'}{(T_a - T_0)} h(\xi).
\end{aligned} \tag{5.64}
$$

This produces again exactly the same problem (5.37), (5.39) for f, g, h, where now A satisfies

$$
s(s^3 s')' = \frac{A(T_a - T_0)^4}{T_a^{10}} = \beta. \tag{5.65}
$$

We can easily see that there is no γ in this relation like (5.58). With A and T_a known, we may write the differential equation in (5.65) as

$$
s^3 s'(s^3 s')' = \beta s^2 s', \tag{5.66}
$$

which gives

$$
\frac{1}{2}(s^3 s')^2 = \frac{1}{3}\beta\left(s^3 - s_c^3\right), \tag{5.67}
$$

where s_c is the value of s where $s' = 0$. We could choose $s_c = s_0 = s(0)$ if we believe the lid slope is zero at $X = 0$, or $s_c < s_0$ if we want $s' > 0, \forall X$. In fact, $s'(0) = 0$ is a reasonable choice because it ensures that $\psi \to 0$ as $X \to 0$ (because of the boundary condition at $x = 0$). Thus we obtain from (5.67)

$$\int \frac{s^3 ds}{\sqrt{s^3 - s_c^3}} = \int \sqrt{\frac{2\beta}{3}} dX. \tag{5.68}$$

Let $s/s_c = \sigma$, and we get

$$\int \frac{\sigma^3 d\sigma}{\sqrt{\sigma^3 - 1}} = \int \sqrt{\frac{2\beta}{3 s_c^5}} dX. \tag{5.69}$$

Let us choose $s_c = s_0$, so that $\sigma = 1$ at $X = 0$. This leads to

$$\int_1^\sigma \frac{\sigma^3 d\sigma}{\sqrt{\sigma^3 - 1}} = \int_0^X \sqrt{\frac{2\beta}{3 s_0^5}} dX, \tag{5.70}$$

and solving this, we have

$$\frac{\sqrt{\pi}\,\Gamma(-5/6)}{3\Gamma(-1/3)} + \frac{2}{5}\sigma^{5/2}\,{}_2F_1\left(-\frac{5}{6}, \frac{1}{2}, \frac{1}{6}, \frac{1}{\sigma^3}\right) = \sqrt{\frac{2\beta}{3 s_0^5}} X, \tag{5.71}$$

where σ is expressed in an implicit relation involving a hypergeometric function ${}_2F_1$ and Gamma functions. From this relation (5.71), we may obtain σ and then determine

$$Z = \gamma s(X) = \gamma s_0 \sigma(X), \tag{5.72}$$

if β, s_0 and γ are known. If we choose $T_a = 0.615$ at the moment (the choice will be justified in the next section), then $\beta = 0.79$ for $A = 0.08667, T_0 = 0.1$ from (5.65). However, we do not know s_0, but γs_0 is known from numerics which is 1.29 for $T_a = 0.615$. Thus we solve (5.71) with arbitrary values of s_0 corresponding to small γ (so that $\gamma s_0 = 1.29$) and compare them with the isothermal contour for $T_a = 0.615$ obtained from our full numeric solution shown in Figure 5.2. In Figure 5.7, the lid base profiles are presented in XZ coordinates and we can easily see that as the value of γ is increased, the lid base approximation gets better, even though for $\gamma = 1.1$, real solution can not be found for larger values of X. It should be mentioned here that although we have used the values of $\gamma = 1.0, 1.1$ in the figure, our analysis assumed $\gamma \ll 1$, and therefore, we can not expect high accuracy from these choices of γ. In any case, studying the case of $\gamma \sim 1$ seems like a reasonable alternative option since the curves do not match at any length for small γ. This is in any case suggested by figure, where the lid thickness ~ 0.1 is comparable to the upper core length scale $\varepsilon = 0.065$.

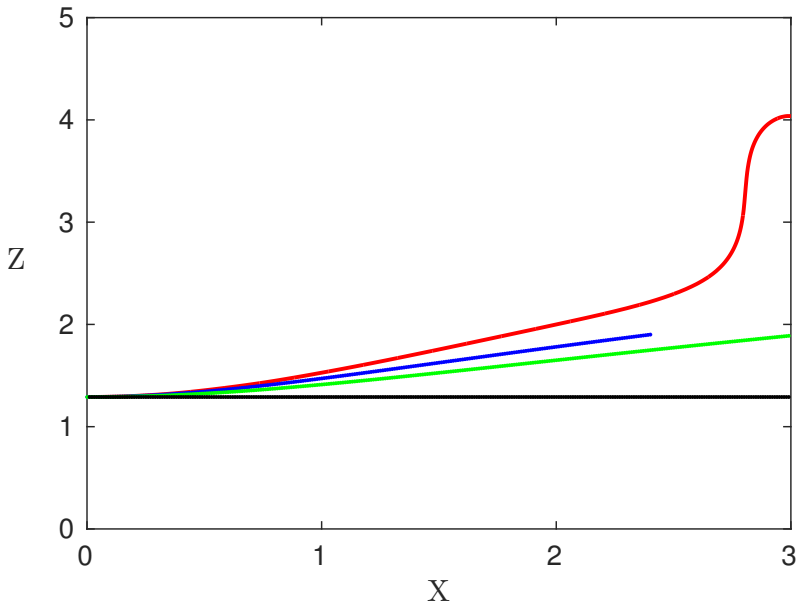

Figure 5.7: Comparison of the lid base profiles, $Z = \gamma s(X)$. The isothermal contour (red) is drawn from COMSOL solution for $T_a = 0.615$ and the lid base is calculated using (5.72) corresponding to $T_a = 0.615, \gamma s_0 = 1.29$ with $\gamma = 0.1$ (black), $\gamma = 1.0$ (green) and $\gamma = 1.1$ (blue).

5.4.2 Case II: $\gamma \sim 1$

In the case where $\gamma = O(1)$, we can without loss of generality assume that

$$\gamma = 1 \qquad \text{and} \qquad \delta = \varepsilon. \tag{5.73}$$

In this case, the aspect ratio of the lid is $O(1)$, and therefore the temperature in the lid is determined by solving the full heat conduction equation, since thermal advection is negligible. We write

$$T = T_0 + (T_a - T_0)\,\Theta, \tag{5.74}$$

where T_a is the asthenospheric temperature at the base of the lid. The problem to solve for Θ is then

$$\begin{aligned} \nabla^2\Theta &= 0, \\ \Theta &= 0, \qquad \text{on} \quad Z = 0, \\ \Theta = 1, \quad \Theta_Z &= G(X), \quad \text{on} \quad Z = s(X), \\ \Theta_X &= 0, \qquad \text{on} \quad X = 0, b, \end{aligned} \tag{5.75}$$

where $G(X)$ is again the unknown heat flux in equations (5.31) and (5.36).

With the assumption (5.73), the scalings for ψ, p, τ_1, τ_3 and η_a in the asthenosphere from (5.27), (5.28) then become

$$\Lambda \sim \frac{1}{\delta}, \tag{5.76a}$$

$$p, \tau_1, \tau_3 \sim \varepsilon^3 Ra, \tag{5.76b}$$

$$\eta_a = \varepsilon^4 \delta^4 Ra = \varepsilon^8 Ra, \tag{5.76c}$$

so that the asthenospheric temperature is

$$T_a = \frac{1}{1 + \mu + \varepsilon \ln \varepsilon^8 Ra}. \tag{5.77}$$

With the values $\varepsilon = 0.065$, $Ra = 10^7$, $\mu = 1$, we have $T_a \approx 0.61488$.

Thus the governing equations (5.30) in the asthenosphere can be written as

$$s' p_\zeta = s' \tau_{1,\zeta} + \tau_{3,\zeta}, \tag{5.78a}$$

$$-p_\zeta = -s' \tau_{3,\zeta} + \tau_{1,\zeta} + \theta, \tag{5.78b}$$

$$\tau_1 = -2\eta s' \psi_{\zeta\zeta}, \tag{5.78c}$$

$$\tau_3 = -\eta (1 - s'^2) \psi_{\zeta\zeta}, \tag{5.78d}$$

$$\psi_\zeta \theta_X - \psi_X \theta_\zeta = \left(1 + s'^2\right) \theta_{\zeta\zeta}, \tag{5.78e}$$

$$\eta = \exp\left[-\frac{\theta}{T_a^2} + \frac{\mu s}{T_a}\right], \tag{5.78f}$$

and the boundary conditions are

$$\psi \to 0, \quad \theta_\zeta \sim (T_a - T_0) G \quad \text{as} \quad \zeta \to -\infty, \tag{5.79a}$$

$$\tau_3 \to 0, \quad \theta \to 0 \quad \text{as} \quad \zeta \to \infty. \tag{5.79b}$$

Thus, $\Theta(X, Z)$ satisfies the free boundary problem (5.75), where the free boundary $Z = s(X)$ satisfies the additional equation (5.38), which with $\gamma = 1$ reduces to

$$\left[\frac{s'}{G^3 \left(1 + s'^2\right)^2} \mathrm{e}^{-\mu s / T_a}\right]' = \beta G \left(1 + s'^2\right). \tag{5.80}$$

It should be noted that (5.20) now gives the Nusselt number as

$$Nu = \frac{T_a - T_0}{\varepsilon b (1 - T_0)} \int_0^b \left(1 + s'^2\right) G(X) dX. \tag{5.81}$$

5.4.3 Lid temperature computation

The coupled system (5.75) and (5.80) is a complicated free boundary problem which must generally be solved numerically. If s is known, then it is straightforward in principle to compute G from (5.75) and then (5.80) provides a second order differential equation for s. This provides the nucleus of an iterative procedure for the solution. We will discuss the issue of boundary conditions for s in the next section.

We solve the coupled system (5.75) and (5.80) numerically as follows. We define the harmonic conjugate function

$$\chi = \frac{1}{C} \int_{(0,0)}^{(X,Z)} (\Theta_Z \, dX - \Theta_X \, dZ) \,, \tag{5.82}$$

so that

$$C\chi_X = \Theta_Z, \qquad C\chi_Z = -\Theta_X. \tag{5.83}$$

The potential function χ is well-defined since Θ satisfies Laplace's equation, and C is determined by the requirement that $\Theta = 1$ on $Z = s$, which implies

$$C = \frac{1}{\displaystyle\int_0^s \chi_X dZ}. \tag{5.84}$$

We define the arc length σ on $Z = s$, such that[1]

$$\frac{dX}{d\sigma} = \cos\phi, \qquad \frac{ds}{d\sigma} = \sin\phi, \qquad s_X = \tan\phi, \tag{5.85}$$

where ϕ is the angle made by the curve $Z = s(X)$ with the X-axis and the normal to $Z = s$ is $(-\sin\phi, \cos\phi)$. It follows that χ satisfies

$$\begin{aligned} \nabla^2\chi &= 0, \\ \chi &= 0 \qquad \text{on} \quad X = 0, \\ \chi &= 1 \qquad \text{on} \quad X = b, \\ \chi_Z &= 0 \qquad \text{on} \quad Z = 0, \\ \chi_Z - s_X\chi_X &= 0 \qquad \text{on} \quad Z = s. \end{aligned} \tag{5.86}$$

(The constant value of χ at $X = b$ is arbitrary, as can be seen from (5.82) and (5.84).) The last boundary condition $(5.86)_5$ is the expression for zero normal derivative χ_n on $Z = s$ which comes from

$$\chi_n = \boldsymbol{n} \cdot \nabla\chi = -\sin\phi\chi_X + \cos\phi\chi_Z = 0 \tag{5.87}$$

[1]We will use s_X instead of s' for convenience from now on.

The free boundary condition (5.80) to determine s can be written as

$$\frac{d}{d\sigma}\left[\frac{s_X}{G^3(1+s_X^2)^2}\exp\left(-\frac{\mu s}{T_a}\right)\right] = \beta G\sec\phi, \tag{5.88}$$

using the boundary condition $(5.86)_5$. On $Z = s$, we have

$$G = C\chi_X, \tag{5.89}$$

and the tangential derivative is

$$\frac{d\chi}{d\sigma} = \chi_X\cos\phi + \chi_Z\sin\phi = \frac{G}{C}\sec\phi. \tag{5.90}$$

Thus, (5.88) becomes

$$\frac{d}{d\sigma}\left[\frac{s_X}{G^3(1+s_X^2)^2}\exp\left(-\frac{\mu s}{T_a}\right)\right] = \beta C\frac{d\chi}{d\sigma}, \tag{5.91}$$

Integration of (5.91) yields

$$\frac{s_X}{(1+s_X^2)^2}\exp\left(-\frac{\mu s}{T_a}\right) = \beta C G^3\chi, \tag{5.92}$$

where we assume that the lid slope is zero at the left-hand boundary, i.e. $s_X(0) = 0$. In other words,

$$\frac{s_X}{(1+s_X^2)^2}\exp\left(-\frac{\mu s}{T_a}\right) = \beta D, \tag{5.93}$$

where

$$D = C^4\chi\chi_X^3\Big|_{Z=s}. \tag{5.94}$$

The advantage of this formulation is (i) that it permits one integration of the free boundary condition (5.91), thus the second order differential equation (5.80) reduces to a first order differential equation; (ii) that it clearly separates the determination of χ and s, providing a simple way of iterating towards a solution. To be specific, we could solve (5.86) for given s to determine χ; using the solution of χ, we calculate D using (5.94); then we solve (5.93) for s, providing an update, and then we would iterate the process, on the assumption that the iteration converges. In practice, the solution is so sensitive that we adopt an alternative strategy, as described below.

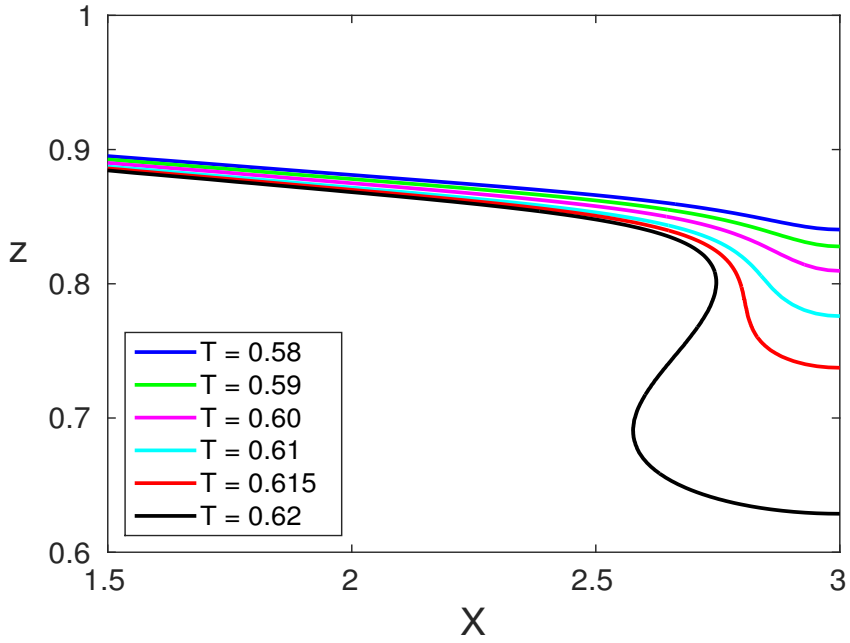

Figure 5.8: Plume formation at the end of the asthenosphere. As indicated, the contours are those of constant temperature $T = 0.58$, $T = 0.59$, $T = 0.60$, $T = 0.61$, $T = 0.615$, $T = 0.62$ taken from the full numerical solution at $Ra = 10^7$, $\varepsilon = 0.065, \mu = 1.0$ with $b = 3$ (so the cell is of width 3ε in x). Only half of the lid $1.5 < X < 3$, is shown to get a better view.

5.4.3.1 Boundary conditions

Since we have defined the lid base $Z = s(X)$ by the isotherm at $T = T_a$, the boundary conditions for s are apparently

$$s_X = 0 \qquad \text{at} \qquad X = 0, b, \tag{5.95}$$

since $\theta_X = 0$ there. The question then arises as to which isotherm to use in practice. Figure 5.8 shows a sequence of isotherms within the asthenosphere which nicely delineate the formation of a weak plume at the right margin, taken from the computation of the steady state solution of (5.2) with (5.3), using parameter values $b = 3, \varepsilon = 0.065, \mu = 1.0, Ra = 10^7$. Particularly, the choice of $T_a = 0.615$ as defining the lid base is actually exactly that defined by (5.77), and seems an apt choice.

As pointed out above, in neglecting the integration constant in (5.92) we have already imposed $s_X = 0$ at $X = 0$. We can also see that the function $\dfrac{s_X}{(1 + s_X^2)^2}$ has a maximum at $s_X = \frac{1}{\sqrt{3}}$. Thus equation (5.93) admits a real solution for s_X only if

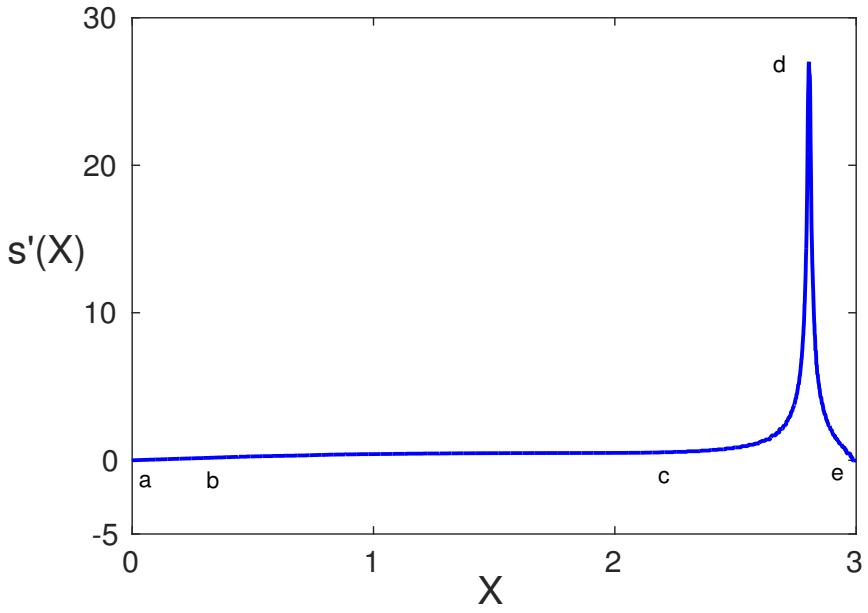

Figure 5.9: Slope of the isotherm for $T = 0.615$ derived from the computed solution plotted in Figure 5.8. The letters a, b, c, d, e are those discussed in the caption to Figure 5.11.

$\beta D e^{\mu s/T_a} \leqslant \dfrac{3\sqrt{3}}{16}$, in which case two solutions exist, one either side of $s_X = \frac{1}{\sqrt{3}}$. Since $s_X = 0$ at $X = 0$, the value of s_X in (5.93) must be to the left of the maximum, at least for small X, i.e., $s_X < \dfrac{1}{\sqrt{3}}$, or equivalently $\phi < \frac{\pi}{6}$.

Similarly, $s_X = 0$ at $X = b$ follows from $(5.86)_5$, since $\chi_Z = 0$ at $X = b$. However, this leads to an inconsistency in (5.93). A local expansion of χ near the corner $(b, s(b))$ indicates that if $s_X = 0$ at $X = b$, then

$$\chi \sim 1 - \alpha(b - X) \quad \text{near} \quad X = b,\ Z = s, \tag{5.96}$$

where α is some arbitrary constant ($\alpha \neq 0$), so that $\chi_X \neq 0$ at $X = b$. In consequence, $D \neq 0$ in (5.94), and thus (5.93) implies $s_X \neq 0$ at $X = b$. The coupled problem as stated has no solution satisfying $s_X = 0$ at $X = b$.

However, if we suppose $s_X \neq 0$ at $X = b$, a local expansion for χ then implies

$$\chi \sim 1 - \alpha r^q \sin q\lambda, \tag{5.97}$$

where $b - X = r \sin\lambda$ and λ is the angle with $X = b$. According to (5.87), the normal derivative is zero on $Z = s$, i.e.

$$\chi_\lambda = -\alpha q r^{q-1} \cos q\lambda = 0. \tag{5.98}$$

If $s_X = \tan\phi$, then $\lambda = \dfrac{\pi}{2} - \phi$ on $Z = s$ and this gives from above

$$q = \frac{\pi}{\pi - 2\phi} > 1, \tag{5.99}$$

and in particular $\chi_X = 0$ at $X = b$. This is consistent with (5.86), but again, not with (5.93).

Hence there is apparently no solution of the combined system (5.86) and (5.93) in which the slope of s is finite, and the only way in which the system can be solved is by supposing that $s_X \to \infty$ (thus effectively q is infinite in (5.99)), meaning $\chi_X \to 0$, and thus also $D \to 0$. This idea receives corroboration from the computed isotherm for $T = 0.615$, whose slope (thus s_X) is shown in Figure 5.9. Apparently, a near blow-up occurs at $X \approx 2.8$. In more detail, examination of D (see Figure 5.10) suggests that it approaches zero at almost the same value, which is necessary in (5.93) if the slope is to become very large.

The resolution of this conundrum is the following. It is clear that the prescription of $s_X = 0$ at $X = 0$ allows ψ and τ_3 defined in the asthenosphere by (5.36) to be zero, and also θ_X, using the definition of G in (5.89). However, use of (5.36) shows that $\psi = O(1)$ as $X \to b$, and thus a boundary layer is necessary to accommodate the boundary condition for ψ and also τ_3 and θ. We discuss this *corner layer* in the next section. For the moment, we can say that it arises because (5.78) is a singular limit of (5.25), and thus the lid equation (5.80) and hence (5.93) should be also. Thus we presume that the appropriate condition for (5.93) is a matching condition of some type.

In fact the lid equation is not uniformly valid near $X = 0$ either, although it automatically satisfies the zero slope boundary condition. This can be seen by consideration of (5.25), for example, which shows that the definition of ψ in (5.36) does not yield zero shear stress at $X = 0$ unless $s_{XXX} = 0$, due to the term $\varepsilon^2\psi_{XX}$. This term arises when the scalings from (5.76) are applied on (5.25d) and we obtain

$$\tau_3 = \eta\left[\varepsilon^2\psi_{XX} - \varepsilon\left(2s'\psi_{X\zeta} + s''\psi_\zeta\right) - (1 - s'^2)\psi_{\zeta\zeta}\right]. \tag{5.100}$$

While $\varepsilon^2\psi_{XX}$ is apparently a small term, it is not uniformly so as the viscosity becomes large as we enter the lithosphere.

Some insight can be gained by consideration of a singularly perturbed modification of (5.93), namely

$$\nu s_{XX} + \frac{s_X}{(1 + s_X^2)^2} = \beta D \exp\left(\frac{\mu s}{T_a}\right), \tag{5.101}$$

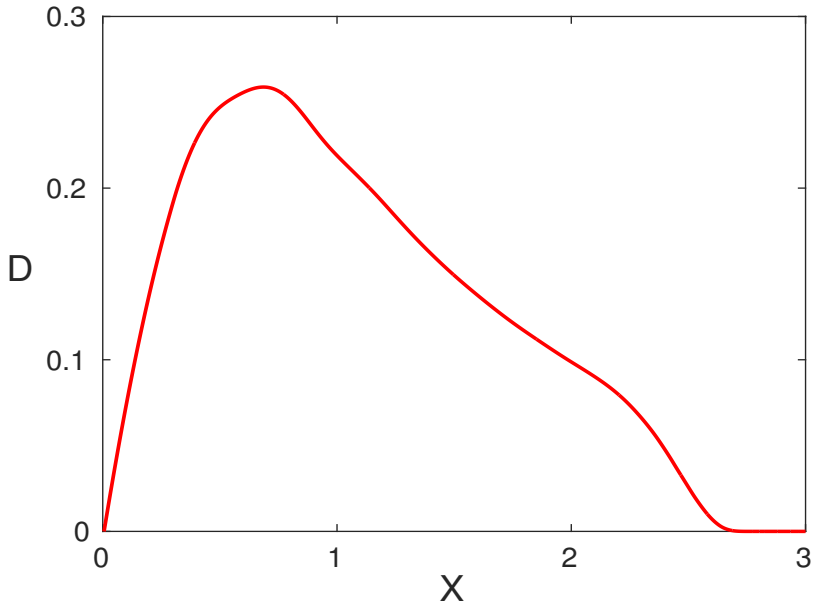

Figure 5.10: Numerical calculation of $D(X)$ from the solution of (5.94) for χ with the lid $s(X)$ determined by the full numerical isotherm $T = 0.615$.

where we suppose $\nu \ll 1$. It should be noted immediately that the leading-order approximation to (5.101) is just (5.93). However, (5.101) has the ability to mimic some features of the corner layer illustrated in Figure 5.8 and Figure 5.9.

A phase plane analysis of (5.101) in the $(w = s_X, s)$ phase plane shows that as X increases, (5.93) is approximately satisfied until $s_X = \frac{1}{\sqrt{3}} = \tan\frac{\pi}{6}$, following which s begins to increase rapidly, and if D were constant, s would blow up. On the other hand, assuming this is near $X = b$, the discussion earlier indicates that then D must reach zero. Examination of the solution for χ computed assuming s is given by the $T_a = 0.615$ isotherm from the full numerical solution shows that D does indeed approach zero as the slope starts to blow up (Figure 5.10), and the consequence of this is to bring the trajectory back below the s_X-nullcline given by (5.93), and s_X can decrease to a value near zero. This description is illustrated in Figure 5.11.

In more detail, the solution of (5.101) is described in the (w, s) phase plane, where

$$\begin{aligned} s_X &= w, \\ \nu w_X &= \beta D \exp\left(\frac{\mu s}{T_a}\right) - \frac{w}{(1+w^2)^2}; \end{aligned} \tag{5.102}$$

trajectories move rapidly to the left hand branch of the w-nullclines, illustrated for values (progressing upwards) of $D = 0.042, 0.012$ and 10^{-7}. As D increases from

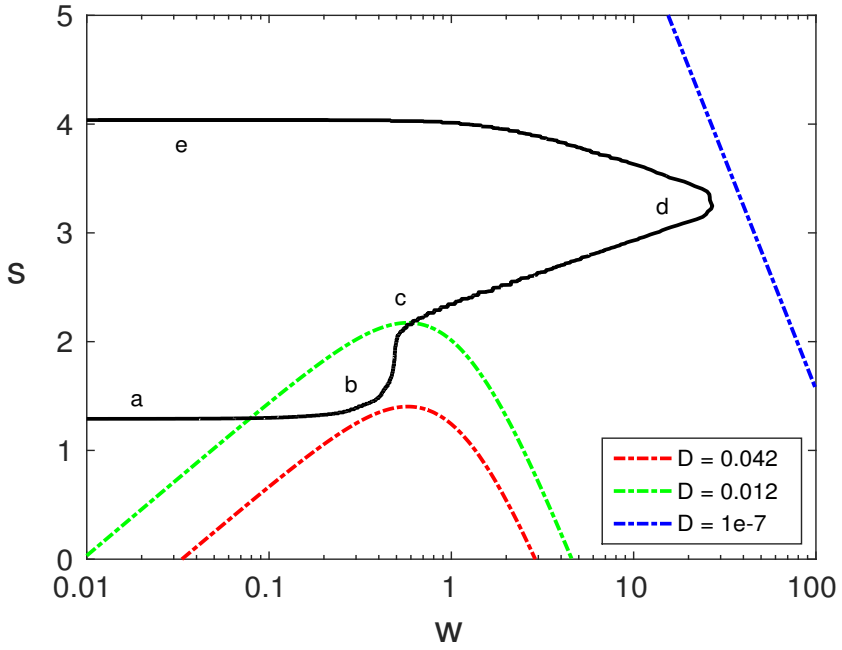

Figure 5.11: Blow-up and collapse of the slope of the T_a isotherm in the solution of (5.101). The curve $abcde$ is the isotherm $T = 0.615$ from the full numerical solution, and consists of four phases: inlet adjustment ab, $0 < X < 0.3$; quasi-static bc, $0.3 < X < 2.3$; blow-up cd, $2.3 < X < 2.8$; and collapse de, $2.8 < X < 3$. Also plotted are the (w, s) nullclines given by (5.93) for the indicated values of D.

zero at $X = 0$, the nullclines descend rapidly, and as they do, the solution resides on the left hand stable branch and moves horizontally (since $w \ll 1$) along the inlet adjustment region ab. At the point b, the value of w approaches the maximum value of $\frac{1}{\sqrt{3}} \approx 0.577$. Beyond this value, slow variation of w can only be maintained by having s increase while w remains constant, and this is enabled by having D decrease, as shown in Figure 5.10, which lifts the w-nullcline. This *quasi-static* phase bc is necessary because the cell width (here $b = 3$) is so large. Eventually, this phase can not be maintained, and a blow-up (cd) occurs, in which

$$\nu s_{XX} \approx \beta D \exp\left(\frac{\mu s}{T_a}\right), \tag{5.103}$$

and this would continue until s becomes infinite, except for the consequent rapid approach of D to zero. When D becomes sufficiently low, the nullcline overtakes the trajectory, so that it reverses direction, and w rapidly decreases towards zero; this is the collapse phase de, in which approximately (for (5.102))

$$\nu w_X \approx -\frac{w}{(1+w^2)^2}. \tag{5.104}$$

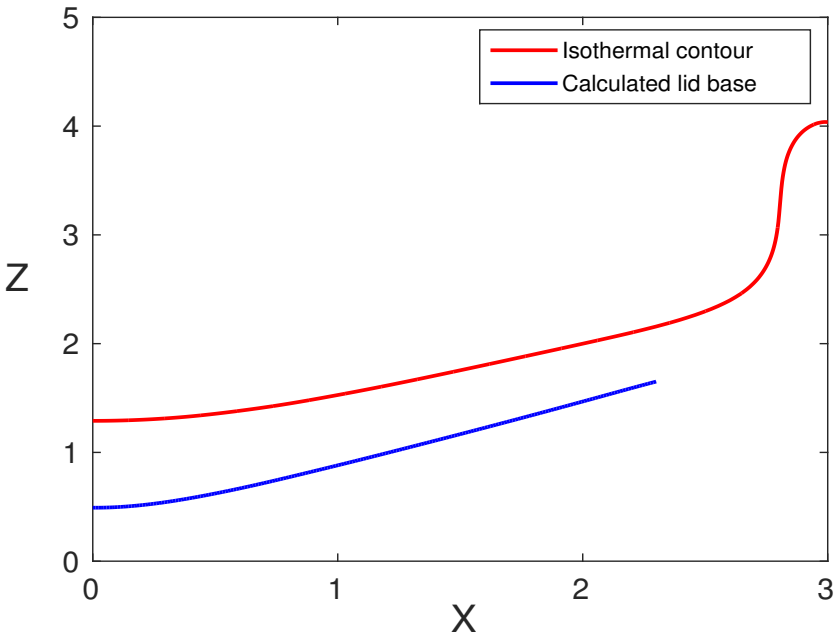

Figure 5.12: Comparison of the solution of (5.101) (blue curve) with the full numerical isotherm for $T_a = 0.615$, using the value $\nu = 0.0042 \sim \varepsilon^2$, $\beta = 0.79, \mu = 1.0$ with $s_X(0) = 0, s_X(2.3) = \frac{1}{\sqrt{3}}$; $X = 2.3$ is the value where the numerically computed slope reaches the critical value $\frac{1}{\sqrt{3}}$. The function D in (5.101) is calculated from the solution of the system (5.86) which is shown in Figure 5.10.

If we suppose that (5.101) is indeed the appropriate regularisation of (5.93), then the requirement of a boundary layer at $X = b$ implies we should require that the outer solution satisfy

$$s_X = \frac{1}{\sqrt{3}} \qquad \text{at} \qquad X = b. \tag{5.105}$$

We use this idea to close the problem. We formally choose the boundary condition for (5.93) to be (5.105), and this closes the prescription for s. In practice, the numerical solution of (5.93) is done rather differently. We actually solve a regularisation of (5.93) such as that given by (5.101) using a value of $\nu \sim \varepsilon^2$, on the basis firstly that this is a simpler strategy, secondly it may be more accurate than solving (5.93) in comparing with the full numerical solution, and thirdly we solve it as a boundary value problem, using $s_X = 0$ at $X = 0$, and also $s_X = \frac{1}{\sqrt{3}}$ at the value indicated by the full numerical solution; for $T_a = 0.615$, this is $X = 2.3$. The comparison is shown in Figure 5.12. Since it does not agree very well with the numerical solution, we try to vary the value of ν, such that in addition, $s(0)$ is the value obtained from the full

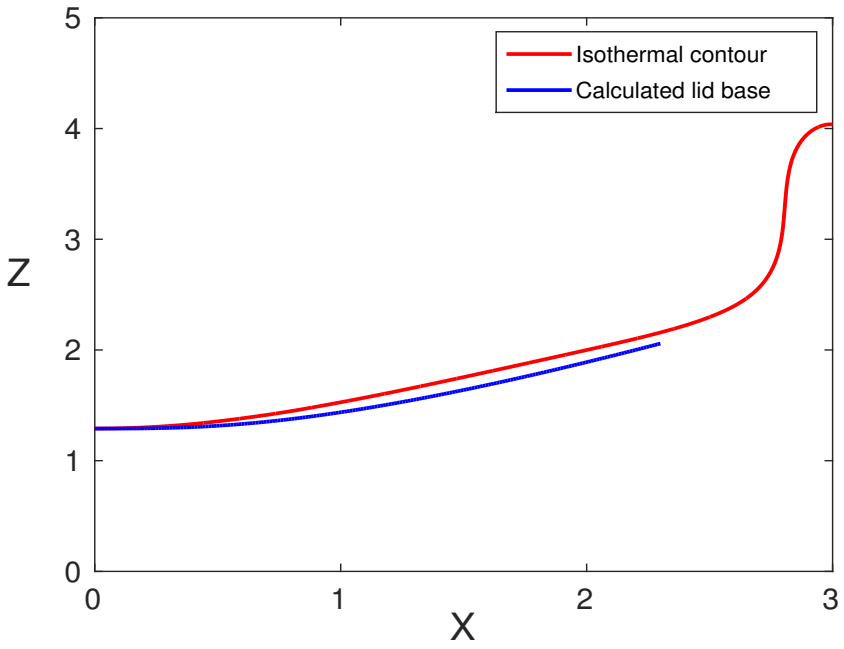

Figure 5.13: Comparison of the solution of (5.101) (blue curve) with the full numerical isotherm for $T_a = 0.615$, using the value $\nu = 3.3$, $\beta = 0.79, \mu = 1.0$ such that $s_X(0) = 0, s(0) = 1.29$ is the numerically computed value, and $s_X(2.3) = \frac{1}{\sqrt{3}}$; $X = 2.3$ is the value where the numerically computed slope reaches the critical value $\frac{1}{\sqrt{3}}$. The function D in (5.101) is calculated from the solution of the system (5.86) which is shown in Figure 5.10.

numerics. The result of this process is shown in Figure 5.13, where we observe a much improved agreement.

This now raises an additional difficulty. For $T_a = 0.615$, the value of ν we obtain is $\nu = 3.3$, which is hardly small. Indeed, comparison of Figure 5.11 with Figure 5.10 shows that the 'useful' values of D are not actually those where the transitions take place, which are $D \approx 0.2$ at b and $D \approx 0.07$ at c, instead of our indicated values 0.042 and 0.012. The resolution of this awkwardness appears to lie in the choice of regularisation of (5.93), which is of course not unique. Indeed, if instead we choose a regularisation given by

$$\nu s_{XX} + \frac{s_X}{(1+s_X^2)^2} \exp\left(-\frac{\mu s}{T_a}\right) = \beta D, \tag{5.106}$$

then the choice of ν which provides the correct value of $s(0)$ is $\nu = 0.284$, and we consider this reasonable. Figure 5.14 shows that the agreement of this procedure with the actual position of the isotherm is very good. It might be useful to mention specif-

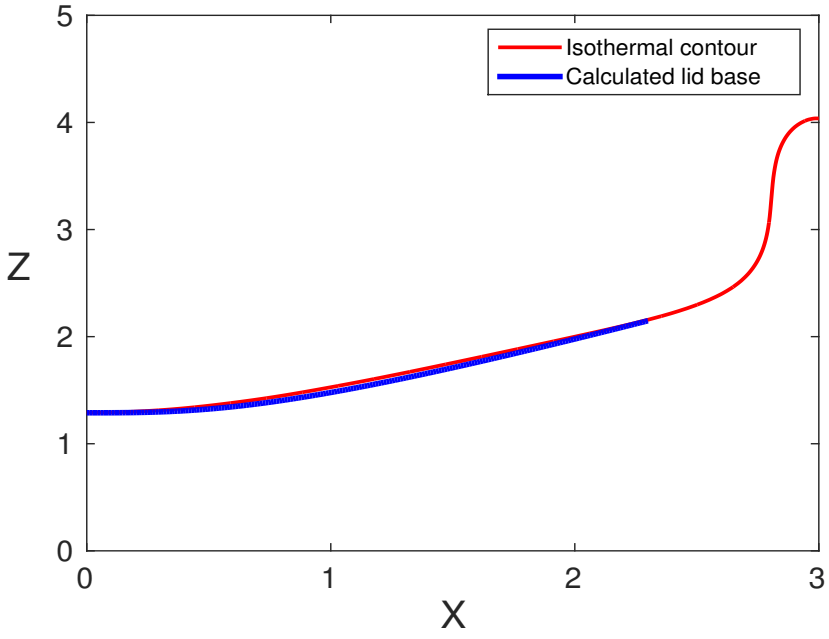

Figure 5.14: Comparison of the solution of (5.106) (blue curve) with the full numerical isotherm for $T_a = 0.615$, using the value $\nu = 0.284$ such that $s_X(0) = 0, s(0) = 1.29$ is the numerically computed value, and $s_X(2.3) = \frac{1}{\sqrt{3}}$; $X = 2.3$ is the value where the numerically computed slope reaches the critical value $\frac{1}{\sqrt{3}}$. The function D in (5.106) is calculated from the solution of the system (5.86) which is shown in Figure 5.10.

ically that in solving (5.101) and (5.106), the function D that is used is calculated from the solution of the system (5.86) which is shown in Figure 5.10.

On the other hand, while the phase plane up to the quasi-static region is well represented, (5.106) does not permit blow up. A possible compromise to accommodate both effects is the regularisation

$$\nu s_{XX} + s_X \exp\left(-\frac{\mu s}{T_a}\right) = \beta D \left(1 + s_X^2\right)^2, \tag{5.107}$$

which permits blow-up in s_X but not s. Optimisation of ν to achieve $s(0) = 1.29$ yields $\nu = 0.363$. While it is tempting to pursue even better such terms, it may be a rudderless and fruitless exercise.

5.5 Corner layer

We now return to the full asthenosphere equations (5.25) with $\gamma = 1$. The appropriate rescaling required in the corner layer to bring ψ down to zero is

$$Z = s(b) + \varepsilon\zeta, \qquad X = b - \varepsilon Y, \tag{5.108}$$

and the equations reduce to the full Stokes equations in the form

$$\begin{aligned} p_Y &= \tau_{1,Y} + \tau_{3,\zeta}, \\ p_\zeta &= \tau_{3,Y} - \tau_{1,\zeta} - \theta, \\ \tau_1 &= -2\eta\psi_{Y\zeta}, \\ \tau_3 &= \eta(\psi_{YY} - \psi_{\zeta\zeta}), \end{aligned} \tag{5.109}$$

and η is given by

$$\eta \approx \exp\left[-\frac{\theta}{T_a^2} + \frac{\mu s(b)}{T_a}\right]. \tag{5.110}$$

The scaled temperature is determined by

$$\psi_Y\theta_\zeta - \psi_\zeta\theta_Y = \varepsilon\nabla^2\theta, \tag{5.111}$$

so that $\theta \approx \theta(\psi)$, and the temperature is advected round the corner. The solution of (5.109) enables the passage of ψ and τ_3 to zero at the boundary, but the zero heat flux condition cannot be satisfied, since $\theta_Y \approx \theta'(\psi)\psi_Y \neq 0$ at $Y = 0$.

5.5.1 Corner plume

There is thus a further layer, which is a weak thermal plume, in which

$$Y = \varepsilon^{1/2}\tilde{Y}, \qquad \psi \sim \varepsilon^{1/2}v_p(\zeta)\tilde{Y}, \tag{5.112}$$

where v_p is the downwards side wall velocity determined in principle from the corner layer solution. The scaled temperature θ then satisfies the approximate equation

$$v_p\theta_\zeta - v_p'\tilde{Y}\theta_{\tilde{Y}} = \theta_{\tilde{Y}\tilde{Y}}, \tag{5.113}$$

and this enables the satisfaction of the thermal boundary condition $\theta_{\tilde{Y}} = 0$ at $\tilde{Y} = 0$.

5.6 Upper mantle core revisited

Emerging from the asthenosphere, $f \sim \zeta$, where f is the normalised stream function defined in (5.36) and again assuming $\delta = \varepsilon$, (5.48) suggests the scalings

$$\begin{aligned} \tau_1, \tau_3, p &\sim \varepsilon^4 Ra, \\ \psi &\sim \frac{1}{\varepsilon^2}, \\ T &= T_a + \varepsilon\theta, \\ \eta &\sim \eta_a. \end{aligned} \tag{5.114}$$

Hence the governing equations (5.49) reduce to those of Stokes flow with a variable viscosity, i.e.

$$\begin{aligned} p_X &= \tau_{1,X} - \tau_{3,Z}, \\ -p_Z &= \tau_{3,X} + \tau_{1,Z} + \frac{\theta}{\varepsilon^2}, \\ \tau_1 &= 2\eta\psi_{XZ}, \\ \tau_3 &= \eta(\psi_{XX} - \psi_{ZZ}), \\ \varepsilon^2\theta_t + \psi_Z\theta_X - \psi_X\theta_Z &= \varepsilon^2\nabla^2\theta, \\ \eta &= \exp\left[\frac{\mu Z}{T} + \frac{1}{\varepsilon}\left(\frac{1}{T} - \frac{1}{T_a}\right)\right] \approx \exp\left[\frac{\mu Z}{T_a} - \frac{\theta}{T_a^2}\right]. \end{aligned} \tag{5.115}$$

Following the same reasoning as explained in section 5.3.4, the streamlines having $\psi \sim O(1)$ are closed, so we can take $\theta = 0$ when $\theta \approx \varepsilon^2\theta_1(\psi)$ and the model reduces to a modified Stokes flow with $\eta = e^{\mu Z/T_a}$. However, there are some streamlines which are not closed in the upper core but invade the lower mantle core as $\psi \to 0$.

5.7 Summary

In this chapter, we have presented the asymptotic structure of the upper mantle of a narrow cell which mainly consists of the stagnant lid, the asthenosphere and the upper mantle core. The upper-most part which is attached to the surface of the Earth is the stagnant lid. Below the stagnant lid, the asthenosphere is a relatively rapid shear flow which drives an approximately isothermal circulation in the upper mantle, also called the upper core. Guided by the numerical computations and the linear stability analysis in chapter 4, we assume that the width of the convection cell scales with the sensitivity parameter for temperature ε. We also assume that the thickness of the lid is of $O(\varepsilon\gamma)$, where $\varepsilon\gamma \ll 1$. A self-consistent determination of γ is one of the harder parts of the theory. We also suppose that the upper core

has dimensions like $O(\varepsilon) \times O(\varepsilon)$ and in between the stagnant lid and the upper core, the thin shear layer, i.e. the asthenosphere, has a thickness of $O(\varepsilon\delta)$. The scaling parameters $\gamma, \delta, \varepsilon$ are related by $\gamma = \dfrac{\delta}{\varepsilon}$, where both γ and δ are unknown. For γ, two possibilities are considered, (i) $\gamma \ll 1$ and (ii) $\gamma = O(1)$. For $\gamma \ll 1$, it is required that $\delta \ll \varepsilon$ and with this assumption we attempt to compare the lid-base profiles with the isothermal contour calculated from the numerical results given in section 5.2. However, the choice of $\gamma \ll 1$ does not seem to give solutions that agree with our numerical solutions. So, we hypothesize that $\gamma = O(1)$, in particular we choose $\gamma = 1$ so that $\delta = \varepsilon$ is the appropriate choice. This closes the determination of the parameters and in particular gives the value of the asthenospheric temperature T_a in (5.77), which agrees with that derived from the full solution. With the assumption that $\gamma = 1$, we are able to estimate the lid-base profile following an extensive study, and the computed lid base matches very well with the isothermal contour calculated from the numerical simulations. Even though $\gamma \ll 1$ does not appear to be a suitable choice for our analysis, we will continue to investigate both approaches in the next chapter.

Chapter 6

Asymptotic Analysis: Lower Mantle

6.1 Introduction

In this chapter we continue to study the asymptotic structure of convection of a fluid with strongly temperature and pressure-dependent viscosity in narrower cells where the Rayleigh number Ra is very large. In chapter 5, we have discussed different regions of the upper mantle and in this chapter, we will analyse the convection structure of the lower mantle. We have observed in Figure 5.3 and Figure 5.4 that the lower mantle is quite slow moving compared to the upper mantle and there is a gradual increase of viscosity from top to bottom as well as across the mantle. For analysis, we study the lower mantle in two parts mainly: the basal thermal boundary layer and the lower mantle core. The boundary layer analysis predicts the presence of a thin thermal boundary layer at the core-mantle boundary which is identified as the basal thermal boundary layer and it is only thin relative to the total depth; it is comparable in thickness to the width of the cell. The rest of the sluggish lower mantle is labelled as the lower mantle core here. Through our analysis we estimate the temperature profiles in the lower mantle and compare them with the full numerical solution. We also wish to investigate whether there is a transition zone between the upper mantle core and the lower mantle core. In doing so, we consider both the assumptions, $\gamma \ll 1$ and $\gamma = 1$, where γ is the unknown pre-constant in the lid-base profile relation $Z = \gamma s(X)$ as mentioned in chapter 5. We also wish to see whether lower mantle analysis provides us any further information regarding the choice of γ.

6.2 Lower mantle scaling

For the lower mantle, we first rescale the upper mantle vertical coordinate Z as

$$z = 1 - \varepsilon Z. \tag{6.1}$$

Hence from the scaled upper mantle system of equations (5.49), we obtain the scaled lower mantle system

$$\begin{aligned} p_X &= \tau_{1,X} + \varepsilon\tau_{3,z}, \\ \varepsilon p_z &= \tau_{3,X} - \varepsilon\tau_{1,z} + \frac{\theta}{\delta^2}, \\ \tau_1 &= -2\eta\varepsilon\psi_{Xz}, \\ \tau_3 &= \eta\left(\psi_{XX} - \varepsilon^2\psi_{zz}\right), \\ \delta^2\theta_t + \varepsilon\left(\psi_X\theta_z - \psi_z\theta_X\right) &= \delta^2\left(\theta_{XX} + \varepsilon^2\theta_{zz}\right), \\ T &= T_a + \varepsilon\theta, \\ \eta &= \exp\left[\frac{\mu(1-z)}{\varepsilon T} + \frac{1}{\varepsilon}\left(\frac{1}{T} - \frac{1}{T_a}\right)\right]. \end{aligned} \tag{6.2}$$

The boundary conditions are

$$\begin{aligned} &\psi = \tau_3 = T_X = 0 \quad \text{on} \quad X = 0, b, \\ &\psi = \tau_3 = 0, \quad T = 1 \quad \text{on} \quad z = 0, \end{aligned} \tag{6.3}$$

where $X = b$ is the scaled width of the convection cell.
For the lower mantle, we define the viscosity function as

$$\eta = \eta_L e^{-\Theta}, \tag{6.4}$$

where η_L is the scaling for η in the lower mantle. Using some algebra on the definition of η in $(5.115)_6$, we find

$$\eta_L = \exp\left[\frac{1+\mu(1-z)}{\varepsilon T_L} - \frac{1}{\varepsilon T_a}\right], \tag{6.5}$$

$$\text{and} \qquad \Theta = \left[\frac{1+\mu(1-z)}{\varepsilon T_L} - \frac{1+\mu(1-z)}{\varepsilon T}\right]. \tag{6.6}$$

If in addition, we define the lower mantle temperature

$$T_L(z) = \frac{1+\mu(1-z)}{S_L}, \tag{6.7}$$

and

$$S_L = \frac{1}{T_a} + \varepsilon \ln \eta_L, \tag{6.8}$$

then the above relations lead us to

$$\Theta = \frac{S_L}{\varepsilon}\left(1 - \frac{T_L}{T}\right), \tag{6.9}$$

and to leading order we have

$$T \approx T_L + \frac{\varepsilon T_L \Theta}{S_L}. \tag{6.10}$$

To find the appropriate scalings, we choose a balance of terms in which thermal advection balances conduction and buoyancy balances shear stress, which itself balances shear strain rate. This leads to the lower core rescaling from (6.2) as

$$\begin{aligned} p &\sim \frac{1}{\varepsilon^2 \delta^2}, \\ \tau_1 &\sim \frac{\varepsilon}{\delta^2}, \\ \tau_3 &\sim \frac{1}{\delta^2}, \\ \psi &\sim \delta^2, \\ \eta \sim \eta_L &= \frac{1}{\delta^4}, \end{aligned} \tag{6.11}$$

which defines η_L and thus S_L, and we thus have (the rescaled)

$$\eta = e^{-\Theta}. \tag{6.12}$$

Using (6.10) and substituting the scalings (6.11) into (6.2), we obtain the scaled lower core equations

$$\begin{aligned} p_X &= \varepsilon^3 \left(\tau_{1,X} + \tau_{3,z}\right), \\ \frac{1}{\varepsilon}\left\{p_z - (T_L - T_a)\right\} &= \tau_{3,X} - \varepsilon^2 \tau_{1,z} + \frac{T_L \Theta}{S_L}, \\ \tau_1 &= -2\eta \psi_{Xz}, \\ \tau_3 &= \eta\left(\psi_{XX} - \varepsilon^2 \psi_{zz}\right), \\ \frac{T_L \Theta_t}{S_L} + \psi_X \left(1 + \frac{\varepsilon \Theta}{S_L}\right) T_L' + \frac{\varepsilon T_L}{S_L}\left(\psi_X \Theta_z - \psi_z \Theta_X\right) + \cdots & \\ = \frac{T_L \Theta_{XX}}{S_L} + \frac{\varepsilon^2}{S_L}\left(2T_L' \Theta_z + T_L \Theta_{zz}\right) + \cdots, & \\ \eta = e^{-\Theta}. & \end{aligned} \tag{6.13}$$

In case $\delta = \varepsilon$ (i.e. $\gamma = 1$), then the scalings in (6.11) are simply

$$p \sim \frac{1}{\varepsilon^4}, \qquad \tau_1 \sim \frac{1}{\varepsilon}, \qquad \tau_3 \sim \frac{1}{\varepsilon^2}, \qquad \psi \sim \varepsilon^2, \qquad \eta_L = \frac{1}{\varepsilon^4}, \tag{6.14}$$

and these scalings of (6.14) would produce the same set of equations as in (6.13).

6.3 Lower mantle core

We retain the time derivative for the moment and use prime ($'$) to denote an ordinary z derivative. At leading order, the system (6.13) becomes

$$\begin{aligned} p &= p(z), && \text{(6.15a)}\\ p' &= T_L - T_a + \varepsilon\Pi'(z), && \text{(6.15b)}\\ \tau_{3,X} &= -\frac{T_L\Theta}{S_L} + \Pi'(z), && \text{(6.15c)}\\ \tau_3 &= \psi_{XX}e^{-\Theta}, && \text{(6.15d)}\\ \frac{T_L\Theta_t}{S_L} + \psi_X T_L' &= \frac{T_L\Theta_{XX}}{S_L}, && \text{(6.15e)} \end{aligned}$$

where $\Pi(z)$ is to be determined. The equations (6.15) are subject to the boundary conditions

$$\tau_3 = \psi = \Theta_X = 0 \quad \text{on} \quad X = 0, b. \tag{6.16}$$

Solving (6.14c), we have

$$\tau_3 = -\frac{T_L}{S_L}\int_0^X \Theta\, dX + \Pi'(z)X, \tag{6.17}$$

whence

$$\Pi'(z) = \frac{T_L}{bS_L}\int_0^b \Theta\, dX. \tag{6.18}$$

If we write

$$W = \frac{\mu\psi_X}{T_L}, \tag{6.19}$$

(noting that $T_L' = -\dfrac{\mu}{S_L}$), then Θ and W satisfy the coupled system

$$\begin{aligned} \Theta_t &= \Theta_{XX} + W, && \text{(6.20a)}\\ \left[e^{-\Theta}W_X\right]_X &= -\frac{\mu}{S_L}\left(\Theta - \frac{1}{b}\int_0^b \Theta\, dX\right), && \text{(6.20b)} \end{aligned}$$

subject to

$$\Theta_X = W_X = 0 \quad \text{on} \quad X = 0, b. \tag{6.21}$$

The conditions on W_X are required by those on τ_3 in (6.16), using (6.15d). However, the conditions on ψ in (6.16) also require $\int_0^b W\, dX = 0$. It then follows from (6.20a) that is true providing $\int_0^b \Theta\, dX$ is time-independent. All the boundary conditions can be satisfied at the sides, as in effect the basal plumes occupy the entire width of the cell.

Eliminating W from (6.20), we obtain

$$\left[\left(\Theta_{XXX} - \Theta_{Xt}\right) e^{-\Theta}\right]_X = \frac{\mu}{S_L}\left(\Theta - \frac{1}{b}\int_0^b \Theta \, dX\right), \tag{6.22}$$

with the boundary conditions

$$\Theta_X = \Theta_{XXX} = 0 \quad \text{on} \quad X = 0, b. \tag{6.23}$$

(The term Θ_{Xt} in the W_X condition is automatically zero because of the Θ_X condition.)

To understand the temperature profile in the lower mantle, we need to find the solution of (6.22)-(6.23) and to solve this problem, we define

$$m(z) = \frac{1}{b}\int_0^b \Theta \, dX \tag{6.24}$$

(m is independent of t in view of the remark after (6.21)), and we write

$$\Theta = m(z) + \Phi, \quad X = by, \quad t = b^2\hat{t}, \tag{6.25}$$

so that Φ satisfies (dropping $\hat{}$)

$$\left[\left(\Phi_{yyy} - \Phi_{ty}\right) e^{-\Phi}\right]_y = \lambda\Phi, \tag{6.26}$$

where

$$\lambda = \frac{\mu b^4 e^m}{S_L}, \tag{6.27}$$

and

$$\Phi_y = \Phi_{yyy} = 0 \quad \text{on} \quad y = 0, 1; \tag{6.28}$$

λ is to be determined.

6.3.1 Steady solutions

We now consider the steady state solutions of

$$\left[\Phi_{yyy} e^{-\Phi}\right]_y = \lambda\Phi, \tag{6.29}$$

subject to the boundary conditions (6.28). This is a nonlinear eigenvalue problem: $\Phi(0) \equiv 0$ satisfies the problem (6.29), (6.28) identically, and we are seeking values of λ such that nontrivial solutions $\Phi(y)$ exist. It should be noted that

$$\int_0^1 \Phi dy = 0, \tag{6.30}$$

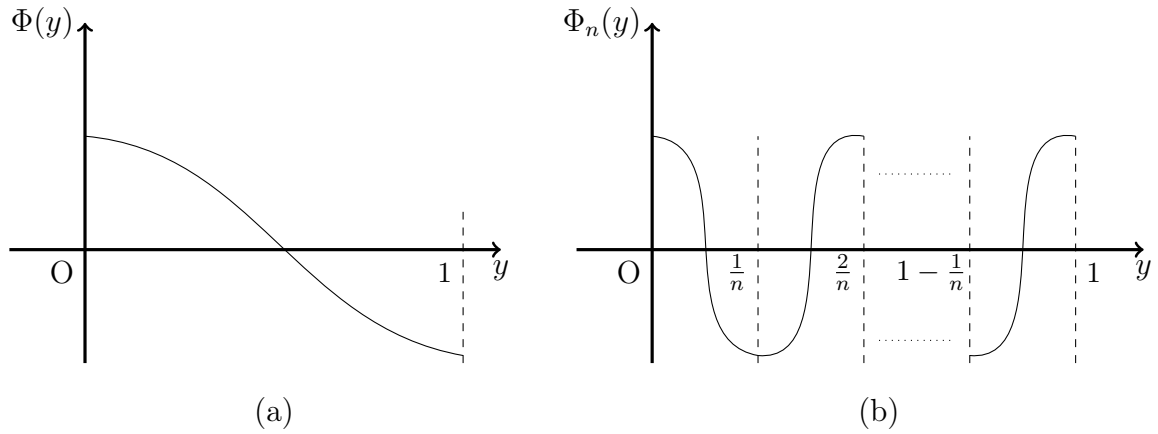

(a) (b)

Figure 6.1: (a) Anticipated behaviour of the lowest mode solution for $\Phi(y)$. (b) Higher mode obtained by scaling and reflecting solution from diagram (a).

and therefore $\Phi(y)$ must change sign for $y \in (0,1)$. Without loss of generality, we suppose that $\Phi(0) > 0$, $\Phi(1) < 0$ and $\Phi'(y) < 0$ for $y \in (0,1)$ as illustrated in Figure 6.1(a). Higher modes can then be constructed by patching together scaled and reflected copies of $\Phi(y)$, as illustrated in Figure 6.1(b). The resulting solution $\Phi_n(y)$, which changes sign n times on $(0,1)$, satisfies equation (6.29) with parameter value $\lambda_n = n^4\lambda$.

6.3.2 Bifurcation analysis

First we examine how nontrivial solutions bifurcate from the base state $\Phi = 0$ by linearizing (6.29) to obtain

$$\Phi_{yyyy} \approx \lambda\Phi. \tag{6.31}$$

The solution subject to the boundary conditions (6.28) is

$$\Phi_n(y) \approx A\cos n\pi y, \tag{6.32}$$

where A is an arbitrary constant and

$$\lambda_n \approx n^4\pi^4. \tag{6.33}$$

As noted above, we focus on the lowest mode $n = 1$, and we see that this mode bifurcates away from $\Phi = 0$ when $\lambda = \pi^4$.

To analyse the bifurcation behaviour close to this bifurcation point, we next perform a weakly nonlinear analysis, in which we allow solutions to be time-dependent.

We revert to the nonlinear equation (6.26) and expand as follows:

$$\begin{aligned}\lambda &= \pi^4 + \epsilon^2\lambda_1,\\ t &= \frac{1}{\epsilon^2}T,\\ \Phi &= \epsilon(\Phi_0 + \epsilon\Phi_1 + \epsilon^2\Phi_2 + \epsilon^3\Phi_3 + \dots),\end{aligned} \tag{6.34}$$

where $\varepsilon \ll 1$ and $\lambda_1 = \pm 1$ to allow for supercritical or subcritical bifurcation. Equation (6.26) becomes

$$\begin{aligned}&\left[\left\{\left(\Phi_0 + \epsilon\Phi_1 + \epsilon^2\Phi_2 + \dots\right)_{yyy} - \epsilon^2\left(\Phi_0 + \epsilon\Phi_1 + \epsilon^2\Phi_2 + \dots\right)_{yT}\right\}\left\{1 - \epsilon\left(\Phi_0 + \epsilon\Phi_1 + \epsilon^2\Phi_2 + \dots\right)\right.\right.\\ &\left.\left. + \frac{\epsilon^2}{2}\left(\Phi_0 + \epsilon\Phi_1 + \epsilon^2\Phi_2 + \dots\right)^2 + \dots\right\}\right]_y = \left(\pi^4 + \epsilon^2\lambda_1\right)\left(\Phi_0 + \epsilon\Phi_1 + \epsilon^2\Phi_2 + \dots\right),\end{aligned} \tag{6.35}$$

and we obtain the following sequence of problems on equating like powers of ϵ:

$$\text{At } O(\epsilon^0) \quad : \quad \Phi_{0yyyy} = \pi^4\Phi_0, \tag{6.36a}$$

$$\text{At } O(\epsilon^1) \quad : \quad \left(\Phi_{1yyy} - \Phi_0\Phi_{0yyy}\right)_y = \pi^4\Phi_1, \tag{6.36b}$$

$$\text{At } O(\epsilon^2) \quad : \quad \left(\Phi_{2yyy} - \Phi_{0yT} - \Phi_0\Phi_{1yyy} - \Phi_1\Phi_{0yyy} + \frac{\Phi_0^2}{2}\Phi_{0yyy}\right)_y = \pi^4\Phi_2 + \lambda_1\Phi_0. \tag{6.36c}$$

Solving (6.36a) subject to the boundary conditions (6.28) gives

$$\Phi_0 = A_0\cos\pi y, \tag{6.37}$$

where A_0 is a function of T. Similarly solving (6.36b) produces

$$\Phi_1 = A_1\cos\pi y + \frac{1}{15}A_0^2\cos 2\pi y, \tag{6.38}$$

where A_1 may be set to zero by absorbing the first term into Φ_0. We substitute (6.37) and (6.38) in (6.36c) and obtain

$$\Phi_{2yyyy} - \pi^4\Phi_2 = \left(\lambda_1 A_0 - \pi^2\dot{A}_0 + \frac{13}{120}A_0^3\pi^4\right)\cos\pi y + \frac{21}{40}A_0^3\pi^4\cos 3\pi y, \tag{6.39}$$

where $\dot{} = d/dT$. Given the boundary conditions $\Phi_{2y} = \Phi_{2yyy} = 0$ at $y = 0, 1$, the solvability condition requires

$$\lambda_1 A_0 - \pi^2\dot{A}_0 + \frac{13}{120}A_0^3\pi^4 = 0. \tag{6.40}$$

When $\lambda_1 = -1$, we get

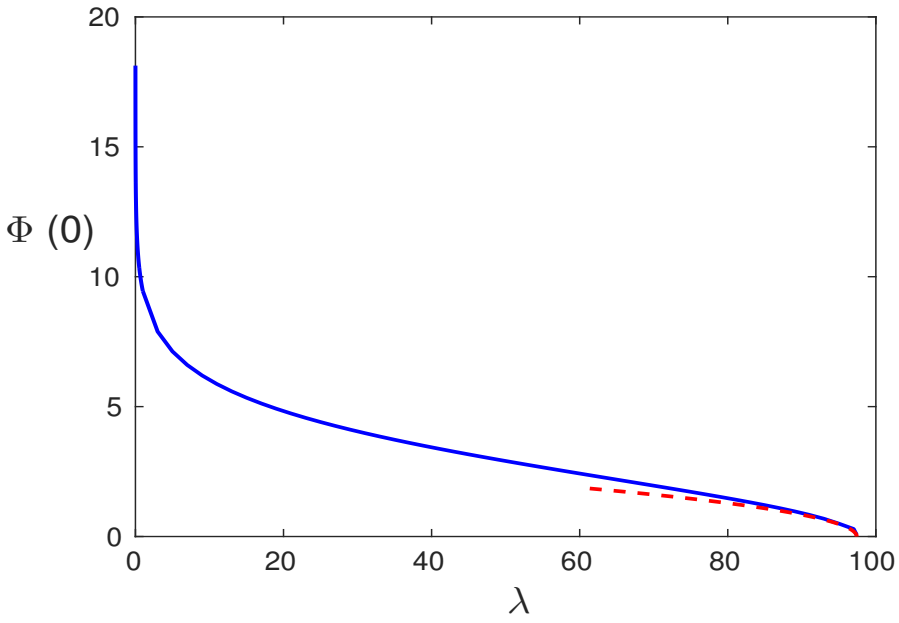

Figure 6.2: The variation of $\Phi(0)$ with λ for numerical solutions of the boundary value problem (6.29)-(6.28). The dashed curve shows the weakly nonlinear approximation (6.42) as $\lambda \to \pi^4$.

$$\frac{dA_0}{dT} = -\frac{1}{\pi^2}A_0 + \frac{13\pi^2}{120}A_0^3. \tag{6.41}$$

Thus the bifurcation is a subcritical pitchfork bifurcation with the nontrivial solution branch emerging from $\lambda = \pi^4$ in the form $\Phi \approx A\cos\pi y$ with

$$A^2 = \frac{120}{13}\left(1 - \frac{\lambda}{\pi^4}\right), \tag{6.42}$$

for $\lambda \lesssim \pi^4$. This is confirmed in Figure 6.2, where we show the computed response diagram for $\Phi(0)$ versus λ for numerical solutions of the problem (6.28)-(6.29). So, Figure 6.2 is consistent with the fact that the steady solution emerges from $\Phi = 0$ at $\lambda = \pi^4$ in a sub-critical pitchfork bifurcation, and is actually unstable, which is ascertained by the weakly nonlinear analysis numerical solution. However, we have not found such instability in our numerical calculations, which suggests that a further stabilising bifurcation may occur at smaller λ.

6.3.3 Small λ limit

We now revert back to consideration of the steady problem. It can be seen in Figure 6.2 that $\Phi(0)$ becomes large as $\lambda \to 0$, and Figure 6.3 shows a sequence of solutions

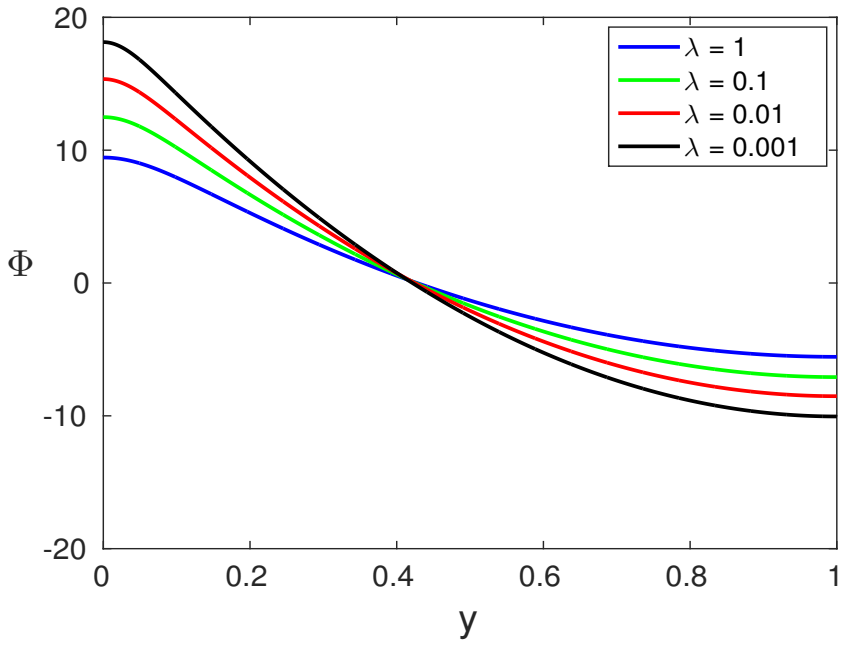

Figure 6.3: Solutions of (6.29) with (6.28) for various values of λ.

at small λ. These solutions suggest that $\Phi(0) \gg 1$ when $\lambda \ll 1$ and that there exists a boundary layer near $y = 0$ where the slope adjusts to zero. Later we shall find that the closure condition to determine λ is satisfied with this assumption.

For the outer solution where $y = O(1)$, we put

$$\Phi = \Lambda\phi, \tag{6.43}$$

where $\Lambda \gg 1$ and is approximately equal to the maximum $\Phi(0)$. The relation between Λ and λ will be identified below but we assume that $e^{-\Lambda\phi} \gg \lambda$. Then (6.28) and (6.29) imply that

$$\phi_{yyy} = 0, \tag{6.44}$$

correct to exponentially small terms in Λ. The solution satisfying the conditions

$$\phi_y = \phi_{yyy} = 0 \quad \text{on} \quad y = 1, \qquad \text{and} \qquad \int_0^1 \phi \, dy = 0, \tag{6.45}$$

is

$$\phi(y) = A\left(1 - 3y + \frac{3}{2}y^2\right), \tag{6.46}$$

where A is a constant, which may be taken to be Λ, and hence

$$\Phi \approx \Lambda(1 - 3y + \frac{3}{2}y^2). \tag{6.47}$$

This implies that when $\Phi(0) \gg 1$, $\Phi(y)$ passes through zero at $y = 1 - \dfrac{1}{\sqrt{3}} \approx 0.423$ independently of λ, in agreement with Figure 6.3.

The outer solution (6.47) does not satisfy the boundary conditions (6.28) at $y = 0$, instead giving

$$\Phi_y \sim -3\Lambda \qquad \text{as} \qquad y \to 0. \tag{6.48}$$

Hence there must be an inner region where Φ_y adjusts to zero. To examine this region, we rescale as follows:

$$\Phi = \Lambda + u \qquad \text{and} \qquad y = \frac{Y}{\Lambda}. \tag{6.49}$$

Using these in (6.29), we obtain

$$\Lambda^4 e^{-\Lambda} \left[u_{YYY} e^{-u}\right]_Y = \lambda\Lambda \left(1 + \frac{u}{\Lambda}\right) \approx \lambda\Lambda, \tag{6.50}$$

to lowest order as $\Lambda \to \infty$. Now we define the following relationship between Λ and λ:

$$\lambda = \Lambda^3 e^{-\Lambda}, \tag{6.51}$$

so that $\Lambda \sim \ln \dfrac{1}{\lambda}$, and the earlier assumption that $e^{-\Lambda\phi} \gg \lambda$ is satisfied if $\Lambda^3 e^{-\Lambda+\Lambda\Phi} \ll 1$, which is true for $y = O(1)$. Thus (6.50) reduces to

$$\left[u_{YYY} e^{-u}\right]_Y \approx 1. \tag{6.52}$$

One integration yields

$$u_{YYY} = Y e^u, \tag{6.53}$$

which is subject to the boundary condition

$$u_Y = 0 \quad \text{at} \quad Y = 0 \tag{6.54}$$

and also

$$u_Y \to -3 \qquad \text{as} \qquad Y \to \infty, \tag{6.55}$$

by matching with (6.48).

To solve (6.53)-(6.55) numerically, we solve an initial value problem

$$\tilde{u}''' = \tilde{Y} e^{\tilde{u}} \tag{6.56}$$

with

$$\tilde{u}(0) = \tilde{u}'(0) = 0, \quad \tilde{u}''(0) = -C. \tag{6.57}$$

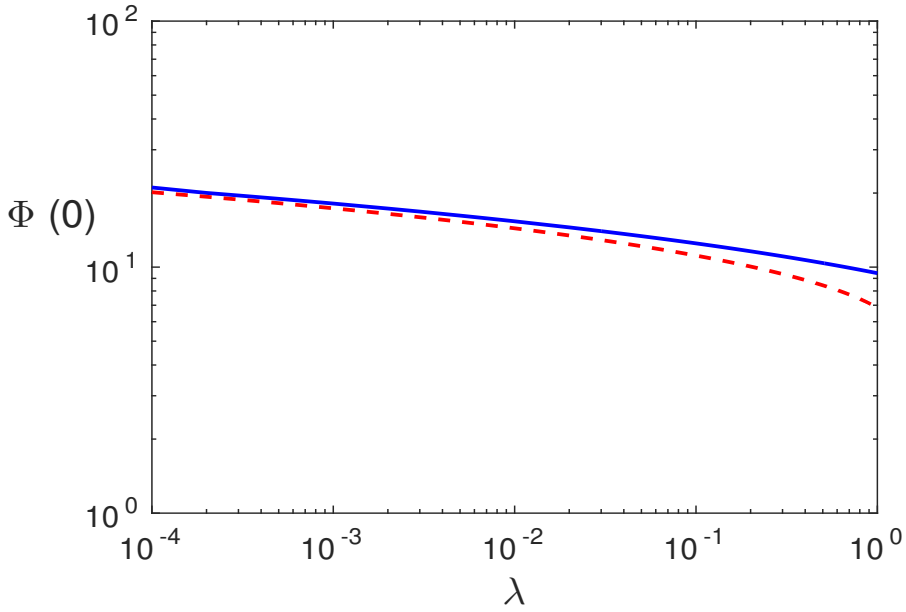

Figure 6.4: The variation of $\Phi(0)$ with small λ. The blue curve shows the results of the numerical solution of (6.29), and the dashed red curve shows the asymptotic result (6.65) using (6.51).

We choose the unique value of C such that $\tilde{u}''(\infty) = 0$ as required by the matching condition (6.55). This process results in

$$C = -\tilde{u}''(0) \approx 1.1381 \tag{6.58}$$

and we thus obtain

$$K = -\tilde{u}'(\infty) \approx 1.6877. \tag{6.59}$$

Now if we write

$$u(Y) = \alpha + \tilde{u}(\beta Y) \quad \text{with} \quad \tilde{Y} = \beta Y, \tag{6.60}$$

then

$$u'''(Y) = \beta^3 \tilde{u}'''(\tilde{Y}) = \beta^3 \tilde{Y} e^{\tilde{u}} = \beta^4 Y e^{u-\alpha}, \tag{6.61}$$

and

$$u_Y \to -\beta K \qquad \text{as} \qquad Y \to \infty. \tag{6.62}$$

To ensure that (6.61) and (6.62) agree with (6.53) and (6.55), we obtain

$$\beta = \frac{3}{K} \quad \text{and} \quad \alpha = 4 \ln \frac{3}{K}. \tag{6.63}$$

Hence, we may write (6.60) as

$$u(Y) = 4\ln\left(\frac{3}{K}\right) + \tilde{u}\left(\frac{3Y}{K}\right). \tag{6.64}$$

From (6.49), we have

$$\Phi(0) = \Lambda + u(0) \approx \Lambda + 4\ln\left(\frac{3}{K}\right) \approx \Lambda + 2.3, \tag{6.65}$$

where Λ is related to λ through (6.51). Figure 6.4 gives a comparison between numerical and asymptotic values of $\Phi(0)$ for small λ and it shows that the behaviours of $\Phi(0)$ are in good agreement when $\lambda \to 0$.

To complete the lower core solution, we need to choose the value of $m(z)$ in (6.24). Equivalently, we need to choose the value of λ in (6.27). To do this, at first we consider the case of $\gamma \ll 1$. The exact integral constraint from (5.15) and (5.53) implies that

$$\int_0^b (T\psi_X + T_Z)dX = \frac{(T_a - T_0)}{\gamma}\int_0^b \frac{dX}{s} = \varepsilon b(1 - T_0)Nu. \tag{6.66}$$

Using (6.10), we can write

$$\int_0^b (T\psi_X + T_Z)dX \approx \varepsilon\int_0^b \left(\frac{T_L}{S_L}\Theta\psi_X - T_L'\right)dX = \frac{(T_a - T_0)}{\gamma}\int_0^b \frac{dX}{s}. \tag{6.67}$$

We substitute for ψ_X from (6.19), (6.20a) and (6.25), and integrate by parts, to get

$$\frac{T_L^2}{\mu S_L}\int_0^b \Phi_X^2 dX = \frac{T_a - T_0}{\delta}\int_0^b \frac{dX}{s} - \frac{\mu b}{S_L} \tag{6.68}$$

To calculate the integral, let us anticipate that $\lambda \ll 1$. From (6.47), it follows that

$$\int_0^b \Phi_X^2 dX \approx \frac{3\Lambda^2}{b}, \tag{6.69}$$

and thus m is in principle determined in terms of the lid thickness s by requiring

$$\frac{3\Lambda^2 T_L^2}{b\mu S_L} = \frac{T_a - T_0}{\delta}\int_0^b \frac{dX}{s} - \frac{\mu b}{S_L}. \tag{6.70}$$

We see from (6.70) that $\Lambda \sim \dfrac{1}{\sqrt{\delta}}$, which is consistent with the assumption $\lambda \ll 1$. More generally, if $\delta s \ll 1$, then (6.70) implies that $\Lambda \gg 1$ and hence $\lambda \ll 1$.

Next we consider the case $\gamma = 1$, i.e. $\delta = \varepsilon$. This time the exact integral constraint from (5.15) and (5.81) gives

$$\int_0^b (T\psi_X + T_Z)dX \approx \varepsilon\int_0^b \left(\frac{T_L}{S_L}\Theta\psi_X - T_L'\right)dX = (T_a - T_0)\int_0^b (1 + s_X^2)G(X)dX, \tag{6.71}$$

and this reduces to

$$\frac{T_L^2}{\mu S_L}\int_0^b \Phi_X^2 dX = \frac{T_a - T_0}{\varepsilon}\int_0^b (1+s_X^2)G(X)dX - \frac{\mu b}{S_L}. \tag{6.72}$$

The same reasoning leads to (6.69) and thus m is chosen in terms of the lid thickness s by requiring

$$\frac{3\Lambda^2 T_L^2}{b\mu S_L} = \frac{T_a - T_0}{\varepsilon}\int_0^b (1+s_X^2)G(X)dX - \frac{\mu b}{S_L}, \tag{6.73}$$

assuming $\lambda \ll 1$. We see from (6.73) that $\Lambda \sim \dfrac{1}{\sqrt{\varepsilon}}$, so that the assumption $\lambda \ll 1$ is again justified a posteriori.

We can compare these asymptotic temperature profiles with those computed from the full numerical simulation. In order to do this we need to estimate $m(z)$. In principle we can use (6.73), but this is somewhat circuitous, and it is more direct to use the full numerical solution in the lower mantle directly.

6.3.4 Lower mantle temperature profile

In this section, we estimate the lower mantle temperature profile and see how they match with the numerical solution. From (6.10), (6.7) and (6.25), we have

$$T = \frac{1+\mu(1-z)}{S_L}\left[1 + \frac{\varepsilon(m(z)+\Phi(y,\lambda))}{S_L}\right], \tag{6.74}$$

where $m(z)$, λ and S_L are related by (6.27). To calculate T, we need to assess useful values of both $m(z)$ and S_L.

From (6.7), (6.8) and (5.22), we have

$$S_L = 1 + \mu + \varepsilon \ln(\varepsilon^4 Ra). \tag{6.75}$$

For $\varepsilon = 0.065, \mu = 1$ and $Ra = 10^7$, (6.75) gives $S_L = 2.337$. But we still need to calculate $m(z)$ and for this, we use our numerical solutions of T at different depths.

From (6.25) and (6.10), we can write

$$m(z) + \Phi(y,\lambda) = \frac{S_L}{\varepsilon}\left(1 - \frac{T_L}{T}\right). \tag{6.76}$$

This should be true for all $y \in [0,1]$, but for comparison with our numerical results it is helpful to focus on the values at the two walls $y = 0, 1$, i.e.

$$m(z) + \Phi(0,\lambda) = \frac{S_L}{\varepsilon}\left(1 - \frac{T_L}{T_-}\right), \tag{6.77}$$

$$m(z) + \Phi(1,\lambda) = \frac{S_L}{\varepsilon}\left(1 - \frac{T_L}{T_+}\right), \tag{6.78}$$

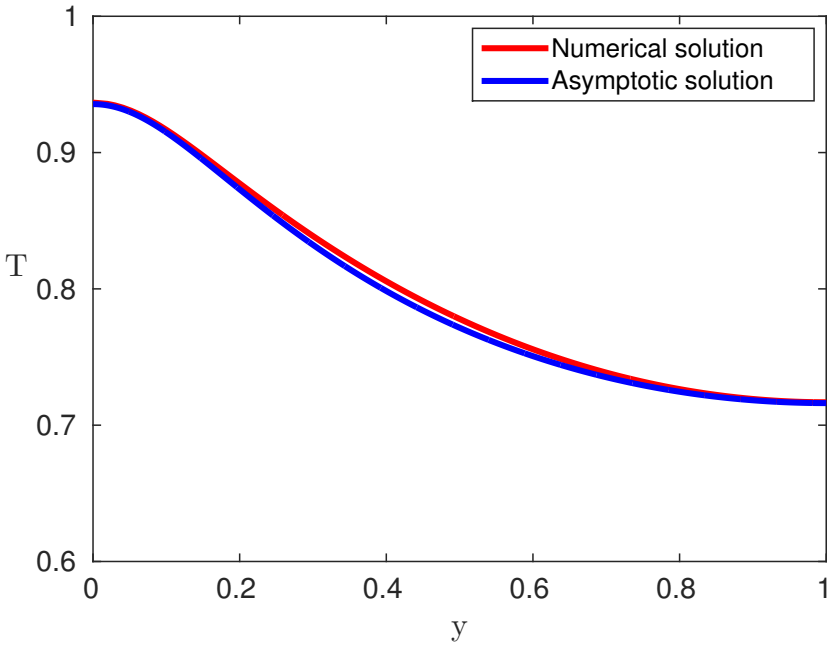

Figure 6.5: Comparison of full numerical and asymptotic solutions for lower mantle temperature T as a function of y at $z = 0.1$. The numerical solution is taken from the convection cell with $\varepsilon = 0.065, \mu = 1.0, Ra = 10^7$ and $a = 3\varepsilon$ shown in Figure 5.2.

where T_-, T_+ are the dimensionless temperatures at $y = 0$ and $y = 1$ respectively. Eliminating $m(z)$ from the above relations and using the definition of $T_L(z)$ from (6.7), we find that

$$\Phi(0,\lambda) - \Phi(1,\lambda) = \frac{1+\mu(1-z)}{\varepsilon}\left(\frac{1}{T_+} - \frac{1}{T_-}\right). \tag{6.79}$$

We calculate the right hand side of (6.79) and denote it by p (note p here does not denote the pressure):

$$p = \frac{1+\mu(1-z)}{\varepsilon}\left(\frac{1}{T_+} - \frac{1}{T_-}\right), \tag{6.80}$$

and the solutions of Φ for a range of λ values from (6.29) help us to calculate

$$q = \Phi(0,\lambda) - \Phi(1,\lambda). \tag{6.81}$$

Finally, we choose the value of λ such that $|p - q| < 0.001$ at a fixed z. With this specific value of λ and S_L from (6.75), we evaluate $m(z)$ using (6.27) as

$$m(z) = \ln \frac{\lambda S_L}{\mu b^4}. \tag{6.82}$$

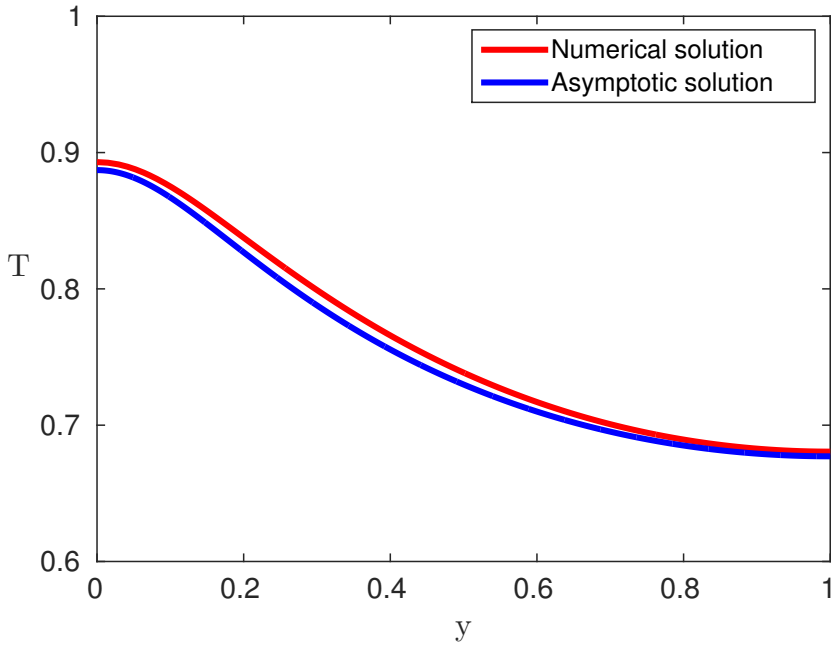

Figure 6.6: Comparison of full numerical and asymptotic solutions for lower mantle temperature T as a function of y at $z = 0.2$. The numerical solution is taken from the convection cell with $\varepsilon = 0.065, \mu = 1.0, Ra = 10^7$ and $a = 3\varepsilon$ shown in Figure 5.2.

From (6.10), we have

$$T = \frac{T_L}{1 - \dfrac{\varepsilon\Theta}{S_L}}, \tag{6.83}$$

which can be written as

$$T = \frac{1 + \mu(1 - z)}{S_L - \varepsilon(m + \Phi)}. \tag{6.84}$$

We plot the temperature T profiles obtained from our numerics for the particular case with $\varepsilon = 0.065, \mu = 1.0, Ra = 10^7$ and $a = 3\varepsilon$, and the recomputed temperature T profiles from (6.84) at different depths using appropriate scalings in Figures 6.5-6.6. The figures establish the fact that our numerical solution is consistent with the asymptotic analysis.

Comment on the absence of plumes

The lower core scaling is based on the apparent computational observation that there is no identifiable plume in the lower core. In retrospect, we have found that in fact there is a mild plume of thickness $O(\varepsilon^{1/2})$, which comes from (6.73) and (6.49) assuming $\lambda \ll 1$. This is also manifested in Figure 5.3, for example, by the mild

clustering of streamlines at the left hand side. However, it is convenient to have proceeded as we have done, since our analysis includes this possibility, and the plume is rather weak ($\varepsilon^{1/2} \approx 0.25$ for $\varepsilon = 0.065$). Note, however, that a consequence of (6.73), (6.43) and (6.19) below is that strictly speaking $\psi \sim \varepsilon^{3/2}$, rather than the choice in (6.14), and other scales are affected similarly. There is no consequent effect on our analysis, however. Thus from our analysis, we get a boundary layer which is the plume for small λ and since $\lambda \propto \mu$ (from (6.27)), it also appears as $\mu \to 0$, which shows that plumes actually have a strong connection with temperature dependent viscosity.

6.4 Basal thermal boundary layer

The solutions of the lower mantle core equations (6.13) satisfy all the boundary conditions at the sides, but they do not satisfy the basal boundary conditions, which are of the form (in terms of lower mantle scaled variables)

$$\begin{aligned} \tau_3 = \psi = 0, \\ \Theta = \Theta_b \equiv \ln\left(\varepsilon^4 Ra\right), \quad \text{at} \quad z = 0, \end{aligned} \tag{6.85}$$

where we have used (5.28) to determine T_a in (5.22), and used (6.11) to define S_L in (6.8). The lower mantle equations are given by (6.13) and the basal thermal boundary layer equations are obtained by writing

$$\begin{aligned} z &= \varepsilon Z, \\ \tau_1 &\sim \frac{1}{\varepsilon}, \\ p &= \int_0^z (T_L - T_a) dz + \varepsilon^2 P, \end{aligned} \tag{6.86}$$

which yields the rescaled equations, to leading order,

$$\begin{aligned} P_X &= \tau_{1,X} + \tau_{3,Z}, \\ P_Z &= \tau_{3,X} - \tau_{1,Z} + \frac{T_L \Theta}{S_L}, \\ \tau_1 &= -2\eta\psi_{XZ}, \\ \tau_3 &= \eta\left(\psi_{XX} - \psi_{ZZ}\right), \\ -\mu\psi_X + T_L\left(\psi_X\Theta_Z - \psi_Z\Theta_X\right) &= T_L\nabla^2\Theta, \\ \eta &= e^{-\Theta}, \end{aligned} \tag{6.87}$$

wherein we can take

$$T_L \approx T_L(0) = \frac{1+\mu}{S_L}. \tag{6.88}$$

Again, we have the full Stokes equations. The solutions must satisfy the basal boundary conditions (6.85), the side wall boundary conditions (6.16), and the matching conditions as $Z \to \infty$ in which Θ, τ_3 and ψ tend to the limits given by (6.17) and the steady state form of (6.22).

There seems to be some mild scope for further approximation, since the basal value of Θ in (6.85) is 'large' if $Ra \gg \varepsilon^{-4}$. In practice, there is little to be gained, since apparently computation of the basal boundary layer is not necessary for the determination of the rest of the solution, and in any case Θ_b is not typically that large. For our typical values of $\varepsilon = 0.065$ and $Ra = 10^7$, we have $\Theta_b \approx 5.2$, although the consequent basal viscosity is thus ~ 0.005 relative to the lower core, as can be seen in Figure 5.4.

Using the values of S_L and T_L from (6.75), (6.88) with $\Theta_b = 5.2$, $\varepsilon = 0.065$, (6.10) gives the basal temperature $T = 0.979 \approx 1$ which is consistent with our boundary condition at the basal boundary.

Next we perform integration of the energy equation $(6.87)_5$ over the flow domain to yield the Nusselt number relation. The integration gives

$$\int_0^\infty \int_0^b \left\{-\mu\psi_X + T_L\left(\psi_X\Theta_Z - \psi_Z\Theta_X\right)\right\}\, dX\, dZ = \int_0^\infty \int_0^b T_L\left(\Theta_{XX} + \Theta_{ZZ}\right)\, dX\, dZ. \tag{6.89}$$

Using integration by parts together with the boundary conditions $\psi = 0, \Theta_X = 0$ on $X = 0, b$, we obtain

$$-T_L \int_0^b \left[\psi\Theta_X\right]_{Z=0}^\infty dX = T_L \int_0^b \left[\Theta_Z\right]_{Z=0}^\infty dX. \tag{6.90}$$

Again, we know that $\psi = 0$ on $Z = 0$ and as $Z \to \infty$, $\Theta \sim \Theta(X)$ so that we have $\Theta_Z = 0$ at infinity. Incorporating these values, we obtain

$$-T_L \int_0^b \left[\psi\Theta_X\right]_{Z\to\infty} dX = -T_L \int_0^b \Theta_Z\Big|_{Z=0} dX. \tag{6.91}$$

As $Z \to \infty$, we can use the lower mantle relation $\psi = -\dfrac{T_L\Theta_X}{\mu}$ from (6.15e) and this yields

$$\frac{T_L^2}{\mu} \int_0^b \Theta_X^2\Big|_{Z\to\infty} dX = -T_L \int_0^b \Theta_Z\Big|_{Z=0} dX. \tag{6.92}$$

As $Z \to \infty$, Θ must match with the lower core solution and hence we can write

$$-\int_0^b \Theta_Z\Big|_{Z=0} dX = \frac{T_L}{\mu b} \int_0^1 \Phi_y^2\, dy, \tag{6.93}$$

where Φ is the solution of (6.28), (6.29). This is the Nusselt number relation between the lower core temperature profile and the heat flux through the base. Even though we have not solved the system (6.87) directly, we investigated the viscosity and temperature jump at the basal boundary.

6.5 Transition zone

It is clear that a transition zone between the upper and the lower core is necessary, since the variables, and specifically the temperature, do not directly match. The upper core approximations become invalid because the viscosity increases exponentially with depth, the stream function in the upper core tends exponentially to zero, but the approximations involved in the upper core, specifically the loss of the conduction term, become invalid when $\psi \sim \delta^2$ considering the case when $\gamma \ll 1$, i.e. $\delta \ll \varepsilon$, and this heralds the occurrence of a transition zone. Just as in the lower core, this occurs when $\eta \sim \eta_L = \dfrac{1}{\delta^4}$, but since $\eta = \exp\left(\dfrac{\mu Z}{T_a}\right)$ in the upper mantle, this tells us that the transition region is accessed by rescaling Z as

$$Z = Z_L + Y, \qquad Z_L = \frac{T_a}{\mu} \ln\left(\frac{1}{\delta^4}\right), \tag{6.94}$$

and the other variables are rescaled as

$$\begin{aligned} p, \tau_1, \tau_3 &\sim \frac{1}{\delta^2}, \\ \psi &\sim \delta^2, \\ \eta &\sim \frac{1}{\delta^4}. \end{aligned} \tag{6.95}$$

Using these scalings in the system of upper mantle equations (5.49), we find

$$\begin{aligned} p_X &= \tau_{1,X} - \tau_{3,Y}, \\ -p_Y &= \tau_{3,X} + \tau_{1,Y} + \theta, \\ \tau_1 &= 2\eta\psi_{XY}, \\ \tau_3 &= \eta(\psi_{XX} - \psi_{YY}), \\ \psi_Y\theta_X - \psi_X\theta_Y &= \nabla^2\theta, \\ \eta &= e^{-\Theta}, \end{aligned} \tag{6.96}$$

and the relation of θ and Θ follows from the combination

$$T = T_a + \varepsilon\theta, \tag{6.97}$$

$$\ln\eta_L - \Theta = \frac{\mu(Z_L + Y)}{T} + \frac{1}{\varepsilon}\left(\frac{1}{T} - \frac{1}{T_a}\right), \tag{6.98}$$

which leads to the approximate relation

$$\theta \approx \mu T_a Y + T_a^2 \Theta. \tag{6.99}$$

The equations (6.96) are the full Stokes equations, together with the full temperature equation. The boundary conditions at the sides are as before in (6.16), the matching conditions as $Y \to \infty$ follow from (6.17) and the solutions of (6.20), and the matching conditions as $Y \to -\infty$ are discussed in the next section.

However, if $\delta = \varepsilon$, then the transition region should be accessed by rescaling Z as

$$Z = Z_L + Y, \qquad Z_L = \frac{T_a}{\mu} \ln\left(\frac{1}{\varepsilon^4}\right), \tag{6.100}$$

and the other variables are rescaled as

$$\begin{aligned} p, \tau_1, \tau_3 &\sim \frac{1}{\varepsilon^2}, \\ \psi &\sim \varepsilon^2, \\ \eta &\sim \frac{1}{\varepsilon^4}. \end{aligned} \tag{6.101}$$

It should be noted that for the computations in Figure 5.2, 5.3 and 5.4, $Z_L = 6.72$, corresponding to $z = 0.56$. Substituting these new scales into (5.115), we obtain the same system as in (6.96) and the relation of θ and Θ is again given approximately by (6.99).

Of principal interest is the transition in the temperature, where apparent matching conditions should be

$$\begin{aligned} \theta &\to 0 \quad \text{as} \quad Y \to -\infty, \\ \theta &\sim \mu T_a Y + T_a^2 \Theta_1(X) \quad \text{as} \quad Y \to \infty, \end{aligned} \tag{6.102}$$

where $\Theta_1(X)$ is the value of Θ in the lower core when $z \to 1$. Using the relation (6.15e), we have $\psi = -\dfrac{T_a}{\mu}\Theta_{1X}$, since $S_L \approx \dfrac{1}{T_a}$ as $z \to 1$. This leads to $\psi \approx -\dfrac{1}{\mu T_a}\theta_X$ in the lower core (and is independent of Y as $z \to 1$). If we use this for the vertical advection term, then the equation for θ in $(6.96)_5$ is simply

$$\left[1 - \frac{\theta_Y}{\mu T_a}\right] \theta_{XX} + \theta_{YY} = 0, \tag{6.103}$$

together with the matching conditions in (6.102), and $\theta_X = 0$ at $X = 0, b$ and a solution of this seems feasible.

6.5.1 Upper core far field behaviour

In this section, we will follow a different approach to get some idea about transition zone when $\gamma \ll 1$, i.e. $\delta \ll \varepsilon$. In the absence of an upper plume, the boundary conditions for (5.50) are

$$\psi \to 0, \quad \psi_Z \to u_a \quad \text{at} \quad Z = \gamma s(X), \tag{6.104}$$

where u_a is the asthenospheric velocity determined from the asthenosphere equations (5.62), the side wall conditions

$$\tau_3 = \psi = 0, \quad \text{at} \quad X = 0, b, \tag{6.105}$$

and the stagnation condition

$$\psi \to 0 \quad \text{as} \quad Z \to \infty. \tag{6.106}$$

Of interest is the asymptotic behaviour of ψ, as this may provide the matching condition for the transition flow. Simplification of (5.50) leads to

$$\eta \nabla^4 \psi + 2\eta_Z \nabla^2 \psi_Z + \eta_{ZZ}(\psi_{ZZ} - \psi_{XX}) = 0, \tag{6.107}$$

and the use of the definition of $\eta = \exp\left(\dfrac{\mu Z}{T_a}\right)$ yields the linear differential equation for ψ

$$\nabla^4 \psi + \frac{2\mu}{T_a}\nabla^2 \psi_Z + \left(\frac{\mu}{T_a}\right)^2 (\psi_{ZZ} - \psi_{XX}) = 0. \tag{6.108}$$

Now we introduce two new variables ξ and χ such that

$$\xi = \frac{\mu X}{T_a} \quad \text{and} \quad \chi = \frac{\mu Z}{T_a} \tag{6.109}$$

so that (6.108) becomes

$$\nabla^4 \psi + 2\nabla^2 \psi_\chi + (\psi_{\chi\chi} - \psi_{\xi\xi}) = 0, \tag{6.110}$$

with boundary conditions

$$\psi = \psi_{\xi\xi} = 0 \quad \text{on} \quad \xi = 0, \frac{\mu b}{T_a}, \tag{6.111}$$

$$\psi = 0, \ \psi_\chi = \frac{u_a T_a}{\mu} \quad \text{on} \quad \chi = \frac{\mu \gamma s(X)}{T_a} \quad \text{and} \quad \psi \to 0 \quad \text{as} \quad \chi \to \infty. \tag{6.112}$$

Equation (6.110) suggests solutions of the form

$$\psi = g(\xi)\exp(-\alpha\chi) \tag{6.113}$$

with

$$g = g'' = 0 \quad \text{on} \quad \xi = 0, \frac{\mu b}{T_a}. \tag{6.114}$$

Substituting (6.113) into (6.110) gives

$$g^{iv} + (2\alpha^2 - 2\alpha - 1)g'' + (\alpha^4 - 2\alpha^3 + \alpha^2)g = 0. \tag{6.115}$$

To satisfy the boundary conditions (6.114), let us choose the function $g(\xi)$ as

$$g(\xi) = \sin \lambda\xi \tag{6.116}$$

so that we can actually write ψ as a Fourier series with

$$\lambda = \frac{n\pi T_a}{\mu b}. \tag{6.117}$$

Putting (6.116) in (6.115), we find

$$\lambda^2 = \alpha^2 - \alpha - \frac{1}{2} \pm \left(\frac{1}{4} + \alpha - \alpha^2\right)^{1/2}. \tag{6.118}$$

Some algebraic calculation then leads us to

$$\alpha = \frac{1}{2} \pm \left(\lambda^2 \pm i\lambda + \frac{1}{4}\right)^{1/2}. \tag{6.119}$$

Defining

$$\left(\lambda^2 + i\lambda + \frac{1}{4}\right)^{1/2} = p + iq, \tag{6.120}$$

we get

$$\alpha = \frac{1}{2} \pm (p \pm iq), \tag{6.121}$$

so that

$$\text{Re } \alpha = \frac{1}{2} \pm p \tag{6.122}$$

and p is the unique real positive root of

$$p^2 - \frac{\lambda^2}{4p^2} = \lambda^2 + \frac{1}{4}. \tag{6.123}$$

This shows us that

$$p^2 = \frac{1}{8}\left[4\lambda^2 + 1 + \left\{\left(4\lambda^2 + 1\right)^2 + 16\lambda^2\right\}^{1/2}\right], \tag{6.124}$$

and

$$p^2 > \lambda^2 + \frac{1}{4} > \frac{1}{4}, \tag{6.125}$$

i.e.

$$p > \frac{1}{2}. \tag{6.126}$$

As we require $\psi \to 0$ as $Z \to \infty$, from (6.113) it follows that we must select only the roots with Re α positive, i.e.

$$\alpha = \frac{1}{2} + p \pm iq, \tag{6.127}$$

and

$$\text{Re } \alpha > 1. \tag{6.128}$$

In general, n is any integer in (6.117), but the asymptotic behaviour is determined by the most slowly decaying mode, and since p increases with λ, we select $n = 1$. Finally, solving for p using (6.123), we have the value for Re $\alpha = \alpha_R$,

$$\alpha_R = \frac{1}{2} + \left[\frac{1}{8}\left\{4\lambda^2 + 1 + \left(16\lambda^4 + 24\lambda^2 + 1\right)^{1/2}\right\}\right]^{1/2}, \tag{6.129}$$

$$\lambda = \frac{\pi T_a}{\mu b}. \tag{6.130}$$

The asymptotic far field behaviour of the upper core stream function is thus

$$\psi \sim \exp\left(-\frac{\alpha_R \mu Z}{T_a}\right), \tag{6.131}$$

and at the transition zone this implies

$$\psi \sim \exp\left(-\frac{\alpha_R \mu Z_L}{T_a}\right) \sim \left(\delta^4\right)^{\alpha_R} \ll \delta^4. \tag{6.132}$$

However, we see from (6.95) that $\psi \sim \delta^2$ in the transition zone, and so the leading order upper core value of ψ does not provide a matching condition to the transition zone. Thus the appropriate matching condition for the transition zone might be $\psi \to 0$ as $Y \to -\infty$. We may also recall from section 5.3.4 that we have neglected some streamlines which invade the lower mantle core and hence this mismatch might be an outcome of that. In any case, it seems this approach has not provided us anything conclusive for the case $\delta \ll \varepsilon$.

6.6 Discussion

The mid-cell vertical temperature profile from the full numerical solution is shown in Figure 6.7, and it can be compared to figure 2 of Fowler (1983), for example. The main difference between the solution structure suggested there and that found here is that slightly larger variations in viscosity are admitted in the asymptotic

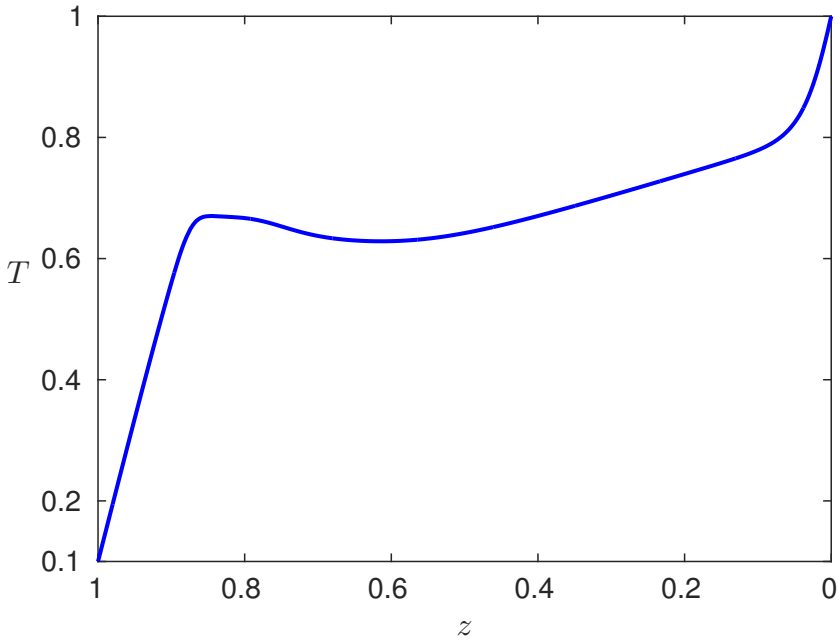

Figure 6.7: The mid-cell temperature at $X = \frac{1}{2}b$ as a function of z. This is taken from the full numerical solution with $b = 3, \varepsilon = 0.065, Ra = 10^7, \mu = 1$ and $T_0 = 0.1$. Note that the profile is drawn from the surface towards the base to compare with some previous results of Fowler (1983).

solution. For example, the jump ΔT of temperature in the basal boundary layer of Figure 6.7 corresponds to a dimensional jump of about 600 K, while Fowler's (1983) order of magnitude suggestion was $\Delta T \sim \varepsilon$, corresponding to a dimensional jump $\sim \varepsilon T_b \sim 200$ K for the values we use here; associated with the 600 K jump is a viscosity decrease (see Figure 5.4) of some two to three orders of magnitude. The actual value is larger than the earlier estimate because of the basal thermal boundary condition in (6.85) involving $\ln(\varepsilon^4 Ra)$. Interestingly, this relatively large jump is similar to that found by Loper (1985), whose work remarkably described mantle convection as a finger-like flow (in the sense of being essentially a vertical exchange flow). Loper also asserted the tendency of the medium to become isoviscous. It seems unlikely that such a large temperature jump could be supported unless the cells are narrow. To put it the other way round, one expects such a high temperature jump to be very unstable, and thus to cause the width of convective boundary layers to be narrow.

Our analysis shows that the convective structure consists of a stagnant lid, and a relatively fast shearing return flow in the upper mantle beneath the lid, whose velocities for the parameters in Figure 5.3 are of order 3 mm y^{-1}; obviously less than plate

tectonic velocities on the Earth, but we are not describing the oceanic subduction driven plate motion. In the lower mantle there is an essentially vertical return flow with downwards velocities of order $0.8\,\mathrm{mm\,y^{-1}}$, and upwards ('plume') velocities of the order of $4\,\mathrm{mm\,y^{-1}}$, which accelerate in the upper mantle (see Figure 5.3). The relative sluggishness of the lower mantle apparent in Figure 5.3 is a consequence of the tallness of the convective cells.

In the stagnant lid, the viscosity is enormous, but below this, there is a pronounced structure. The lowest viscosity is in the upper mantle (down to a dimensional depth of about 900 km), where it is about two orders of magnitude lower than the basal viscosity, and then it is higher in the lower mantle, ranging horizontally from the basal viscosity to a value about four orders of magnitude higher. Supposing as we expect that it is the lower viscosity material which controls short term post-glacial rebound, for example, these results are consistent with inferred estimates of mantle viscosity.

The temperature shown in Figure 5.2 or Figure 6.7, for example, is distinctly non-isothermal below the rigid conductive lid. There is a relatively small isothermal upper core down (in Figure 6.7) to about $z = 0.8$, and below this a transition zone in which the temperature drops, before reaching a profile in the lower mantle which increases linearly with depth; however, the slope in Figure 6.7 is 0.35, whereas an isoviscous gradient would be a touch under 0.5. The difference is not large, but enough to cause several orders of magnitude change in viscosity.

6.7 Summary

In this chapter, we have studied analytically the lower mantle of a narrower convecting cell with a strong temperature- and pressure- dependent viscosity. Following a thorough analysis, we have found the self-consistent asymptotic structure of the lower mantle and we have also identified the transition zone between the upper mantle and lower mantle.

Section 6.3 gives the asymptotic temperature profile in the lower mantle which apparently agrees well with numerics (e.g. Figures 6.5 - 6.6). But weakly nonlinear stability analysis leading to (6.41) implies that the nontrivial solution branch is unstable. The explanation might be related to the plumes and mega-plumes. The issue of plume and mega-plume formation can not be readily addressed, as such features are essentially associated with time-dependent convection. Constant viscosity convection certainly becomes unstable and plume-like at high Rayleigh number. We

have not found such instability in our numerical calculations, which suggests that a further stabilising bifurcation may occur at smaller λ. It is then tempting to suppose that if this instability is real, the result could be plume formation on a horizontal scale comparable to the finger width, perhaps of order $l = 300$ km (corresponding to $a = 1.8, \varepsilon = 0.055, d = 3{,}000$ km). It is noteworthy that this scale is comparable to that of coronae on Venus, which may also represent the surface expression of mantle plumes (Solomon and Head, 1991). We might expect such plumes to punch their way through the upper mantle oceanic return flow. Their development time scale is $\frac{l^2}{\kappa} \sim 3000$ Ma, so that although there might be many fingers, relatively few would provide plumes at any one time. It is less easy to see how mega-plumes might form, however, unless from a punch through of a subducting slab to the lower mantle and its subsequent foundering at the core-mantle boundary.

We have continued our studies with both $\gamma \ll 1$ and $\gamma \sim 1$ in this chapter and we have not found any result in favour of $\gamma \ll 1$, i.e. $\delta \ll \varepsilon$. In fact, the matching between all the regions of the mantle requires $\gamma = 1$. Thus we formally conclude that $\gamma = 1$, i.e. $\delta = \varepsilon$ is our correct assumption for the narrow cell convection with temperature and pressure dependent viscosity to ensure a self-consistent asymptotic analysis.

Chapter 7

Conclusions

The principal aim of this thesis has been to study the high Rayleigh number convection with strongly temperature- and pressure-dependent viscosity relative to the Earth's mantle. The summaries and discussions at the end of chapters 2, 3, 4, 5 and 6 provide detailed reviews of the key results obtained in the corresponding chapters. Here a summary of the conclusions is presented, and possible areas for future work are suggested.

Chapter 2 focussed on deriving a simple model for mantle convection in a unit aspect-ratio cell with free-slip boundary conditions and constant viscosity. By ignoring compressibility, internal heating, partial melting, solid phase change, this may be seen as a large simplification of the real mantle, but the intention was to keep the model equations simple enough to gain analytical and numerical understanding whilst still being consistent in the application of conservation laws. We solved our Rayleigh-Bénard convection model by using the finite element based PDE solver Comsol Multiphysics and our code is verified with benchmark values.

In chapter 3, we continued with the simplified model, but included viscosity as a variable. In doing so, we chose the Arrhenius form of viscosity, which is often approximated by a Frank-Kamenetskii form in the literature. In this chapter, we focussed on the temperature dependent viscosity case and observed the differences between constant viscosity and variable viscosity. Even though it was a significant improvement for a convection model of the mantle, there were some features which could not be explained by the temperature-dependent viscosity case. We also used a low temperature cut-off viscosity function that helped us to investigate convection with high viscosity contrast across the mantle.

We then considered temperature and pressure dependent viscosity in our convection model in chapter 4 and observed some remarkable characteristics of the convection cell at extreme viscosity contrasts of about 10^{30}. We observed that the bulk

fluid is no longer isothermal or isoviscous, but, in fact, there exists a warm upper core and a quite distinct cooler lower core. This is quite a distinguishing feature compared to convection with strong temperature dependent viscosity. To investigate the convection with high viscosity contrasts further, we adopted the cut-off viscosity function which allowed us to isolate the upper part of the convection cell where most of the viscosity contrast occurs and where the velocity is practically zero. It should be mentioned again that the ultra-high values of viscosity in the lid are neglected but the extreme sensitivity of η due to the pressure number μ of $O(1)$ and the small viscous temperature parameter ε in the bulk fluid are unaffected, as shown in Figure 4.7. This new form of viscosity function enabled us to explore solutions with extremely high viscosity contrasts and showed some even more striking phenomena. We found that the square cells become unstable and broke into narrower cells. This led us to study convection with extremely high viscosity variation in narrower cells, and finally to conclude that narrower cells are preferred at such extreme viscosity contrasts. A linear stability analysis supported our observations. In fact, both numerics and linear stability analysis suggest that the aspect ratio a should be proportional to the temperature parameter ε at high viscosity contrasts and in support of this, some numerical simulations have been done for the specific case of $a = 3\varepsilon$.

The results we have found may have serious implications for the style of convection in the mantle of the Earth and other terrestrial planets. For example, we earlier estimated the viscosity contrast for the Earth's mantle to be 10^{50} or more, whereas for Venus and Mars, it is around 10^{20} and 10^{50} respectively (Armann and Tackley, 2012, Huang et al., 2013, Schubert et al., 2001). Extreme parameter values ensure simultaneous strong temperature and pressure dependence on the viscosity function and we have found the strong pressure dependence to have a significant effect on the dynamics. Thus, without such extreme parameter values, we are unable to obtain a proper asymptotic structure of mantle convection for Earth and other planets.

In chapters 5 and 6, we performed a detailed asymptotic analysis of a narrow convection cell where the aspect-ratio a and the viscous temperature parameter ε are related by $a = 3\varepsilon$. We treated different regions of the upper mantle and the lower mantle separately in chapters 5 and 6 respectively and we found good matching between the regions. A stagnant lid, an asthenosphere and an upper mantle core constitute the upper mantle. The lower mantle or lower core below this is an approximately vertical return flow in which there is a mild excess of buoyancy in a slowly upwelling plume. There are other regions like the corner layers at each end of the as-

thenosphere, a transition zone between upper and lower mantle, and a basal thermal boundary layer.

In chapter 5, we predicted the position of the lithospheric lid which can be treated as the boundary between the stagnant lid and the asthenosphere and compared it with the numerical solution which is estimated from an isothermal contour. In chapter 6, we determined the temperature profile in the lower mantle. In both cases, we found excellent agreement with the numerics. But our analysis of the lid base is certainly one that warrants further technical examination; and indeed, there are a number of other lines of enquiry which could be pursued. We have delineated approximating equations in numerous areas (for example, the upper core, the basal boundary layer) without attempting to provide a numerical solution. Largely this is because such investigations do not add significant information to our study.

During the process of scaling analysis, we followed two approaches: one where the lid base slope γ is very small i.e. $\gamma \ll 1$ and the other with $\gamma \sim 1$. Our detailed analysis showed that $\gamma \sim 1$ is the appropriate choice for convection in a narrow cell with viscosity strongly dependent on temperature and pressure.

We believe that we have essentially solved the problem of elucidating the asymptotic structure of high Rayleigh number convection in a fluid whose viscosity depends exponentially strongly on both temperature and pressure. There are two central obstacles to establishing the results. The first is practical: computations with viscosity contrasts even as large as 10^{15} fail to portray an obvious asymptotic structure, and previous computational work has failed to progress beyond this. The second obstacle is the fundamental issue of how a rapidly convecting thermobaroviscous fluid reconciles its tendency to be isothermal (or more generally, adiabatic) with the necessity to be relatively isoviscous (below the rigid lid). By relatively isoviscous, we mean to allow variations of perhaps five orders of magnitude, but not twenty. Fowler (1983) suggested that a relatively isoviscous lower mantle could satisfy constraints associated with dynamics, mantle viscosity estimates, core mantle temperature estimates, as well as a low viscosity asthenosphere, a vigorous upper mantle flow and a sluggish lower mantle flow, but he was unable to substantiate these claims by means of an actual solution.

As we now see, this inability is largely due to the inability to recognise that the way the flow copes with the necessity to be relatively isoviscous in the lower mantle is by adopting the form of narrow convection cells. This revelation allowed us to push the computed results to extreme viscosity contrasts and thereby identify the

appropriate asymptotic limits. Even with this insight, however, the unravelling of the flow structure has been a laborious process.

Throughout our analysis, we have referred to the different parts of the flow by their geophysical counterparts, simply because there is a natural correspondence. There is a rigid lid, and this is the lithosphere. There is a low viscosity zone below this, which is the asthenosphere. The circulatory flow in the upper core corresponds to the upper mantle, while the more or less vertical exchange flow in the lower core corresponds to the lower mantle. One might even associate the core-mantle thermal boundary layer with the D'' layer, although it seems more likely that this is associated with the reaction between the outer core and the lower mantle (Knittle and Jeanloz, 1991), and the post-perovskite transition alluded to above (Jaupart et al., 2009).

The main and obvious difference is that there is no subduction. Various authors (Fowler, 1985a, 1993b, Fowler and O'Brien, 2003, Tackley, 1998, 2000*a*,*b*) have suggested that the weakening of the lithosphere necessary to initiate subduction is associated with viscoplastic yielding induced by the enormous stresses produced in the lithosphere, which are there essentially because they are necessary to support a heavy stagnant lithosphere. Numerical computations of lid stresses are rarely reported except some works by Solomatov (2004), Wong and Solomatov (2015), unsurprisingly since the computations tend to exhibit instability, but they can be analysed asymptotically (Fowler, 1985a). Although we have not done so here, the analysis should be similar. Lid stresses become huge, and provide a mechanism for subduction.

The tantalising question is then, how should we expect convection to occur in a thermobaroviscous mantle when there is active subduction? For sub-continental lithosphere, we expect the structure to be that described here. The most obvious distinction for oceanic lithosphere is that the plunge of the heavy lid causes a near horizontal return flow with a much larger horizontal length scale, but this will be restricted to the upper mantle; the lower mantle maintains its higher viscosity and sluggish convection. If we suppose, as we seemingly should, that the lower mantle retains its finger-style convection, then it seems that leakage of upper mantle lithosphere to the lower mantle will occur locally, and most of the lower mantle may be effectively segregated from the upper mantle. But in any case, the residence time in the lower mantle for a 3 mm y^{-1} flow descending and then ascending a 2,300 km deep finger cell is 1.5×10^9 y, and this seems to provide a robust way to segregate the mantle.

Future work

We think that the most significant point worthy of further study is the issue of the lid base equation. In particular, we note that the treatment of the lid base for thermoviscous convection (Fowler, 1985a) was over-simplified, and itself deserves further study. Crucial in our analysis is the idea that the lid base is self determining without reference to the flow elsewhere, and this is in stark contrast to the constant viscosity flow (Roberts, 1979). In the thermoviscous case, the lid thickness (the parameter γ in (5.16)) was determined by the connection of the buoyant plume to the asthenospheric shear flow, but in the present case, the buoyancy of the plume is insignificant in the upper core and the upper core flow is driven by the asthenospheric shear flow, which itself is driven by the lid slope.

In building our mathematical model, we ignored some effects like internal heating due to radioactive elements, compressibility and viscous dissipation. These effects undoubtedly have an influence on the fluid dynamics and thus including these effects will make the models more realistic. Also, once heat sources are included, it is much more likely that the preferable mode of convection is unsteady. Further work should investigate these factors thoroughly. In addition to these, it may be argued that choosing a spherical shell would have been more appropriate than a Cartesian 2D model. Sphericity breaks the heat flux symmetry between the top and bottom boundary layers. For purely basally heated spherical shells, conservation of energy prescribes that for a stable convective solution, the total heat input through the bottom boundary must be equal to the heat output through the top. However, because of sphericity, the bottom boundary has significantly less surface area than the top boundary through which heat passes; to compensate for this smaller area, the thickness of the stagnant lid may be significantly larger.

In most of the literature related to the Earth's mantle, the viscosity is considered as temperature-dependent and the viscosity contrast across the mantle is taken as $10^{15} - 10^{20}$ at most. Hence, the actual viscosity function which is strongly dependent on temperature and pressure (and stress) is widely neglected in literature. The novelty of this thesis is that we treated mantle convection with a variable viscosity which is strongly dependent on both temperature and pressure. We solved our numerical model using a cut-off viscosity function for extreme viscosity contrasts with significant effects of temperature and pressure. We also performed a detailed asymptotic analysis for the convection model and found excellent agreement between analytic result and numerical solution. The verification is presented through the calculation of stagnant

lid base profile and the lower mantle temperature profile. The findings are also presented in two papers Khaleque et al. (2015) and Fowler et al. (2015).

Our study has been motivated by convection in the Earth's mantle, but has been an idealised one. Despite all the limitations, it is hoped that the theory may have implications for extra-solar 'super-Earths', where larger values of mantle depths may lead to larger values of the viscous pressure number μ (Tackley et al., 2013). Besides this, introducing a plastic yielding in the viscosity function may lead us to the investigation of initiation of subduction (Bello et al., 2015).

It is hoped that our study has discovered some significant characteristics of convection with strong temperature and pressure-dependent viscosity which are relevant to the mantle of the Earth and other terrestrial planets. Our model may be very simplistic compared to the complexity of the mantle, but we hope that our study points towards future avenues for research.

Appendix A

Weak formulation and the finite element method

Let Ω be a bounded open set in $\mathbb{R}^n$, and consider the linear second-order partial differential equation (PDE) with homogeneous Dirichlet boundary condition

$$-\sum_{i,j=1}^{n} \frac{\partial}{\partial x_j}\left(a_{ij}\frac{\partial u}{\partial x_i}\right) + \sum_{i=1}^{n} b_i(x)\frac{\partial u}{\partial x_i} + c(x)u = f(x), \quad x \in \Omega, \tag{A.1}$$

$$u = 0 \quad \text{on} \quad \partial\Omega, \tag{A.2}$$

where the coefficients a_{ij}, b_i, c and f satisfy the following conditions:

$$\begin{aligned} a_{ij} &\in C^1(\bar{\Omega}), && i,j = 1,\ldots,n; \\ b_i &\in C(\bar{\Omega}), && i = 1,\ldots,n; \\ c &\in C(\bar{\Omega}), && f \in C(\bar{\Omega}), \end{aligned} \tag{A.3}$$

and

$$\sum_{i,j=1}^{n} a_{ij}(x)\xi_i\xi_j \geq \hat{c}\sum_{i=1}^{n}\xi_i^2, \quad \forall \xi = (\xi_1,\ldots,\xi_n) \in \mathbb{R}^n, \quad x \in \bar{\Omega}; \tag{A.4}$$

$\hat{c}$ is a positive constant independent of x and ξ. A function $u \in C^2(\Omega)\bigcap C(\bar{\Omega})$ satisfying (A.1) and (A.2) is called a classical solution of this problem. The theory of partial differential equations tells us that (A.1) and (A.2) have a unique classical solution, provided that a_{ij}, b_i, c, f and $\partial\Omega$ are sufficiently smooth. However, in many applications one has to consider equations where these smoothness requirements are violated, and for such problems the classical theory is inappropriate. In order to overcome the limitations of the classical theory, for any $v \in C_0^1(\Omega)$, (A.1) can be written as

$$-\sum_{i,j=1}^{n}\int_\Omega \frac{\partial}{\partial x_j}\left(a_{ij}\frac{\partial u}{\partial x_i}\right)\cdot v dx + \sum_{i=1}^{n}\int_\Omega b_i(x)\frac{\partial u}{\partial x_i}\cdot v dx + \int_\Omega c(x)uv dx = \int_\Omega f(x)v(x)dx. \tag{A.5}$$

Upon integration by parts in the first integral and noting that $v = 0$ on $\partial\Omega$, we obtain:

$$\sum_{i,j=1}^{n} \int_\Omega a_{ij}(x) \frac{\partial u}{\partial x_i} \frac{\partial v}{\partial x_j} dx + \sum_{i=1}^{n} \int_\Omega b_i(x) \frac{\partial u}{\partial x_i} v dx + \int_\Omega c(x) uv dx \quad = \int_\Omega f(x) v(x) dx, \quad \forall v \in C_0^1(\Omega). \tag{A.6}$$

In order for this equality to make sense, we no longer need to assume that $u \in C^2(\Omega)$; it is sufficient that $u \in L^2(\Omega)$ and $\partial u/\partial x_i \in L^2(\Omega), i = 1, \cdots, n$. Thus a function $u \in H_0^1(\Omega)$ satisfying

$$\begin{aligned} \sum_{i,j=1}^{n} \int_\Omega a_{ij}(x) \frac{\partial u}{\partial x_i} \frac{\partial v}{\partial x_j} dx \quad + \quad \sum_{i=1}^{n} \int_\Omega b_i(x) \frac{\partial u}{\partial x_i} v dx \\ + \int_\Omega c(x) uv dx \quad = \quad \int_\Omega f(x) v(x) dx, \quad \forall v \in H_0^1(\Omega), \end{aligned} \tag{A.7}$$

is called a weak solution of (A.1) and (A.2), where H_0^1 is defined as

$$H_0^1 = \left\{ u \in L_2(\Omega) : \frac{\partial u}{\partial x_i} \in L_2(\Omega),\ i = 1, \cdots, n,\ u = 0 \quad \text{on} \quad \partial\Omega \right\}. \tag{A.8}$$

It should be noted that $C_0^1(\Omega) \subset H_0^1(\Omega)$ and (A.7) is called the *weak formulation* of (A.1)-(A.2).

Finite element method

Let us consider a bounded domain Ω in $\mathbb{R}^2$. If we seek solution $u \in V$, where V is the finite dimensional subspace of H_0^1, then a special case of (A.7) with $n = 2$, $a_{ij}(x) \equiv 1$ for $i = j$ and $\equiv 0$ for $i \neq j$, $b_i(x) \equiv 0$ for all i and $c(x) \equiv 0$, can be written as

$$\int_\Omega \left(\frac{\partial u}{\partial x} \frac{\partial v}{\partial x} + \frac{\partial u}{\partial y} \frac{\partial v}{\partial y} \right) dx\, dy = \int_\Omega f v dx\, dy, \quad \forall v \in V. \tag{A.9}$$

After the weak formulation of the PDE, comes the issue of discretization. Firstly, the domain needs to be segmented into a number of elements which is known as meshing. The elements can be of triangular or quadrilateral or any other suitable shape. If the solution space V is spanned by $\phi_1, \cdots, \phi_N$, then we can write

$$u = \sum_i^N U_i \phi_i(x, y) \qquad \text{and} \qquad v = \sum_j^N U_j \phi_j(x, y). \tag{A.10}$$

Substituting these in (A.9) yields

$$\sum_i^N U_i \left[\int_\Omega (\nabla \phi_i \cdot \nabla \phi_j)\, dx\, dy \right] = \int_\Omega f \phi_j dx\, dy, \quad \text{for} \quad j = 1, \cdots, N. \tag{A.11}$$

Let $A = (a_{ij})$, $F = (F_1, \cdots, F_N)^T$,

$$a_{ij} = a_{ji} = \int_\Omega \left(\frac{\partial \phi_i}{\partial x} \frac{\partial \phi_j}{\partial x} + \frac{\partial \phi_i}{\partial y} \frac{\partial \phi_j}{\partial y} \right) dx\, dy, \tag{A.12}$$

$$F_j = \int_\Omega f \phi_j dx\, dy. \tag{A.13}$$

The finite element approximation can be written as a system of linear equations

$$AU = F. \tag{A.14}$$

Solving this, we obtain $U = (U_1, \cdots, U_N)^T$, and hence the approximate solution

$$u(x, y) = \sum_i^N U_i \phi_i(x, y). \tag{A.15}$$

The particular feature of the finite element method lies in the choice of the basis functions or shape functions, $\phi_j(x, y)$. Finite element bases are constructed so that ϕ_j is non-zero only on elements containing an entity (e.g. a vertex, edge or element in two dimensions) indexed by j. The basis functions can be taken to be higher order and the number of unknowns U_i rises with the order of the basis functions. The number of basis function rises with order as well.

Appendix B

Shanks transformation

According to Bender and Orszag (1999), Shanks transformation is used to improve the convergence rate of a sequence by eliminating its most pronounced transient behaviour. Suppose the n-th term in the sequence takes the form

$$A_n = A + \alpha q^n, \quad \text{with} \quad |q| \leq 1, \tag{B.1}$$

so that $A_n \rightarrow$A as $n \rightarrow \infty$. Here αq^n is the transient term. Since any member of this sequence depends on the three parameters A, α and q, it follows that A can be determined from three terms of the sequence. Suppose that

$$A_{n-1} = A + \alpha q^{n-1}, \tag{B.2}$$

$$A_n = A + \alpha q^n, \tag{B.3}$$

$$A_{n+1} = A + \alpha q^{n+1}, \tag{B.4}$$

then solving the system of equations for A gives

$$A = \frac{A_{n+1}A_{n-1} - A_n^2}{A_{n+1} + A_{n-1} - 2A_n}. \tag{B.5}$$

If the most pronounced transient has the form $\alpha q^n,\ |q| < 1$, then the nth term in the sequence takes the form $A_n = A(n) + \alpha q^n$, where for large n, $A(n)$ is a more slowly varying function of n than A_n. Let us suppose that $A(n)$ varies sufficiently slowly so that $A(n-1), A(n)$ and $A(n+1)$ are all approximately equal (Bender and Orszag, 1999). Then we can apply the nonlinear transformation,

$$S(A_n) = \frac{A_{n+1}A_{n-1} - A_n^2}{A_{n+1} + A_{n-1} - 2A_n}, \tag{B.6}$$

known as Shanks transformation (Shanks, 1955). This transformation creates a new sequence $S(A_n)$ which often converges more rapidly than the old sequence A_n, even

if the old sequence has more than one transient (Bender and Orszag, 1999). The sequences $S^2(A_n) = S[S(A_n)]$, $S^3(A_n) = SS[S(A_n)]$, and so on, may be even more rapidly convergent.

Bibliography

Ammann, M. W., Brodholt, J. P. and Dobson, D. P. (2009), 'DFT study of migration enthalpies in mgsio$_3$ perovskite', *Phys. Chem. Miner.* **36**, 151–158.

Armann, M. and Tackley, P. J. (2012), 'Simulating the thermochemical magmatic and tectonic evolution of Venus's mantle and lithosphere: Two-dimensional models', *J. Geophys. Res.* **117**(E12003).

Baumgardner, J. R. (1985), 'Three dimensional treatment of convection flow in the Earth's mantle', *J. Stat. Phys.* **39**(5/6), 501–511.

Bello, L., Coltice, N., Tackley, P. J., Müller, R. D. and Cannon, J. (2015), 'Assessing the role of slab rheology in coupled plate-mantle convection models', *Earth Planet. Sci. Lett.* **430**, 191 – 201.

Bender, C. M. and Orszag, S. A. (1999), *Advanced Mathematical Methods for Scientists and Engineers*, Springer, New York.

Bercovici, D. (1993), 'A simple model of plate generation from mantle flow', *Geophys. J. Int.* **114**(3), 635–650.

Bercovici, D. (2003), 'The generation of plate tectonics from mantle convection', *Earth Planet. Sci. Lett.* **205**(3), 107–121.

Bercovici, D. (2009), *Mantle Dynamics*, Vol. 7 of *Treatise on Geophysics*, Elsevier, Amsterdam.

Bercovici, D., Ricard, Y. and Richards, M. (2000), 'The relation between mantle dynamics and plate tectonics: A primer', *Geophysical Monograph-American Geophysical Union* **121**, 5–46.

Blankenbach, B., Busse, F., Christensen, U., Cserepes, L., Gunkel, D., Hansen, U., Harder, H., Jarvis, G., Koch, M., Marquart, G. et al. (1989), 'A benchmark comparison for mantle convection codes', *Geophys. J. Int.* **98**(1), 23–38.

Bunge, H. P., Richards, M. A. and Baumgardner, J. R. (1996), 'Effect of depth-dependent viscosity on the planform of mantle convection', *Nature* **379**, 436–438.

Burden, R. L. and Faires, J. D. (2011), *Numerical Analysis*, ninth edn, Brooks/Cole, Cengage Learning.

Busse, F. (1978), 'Non-linear properties of thermal convection', *Rep. Prog. Phys.* **41**, 1929–68.

Chandrasekhar, S. (1961), *Hydrodynamic and Hydromagnetic Stability*, Oxford University Press, London.

Christensen, U. (1995), 'Effects of phase transitions on mantle convection', *Ann. Rev. Earth Planet. Sci.* **23**, 65–87.

Christensen, U. and Harder, H. (1991), '3-D convection with variable viscosity', *Geophys. J. Int.* **104**(1), 213–226.

Christensen, U. R. (1984a), 'Heat transport by variable viscosity convection and implications for the Earth's thermal evolution', *Phys. Earth Planet. Inter.* **35**, 264–282.

Christensen, U. R. (1984b), 'Convection with pressure- and temperature-dependent non-Newtonian rheology', *Geophys. J. R. Astron. Soc.* **77**, 343–384.

Christensen, U. R. (1989), 'The heat transport by convection rolls with free boundaries at high Rayleigh number', *Geophys. Astrophys. Fluid Dyn.* **46**, 93–103.

Christensen, U. R. and Yuen, D. A. (1985), 'Layered convection induced by phase transitions', *J. Geophys. Res.* **90**(B12), 10291–10300.

COMSOL Multiphysics (2014), 'User's guide version 5.0', *http://www.comsol.com* .

Cserepes, L. (1993), 'Effect of depth-dependent viscosity on the pattern of mantle convection', *Geophys. Res. Lett.* **20**(19), 2091–2094.

Dalrymple, G. B. (2001), 'The age of the earth in the twentieth century: a problem (mostly) solved', *Geological Society, London, Special Publications* **190**(1), 205–221.

Davies, G. F. (1999), *Dynamic earth: Plates, Plumes and Mantle convection*, Cambridge University Press, Cambridge.

Davies, G. F. and Richards, M. A. (1992), 'Mantle convection', *J. Geology* **100**, 151–206.

Deschamps, F., Li, Y. and Tackley, P. (2015), *The Earth's Heterogeneous Mantle*, Springer International Publishing, chapter Large-Scale Thermo-chemical Structure of the Deep Mantle: Observations and Models.

Deuflhard, P. (1974), 'A modified newton method for the solution of ill-conditioned systems of nonlinear equations with application to multiple shooting', *Numer. Math.* **22**, 289–315.

Dietz, R. S. (1961), 'Continent and ocean basin evolution by spreading of the sea floor', *Nature* **190**, 854–7.

Doin, M., Fleitout, L. and Christensen, U. (1997), 'Mantle convection and stability of depleted and undepleted continental lithosphere', *J. Geophys. Res.* **102**(B2), 2771–2787.

Drazin, P. G. and Reid, W. H. (1981), *Hydrodynamic Stability*, Cambridge University Press, Cambridge.

Dumoulin, C., Doin, M. and Fleitout, L. (1999), 'Heat transport in stagnant lid convection with temperature-and pressure-dependent Newtonian or non-Newtonian rheology', *J. Geophys. Res.* **104**(B6), 12–759.

Durham, W., Mei, S., Kohlstedt, D., Wang, L. and Dixon, N. (2009), 'New measurements of activation volume in olivine under anhydrous conditions', *Phys. Earth Planet. Int.* **172**, 67–73.

Fleitout, L. and Yuen, D. (1984), 'Steady state, secondary convection beneath lithospheric plates with temperature- and pressure-dependent viscosity', *J. Geophys. Res.* **89**(B11), 9227–9244.

Fowler, A. C. (1983), 'On the thermal state of the Earth's mantle', *J. Geophys.* **53**, 42–51.

Fowler, A. C. (1985a), 'Fast thermoviscous convection', *Stud. Appl. Math.* **72**, 189–219.

Fowler, A. C. (1985b), 'Secular cooling in convection', *Stud. Appl. Math.* **72**, 161–171.

Fowler, A. C. (1986), 'Thermal runaway in the Earth's mantle', *Stud. Appl. Math.* **74**, 1–34.

Fowler, A. C. (1993a), 'Towards a description of convection with temperature- and pressure-dependent viscosity', *Stud. Appl. Math.* **88**, 113–139.

Fowler, A. C. (1993b), 'Boundary layer theory and subduction', *J. Geophys. Res.* **98**, 21,997–22,005.

Fowler, A. C. (1997), *Mathematical Models in the Applied Sciences*, Cambridge University Press, Cambridge.

Fowler, A. C. (2011), *Mathematical Geoscience*, Springer, London.

Fowler, A. C., Howell, P. D. and Khaleque, T. S. (2015), 'Convection of a fluid with strongly temperature and pressure dependent viscosity', *Geophys. Astrophys. Fluid Dyn. submitted* .

Fowler, A. C. and O'Brien, B. G. (2003), 'Lithospheric failure on Venus', *Proc. R. Soc. Lond. A.* **459**(2039), 2663–2704.

Gordon, R. B. (1965), 'Diffusion creep in the Earth's mantle', *J. Geophys. Res.* **70**(10), 2413–18.

Gurnis, M. and Davies, G. (1986), 'Numerical study of high Rayleigh number convection in a medium with depth-dependent viscosity', *Geophys. J. Roy. Astron. Soc.* **85**(3), 523–542.

Gutenberg, B. (1913), 'Uber die konstitution des erdinnern, erschlossen aus erdbebenbeobachtungen', *Phys. Z.* **14**, 1217–18.

Hansen, U., Yuen, D. A., Kroening, S. E. and Larsen, T. B. (1993), 'Dynamical consequences of depth-dependent thermal expansivity and viscosity on mantle circulations and thermal structure', *Phys. Earth. Planet. Inter.* **77**, 205–223.

Haskell, N. A. (1937), 'The viscosity of the asthenosphere', *Am. J. Sci.* **33**, 22–28.

Helffrich, G. R. and Wood, B. J. (2001), 'The Earth's mantle', *Nature* **412**, 501–507.

Hess, H. H. (1962), History of ocean basins, *in* 'Petrologic Studies-A volume in Honor of A . F. Buddington', Geol. Soc. America, New York, pp. 599–620.

Holmes, A. (1931), 'Radioactivity and Earth movements', *Trans. Geol. Soc. Glasgow, XVIII-Part III, 1928-31* **18**, 559–606.

Holmes, A. (1933), 'The thermal history of Earth', *J. Wash. Acad. Sci.* **23**, 169–95.

Houston, M. and De Bremaecker, J.-C. (1975), 'Numerical models of convection in the upper mantle', *Journal of Geophysical Research* **80**(5), 742–751.

Huang, J., Yang, A. and Zhong, S. (2013), 'Constraints of the topography, gravity and volcanism on Venusian mantle dynamics and generation of plate tectonics', *Earth Planet. Sci. Lett.* **362**, 207–214.

Huang, J. and Zhong, S. (2005), 'Sublithospheric small-scale convection and its implications for the residual topography at old ocean basins and the plate model', *J. Geophys. Res.: Solid Earth* **110**(B5).

Huang, J., Zhong, S. and van Hunen, J. (2003), 'Controls on sublithospheric small-scale convection', *J. Geophys. Res.: Solid Earth* **108**(B8).

Isacks, B., Oliver, J. and Sykes, L. R. (1968), 'Seismology and the new global tectonics', *J. Geophys. Res.* **73**, 5855–99.

Jarvis, G. T. (1984), 'Time-dependent convection in the Earth's mantle', *Phys. Earth Planet. Inter.* **36**, 305–27.

Jarvis, G. T. and McKenzie, D. P. (1980), 'Convection in a compressible fluid with infinite Prandtl number', *J. Fluid Mech.* **96**(3), 515–583.

Jarvis, G. T. and Peltier, W. R. (1982), 'Mantle convection as a boundary layer phenomenon', *Geophys. J. R. Astron. Soc.* **68**, 389–427.

Jaupart, C., Labrosse, S. and Mareschal, J.-C. (2009), Temperatures, heat and energy in the mantle of the Earth, *in* 'Treatise on Geophysics: Mantle dynamics', Vol. 7, Elsevier, pp. 253–303.

Jeanloz, R. (1990), 'The nature of the Earth's core', *Annu. Rev. Earth Planet. Sci.* **18**, 357–386.

Jeffreys, H. (1939), 'The times of P, S and SKS, and the velocities of P and S', *Mon. Not. Roy. Astron. Soc.,Geophys. Suppl.* **4**, 498–533.

Jimenez, J. and Zufiria, J. A. (1987), 'A boundary-layer analysis of Rayleigh-Bénard convection at large Rayleigh number', *J. Fluid Mech.* **178**, 53–71.

Kameyama, M. and Ogawa, M. (2000), 'Transitions in thermal convection with strongly temperature-dependent viscosity in a wide box', *Earth Planet. Sci. Lett.* **180**(3), 355–367.

Karato, S. and Wu, P. (1993), 'Rheology of the upper mantle – A synthesis', *Science* **260**(5109), 771–778.

Kearey, P., Klepeis, K. A. and Vine, F. J. (2009), *Global Tectonics*, 3rd edn, Wiley-Blackwell, UK.

Khaleque, T. S., Fowler, A. C., Howell, P. D. and Vynnycky, M. (2015), 'Numerical studies of thermal convection with temperature- and pressure-dependent viscosity at extreme viscosity contrasts', *Phys. Fluids* **27**(076603).

King, S. D. (2009), 'On topography and geoid from 2-D stagnant lid convection calculations', *Geochem. Geophys. Geosyst.* **10**(3).

King, S. D., Raefsky, A. and Hager, B. H. (1990), 'ConMan: Vectorizing a finite element code for incompressible two-dimensional convection in the Earth's mantle', *Phys. Earth Planet. Inter.* **59**, 195–207.

Kirby, S. H. (1983), 'Rheology of the lithosphere', *Rev. Geophys.* **21**(6), 1458–1487.

Kleine, T. and Rudge, J. F. (2011), 'Chronometry of meteorites and the formation of the earth and moon', *Elements* **7**(1), 41–46.

Knittle, E. and Jeanloz, R. (1991), 'Earth's core-mantle boundary: results of experiments at high pressures and temperatures', *Science* **251**, 1,438–1,443.

Koglin Jr, D., Ghias, S., King, S., Jarvis, G. and Lowman, J. (2005), 'Mantle convection with reversing mobile plates: A benchmark study', *Geochem. Geophys. Geosyst.* **6**, Q09003.

Landau, L. D. (1944), 'On the problem of turbulence', *C. R. Acad. Sci. U.R.S.S.* **44**, 311–314.

Larsen, T. B., Malevsky, A. V., Yuen, D. A. and Smedsmo, J. L. (1993), 'Temperature-dependent Newtonian and non-Newtonian convection: Implications for lithospheric processes', *Geophys. Res. Lett.* **20**(23), 2595–2598.

Lehmann, I. (1936), "'P"', *Publ. Bur. Cent. Seism. Int. A* **14**, 87–115.

Loper, D. E. (1985), 'A simple model of whole-mantle convection', *J. Geophys. Res.* **90**(B2), 1809–1836.

Malkus, W. V. R. and Veronis, G. (1958), 'Finite amplitude cellular convection', *J. Fluid Mech.* **4**, 225–260.

Matkowsky, B. (1970), 'A simple non-linear dynamic stability problem', *Bull. Amer. Math. Soc.* **76**, 620–25.

McKenzie, D. P., Roberts, J. M. and Weiss, N. O. (1974), 'Convection in the Earth's mantle: towards a numerical simulation', *J. Fluid Mech.* **62**(3), 465–538.

McKenzie, D. and Weiss, N. (1975), 'Speculations on the thermal and tectonic history of the earth', *Geophys. J. R. Astron. Soc.* **42**, 131–174.

Mitrovica, J. X. and Forte, A. M. (2004), 'A new inference of mantle viscosity based upon joint inversion of convection and glacial isostatic adjustment data', *Earth Planet. Sci. Letts.* **E225**, 177–189.

Moore, D. R. and Weiss, N. O. (1973), 'Two-dimensional Rayleigh-Bénard convection', *J. Fluid Mech.* **58**(2), 289–312.

Moresi, L. and Gurnis, M. (1996), 'Constraints on the lateral strength of slabs from three-dimensional dynamic flow models', *Earth Planet. Sci. Lett.* **138**(1), 15–28.

Moresi, L. and Solomatov, V. (1998), 'Mantle convection with a brittle lithosphere: thoughts on the global tectonic styles of the Earth and Venus', *Geophys. J. Int.* **133**(3), 669–682.

Moresi, L. and Solomatov, V. S. (1995), 'Numerical investigation of 2D convection with extremely large viscosity variations', *Phys. Fluids* **7**(9), 2154–62.

Morris, S. and Canright, D. (1984), 'A boundary-layer analysis of Bénard convection in a fluid of strongly temperature-dependent viscosity', *Phys. Earth Planet. Inter.* **29**, 320–329.

Noack, L. and Breuer, D. (2013), 'First-and second-order Frank-Kamenetskii approximation applied to temperature-, pressure- and stress-dependent rheology', *Geophys. J. Int.* **195**(1), 27–46.

Ogawa, M. (2008), 'Mantle convection: A review', *Fluid Dyn. Res.* **40**, 379–398.

Olson, P. (1987), 'A comparison of heat transfer laws for mantle convection at very high Rayleigh numbers', *Phys. Earth Planet. Inter.* **48**, 153–160.

Olson, P. and Corcos, G. M. (1980), 'A boundary layer model for mantle convection with surface plates', *Geophys. J. R. Astron. Soc.* **62**, 195–219.

Oreskes, N. (2003), *Plate tectonics: An insider's history of the modern theory of the Earth*, Westview Press.

Orth, C. P. and Solomatov, V. S. (2011), 'The isostatic stagnant lid approximation and global variations in the Venusian lithospheric thickness', *Geochem. Geophys. Geosyst.* **12**(7).

Parmentier, E. M., Turcotte, D. L. and Torrance, K. E. (1976), 'Studies of finite amplitude non-Newtonian thermal convection with application to convection in the Earth's mantle', *J. Geophys. Res.* **81**(11), 1839–1846.

Parsons, B. and McKenzie, D. (1978), 'Mantle convection and the thermal structure of the plates', *J. Geophys. Res.* **83**(B9), 4,485–4,496.

Ratcliff, J. T., P. J. Tackley, G. S. and Zebib, A. (1997), 'Transitions in thermal convection with strongly variable viscosity', *Phys. Earth Planet. Inter.* **102**, 201–212.

Ratcliff, J. T., Schubert, G. and Zebib, A. (1996), 'Effects of temperature-dependent viscosity on thermal convection, in a spherical shell', *Physica D* **97**, 242–252.

Reese, C. C., Solomatov, V. S. and Moresi, L. N. (1998), 'Heat transport efficiency of stagnant lid convection with dislocation viscosity: Application to Mars and Venus', *J. Geophys. Res.* **103**, 13643–657.

Reese, C. C., Solomatov, V. S. and Moresi, L.-N. (1999), 'Non-Newtonian stagnant lid convection and magmatic resurfacing on Venus', *Icarus* **139**(1), 67–80.

Reese, C. and Solomatov, V. (2002), 'Mean field heat transfer scaling for non-Newtonian stagnant lid convection', *J. non-Newt. Fluid M.* **107**(1), 39–49.

Roberts, G. O. (1979), 'Fast viscous Bénard convection', *Geophys. Astrophys. Fluid Dyn.* **12**, 235–272.

Rozel, A., Golabek, G., Näf, R. and Tackley, P. (2015), 'Formation of ridges in a stable lithosphere in mantle convection models with a visco-plastic rheology', *Geophys. Res. Lett.* **42**, 4770–4777.

Schaber, G., Strom, R., Moore, H., Soderblom, L., Kirk, R., Chadwick, D., Dawson, D., Gaddis, L., Boyce, J. and Russell, J. (1992), 'Geology and distribution of impact craters on Venus: What are they telling us?', *J. Geophys. Res.* **97**, 13257–13301.

Schubert, G. and Anderson, C. (1985), 'Finite element calculations of very high Rayleigh number thermal convection', *Geophys. J. Roy. Astron. Soc.* **80**, 575–601.

Schubert, G., Cassen, P. and Young, R. (1979), 'Subsolidus convective cooling histories of the terrestrial planets', *Icarus* **38**, 192–211.

Schubert, G., Turcotte, D. P. and Olson, P. (2001), *Mantle Convection in the Earth and Planets*, Cambridge University Press, Cambridge.

Shahraki, M. and Schmeling, H. (2012), 'Plume-induced geoid anomalies from 2D axi-symmetric temperature- and pressure-dependent mantle convection models', *J. Geodyn.* **59-60**, 193–206.

Shanks, D. (1955), 'Non-linear transformation of divergent and slowly convergent sequences', *J. Math. Phys.* **34**, 1–42.

Solomatov, V. S. (1995), 'Scaling of temperature and stress-dependent viscosity convection', *Phys. Fluids* **7**(2), 266–274.

Solomatov, V. S. (2004), 'Initiation of subduction by small-scale convection', *J. Geophys. Res.: Solid Earth* **109**(B1).

Solomatov, V. S. and Moresi, L.-N. (1996), 'Stagnant lid convection on Venus', *J. Geophys. Res.* **101**(E2), 4,737–4,753.

Solomatov, V. S. and Moresi, L. N. (1997), 'Three regimes of mantle convection with non-Newtonian viscosity and stagnant lid convection on the terrestrial planets', *Geophys. Res. Lett.* **24**(15), 1907–1910.

Solomon, S. C. and Head, J. (1991), 'Fundamental issues in the geology and geophysics of Venus', *Science* **252**, 252–260.

Stein, C. and Hansen, U. (2013), 'Arrhenius rheology versus Frank-Kamenetskii rheology - Implications for mantle dynamics', *Geochem. Geophys. Geosyst.* **14**, 2757–2770.

Stemmer, K., Harder, H. and Hansen, U. (2006), 'A new method to simulate convection with strongly temperature-and pressure-dependent viscosity in a spherical shell: Applications to the Earth's mantle', *Phys. Earth Planet. Inter.* **157**(3), 223–249.

Stengel, K. C., Oliver, D. S. and Booker, J. R. (1982), 'Onset of convection in a variable-viscosity fluid', *J. Fluid Mech.* **120**, 411–431.

Stevenson, D. J. (2008), 'A planetary perspective on the deep Earth', *Nature* .

Stevenson, D. J. and Turner, J. S. (1979), Fluid models of mantle convection, *in* 'The Earth, Its Origin, Structure, and Evolution', Academic Press, New York, pp. 227–263.

Tackley, P., Ammann, M., Brodholt, J., Dobson, D. and Valencia, D. (2013), 'Mantle dynamics in super-Earths: Post-perovskite rheology and self-regulation of viscosity', *Icarus* **225**, 50–61.

Tackley, P. J. (1996), 'Effects of strongly variable viscosity on three-dimensional compressible convection in planetary mantles', *J. Geophys. Res.* **101**(B2), 3311–3332.

Tackley, P. J. (1998), 'Self-consistent generation of tectonic plates in three-dimensional mantle convection', *Earth Planet. Sci. Lett.* **157**(1), 9–22.

Tackley, P. J. (2000*a*), 'Self-consistent generation of tectonic plates in time-dependent, three-dimensional mantle convection simulations', *Geochem. Geophys. Geosyst.* **1**(8), 1021.

Tackley, P. J. (2000*b*), 'Self-consistent generation of tectonic plates in time-dependent, three-dimensional mantle convection simulations 2. Strain weakening and asthenosphere', *Geochem. Geophys. Geosyst.* **1**(8), 1026.

Tackley, P. J. (2009), Mantle geochemical dynamics, *in* D. Bercovici, ed., 'Mantle dynamics. Treatise on geophysics, vol. 7', Elsevier, Amsterdam, pp. 437–505.

Tackley, P. J. (2012), 'Dynamics and evolution of the deep mantle resulting from thermal, chemical, phase and melting effects', *Earth-Science Reviews* **110**(1-4), 1–25.

Taylor, F. B. (1910), 'Bearing of the tertiary mountain belt on the origin of the Earth's plan', *Geol. Soc. Am. Bull.* **21**, 179–226.

Torrance, K. E. and Turcotte, D. L. (1971), 'Thermal convection with large viscosity variations', *J. Fluid Mech.* **47**, 113–125.

Trompert, R. A. and Hansen, U. (1998), 'On the Rayleigh number dependence of convection with a strongly temperature-dependent viscosity', *Phys. Fluids* **10**(2), 351–360.

Turcotte, D. L. and Oxburgh, E. (1967), 'Finite amplitude convective cells and continental drift', *J. Fluid Mech.* **28**, 29–42.

van Keken, P. E. and Ballentine, C. J. (1998), 'Whole-mantle versus layered mantle convection and the role of a high-viscosity lower mantle in terrestrial volatile evolution', *Earth Planet. Sci. Letts.* **156**, 19–32.

Vynnycky, M. and Masuda, Y. (2013), 'Rayleigh-Bénard convection at high Rayleigh number and infinite Prandtl number: Asymptotics and numerics', *Phys. Fluids* **25**(11), 113602.

Weertman, J. and Weertman, J. R. (1975), 'High temperature creep of rock and mantle viscosity', *Ann. Rev. Earth Planet. Sci.* **3**, 293–315.

Wegener, A. (1915), *Die Enstehung der Kontinente und Ozeane*, Vieweg, Braunschweig.

Wegener, A. (1929), *Die Enstehung der Kontinente und Ozeane*, 4th edn, Vieweg, Braunschweig.

Wong, T. and Solomatov, V. S. (2015), 'Towards scaling laws for subduction initiation on terrestrial planets: constraints from two-dimensional steady-state convection simulations', *Progress in Earth and Planetary Science* **2**(1).

Wu, P. (1995), 'Can observations of postglacial rebound tell whether the rheology of the mantle is linear or nonlinear?', *Geophys. Res. Lett.* **22**, 1645–48.

Yoshida, M. and Kageyama, A. (2006), 'Low-degree mantle convection with strongly temperature- and depth-dependent viscosity in a three-dimensional spherical shell', *J. Geophys. Res.* **111**(B03412).

Zhang, S. and Yuen, D. A. (1995), 'The influences of lower mantle viscosity stratification on 3D spherical-shell mantle convection', *Earth Planet. Sci. Lett.* **132**, 157–166.

Zhong, S., Zuber, M. T., Moresi, L. and Gurnis, M. (2000), 'Role of temperature-dependent viscosity and surface plates in spherical shell models of mantle convection', *J. Geophys. Res.* **105**(B5), 11063–11.

Zimmerman, W. B. J. (2006), *Multiphysics modelling with finite element methods*, World Scientific Publishing Company, Singapore.